University of Catania
Department of Civil Engineering and Architecture

PhD in
“Evaluation and Mitigation of urban and territorial risks”
XXXII

Study of the static and dynamic behaviour of tunnel-soil-aboveground structure systems in urban areas

Sebastiano Corsico

Tutors
Prof. Maria Rossella Massimino (University of Catania)
Prof. Kyriazis Pitilakis (Aristotle University of Thessaloniki)
Eng. Antonino Pulejo (CMC Cooperativa Muratori e Cementisti Ravenna, Italy)

Coordinator
Prof. Massimo Cuomo

ACKNOWLEDGEMENTS

I am grateful to my supervisor, Prof. Maria Rossella Massimino of the University of Catania (Italy) for encouraging me to pursue postgraduate research, for his constant and fundamental support, for scientific guidance and for her suggestions during my PhD.

I car a lot to thank the Prof. Dimitris Pitilakis of the University of Thessaloniki (Greece) as supervisor during my research period at the University of Thessaloniki in Greece for his contribution to my research and for his constructive comments and suggestions during this research period.

Finally, I am grateful to Eng. Antonino Pulejo, project manager of the CMC (Cooperativa Muratori e Cementisti) company, for his support during the stage period at the metro construction site in Catania and for the opportunity given to me to learn about the various steps of tunnel excavation through Tunnel Boring Machine.

I would like to also thank the reviewers of my PhD thesis, Prof. Francesco Castelli of the Kore University of Enna (Italy) and the Prof. Giovanni Biondi of the University of Messina (Italy) or their useful and constructive suggestions.

Moreover, I am grateful for the help I have received from many people within the period of my PhD. Firstly, I owe a thank to Eng. Glenda Abate, a researcher at the University of Catania for her important scientific support to the review of the achieved results and the final report.

I car to thank the PhD student Zhongkai Huang of the Tonji University (China), for the great contribution made to the numerical model validation during the period of study spent at the Aristotle University of Thessaloniki (Greece).

Heartfelt thanks to all the people who contributed to my research: Prof. Salvatore Grasso and all colleagues from the geotechnical department of the University of Catania (Italy), colleagues from the geotechnical department of the Aristotle University of Thessaloniki (Greece), the entire staff of the CMC of Ravenna including Eng. Nicola Bona for their precious comments and suggestions.

Last, but not least, I own a great thank to my parents, for their endless support and encouragement throughout my studies.

Sebastiano Corsico

Special thanks to my Lord Jesus who supported me in my studies and He will always support me

"And Samuel took a stone and set it between Mizpah and Shen, and called the name of it Eben-ezer, and said: « hitherto the Lord has helped us. »"
Samuel 7,12

"*Allora Samuele prese una pietra, la pose tra Mispa e Sen e la chiamò Eben-Ezer e disse: « Fin qui l'Eterno ci ha soccorsi »"*
Samuele 7,12

ABSTRACT

Nowadays, it is becoming ever more evident that there is a growing need for underground structures, to solve the problems faced by transportation and utility networks. So, over the past fifty years, the geotechnical research community has devoted great attention to the construction of underground structures. Moreover, in seismic areas, it is extremely important to assess the possible damage to the tunnel and to the aboveground structures as a result of earthquakes. Great attention has recently been devoted to tunnel-soil systems, while studies involving tunnel plus soil plus aboveground structures (fully-coupled analyses) are still very rare.

The main purpose of the present thesis is to study the seismic behaviour of a tunnel-soil-aboveground structure system and evaluating the effects of the tunnel on the response of the aboveground building and vice versa employing FEM analyses.

Firstly, aspects concerning the excavation phase were studied proposing a simple and useful procedure for refining the soil profile established in the design phase of the tunnel, analysing the vibrations induced by the Tunnel Boring Machine on the surface during the digging.

After analysing aspects concerning the excavation phase, the dynamic response of the tunnel-soil-aboveground structure system was investigated through a series of parametric analyses employing FEM modelling, starting from a real case-history regarding the Catania (Italy) underground network. Great

attention was devoted to the role of the soil heterogeneity at the depth of the tunnel, not sufficiently studied up to now, performing a parametric analysis varying the degree of heterogeneity (in terms of impedance ratio). Then, other parametric analyses were performed, analysing the influence of: a) the different models adopted to describe the interface behaviour between the soil and the tunnel lining; b) the depth of the tunnel and the location of the aboveground building; c) the input motion applied at the bedrock of the model to study the influence of the frequency content of the earthquake on the seismic response of the coupled system tunnel-soil-aboveground structure. To take into the soil non-linearity, equivalent visco elastic linear analyses and visco elastoplastic analyses were performed, using a constitutive model for the soil with isotropic and kinematic hardening.

The achieved results were reported in terms of: peak ground acceleration, amplification ratios, amplification functions, seismic forces on the building. Bending moments and axial forces acting in the tunnel were also evaluated and compared with those obtained using the closed-form solutions proposed by Wang (1993) and Penzien (2000). The presented work highlights the extremely important role played by geotechnical aspects together with the full-coupled tunnel-soil-aboveground structure interaction.

CONTENTS

Chapter 1

STATE OF THE ART AND OBJECTIVES OF THE PROPOSED RESEARCH

Chapter 2

CONSTITUTIVE MODELS FOR SOILS

Chapter 3

FEM MODEL VALIDATION

Chapter 4

THE RAILWAY NETWORK OF CATANIA (ITALY): FROM A CASE-HISTORY TO PARAMETRIC ANALYSES

LIST OF FIGURES

LIST OF TABLES

INTRODUCTION

Nowadays, it is becoming ever more evident that there is a growing need for underground structures, to solve the problems faced by transportation and utility networks. In particular, tunnels can lead to a lowering of the environmental pollution generated by road traffic, thus improving the quality of life and reducing costs for citizens. So, over the past fifty years, the geotechnical research community has devoted great attention to the construction of underground structures. Moreover, in seismic areas, it is extremely important to assess the possible damage to the tunnel and to the aboveground structures as a result of earthquakes. Historically, tunnels have experienced a lower rate of damage than aboveground structures. Nevertheless, recent studies have documented significant damage suffered by tunnels due to seismic events.

During an earthquake, the presence of shallow tunnels may alter the response of aboveground structures and, at the same time, vibrations of aboveground structures may modify the dynamic response of tunnels.

Great attention has recently been devoted to tunnel-soil systems, while studies involving tunnel plus soil plus aboveground structures (full-coupled analyses) are still very rare.

The main purpose of the present thesis is studying the seismic behaviour of a tunnel-soil-aboveground structure system and evaluating the effects of the tunnel on the response of the aboveground building and vice versa employing FEM analyses.

Initially, a cross-section of the recently-built underground network in Catania (Italy) was analysed. Then, numerous parametric analyses were performed, varying the main characteristics of the system to study their effects on the dynamic tunnel-soil-aboveground structure interaction.

The first chapter deals with the objects of the work and the state-of-art concerning the dynamic response of underground structures. Particular attention was devoted to the analytical solutions for tunnel bending moment and axial force evaluation. In the existing solutions, the response of a tunnel lining was expressed as a function of the compressibility and flexibility ratios of the tunnel and the overburden pressure and at-rest coefficient of the earth pressure of the soil.

The second chapter describes the most used constitutive models for the soil. Because of the complex nature of the soil, the development of constitutive models capable of capturing 'real' soil behaviour is a key aspect of analyses of geotechnical structures. For a long time, elastic modelling has been successfully used in soil mechanics to describe the general behaviour of soil under initial working load conditions, but it fails to predict the behaviour of soil moving toward ultimate conditions because plastic deformations become dominant at this load level while elastic deformations play a minor role. At present, there is much research activity in the field of constitutive models. Among these, the Severn-Trent model, a non-associative elasto-plastic model with isotropic and kinematic hardening (Gajo and Muir Wood, 1999 ab), is briefly described in this Chapter, because it was chosen for modelling the dynamic soil behaviour in the performed FEM analyses.

The third chapter shows the validation of the developed FEM model. The validation of the model was performed in 5 steps: in the first step a visco-elastic-linear analysis of a stiff layered undamped soil on an elastic soil was performed; in the second step a visco-elastic-linear analysis of a soft layered undamped soil on an elastic soil was performed; in the third step an equivalent visco-elastic-linear analysis of a coupled system soil-tunnel was performed; in the fourth step a perfectly plastic analysis of the coupled tunnel-soil system was performed; finally, numerical analyses of a centrifuge test was performed.

The fourth chapter deals with the results of the performed FEM analyses. As previously mentioned, the analyses have initially concerned with a cross-section of the underground network case-history of Catania (Italy); then, numerous parametric analyses were performed.

Firstly, a simple and useful procedure for validating/refining the soil profile established in the design phase of the tunnel is presented. This procedure compared the data obtained from the geotechnical survey at the design phase with the data coming from the HVSR method (Nakamura 1989), applied in the analysed case-history to the microtremors induced on the soil surface layers by the TBM (Tunnel Boring Machin) during tunnelling. The used TBM could dig in two ways: OF (Open Face) and EPB (Earth Pressure Balance) modes, switching frequently from one to the other, due to the strong heterogeneity of the subsoil in Catania, for the different lava flows caused by volcanic eruptions on Mount Etna near Catania. For this kind of subsoil, any additional information on the soil profile involved in the TBM digging is extremely useful. Geological and geotechnical information about the rocks and soils at the digging front is fundamental, firstly to define the appropriate digging mode and, consequently, to choose the correct front pressure to guarantee stability at the digging front. An error in the estimation of the front pressure can cause subsidence or uplift problems with disastrous effects in urban areas.

After analysing aspects concerning the excavation phase, the dynamic response of the tunnel-soil-aboveground structure system was investigated. The chosen cross-section of the underground in Catania (Italy) is characterized by a strong heterogeneity with alternation of incoherent and rock soil. So, firstly, the role of this strong discontinuity present at the depth of the tunnel was analysed, performing a parametric analysis varying the degree of heterogeneity (in terms of impedance ratio). Then, other parametric analyses were performed, analysing the influence of:

- the different models adopted to describe the interface behaviour between the soil and the tunnel lining. Two limit conditions, i.e. "Full-Slip" condition, for which a complete sliding is permitted between the soil and tunnel lining and "No-Slip" condition, for which sliding is not permitted, were modelled. In the real case, the interface behaviour must be described through an intermediate condition between the two limit conditions. So, the results obtained for the two limit conditions were compared with those achieved using a contact surface that permits sliding phenomena;
- the depth of the tunnel and the location of the aboveground building. Initially, the real configuration was analysed, considering a depth of the tunnel equal to 17 meters from the ground surface and the building having its symmetry vertical axis distant 20 meters from the axis of the tunnel. Then, different depths of the tunnel (12 m and 7 m) and different positions of the building (5 m between the building axis and the tunnel one and building axis coincident with the tunnel one) were analysed;
- the input motion applied at the bedrock of the model. Three earthquakes were adopted, scaled to the same PGA, to study the influence of the frequency content of the earthquake on the seismic response of the coupled system tunnel-soil-aboveground structure;
- the different constitutive models adopted for describing the dynamic behaviour of the soil used. In particular, three different constitutive models were used: 1) a linear visco-elastic model; 2) an equivalent linear visco-elastic model using soil "equivalent" properties depending on the achieved strain

level, evaluated by 1D analyses utilizing G-γ and D-γ curves; 3) a visco-elastoplastic constitutive model, characterised by isotropic and kinematic hardening and a non-associated flow rule: the Severn-Trent model (described at Chapter 2);

The achieved results were reported in terms of, peak ground acceleration, amplification ratios, amplification functions, seismic forces on the building. Bending moments and axial forces acting in the tunnel were also evaluated and compared with those obtained using the closed-form solutions proposed by Wang (1993) and Penzien (2000).

The presented work highlights the extremely important role played by geotechnical aspects together with the full-coupled tunnel-soil-aboveground structure interaction, and in turns the influence of input frequency, tunnel depth, building position in the seismic response of tunnel-soil-aboveground structure systems.

Chapter 1

STATE-OF-THE-ART AND OBJECTIVES OF THE PROPOSED RESEARCH

1.1 Introduction

The aim of the proposed research is the study of the static and dynamic behaviour of tunnel-soil-aboveground structure systems in urban areas. The research is performed with the financial support of the PON - FSE-FESR - R&I 2014-2020 “Innovative PhDs with Industrial Characterization”.

In particular, dynamic tunnel-soil-aboveground building interaction is a complex problem and the analysis can be performed through coupled FEM numerical analysis. It is extremely important to evaluate the possible damage to the tunnel and to the aboveground structures, due to a seismic event, to provide adequate mitigation measures (Abate et al., 2015, Biondi et al., 2015). Unfortunately, up to now dynamic tunnel-soil-aboveground structure interaction analyses are still very rare; on the other hand, static tunnel-soil-aboveground structure interaction has already been studied quite extensively (Wasif Naqvi et al. 2020). Several studies were performed to analyse the effects of the construction of building in the vicinity of the tunnel. Haibin et al. (2014) studied the interaction of foundation with the tunnel; other authors studied the effect of piling on the existing tunnel (Yao et al. 2008; Salim and Jafaar Lafta 2017) and the effect of tunnelling on the pile foundation (Jacobsz et al. 2004;

Marshall and Haji 2015; Cheng et al. 2004; Lee et al. 2009; Zidan and Ramadan 2015).

Dynamic analyses are fundamental in areas with high seismic risk, as the eastern Sicily (Cavallaro et al., 2012, Imposa et. Al, 2016, Monaco et al., 2011).

In the last years, the need to build underground structures has increased in order to resolve the problems faced by transportation and utility networks. In particular, the underground structures contribute to the decrease of traffic on the roads and consequently to the reduction of air pollution. For this reason, the geotechnical research community has devoted great attention to this topic over the past fifty years.

Historically, underground structures have experienced a lower rate of damage than aboveground structures (Kawashima 2000). Nevertheless, recent studies have documented significant damage suffered by underground structures due to seismic events (Power et al. 1998; Hashash et al. 2001; Wang et al. 2001, 2009; Kontoe et al. 2008; Gazetas 2014). During an earthquake, the vibrations of aboveground structures may create a complex interaction with tunnels, and as a consequence, they may affect the seismic wave propagation field (Lee and Karl 1992; De Barros and Luco 1993). Thus doing, they may modify the dynamic response of tunnels while, at the same time, the presence of tunnels at shallow depth close to foundations of aboveground structures may alter the response of above- ground structures.

Seismic design of aboveground and underground structures is commonly performed using design spectra provided by national technical codes or, in some “advanced” designs, using design acceleration time-histories resulting from 1D free-field soil response analyses. These procedures can lead to erroneous evaluations of the “real” inputs which hit aboveground and underground structures due to complex interactions involving the soil, the tunnels and the aboveground structures. Great attention has recently been devoted to separated tunnel–soil interaction analyses (St. John and Zahrah 1987; AFPS/AFTES, 2001; Hashash et al. 2005; Anastasopoulos et al. 2007; Kouretzis et al. 2007; Anastasopoulos and Gazetas 2007; 2008; 2010; FHWA 2009; Lanzano et al., 2012; Argyroudis et al. 2017; Huang et al., 2020) and soil–aboveground structure interaction analyses (Abate et al. 2006; Pecker and Chatzigogos 2010; Adamidis et al. 2014; Gazetas 2015; Wang et al. 2017, 2018). On the contrary, studies involving tunnel plus soil plus aboveground structures (fully-coupled analyses) are still very rare (Luco and De Barros 1994; Kouretzis et al.; Kouretzis et al. 2007; Smerzini et al., 2009; Tsinidis et al., 2014; Abate et al., 2015, 2017a; 2017 b).

1.2 Methodologies and contents of the proposed research

Underground structures have features that make their seismic behaviour distinct from most surface structures, most notably their complete enclosure in soil or rock, and their significant length.

Several studies have documented earthquake damage to underground facilities. ASCE (American Society of Civil Engineers, 1974) describes the damage in the Los Angeles area as a result of the 1971 San Fernando Earthquake. JSCE (Japanese Society of Civil Engineers, 1988) describes the performance of several underground structures, including an immersed tunnel during shaking in Japan. Duke and Leeds (1959), Stevens (1977), Dowding and Rozen (1978), Owen and Scholl (1981), Sharma and Judd (1991), Power et al. (1998) and Kaneshiro et al. (2000), present summaries of case histories of damage to underground facilities. Owen and Schollhashas (1981) have updated Dowding and Rozen's work with 127 case histories. Sharma and Judd (1991) generated an extensive database of seismic damage to underground structures using 192 case histories. Power et al. (1998) provide a further update with 217 case histories (Hashash et al., 2001).

The following general observations can be made regarding the seismic performance of underground structures:

- underground constructions suffer appreciably less damage than surface structures;
- deep tunnels seem to be safer and less vulnerable to earthquake shaking than are shallow tunnels;
- underground building in rock, usually, suffer less damage than underground in the soil;
- damage may be related to peak ground acceleration and velocity based on the magnitude and epicentral distance of the affected earthquake and the duration of strong-motion shaking;
- the ground motion may be amplified upon incidence with a tunnel if wavelengths are between one and our times the tunnel diameter.

Earthquake effects on underground structures can be grouped into two categories:

1) ground shaking;
2) ground failure such as liquefaction, fault displacement, and slope instability.

Ground shaking, which is the primary focus of this thesis, refers to the deformation of the ground produced by seismic waves propagating through the earth's crust. The major factors influencing shaking damage include: 1. the shape dimensions and depth of the structure; 2. the properties of the surrounding soil or rock; 3. the properties of the structure; 4. the severity of the ground shaking (Dowding and Rozen, 1978; St. John and Zahrah, 1987).

Underground structures are constrained by the surrounding soil. For this reason, it is unlikely that they could move to any significant extent independently of the soil. Compared to surface structures, which are generally unsupported above their foundations, the underground structures can be considered to display significantly greater degrees of redundancy thanks to the support from the soil. These are the main factors contributing to better earthquake performance data for underground structures than the surface structures.

The inertia of the surrounding soil is much higher than the inertia of the structure itself; consequently, the response of the embedded structure is dominated by the response of the surrounding soil. This feature makes the seismic behaviour of underground structures very distinct from the typical aboveground structures, where the response is mainly related to the inertia of the structure (Wang, 1993; Hashash et al., 2001, Pitilakis and Tsinidis, 2014).

For aboveground structures, the intensity of earthquake ground motion is widely described by the peak ground acceleration, the design response spectra, the inertial forces and the performance of the structures caused by ground shaking. For underground structures, the peak ground acceleration is not a good parameter, because tunnels are more sensitive to the distortions. So, the seismic response of underground structures can be described by the deformations induced by the earthquake on the ground.

The different response characteristics of aboveground and underground structures suggest in routine design the following different approaches (Wang, 1993):

- *Force Method* for Surface Structures for which, the seismic loads are usually expressed in terms of inertial forces. The traditional methods generally involve the application of equivalent or pseudo-static forces in the analysis.
- *Deformation Method* for Underground Structures. The seismic response of underground structures is more sensitive to earthquake-induced deformations.

The response of tunnels to seismic shaking motions has been often approximated to that of an elastic beam subjected to deformations imposed by the surrounding ground.

1.2.1 Seismic response mechanism

Three principal types of deformations describe the response of underground structures to seismic waves (Owen and Scholl, 1981), as shown in Figure 1.1:

- Axial compression and extension (Figure 1.1a, b);
- Longitudinal bending (Figure 1.1c, d);
- Ovaling (for circular tunnels) or racking (for rectangular tunnels such as cut-and-cover tunnels) (Figure 1.1e, f).

Axial deformations in underground structures are generated by the components of seismic waves that produce motions parallel to the axis of the tunnel and cause alternating compression and tension. Bending deformations are caused by the components of seismic waves producing particle motions perpendicular to the longitudinal axis (Wang, 1993).

The ovaling or racking deformations of a tunnel structure may develop when waves propagate in a direction perpendicular or nearly perpendicular to the tunnel axis, resulting in a distortion of the cross-sectional shape of the tunnel lining. The general behaviour of the lining may be simulated as a buried structure subjected to ground deformations under a two-dimensional, plane-strain condition. Ovaling and racking deformations may be caused by vertically, horizontally or obliquely propagating seismic waves of any type. Many previous studies have suggested, however, that the vertically propagating shear wave is the predominant form of earthquake loading that governs the tunnel lining design against ovaling/racking.

Primarily, to evaluate the seismic response of underground structures is necessary to estimate the seismic parameter for the analysis and to evaluate the ground response to shaking.

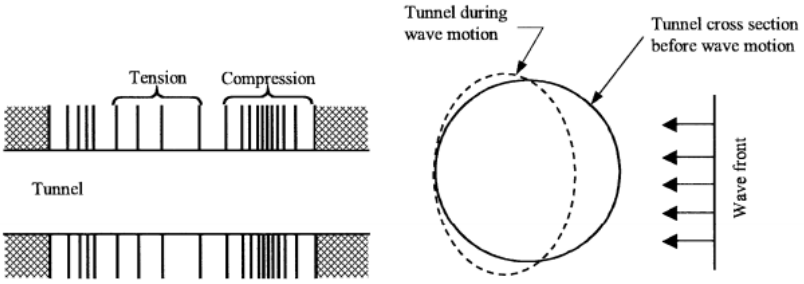

(a) Compression-extension (b) Compression of tunnel section

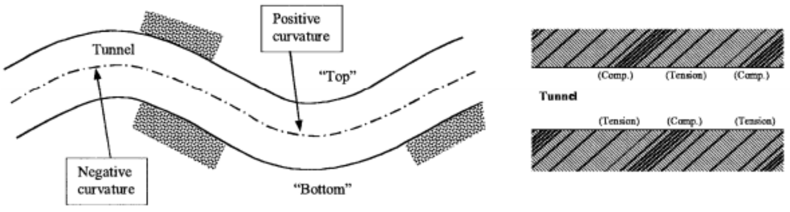

(c) Longitudinal bending (d) Diagonally-propagating wave

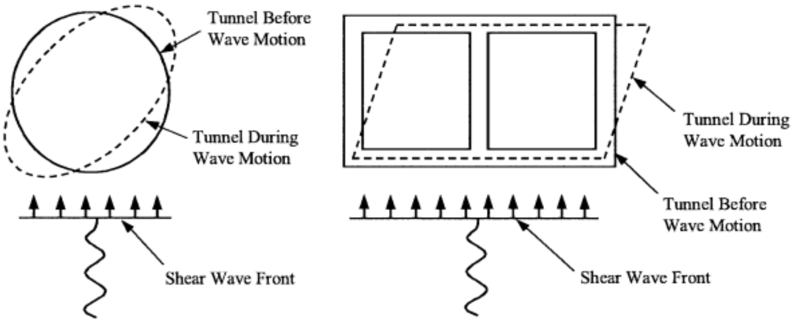

(e) Ovaling of tunnel section (f) Racking of tunnel section

Figure 1.1: Deformation along the tunnel line due to the seismic load (Owen and Scholl, 1981)

1.2.2 Definition of seismic environment

The design level of shaking is typically defined by a design ground motion, which is characterized by the amplitudes and characteristics of expected ground motions and their expected return frequency (Kramer, 1996). A seismic hazard analysis is used to define the level of shaking and the design earthquake.

A seismic hazard analysis typically characterizes the potential for strong ground motions by examining the extent of active faulting in a region, the potential for fault motion, and the frequency with which the faults release stored energy.

There are two methods of analysis:

1) the deterministic seismic hazard analysis (DSHA);
2) the probabilistic seismic hazard analysis (PSHA).

1.2.2.1 Deterministic seismic hazard analysis (DSHA)

To define the seismic scenario for a site, according to the DSHA, the following steps may be performed:

1) identification and characterization of all earthquake sources capable of producing significant ground motion at the site, including definition of the geometry and earthquake potential of each;
2) selection of a source-to-site distance parameter for each source, typically the shortest epicentral or hypo-central distance or the distance to the closest ruptured portion of the fault;
3) selection of a controlling earthquake that produces the strongest shaking level at the site, expressed in terms of a ground motion parameters at the site (attenuation relationship are usually used to define these parameters from data recorded near the site to be analyzed);
4) definition of the seismic hazard at the site in terms of the peak ground acceleration (or velocity and displacements), acceleration response spectrum.

Once the seismic hazard at the site is characterized, the level of design earthquake or seismicity has to be defined.

About that, the Maximum Design Earthquake, MDE, is defined in a DSHA as the maximum level of shaking that can be experienced at the site.

This method is useful to evaluate the worst-case scenarios at the site to analyse, without to provide any information about the frequency of occurrence of the controlling earthquake.

For this reason, a probabilistic seismic hazard analysis is mostly used o evaluate the seismic scenario for a site.

1.2.2.2 Probabilistic seismic hazard analysis (PSHA)

To define the seismic scenario for a site, according to the PSHA, the following steps may be performed Reiter (1990):

1) identification and characterization of earthquake sources, including the probability distribution of potential rupture locations within the source zone;
2) characterization of the seismicity or temporal distribution of earthquake recurrence. Information obtained from historical data can be useful to develop a recurrence relationship that describes the average rate at which an earthquake of a certain size will be exceeded;
3) determination of the ground motion produced at the site by any earthquake using attenuation relationship;
4) combination of the uncertainties to obtain the probability that a given ground motion parameter will be exceeded during a given time.

To define the level of design earthquake, according to PSHA, the probability of exceedance for the ground motion parameters must be estimated. Two design levels are defined according to the NTC18:

- Maximum Design Earthquake (MDE) is defined as an event with a small probability of exceedance during life (5-10%). According to this level of design, the safety shall be maintained during and after the design earthquake;
- Operating Design Earthquake (ODE) is defined as an event with a probability of exceedance during the life of about 63%-81%. During the ODE seismic event, the response of the underground structure must remain within the elastic range.

1.3 Evaluation of ground response to shaking

The evaluation of ground response to shaking can be divided into two groups:

1) ground failure: liquefaction, slope instability and fault displacement are to be noted and it is particularly prevalent at tunnel portals and in shallow tunnels;
2) in the absence of ground failure, the design focus shifts to the ground deformation induced by a seismic wave. Underground structures can be assumed to undergo three primary modes of deformation during seismic shaking: compression/extension, longitudinal bending and ovaling/racking (Figure 1.1).

In this work, the attention has been mainly focused on the ground shaking up to the soil surface, involving or not an aboveground structure, and ovaling/racking on the underground structures.

In the next sections, the effects due to design earthquakes are quantified. This requires an understanding of the deformations induced by seismic waves in the ground and of the interaction of the underground structures and the aboveground structures with the ground.

1.3.1 Free field deformation approach

The ground strains caused by seismic waves in the absence of structures (free field deformations) provide an estimate of the deformation of the structures. This is a simplified approach since it is not taken into account the interaction between the underground structures and the surrounding soil. This simplified approach usually provides an upper-bound estimate of the strains that may be induced in the structures by the travelling waves. The greatest advantage of this approach is that it requires the least amount of input. These deformations may be directly imposed on the structure. This approach may overestimate or underestimate structure deformations depending on the rigidity of the structure relative to the soil.

For practical purposes, a simplified approach was proposed by Newmark (1968) and has been considered by others (Sakurai and Takahashi, 1969; Yeh, 1974; and Agrawal et.al, 1983). This approach is based on the theory of wave propagation in homogeneous, isotropic, elastic media.

This thesis concerns with the behaviour of a circular cross section of underground structures. Along this transversal cross-section, the principal strain is the ovaling deformation (Figure 1.1e) for circular tunnels. Ovaling deformations develop when waves propagate perpendicular to the tunnel axis. Consequently, the design of the tunnel lining under ovaling deformation is carried out analysing the transverse direction, under two-dimensional, plane strain conditions The results are cycles of additional stress concentrations with alternating compressive and tensile stresses in the tunnel lining.

Studies have suggested that while ovaling may be caused by waves propagating horizontally or obliquely, vertically propagating shear waves are the predominant form of earthquake loading that causes these types of deformations (Wang, 1993). It causes in circular tunnels to oval and in rectangular tunnels to rack (sideways motion), as shown in Figure 1.1.

Ground shear distortions can be defined, as shown in Figure 1.2, for non-perforated ground, expressing the maximum diametric strain as a function of the maximum free-field shear strain only:

$$\frac{\Delta d}{d} = \pm \frac{\gamma_{max}}{2} \tag{1.1}$$

The diametric strain in a perforated ground is related to the Poisson's ratio of the medium (soil or rock):

$$\frac{\Delta d}{d} = \pm 2\gamma_{max}(1 - \nu_m) \tag{1.2}$$

Where "d" is the diameter of the tunnel, γ_{max} is the maximum free-field shear strain and ν_m is the Poisson's ratio of the medium.

Both of the equations (1.1) and (1.2) assume the absence of any underground structure, therefore ignore tunnel - soil interaction.

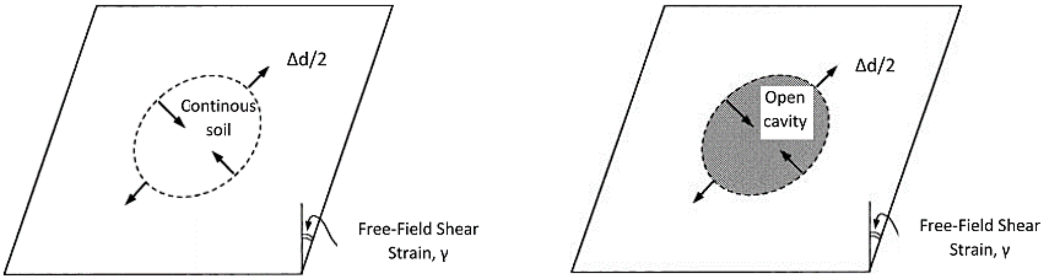

Figure 1.2: Free-field shear distortion of non-perforated and perforated ground - circular shape (Wang, 1993)

When a circular lining is assumed to oval following the deformations imposed by the surrounding ground (e.g., shear), the lining's transverse sectional stiffness is completely ignored. This assumption is probably reasonable for most circular tunnels in rock and in stiff soils because the lining stiffness against distortion is low compared with that of the surrounding medium. Depending on the definition of “ground deformation of a surrounding medium,” however, a design based on this assumption may be overly conservative in some cases and non-conservative in others.

The free-field deformation method is a simple and effective design tool when ground distortions are small (i.e. low shaking intensity, very stiff ground, or the structure is flexible compared to the surrounding soil). However, in many cases, especially in soft soils, the method gives overly conservative designs because free-field ground distortions in soft soils are generally large.

The free-field deformation method is a simple design approach of underground structures, but his validity is limited to small ground distortion.

Consequently, the method is applicably for low seismic event intensity, when the underground structure is surrounded by stiff soil or when the flexibility of the underground structure is low compared to the surrounding soil. For soft soil, the free-field deformation method is conservative for the large deformations that occur during a seismic event.

The free-field method can be used, generally, for a first estimate of the deformations that occur in the soil and on the tunnel lining, but for a better design of the structures, the use of a method that takes into account the soil-structure interaction is necessary.

The next sections show the most used closed-form elastic solutions for circular tunnels subjected to axial force, bending moment and ovaling deformation.

1.3.2 Closed-form elastic solutions for circular tunnels considering soil-tunnel interaction

The presence of an underground structure modifies the free field ground deformations. The following sections describe procedures that model soil-structure interaction. When it is stiff in its longitudinal direction relative to its surrounding soils, the tunnel structure resists, rather than conforms to, the deformations imposed by the ground. Analysis of tunnel-ground interaction that considers both the tunnel stiffness and ground stiffness plays a key role in finding the tunnel response.

To analyse the soil-structure interaction effects, a beam on an elastic foundation approach is generally used. The solution does not take into account inertial interaction effects.

In general, the tunnel-ground system is simulated, according to the theory of wave propagating in an infinite, homogeneous, isotropic medium. When subjected to the axial and curvature deformations caused by the travelling waves in the ground, the tunnel will experience the following forces (see Figure 1.3):

- Axial forces, N, on the cross-section due to the axial deformation;
- Bending moments, M, and shear forces, V, on the cross-section due to the curvature deformation.

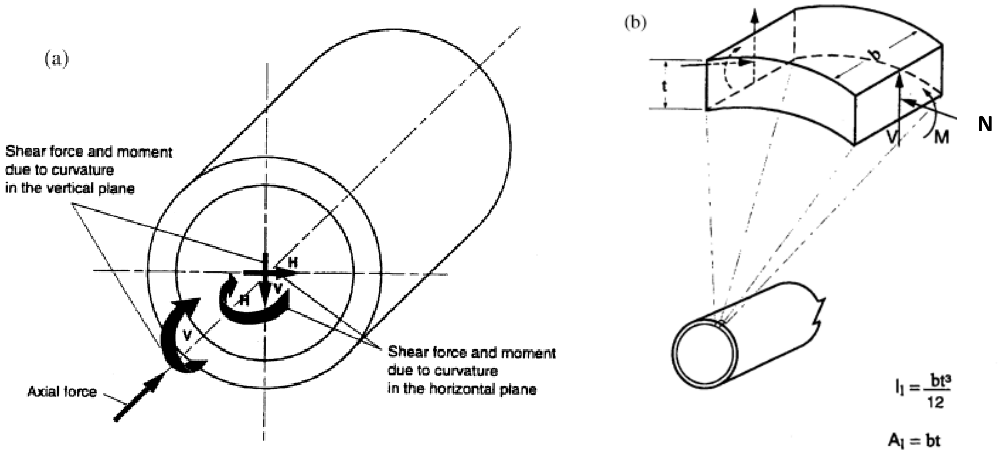

Figure 1.3: Induced forces and moments caused by seismic waves (Power et al., 1996) a) Induced forces and moments caused by waves propagating along tunnel axis; b) Induced circumferential forces and moments caused by waves propagating perpendicular to the tunnel axis.

The maximum axial strain, caused by a 45° incident shear wave, is (St. John and Zahrah, 1987):

$$\varepsilon_{max}^{a} = \frac{\frac{2\pi}{L}A}{2+\frac{E_l A_C}{K_a}\left(\frac{2\pi}{L}\right)^2} \leq \frac{fL}{4E_l A_C} \tag{1.3}$$

where:

- L is the wavelength of a sinusoidal shear wave;
- A is the free-field displacement response amplitude of an ideal sinusoidal shear wave according to the following expressions:

$$\frac{2\pi A}{L} = \frac{V_S}{C_S} sin\phi cos\phi \quad \text{for free-field axial strains} \tag{1.4}$$

$$\frac{4\pi^2 A}{L^2} = \frac{a_S}{C_S} \cos^3 \phi \quad \text{for free-field bending strains} \tag{1.5}$$

- A_C is the cross-section area of tunnel lining;
- E_l is the elastic modulus of the tunnel lining;
- *f* is the ultimate friction force, per unit length between the tunnel and surrounding soil;
- K_a is the longitudinal spring coefficient of medium, in force per unit deformation per unit length of the tunnel, according to the following expression 1.9 (St. John and Zahrah, 1987)

$$K_a = \frac{16\pi G_m(1-\nu_m)}{3-4\nu_m}\frac{d}{L} \tag{1.6}$$

where G_m and ν_m are the shear modulus and Poisson's ratio of the soil, "d" is the diameter of circular tunnel or height of the rectangular structure.

The maximum bending strain, caused by a 0° incident shear wave, is:

$$\varepsilon_{max}^{b} = \frac{\left(\frac{2\pi}{L}\right)^2 A}{1+\frac{E_l A_C}{K_t}\left(\frac{2\pi}{L}\right)^4} r \tag{1.7}$$

where:

- $K_t = K_a$ for isotropic medium;
- I_C is the moment of inertia of the tunnel section;
- "r" is the radius of the circular tunnel or half height of a rectangular tunnel;

Since both the liner and the medium are assumed to be linear elastic, these strains may be superimposed.

The following expressions show the maximum shear force and the maximum bending moment acting a tunnel cross-section:

$$V_{max} = \frac{\left(\frac{2\pi}{L}\right)^3 E_l I_C A}{1+\frac{E_l I_C}{K_t}\left(\frac{2\pi}{L}\right)^4} = \left(\frac{2\pi}{L}\right) \tag{1.8a}$$

$$M_{max} = \left(\frac{2\pi}{L}\right)\left(\frac{E_l I_C \varepsilon_{max}^b}{r}\right) \tag{1.8b}$$

A conservative estimate of the total axial strain and stress is obtained by combining the strains from the axial and bending forces modified from Power et al.,. 1996:

$$\varepsilon^{ab} = \varepsilon_{max}^a + \varepsilon_{max}^b \tag{1.9}$$

Summing up:

- the ground stiffness and the tunnel stiffness are represented by spring coefficients (K_a or K_t) and sectional modulus ($E_C A_C$ or $E_C I_C$), respectively. These spring constants represent the ratio of pressure between the tunnel and the medium and the reduced displacement of the medium when the tunnel is present;
- the application of these equations is necessary only when tunnel structures are built-in soft ground. For structures in rock or stiff soils, the evaluation

based on the free-field ground deformation approach described above, in general, is satisfactory.

Matsubara et al. 1995 provide a discussion of input wavelengths for underground structure design. The incident wavelength of a ground motion may be estimated as:

$$L = T \cdot C_S \tag{1.10}$$

where T is the natural period of the soil (Dobry et al., 1976; Power et al., 1996).

Idriss and Seed (1968) recommend that:

$$T = \frac{4h}{C_S} \tag{1.11}$$

where "h" is the thickness of the soil deposit, if ground motion can be attributed primarily to shear waves and the medium is assumed to consist of a uniform soft soil layer overlying a stiff layer (St. John and Zahrah, 1987).

Thanks to previous studies of tunnel racking deformations (Burns and Richard 1964; Hoeg 1968), in the '70s Peck et al. (1972) proposed very interesting closed form solutions in terms of bending moments and axial forces under external loading conditions. The response of a tunnel lining was expressed as a function of the compressibility and flexibility ratios of the tunnel and the overburden pressure and at-rest coefficient of the earth pressure of the soil.

In particular, for circular tunnels, the compressibility and flexibility ratios (C and F), which are respectively measures of the extensional and flexural stiffness of the soil relative to the tunnel, are given by (Merritt et al. 1985):

$$C = \frac{E_m(1-\nu_l^2)R}{E_l t(1+\nu_m)(1-2\nu_m)} \tag{1.12}$$

$$F = \frac{E_m(1-\nu_l^2)R^3}{6E_l I(1+\nu_m)} \tag{1.13}$$

where:

- E_m is the modulus of elasticity of the medium;
- E_l is the modulus of elasticity of the tunnel lining;
- “I” is the moment of inertia of the tunnel lining (per unit width);
- ν_m is the Poisson's ratio of the medium;
- ν_l is the Poisson's ratio of the tunnel line;
- R and “t” are the radius and the thickness of the tunnel lining.

The value of the flexibility ratio, F, is closely related to the expected stress level on the structure:

- $F \rightarrow 0$: the structure is quite rigid and will not display any deformation;
- $F < 1$: the structure is stiffer than the surrounding soil, thus the structural deformation level will be smaller than the free-field deformation level;
- $F = 1$: the structure and the surrounding soil share the same level of stiffness, therefore the tunnel will follow the free-field deformation;
- $F > 1$: the surrounding soil is stiffer than the structure, therefore the deformation of the structure is amplified compared to the free-field deformations.

Wang (1993) reformulated the equations given by Peck et al. (1972) for evaluating the diametric strain, the maximum bending moment M_{max} and the maximum axial force N_{max}, in the lining in the transverse section per unit of longitudinal dimension, due to seismic loadings caused by shear waves.

For both Full-Slip and No-Slip conditions at the soil–tunnel interface M_{max} can be computed as:

$$\frac{\Delta d}{d} = \pm \frac{1}{3} K_1 F \cdot \gamma_{max} \tag{1.14}$$

$$M_{max} = \pm \frac{1}{6} K_1 \frac{E_m}{(1+\nu_m)} r^2 \cdot \gamma_{max} \tag{1.15}$$

where γ_{max} is the maximum shear strain at tunnel depth and:

$$K_1 = \frac{12(1-\nu_m)}{2F+5-6\nu_m} \tag{1.16}$$

As regards N$_{max}$, for Full-Slip conditions it is:

$$N_{max} = \pm \frac{1}{6} K_1 \frac{E_m}{(1+\nu_m)} r \cdot \gamma_{max} \tag{1.17}$$

According to various studies, slip at the interface is only possible for tunnels in soft soils or cases of severe seismic loading intensity. For most tunnels, the interface condition is between Full-Slip and No-Slip, so both cases should be investigated for critical lining forces and deformations. However, Full-Slip assumptions under simple shear strain may cause significant underestimation of the maximum axial force, so it has been recommended that the No-Slip assumption of complete soil continuity be made in assessing the lining axial response (Hoeg,. 1968; Schwartz and Einstein, 1980). Thus, as regards N$_{max}$, for Full-Slip conditions it is:

$$N_{max} = \pm K_2 \tau_{max} \cdot r = \pm K_2 \frac{E_m}{2(1+\nu_m)} r \gamma_{max} \tag{1.18}$$

where:

$$K_2 = 1 + \frac{F[(1-2\nu_m)-(1-2\nu_m)C]-\frac{1}{2}(1-2\nu_m)^2+2}{F[(3-2\nu_m)+(1-2\nu_m)C]+C\left[\frac{5}{2}-8\nu_m+6\nu_m^2\right]+6-8\nu_m} \tag{1.19}$$

The axial forces induced by the seismic wave increase with decreasing compressibility and flexibility ratios when the Poisson's ratio of the surrounding ground is less than 0.5. As Poisson's ratio approaches 0.5 (i.e. saturated undrained clay), the thrust response is independent of compressibility because the soil is considered incompressible (Wang, 1993).

The normalized lining deflection provides an indication of the importance of the flexibility ratio in lining response, and is defined as (Wang, 1993) :

$$\frac{\Delta d_{lining}}{\Delta d_{free-field}} = \frac{2}{3} K_1 F \tag{1.20}$$

According to this equation, a tunnel lining will deform less than the free field when the flexibility ratio is less than one (i.e. stiff lining in soft soil). As the flexibility ratio increases, the lining deflects more than the free field and may reach an upper limit equal to the perforated ground deformations. This condition continues as the flexibility ratio becomes infinitely large i.e. perfectly flexible lining.

Penzien (2000) provided an analytical procedure for evaluating racking deformations of rectangular and circular tunnels that supplemented the previous studies. To estimate the distortion of the structure, a lining-soil racking ratio is defined as:

$$R = \frac{\Delta_{structure}}{\Delta_{free-field}} \tag{1.21}$$

In the case of the circular tunnel, R is the ratio of lining diametric deflection and free-field diametric deflection. Assuming Full-Slip condition, solutions for bending moment, axial force, and in circular tunnel linings caused by soil-structure interaction during a seismic event are expressed as (Penzien, 2000):

$$\pm\Delta d_{lining}^{n} = \pm R^{n}\Delta d_{free-field}^{n} \tag{1.22}$$

$$M(\theta) = \pm\frac{6E_l I\Delta d_{lining}^{n}}{d^2(1-\nu_l^2)}cos2\left(\theta+\frac{\pi}{4}\right) \tag{1.23}$$

$$N(\theta) = \pm\frac{12E_l I\Delta d_{lining}^{n}}{d^3(1-\nu_l^2)}cos2\left(\theta+\frac{\pi}{4}\right) \tag{1.24}$$

$$V(\theta) = \pm\frac{24E_l I\Delta d_{lining}^{n}}{d^3(1-\nu_l^2)}sin2\left(\theta+\frac{\pi}{4}\right) \tag{1.25}$$

where:

$$R^{n} = \pm\frac{4(1-\nu_m)}{(\alpha^{n}+1)} \tag{1.26}$$

$$\alpha^{n} = \frac{12E_l I(5-6\nu_m)}{d^3\,G_m(1-\nu_l^2)} \tag{1.27}$$

In the case of the No-Slip condition, the formulations are presented as:

$$\pm\Delta d_{lining} = \pm R^{n}\Delta d_{free-field} \tag{1.28}$$

$$M(\theta) = \pm\frac{6E_l I\Delta d_{lining}}{d^2(1-\nu_l^2)}cos2\left(\theta+\frac{\pi}{4}\right) \tag{1.29}$$

$$N(\theta) = \pm\frac{24E_l I\Delta d_{lining}}{d^3(1-\nu_l^2)}cos2\left(\theta+\frac{\pi}{4}\right) \tag{1.30}$$

$$V(\theta) = \pm\frac{24E_l I\Delta d_{lining}}{d^3(1-\nu_l^2)}sin2\left(\theta+\frac{\pi}{4}\right) \tag{1.31}$$

where:

$$R = \pm\frac{4(1-\nu_m)}{(\alpha+1)} \tag{1.32}$$

$$\alpha = \frac{24E_l I(3-4\nu_m)}{d^3\,G_m(1-\nu_l^2)} \tag{1.33}$$

In the following the attention will be devoted to axial forces and bending moments, being the most important lining forces for tunnels.

Finally, it is important to underline that the behaviour of the interface between the tunnel lining and the surrounding soil can play an important role on the seismic response of the system (Huo et al., 2005; Sedarat et al., 2009; Kouretzis et al., 2013).

The presence of shear stresses along the interface may affect the structure deformation modes. A rough interface capable to accommodate high shear stresses with limited deformations will result in high stresses on the lining.

For stiff underground compared to the stiffness of the soil, will produce fewer displacements of the surrounding soil, resulting in a less degradation on the shear modulus of the soil. On the contrary, for stiff structures but with a smooth interface between the soil and the tunnel, will produce fewer shear stresses on the underground structure and it will result in higher shear deformation around the tunnel, while separation phenomena may occur along with the interface. The phenomena described will produce higher shear deformation around the tunnel and degradation of the soil shear modulus.

In turn, this stiffness degradation will cause larger deformations in the surrounding soil and high normal stresses at the interface. Hence, the potential to develop considerable soil deformations will be increased, although the capability to transmit them in shear to the structure will be reduced (Huo et al., 2005). To this end, the soil-structure relative stiffness and the interface characteristics are correlated and may have opposite effects on the response of the structure (Huo et al., 2005; Pitilakis and Tsinidis, 2014)

Figure 1.4 shows the effect of the soil-tunnel interface on the seismic response of the all system, in terms of shear modulus degradation computed along the perimeter of the Daikai subway station (Huo et al., 2005).

In particular, Figure 1.4a shows the results for Full-Slip conditions, while Figure 1.4b shows the results for No-Slip conditions.

For Full-Slip conditions, the area of influence is reduced, allowing high deformation of the soil around the tunnel and therefore high degradation of the soil for high distance from the underground structure. Instead, for No-Slip condition, the soil is constrained more by the structure and therefore the soil shear modulus degradation is reduced.

In conclusion, the behaviour of the soil-tunnel interface is important to describe the seismic behaviour of the tunnel.

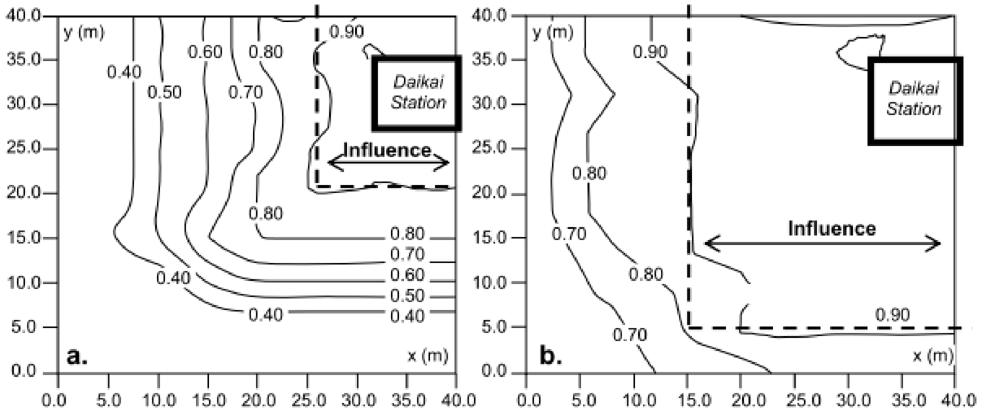

Figure 1.4: Shear modulus degradation computed at the time step of maximum racking distortion of the station for a) Full-Slip condition, b) No-Slip condition (Huo et al., 2005)

1.4 Methodologies and contents of the proposed research

The above described methods must be used exclusively for a first estimate of the dynamic behaviour of underground structures. In fact, these methods do not take into account the complex phenomena of the interaction of the entire system tunnel-soil-aboveground structure.

The presence of the underground structure has impacts on the dynamic properties of the surrounding soil since the construction of underground structure changes the original stress state of surrounding soil and the geometry, and further influences the seismic response of ground adjacent buildings. For this reason, the soil surrounding, the underground structure and the building on the surface have to be analysed as a single complex system, studying their interactive rule of the seismic response.

Most analyses were performed analysing, separately, only two components of the system soil surrounding-underground structure-aboveground building, neglecting several aspects of the all system interaction (Hashash et al. 2005; Kouretzis et al. 2007; Anastasopoulos et al., 2010; Lanzano et al., 2012; Kouretzis et al. 2007; Smerzini et al., 2009).

1.4.1 Main results concerned with the tunnel-soil-aboveground structure dynamic interaction

The seismic response of the complex system is strongly influenced by the presence of the underground structure and the buildings on the surface, caused by several refractions and reflection phenomena of the seismic waves in their propagation in the soil.

The seismic response of the tunnel can be modified, while, at the same time, the presence of the tunnel at a shallow depth close to the foundations of aboveground structures may alter the response of the aboveground structures themselves.

Navarro (1992) studied the effect of the nuclear power station on the seismic response of the adjacent underground structure and it was found that the distance between the adjacent underground tunnel and ground structure has influenced the seismic response of the tunnel. Mitra et al. (2007) and Smerzini et al. (2009) have studied the seismic behaviour of a circular tunnel considering the influence of the diameter and embedded depth of tunnel and the relative stiffness between the tunnel and surrounding soil. The influence zone of the existing tunnel on the dynamic behaviour of the surrounding soil mass was about

3 times the diameter of the tunnel. Guo and al. (2013) and Wang et al. (2013) studied on the rule of seismic response of the coupled system underground structure-ground structure analysing several aspects like the distance between the underground structure and ground structure, the shear velocity and damping ratio of soil surrounding and the buried depth and the span of underground structure, the input direction of the seismic wave. From the analyses, important results were found about the dynamic interaction underground structure-ground structure. In particular, the seismic behaviour of the ground buildings with low height was influenced by the underground structure. Moreover, the distance between the structures and the frequency of the seismic wave were the main factors influencing the dynamic behaviour of the system.

Important results were found by Kyrazis et al. (2014) performed a full dynamic time history analysis method to study the seismic response of the coupled system soil-tunnel-ground building. In particular, the size and the embedded depth of the tunnel, nonlinear properties of soil and the stiffness ratio of soil to structure were analysed. From the results, the ground building had a great influence on the dynamic response of the shallow tunnel with large stiffness was found.

Tsinidis et al. (2014) presented several results, in terms of tunnel deformations and dynamic internal forces of the lining. The variation of the ovaling ratio R with the flexibility ratio F (soil to tunnel relative flexibility), with the existence of aboveground structures, the soil dynamic behaviour (linear or non-linear response) and the tunnel burial depth was analysed by the authors. In the absence of aboveground structures numerical results are in good agreement with the F-R relation proposed by Penzien (2000). Generally, elastoplastic analyses predict slightly higher diametric deflection for the tunnel, due to the soil yielding. This observation is more significant for flexible structures and for small burial depths (e.g. $F > 8$). For the majority of the cases, the presence of over structures produces an increase of the tunnel's diametric deflection (larger ovaling ratio for the same flexibility ratio) compared to the case where no surface structures exist. This increase is larger for shallow tunnels. Naturally, the increase of racking ratio R for deeper tunnels is lower compared to the case where no surface structures exist. Similar to the "free-field conditions" case, elastoplastic analyses predict higher values for ovaling ratio as a result of soil yielding around the tunnel.

An increase of the tunnel ovaling or racking deflection produces an increase of the dynamic lining internal forces, with the effect being more significant for stiffer tunnels, due to their relative inability to follow these increased deformations. Shallow and stiffer tunnels are affected more by the presence of above-ground structures. For circular tunnels and concerning the axial forces, elasto-plastic analyses predict higher amplification compare to the visco-elastic analyses, due to stress redistributions within the soil caused by the soil yielding. For the cases where only one structure is considered, the dynamic axial force increase due to the above-ground structure existence. In terms of dynamic bending moment, the amplification (compared to the free-field environment) is higher, compared to the case where the above-ground structures are precluded. The influence of soil-tunnel interface characteristics is important in the estimation of the lining dynamic forces.

Masoud & Mohammad (2016) performed a 1g shaking table test and numerical analyses to study the soil amplification varying the shear velocity of soil, the depth of the tunnel and the frequency of the input motion. From the results achieved, a small influence on the soil amplification was shown by the presence of the tunnel. However, the tunnel had influenced the seismic response of the aboveground structure with a low period.

Wang (2018) analysed the dynamic interaction and the interactive influence on seismic response of the adjacent surface structure and underground structure through numerical analysis. A parametric analysis was performed to analyse the influence of arrangement of structures, distances between structures, shaking direction of seismic wave, shear wave velocity and damping of soil, depth of the underground structure, storey number, stiffness on the dynamic response of the coupled system soil-underground structure and aboveground building, in terms of horizontal acceleration of surface structure and horizontal relative displacement of the underground structure. The interaction varies for different arrangements, distances between structures and shaking directions, and the dynamic response of structure may even increase or decrease, depending on the configuration. Moreover, the dynamic interaction is very depending on the excitation frequency. Experiments and observations from real cases have shown that underground structure exhibits a significantly different seismic response from surface structures as they do not respond in resonance with the ground motion, but rather based on the response of the surrounding soil. This special behaviour
occurs because the mass effect is much smaller in underground than in surface structures and because the damping in underground structures is very high due to the energy radiating from them into the surrounding ground.

The fundamental frequency of the underground structure-soil system is approximately equal to that of the free-field. When the fundamental frequency of the surface structure is approximate to that of free-field, the surface structure might produce a more obvious influence on adjacent underground structure.

Obviously, with the increase of distance the interaction between structures fades away. In general, the influence of surface structures on the underground structure is smaller than that of underground structure on the surface structure.

Moreover, the dynamic response of the underground structures is little affected by the stiffness of the aboveground structure.

Depending on the distance between adjacent structures, the seismic response of the surface structure can either increase or decrease. But the interaction surely fades away if the distance is large enough.

When the fundamental frequency of the aboveground structure is approximate to that of free-field, the aboveground building may have more considerable influences on the adjacent underground structure. So, further studies about the dynamic interaction between tunnel-soil-aboveground structure phenomena and their influence on structural seismic risk are needed, as it has been shown that nearby buildings can significantly increase the seismic response of a structure.

Consequently, the complex phenomena that occur during an earthquake can lead to erroneous evaluations of the "real" inputs which hit aboveground and underground structures due to complex interactions involving the soil, the tunnels and the aboveground structures.

During the last decades, several subways have been built in Italy to respond to the strong demand for mobility and reduction of pollution. In Italy, in addition to the city of Catania, subways have been built in Naples, Rome, Milan and Florence. Unfortunately, few scientific contributions have been made to study the dynamic interaction of the complex system tunnel-soil-aboveground structure. Some works mainly concern the assessment and mitigation of settlements induced by excavation (Rampello et al. 2012, 2019; Miliziano & De Lillis, 2019). Some results were achieved about the dynamic interaction of the only soil-tunnel system. Silvestri et al. (2017) analysed the seismic response of the soil-tunnel system through two methods: 1) Pseudo-static analysis; 2) full dynamic analysis.

With the first approach, the effect of an earthquake is simulated with an equivalent seismic load, statically applied to the boundaries of the numerical model as a distribution of inertia forces or displacements (e.g. Argyroudis & Pitilakis, 2012; Do et al. 2015). The comparison showed that the pseudo-static analysis underestimated the increment of lining forces with respect to the full dynamic analysis. Literature shows that the difference between the two approaches is strongly dependent on the soil-structure relative stiffness and the interface behaviour; in particular, the difference increases with the lining flexibility and for a condition closer to "No-Slip " interaction (Tsinidis et al., 2016). In the case of Metro Line of Napoli, characterized by a rather flexible lining with a soil-structure interface closer to "No-Slip " rather than a "Full-Slip " condition, the two approaches showed a difference up to about 60% in the most loaded tunnel sections. This result is in agreement with previous studies (Bilotta et al., 2007; Argyroudis & Pitilakis, 2012; Tsinidis et al., 2016) showing, in almost all cases of flexible lining, an underestimation of the dynamic increment of the internal forces with the simplified pseudo-static approach, as a function of the interface behaviour and lining flexibility.

Given the importance of the tunnel-soil-aboveground structure interaction, the present thesis deals with the dynamic response of a tunnel-soil-aboveground structure system and analyses the dynamic effects on the all coupled system through a FEM model using Adina code. Analysing the complex system with the use of Finite Element Analysis, constitutive models for the can be used to describe the seismic response of the soil

In particular, starting by a real case of the underground in Catania (Italy), a parametric analysis was performed to analyse the influence of:

- the heterogeneity of the soil profile on the seismic response of the tunnel in terms of bending moments and axial forces along the lining tunnel;

- the different models used to model the interface between the soil and the tunnel lining and the soil with the foundation of the building located on the surface;
- the depth of the tunnel and the location of the aboveground structure;
- the input motion used at the bedrock of the model and the influence of the frequency content of the earthquake on the seismic response of the coupled system tunnel- soil-aboveground structure;
- the different constitutive models for the soil used to describe the dynamic behaviour of the medium.

Chapter 2

CONSTITUTIVE MODELS FOR SOILS

2.1 Introduction

The issue of formulating a constitutive model capable of adequately describing the mechanical behaviour of the soil was in recent years and still is, one of the most topical topics of international geotechnical scientific research.

As known, the behaviour of the soil is very complex and it is very difficult to mathematically describe it. The soil behaviour is non-linear, irreversible, it largely depends on the stress path and geological history. Moreover, the behaviour of the soil depends on time, temperature and load velocity. This suggests developing very complex constitutive models of the soil, with the use of many parameters to be obtained experimentally through laboratory tests. Nevertheless, the evaluation of a great number of soil parameters is not so easy. In the following sections, some constitutive models for the soil will be described.

Figure 2.1 shows the behaviour of soil models in the $\sigma-\varepsilon$ plane .

For small stresses/strains, linear- elastic model can be used. A rigid-perfectly plastic model can conveniently be used to investigate the failure conditions regardless of strains. Hardening provides for a variation of the yield level with the plastic strains. In isotropic hardening yield level increases or decreases with the increases or decreases of the stress level, respectively. In kinematic hardening, yield level can increase or decrease regardless of the stress level, for example in relation to the cyclicity of the stress. Then, particularly suitable for dynamic problems are the elastic-plastic model including both isotropic and kinematic hardening. In dynamic problems, a fundament role is also played by the material viscosity. In the following sections, some constitutive models will be described focusing on the constitutive models used for numerical analyses described in the present thesis.

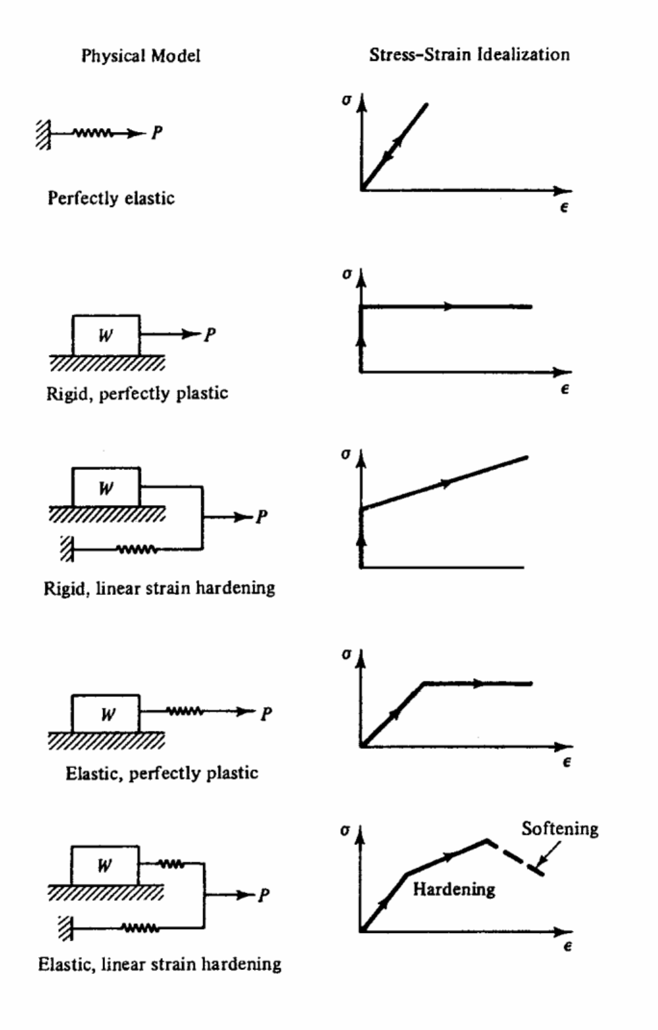

Figure 2.1: Stress-strain idealization for the physical model

2.2 Linear-elastic model

A linear relationship between stress and strain (Figure 2.2) is the simplest link that can be proposed, implying a constant proportionality between general stress increments and strain increments. For an isotropic elastic-linear material, the strains return to the initial zero value when the load magnitude is zero and the mechanical properties of the soil are the same in each direction.

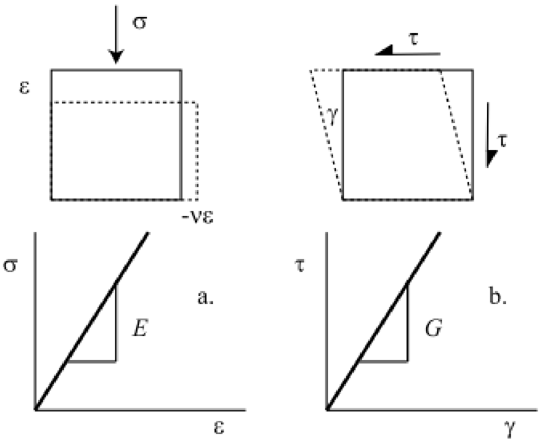

Figure 2.2: Linear relationship between stress and strain for (a) compression and (b) shearing of an elastic element (M. Wood, 2004)

In this case, the relation between the general stress increments and strain increments can be written as a compliance relationship (Hooke's law):

$$\begin{pmatrix} \delta\epsilon_{xx} \\ \delta\epsilon_{yy} \\ \delta\epsilon_{zz} \\ \delta\gamma_{yz} \\ \delta\gamma_{zx} \\ \delta\gamma_{xy} \end{pmatrix} = \frac{1}{E} \begin{pmatrix} 1 & -\nu & -\nu & 0 & 0 & 0 \\ -\nu & 1 & -\nu & 0 & 0 & 0 \\ -\nu & -\nu & 1 & 0 & 0 & 0 \\ 0 & 0 & 0 & 2(1+\nu) & 0 & 0 \\ 0 & 0 & 0 & 0 & 2(1+\nu) & 0 \\ 0 & 0 & 0 & 0 & 0 & 2(1+\nu) \end{pmatrix} \begin{pmatrix} \delta\sigma'_{xx} \\ \delta\sigma'_{yy} \\ \delta\sigma'_{zz} \\ \delta\tau'_{yz} \\ \delta\tau'_{zx} \\ \delta\tau'_{xy} \end{pmatrix} \quad (2.1)$$

Or in the short form:

$$\{\varepsilon\} = [C] \cdot \{\sigma'\} \tag{2.2}$$

where [C] is the compliance matrix.

It is important to underline that the constitutive model has to be written in terms of effective stresses for the soil, according to Terzaghi's Principle.

Alternatively, general stress increments and strain increments can be linked by the following stiffness relationship:

$$\begin{pmatrix} \delta\sigma'_{xx} \\ \delta\sigma'_{yy} \\ \delta\sigma'_{zz} \\ \delta\tau'_{yz} \\ \delta\tau'_{zx} \\ \delta\tau'_{xy} \end{pmatrix} = \frac{1}{E} \begin{pmatrix} 1 & -\nu & -\nu & 0 & 0 & 0 \\ -\nu & 1 & -\nu & 0 & 0 & 0 \\ -\nu & -\nu & 1 & 0 & 0 & 0 \\ 0 & 0 & 0 & 2(1+\nu) & 0 & 0 \\ 0 & 0 & 0 & 0 & 2(1+\nu) & 0 \\ 0 & 0 & 0 & 0 & 0 & 2(1+\nu) \end{pmatrix} \begin{pmatrix} \delta\epsilon_{xx} \\ \delta\epsilon_{yy} \\ \delta\epsilon_{zz} \\ \delta\gamma_{yz} \\ \delta\gamma_{zx} \\ \delta\gamma_{xy} \end{pmatrix} \tag{2.3}$$

Or in the short form:

$$\{\sigma'\} = [D] \cdot \{\varepsilon\} \tag{2.4}$$

where [D] is the stiffness matrix.

If x, y, and z axis are principal axes, (2.1) and (2.3) became respectively equal to:

$$\begin{pmatrix} \delta\epsilon_{x} \\ \delta\epsilon_{y} \\ \delta\epsilon_{z} \end{pmatrix} = \frac{1}{E} \begin{pmatrix} 1 & -\nu & -\nu \\ -\nu & 1 & -\nu \\ -\nu & -\nu & 1 \end{pmatrix} \begin{pmatrix} \delta\sigma'_{x} \\ \delta\sigma'_{y} \\ \delta\sigma'_{z} \end{pmatrix} \tag{2.5}$$

and in stiffness form:

$$\begin{pmatrix} \delta\sigma'_{x} \\ \delta\sigma'_{y} \\ \delta\sigma'_{z} \end{pmatrix} = \frac{E}{(1+\nu)(1-2\nu)} \begin{pmatrix} 1 & -\nu & -\nu \\ -\nu & 1 & -\nu \\ -\nu & -\nu & 1 \end{pmatrix} \begin{pmatrix} \delta\epsilon_{x} \\ \delta\epsilon_{y} \\ \delta\epsilon_{z} \end{pmatrix} \tag{2.6}$$

It may be remarked that the elastic compliance and stiffness matrices are symmetric: this is a property of the linear-elastic model very useful for numerical analyses.

For the axisymmetric conditions of the triaxial test, so that the x and y axes are radial axes (commonly named r-axix) and z is the vertical axis (commonly named a-axix), the symmetry of the compliance and stiffness matrices is lost. The expressions (2.5) and (2.6) become:

$$\begin{pmatrix}\delta\varepsilon_a\\ \delta\varepsilon_r\end{pmatrix}=\frac{1}{E}\begin{pmatrix}1 & -2\nu\\ -\nu & 1-\nu\end{pmatrix}\begin{pmatrix}\delta{\sigma'}_a\\ \delta{\sigma'}_r\end{pmatrix} \tag{2.7}$$

$$\begin{pmatrix}\delta{\sigma'}_a\\ \delta{\sigma'}_r\end{pmatrix}=\frac{E}{(1+\nu)(1-2\nu)}\begin{pmatrix}1-\nu & 2\nu\\ \nu & 1\end{pmatrix}\begin{pmatrix}\delta\varepsilon_a\\ \delta\varepsilon_r\end{pmatrix} \tag{2.8}$$

To restore the symmetry of the matrices, the mean effective stress, p' and the distortional stress, q, as well as the corresponding work-conjugate strain increments $\delta\varepsilon_p$ and $\delta\varepsilon_q$ have to be considered.

So, in the compliance form:

$$\begin{pmatrix}\delta\varepsilon_p\\ \delta\varepsilon_q\end{pmatrix}=\begin{pmatrix}\frac{1}{K} & 0\\ 0 & \frac{1}{3G}\end{pmatrix}\begin{pmatrix}\delta{\sigma'}_p\\ \delta{\sigma'}_q\end{pmatrix} \tag{2.9}$$

And in stiffness form:

$$\begin{pmatrix}\delta{\sigma'}_p\\ \delta{\sigma'}_q\end{pmatrix}=\begin{pmatrix}K & 0\\ 0 & 3G\end{pmatrix}\begin{pmatrix}\delta\varepsilon_p\\ \delta\varepsilon_q\end{pmatrix} \tag{2.10}$$

where K and G are the bulk modulus and the shear modulus, respectively:

$$K=\frac{E}{3(1-2\nu)} \qquad G=\frac{E}{2(1+\nu)} \tag{2.11}$$

2.3 Non-linear-elastic model

As mentioned above, the soil behaviour is non-linear, irreversible, it largely depends on the stress path and geological history. Unfortunately, it is not possible to describe the behaviour of the soil by linear models; these models are used for high simplicity and when the soil is subjected to small loads, i.e. for the evaluation of the settlements of a building.

However, it is possible to take into account the non-linearity of the soil by characterizing the stress-strain relationships by means of variable modules, using tangent moduli K_t and G_t or secant moduli K_s and G_s (Figure 2.3). This material is defined as Cauchy elastic material, for which the relationship between stresses and strains is not constant, but it depends on the achieved strain or stress level.

By these assumptions, the non-linearity of the soil is taken into account in a non-rigorous way, because a mechanical behaviour independent on the load path is described.

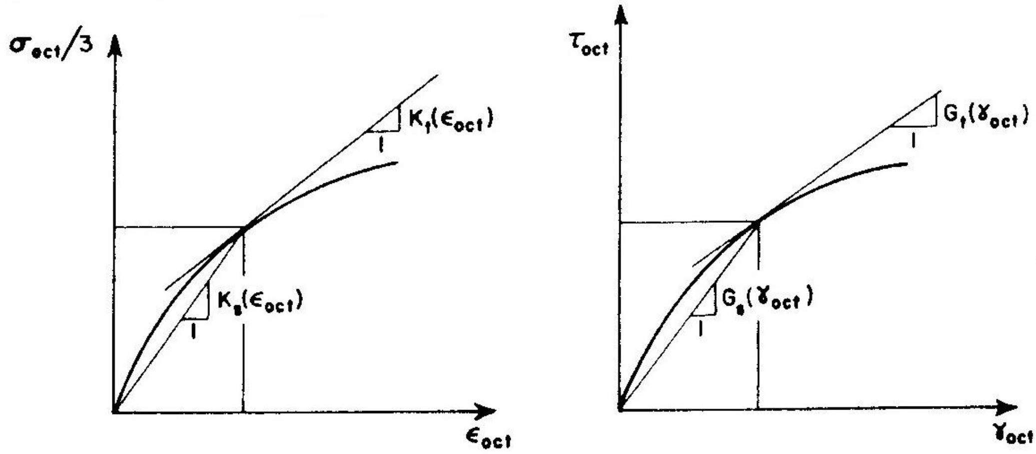

Figure 2.3: Tangent and secant moduli (after Chen & Baladi, 1985)

The irreversibility and the independence of the load path of the two functions ($U(\varepsilon_{ij})$ and $V(\sigma_{ij})$, Strain Energy and Complementary Energy respectively) are not guaranteed:

$$\sigma_{ij} = \frac{\partial U}{\partial \varepsilon_{ij}} \qquad \varepsilon_{ij} = \frac{\partial V}{\partial \sigma_{ij}} \tag{2.12}$$

Indeed, according to the Cauchy model, a material can generate energy for loading-unloading cycles, violating the laws of thermodynamics.

Hyperelastic models could be used to overcome this problem, even if they describe a mechanical behaviour independent of the load path.

2.4 Plasticity

The analysis of experimental test results highlights that the theory of elasticity is not sufficient to fully describe the real behaviour of soils.

To describe accurately the behaviour of the soil, the plasticity theory is necessary.

A quick comparison of the stress-strain response implied by a linear elastic description of soil behaviour with the actual stress-strain response of a typical soil shows that there are many features of soil response that the elastic linear model is unable to capture. In particular, most soils show nonlinear stress-strain relationships with the stiffness. If soil is unloaded from some intermediate, pre-failure condition then it will not recover its initial state but will be left with permanent deformation (plastic deformation).

Figure 2.4 shows a typical strain-stress relationship for a soil sample subjected to a uniaxial compression test.

For small stresses (until point A), the behaviour is linear elastic; if the stress achieves the point B and the soil is unloaded, plastic strain accumulate. Between the points A and B both elastic and plastic strains occur: the first ones are recovered unloading the soil, the plastic strains are permanent. If from point C the soil is loaded, the behaviour is linear elastic until to point B (the greater stress to which the soil has been subjected). Then, from the point B the behaviour is elasto-plastic.

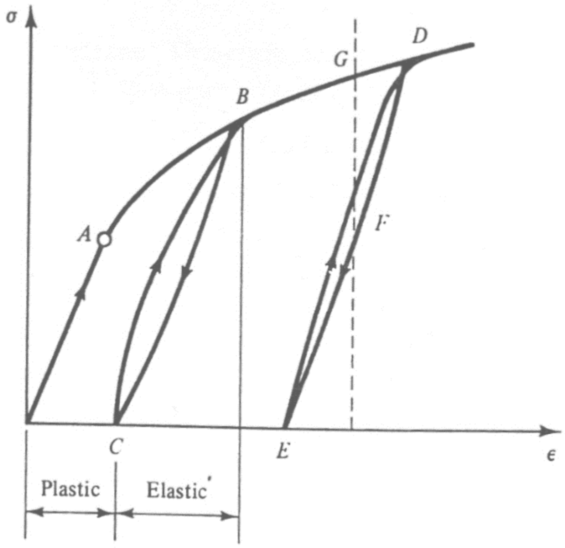

Figure 2.4: Typical strain-stress relationship for the soil

The stress at point A is the yielding stress.

It is important to highlight the dependency by the load path in the behaviour of the soil. Moreover, from Figure 2.4 it is possible to see that the yielding stress is not constant but increases with the plastic strain. This increase of the plasticity limit with the monotonically evolving plastic deformations is known as hardening.

The first step for define a model taking into account the plasticity is setting a stress limit reached which not only elastic but also plastic strains occur, i.e. setting a yielding function. A perfectly-plastic or plastic with hardening (work-hardening) material will be represented by a yielding function which will be a fixed surface or it will be subjected to size changes, translations or rotations depending on the plastic strains.

Important contributions in the theory of plasticity for the soil were offered by Drucker & Prager (1952), which defined the "Drucker-Prager criterion", by Drucker, Gibson and Henkel (1957), which introduced the hardening in the Soil

Mechanics, and by Roscoe and Schofield (1963) which defined the Cam-Clay model.

2.5 Elasto-Plastic model

To define a constitutive model that describes the elastoplastic behaviour of the soil, the following "ingredients" are necessary:

1) *Elastic properties*, which describe the elastic behaviour;
2) *Yielding criterion*, to define a limit beyond which the behaviour is no longer elastic;
3) *Flow rule*, which describes the direction of the plastic strain;
4) *Hardening rule*, which describes the evolution of the yield surface with the plastic strains.

A fundamental assumption of the plastic theory is that the strain increments can be divided into an elastic (recoverable) part, which will be indicated with the apex "e", and a plastic (irrecoverable) part, which will be indicated with the apex "p".

$$\dot{\boldsymbol{\varepsilon}}_{ij} = \dot{\boldsymbol{\varepsilon}}_{ij}^{e} + \dot{\boldsymbol{\varepsilon}}_{ij}^{p} \qquad (2.13)$$

The strain tensor is a six-element vector of cartesian strain components. The elastic strain increment occurs whenever there is any change in stress (where the stress is also a six-dimensional vector of cartesian components):

$$\dot{\boldsymbol{\varepsilon}}_{ij}^{e} = \boldsymbol{C}_{ijkl}^{e} \dot{\boldsymbol{\sigma}}_{kl} \qquad (2.14)$$

where is the elastic compliance matrix. The first ingredient of the model is, therefore, a description of the elastic behaviour.

As for the elastic strain, the increments of plastic strain is:

$$\dot{\boldsymbol{\varepsilon}}_{ij}^{p} = \boldsymbol{C}_{ijkl}^{p}\dot{\boldsymbol{\sigma}}_{kl} \tag{2.15}$$

where is the plastic compliance matrix.

Definitely, the total increments of the strain is:

$$\dot{\boldsymbol{\varepsilon}}_{ij} = (\boldsymbol{C}_{ijkl}^{e} + \boldsymbol{C}_{ijkl}^{p})\dot{\boldsymbol{\sigma}}_{kl} = \boldsymbol{C}_{ijkl}^{ep}\dot{\boldsymbol{\sigma}}_{kl} \tag{2.16}$$

where is the elastoplastic compliance matrix.

The same relationships can be written in the inverse form:

$$\dot{\boldsymbol{\sigma}}_{ij} = (\boldsymbol{D}_{ijkl}^{e} + \boldsymbol{D}_{ijkl}^{p})\dot{\boldsymbol{\varepsilon}}_{kl} = \boldsymbol{D}_{ijkl}^{ep}\dot{\boldsymbol{\varepsilon}}_{kl} \tag{2.17}$$

where, and are the elastic, plastic and elastoplastic stiffness matrix, respectively. In matrix form:

$$\{\dot{\boldsymbol{\sigma}}\} = ([\boldsymbol{D}]^{e} + [\boldsymbol{D}]^{p})\{\dot{\boldsymbol{\varepsilon}}\} = [\boldsymbol{D}]^{ep}\{\dot{\boldsymbol{\varepsilon}}\} \tag{2.18}$$

Figure 2.5 shows a generic loading-unloading test. In the following paragraphs, the remaining "ingredients" for the elasto-plastic theory are described.

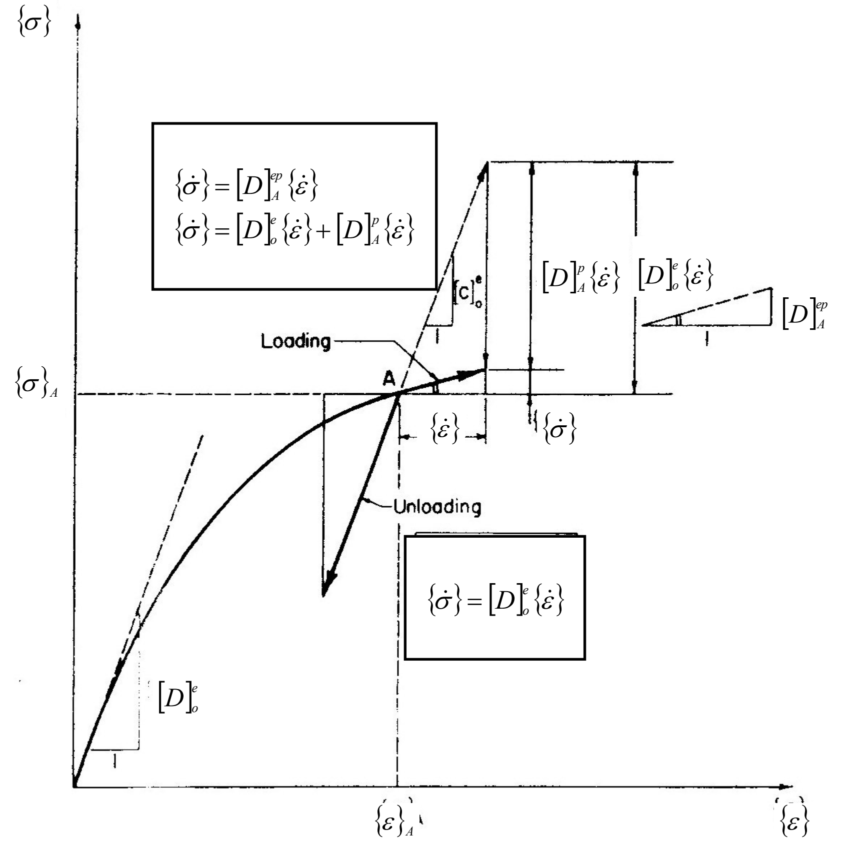

Figure 2.5: Plasticity theory (Chen & Baladi, 1985)

2.5.1 Yielding function

To describe the behaviour of the material during the plastic phase is necessary to define a yielding function as a function of a hardening parameter $f(\sigma, \chi)$.

If:

- $f < 0$ the behaviour of the material is elastic;
- $f = 0$ the behaviour of the material is plastic;
- $f > 0$ is an impossible condition (Figure 2.6).

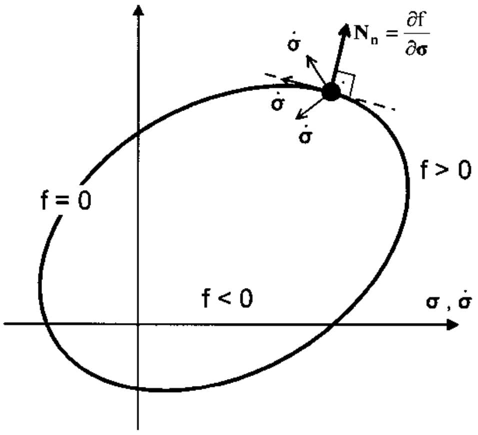

Figure 2.6: Yield surface and possible stress increments (Dafalias & Papadimitriou, 2005)

The yield surface can change in size, shape and position with the plastic strain. In particular, two types of hardening can be defined: isotropic and kinematic hardening.

The isotropic hardening describes a changing of size without chancing of shape and position, while the kinematic hardening describes a rigid translation of the surface without a changing of the size or the shape (Figure 2.7).

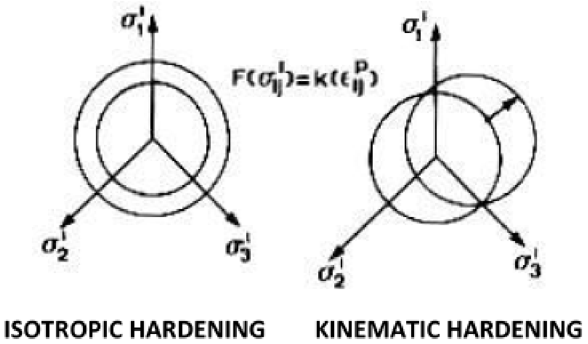

Figure 2.7: Isotropic and kinematic hardening (Lancellotta, 1993)

If the yielding criterion is independent of plastic strain, the yield surface maintains the same shape, size and the same position:

$$f(\sigma'_{ij}) = 0 \tag{2.19}$$

In this case, the behaviour of the material is plastic perfectly and the yielding criterion coincides with the failure criterion.

Summing up, the yield surface evolves until the stress achieves the failure surface or critical state conditions. The *failure surface* is the maximum shear stresses that can be achieved by the material and the *critical state surface* is the surface that envelops all the ultimate states that can be achieved by the material. Several yield surface can be defined inside the failure surface; moreover, the failure surface can be in or out the critical state surface and coincides with it for infinite strains.

Several yielding criteria are present in the literature, classified by Chen & Saleeb, 1986 as criteria characterized by only one parameter, as the Tresca, Von Mises and Lade-Duncan criteria (Figure 2.8), or criteria characterized by two parameters as the extended Tresca, extended von Mises (Drucker-Prager), Mhor-Coulomb and Lode criteria (Figure 2.9).

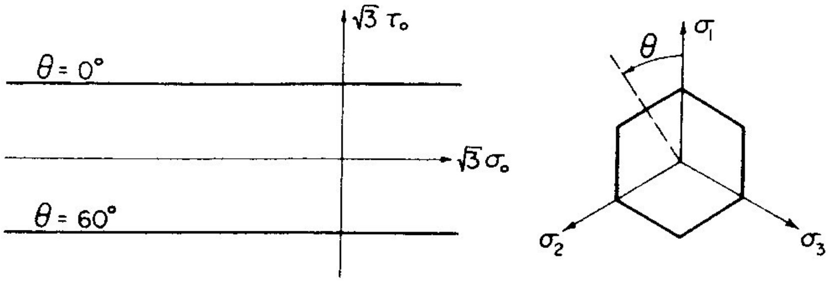

(a) Tresca

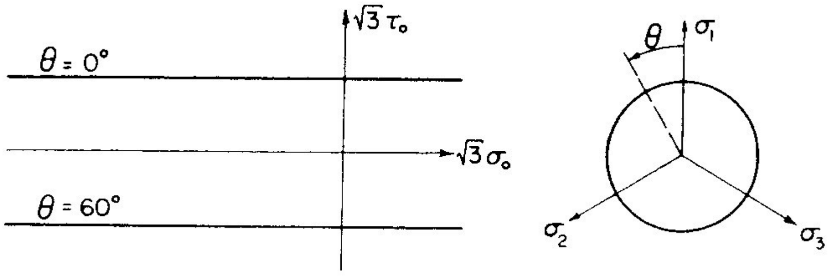

(b) von Mises

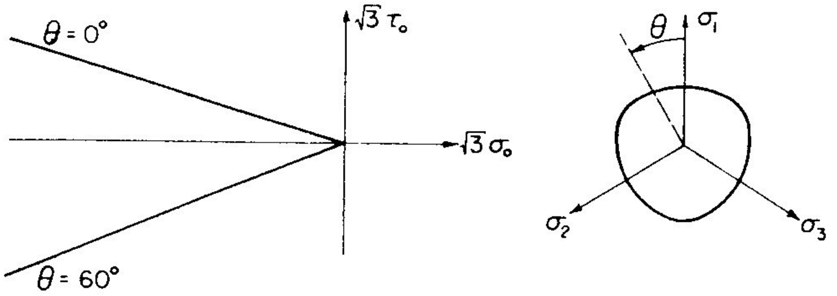

(c) Lade – Duncan

Figure 2.8: Yield criteria with one parameter (Chen & Baladi, 1985)

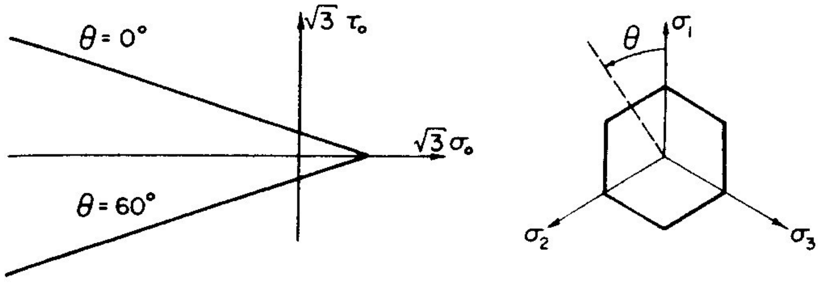

(a) Extended Tresca

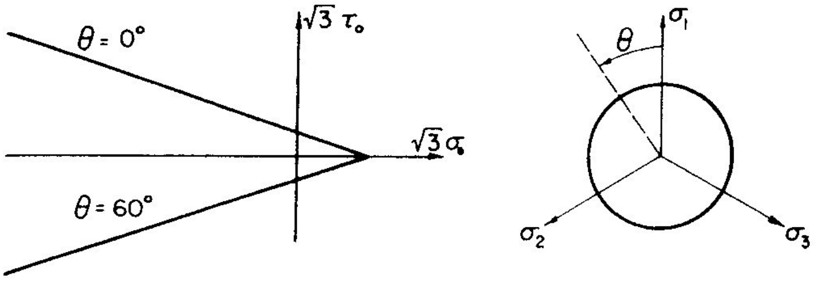

(b) Extended von Mises (Drucker – Prager)

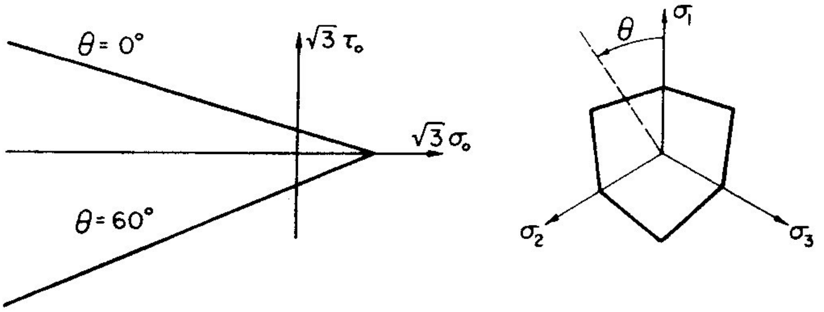

(c) Mohr – Coulomb

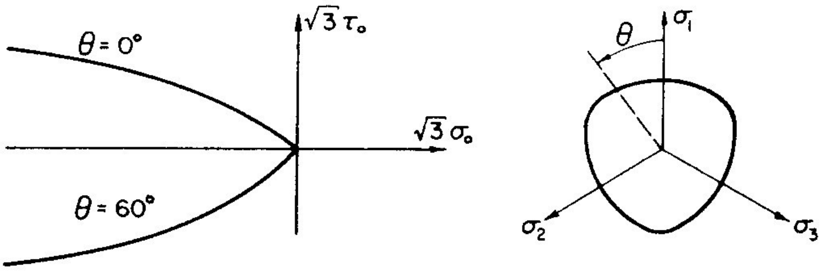

(d) Lade

Figure 2.9: Yield criteria with two parameters (Chen & Baladi, 1985)

2.5.2 Work-hardening and Drucker's postulate

Figure 2.10a shows a typical stress-strain curve for a mono-dimensional load applied to a hardening material. It may have undergone any type of deformation (e.g. elastic or plastic) and it is subjected to the stress $\boldsymbol{\sigma}^*$ (point ***A***). An additional load is now applied to the material, bringing it to the current yield stress $\boldsymbol{\sigma}$ at point ***B*** (if $\boldsymbol{\sigma}^*$ is lower than the yield stress) and then plastically (greatly exaggerated in the figure) through the infinitesimal increment $\boldsymbol{d\sigma}$ to point ***C***. Conventionally, this additional load is called "external factor". Finally, the external factor is removed, bringing the stress back to $\boldsymbol{\sigma}^*$ at point ***D***. The material is said to have undergone a stress cycle.

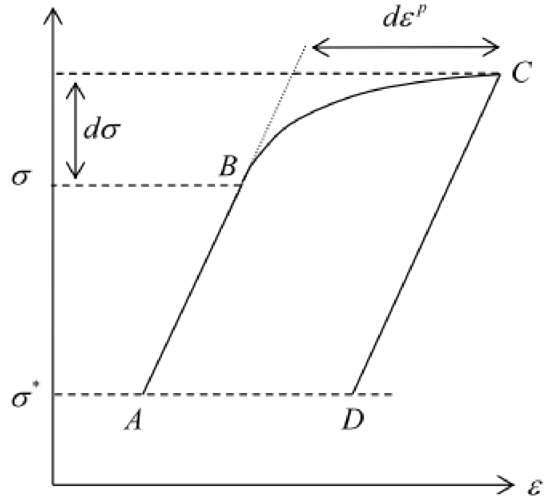

Figure 2.10.a: A stress cycle for a hardening material (Kelly, 2013)

Figure 2.10.b shows a typical stress-strain curve for a mono-dimensional load applied to a softening material. The external factor firstly brings the material to the current yield stress $\boldsymbol{\sigma}$ at point ***B***. To reach point ***C***, the load must be reduced. This cannot be achieved by a controlled-stress test, since a reduction in stress at ***B*** will induce elastic unloading towards ***A***. A controlled-strain (displacement) test must be used, in which case the stress required to induce the plastic strain

will decrease to $\sigma + d\sigma$ ($d\sigma < 0$) at ***C***. The stress cycle is completed by unloading from ***C*** to ***D***.

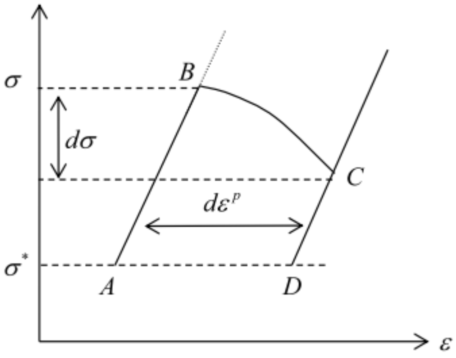

Figure 2.10.b: A stress cycle for a softening material (Kelly, 2013)

Suppose now that $\sigma = \sigma$, so the material is at point ***B***, on the yield surface, before action by the external agency. It is now not possible for the material to undergo a stress cycle since the stress cannot be increased. This provides a means of distinguishing between strain hardening and softening materials:

- Strain-hardening …The material can always undergo a stress-cycle;
- Strain-softening … The material cannot always undergo a stress-cycle.

The "work-hardening" is related to the work to a due to an external factor. The work producing the hardening is not due to all the forces, but just due to the additional forces/stresses occurring after the yielding limit. A definition of "work-hardening" was provided by Drucker (1959), generalizing the mono-axial stress-strain relationship (Figures 2.11.a-b). For a stress $\boldsymbol{\sigma}$, the plastic strain increment satisfies the following relationships:

$\sigma\dot{\varepsilon}^p \geq 0$ for material with positive hardening;

$\sigma\dot{\varepsilon}^p = 0$ for material with neutral hardening (i.e. perfectly-plastic);

$\sigma\dot{\varepsilon}^p < 0$ for material with negative hardening (i.e. softening).

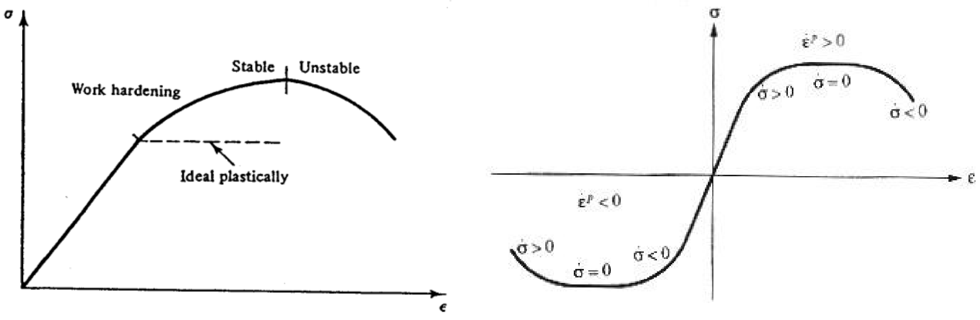

Figure 2.11.a Typical stress-strain curve; b: Drucker's postulate

Drucker defined a stable material as (these statements are also known as ***Drucker's postulate***):

1) The work due to a load increment is positive;
2) The work performed over a stress cycle is non-negative.

By these definitions, it is clear that a material characterized by positive hardening or a perfectly-plastic material is stable. Figure 2.12a shows the work done by the external factor: it is the shaded area in and is clearly positive. On the other hand, for a softening (or perfectly plastic) material the work is non-positive, as shown in Figure 2.12b.

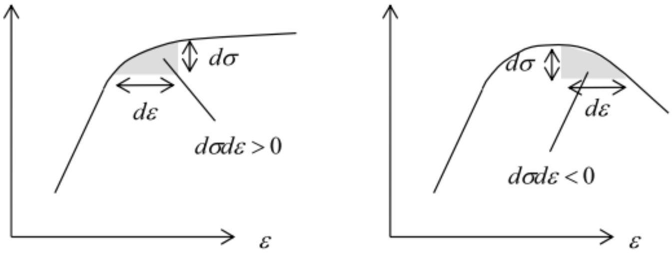

(a) (b)

Figure 2.12: Stable (a) and unstable (b) stress-strain curves (Kelly, 2013)

Defining hardening in terms of work, the above definition can be extended to a generic three-dimensional state of stress-strain:

1) $\dot{\boldsymbol{\sigma}}_{ij}\dot{\boldsymbol{\varepsilon}}_{ij} > 0 \rightarrow \dot{\boldsymbol{\sigma}}_{ij}(\dot{\boldsymbol{\varepsilon}}^{e}{}_{ij} + \dot{\boldsymbol{\varepsilon}}^{p}{}_{ij}) > 0$ (2.20a)

2) $\dot{\boldsymbol{\sigma}}_{ij}\dot{\boldsymbol{\varepsilon}}^{p}{}_{ij} \geq 0$ (2.20b)

The criteria that material is stable have very interesting consequences, provided by Prager (1949):

1) *Continuity condition;*
2) *Unicity condition;*
3) *Irreversibility condition;*
4) *Consistency condition.*

1. Regarding the first condition, if a stress state $\boldsymbol{\sigma}_{ij}$ is on the yield surface, an infinitesimal variation $\delta\boldsymbol{\sigma}_{ij}$ can produce:

- *Load*, if the stress path is towards the outside of the yield surface;
- *Unload*, if the stress path is towards the inside of the yield surface;
- *Neutral load*, if the stress path is tangent to the yield surface.

To avoid dangerous discontinuities in the stress-strain law, the continuity condition requires that the neutral load does not produce any plastic strain.

2. The second condition requires that, given a precise physical state of a body and a system of infinitesimal increases of the surface forces, the resulting system of the stress and strain increments (elastic and plastic) is unique.

3. The third condition requires that, as the plastic strains are irreversible, the work done by a stress system on a plastic strain system, δW^{p}, must be positive $\delta W^{p} = \boldsymbol{\sigma}_{ij}\delta\boldsymbol{\varepsilon}^{p}{}_{ij} > 0$.

4. Finally, the yield surface must follow the evolution of the stress state so that the condition of consistency is always verified:

$$f(\sigma'_{ij},h) \leq 0 \quad \text{e} \quad \delta f = 0 \tag{2.21}$$

If there was a stress state external to the yield surface, the existence of plastic strain during an unloading phase should be admitted, in contrast to the definition of the yield surface (Figure 2.13).

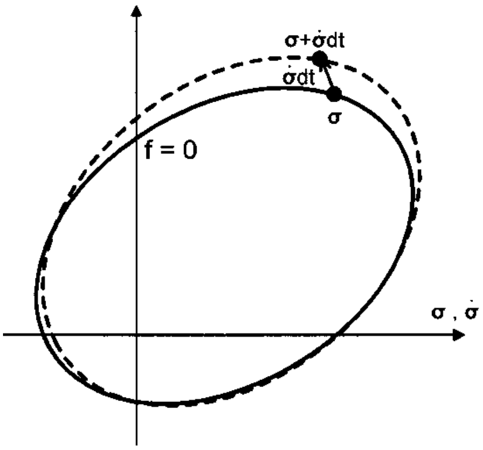

Figure 2.13: Evolution of the yield surface and consistency condition (Dafalias & Papadimitriou, 2005)

The above-mentioned conditions allow us to underline important aspects of plastic behaviour. Figure 2.14 shows the vector of the initial stress state $\boldsymbol{\sigma}$ and the vector of the stress increment $\delta\boldsymbol{\sigma}$, which can be written as:

$$\delta\boldsymbol{\sigma} = \delta\boldsymbol{\sigma}^{(n)} + \delta\boldsymbol{\sigma}^{(t)} \tag{2.22}$$

where $\delta\boldsymbol{\sigma}^{(n)}$ is the normal component to the yield surface of the stress increment, while $\delta\boldsymbol{\sigma}^{(t)}$ is the tangential component.

For the assumption of linearity, the plastic strain increment due to the stress $\boldsymbol{\delta\sigma}$ is equal to the sum of the vectors representing the strain plastic increment due to the $\boldsymbol{\delta\sigma}^{(n}$ and $\delta\sigma^{(t)}$. However, since the continuity condition provides that the plastic strain produced by the vector tangent ($\boldsymbol{\delta\sigma}^{(t)}$) to the yield surface is zero, the plastic strain increment $\boldsymbol{\delta\varepsilon}^{p}$ due to the stress $\boldsymbol{\delta\sigma}$, depends exclusively on the normal component $\boldsymbol{\delta\sigma}^{(n)}$.

Consequently, the vector of the plastic strain increment must be normal to the yield surface and it must be outside the surface. This is the ***normality principle***.

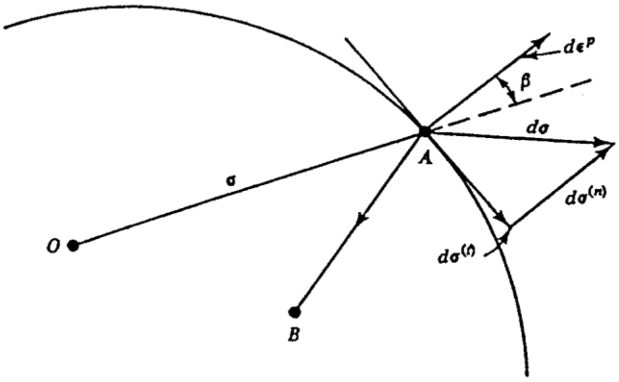

Figure 2.14: Yield surface and Prager's condition (1949)

According to the irreversibility condition (see Figure 2.14):

$$\boldsymbol{\sigma}\dot{\boldsymbol{\varepsilon}}^{p} > 0 \rightarrow |\boldsymbol{\sigma}||\dot{\boldsymbol{\varepsilon}}^{p}|\,cos\,\beta > 0 \tag{2.23}$$

Consequently, the yield surface must be convex. Normality and convexity conditions are the characteristics for the stable materials according to Drucker.

2.5.3 Hardening rule

The yielding function is a function of the stress state and of the internal variables. The hardening rule is the specification of the internal variables, of their evolution laws, of the dependence of the yielding function by the stress state and by these internal variables.

The internal variables are assumed coincident with plastic strains and with a function of these, called hardening variable κ:

$$\kappa = \kappa(\varepsilon^p) \tag{2.24}$$

To define the variation of the *k* variable, a hardening modulus or plastic modulus of the material, called ***H***, will be defined. Hardening modulus can assume positive or negative values: for positive values, the material can be subjected to any increase in load; if plastic strains occur, the yield surface expands; for negative values, the load decreases and the yield surface contracts (softening occurs, see Figure 2.15). If $\boldsymbol{H} < 0$, applying any load increase on the sample is not possible. In this case, if the stress increment path is directed outside the yield surface, the sample collapse. So, the material is "*unstable*" when H assumes negative values.

Defining ***H***, which depends on the stress state, the plastic strains can be found for each assigned load increment.

Two hardening rules are usually adopted: 1) ***isotropic hardening***, for which the yield surface expands or contracts, without changing the shape and the position; 2)***kinematic hardening***, for which a translation of the yield surface occurs maintaining the same size and the same shape.

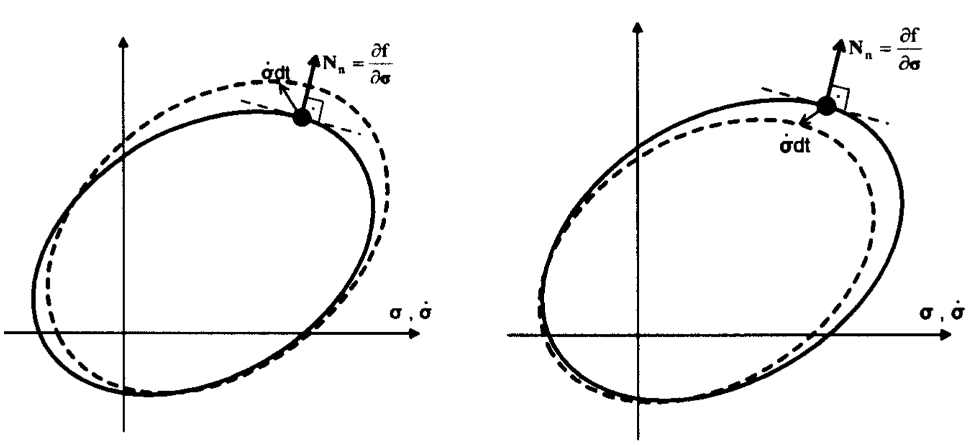

Figure 2.15: Hardening and softening (Dafalias & Papadimitriou, 2005)

2.5.4 Flow law

When the yielding condition is achieved, the material suffers plastic strains. This is known as plastic flow. Now, the direction of the plastic strain has to be defined. By experimental results, it was observed that the stress increments $\dot{\sigma}_{ij}$ do not affect the direction of the plastic strain increments, even if they influence their value.

So, the plastic strain increments can be written:

$$\dot{\boldsymbol{\varepsilon}}_{ij}{}^{p} = \Lambda grad\boldsymbol{g} = \Lambda \frac{\partial g}{\partial \sigma_{ij}} \tag{2.25}$$

where ***g*** depends on the stress tensor but it does not depend on the stress path and so it is defined "***plastic potential***". The expression (2.25) means that the plastic strain increments, , is orthogonal to the "***g***" surface in the stress space. This normality law is known as ***flow rule***.

When ***g=f*** (yield surface), the material follow an associated flow law, while when ***g≠f***, the material follow a not associated flow law.

For associated flow law, important simplifications are achieved in the analysis of the problem and the ***Drucker's postulate*** is verified, so that the material can be stable.

A non-associated flow law is mainly used to describe the behaviour of dense sand or overconsolidated clay, that are characterized by mechanical instability effects.

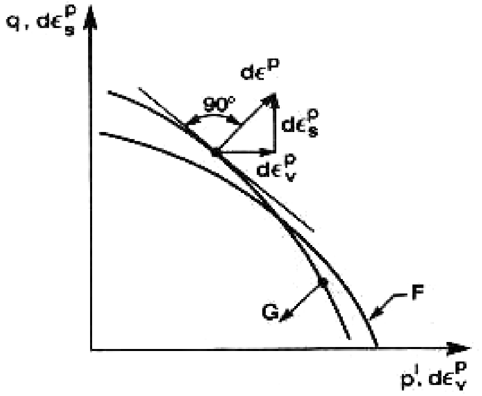

Figure 2.16: Plastic potential and the direction of the plastic strain vector (Lancellotta,1993)

2.6 Elastoplastic with hardening models

To consider the irreversibility of the behaviour of the soil, ***Drucker, Gibson and Henkel*** (1957) suggest an elastoplastic constitutive model with positive hardening, in which the yielding level increases with the plastic strain ($\sigma_y = \sigma_y (\varepsilon_p)$), according to a concept taken from work hardened metals (Figure 2.17).

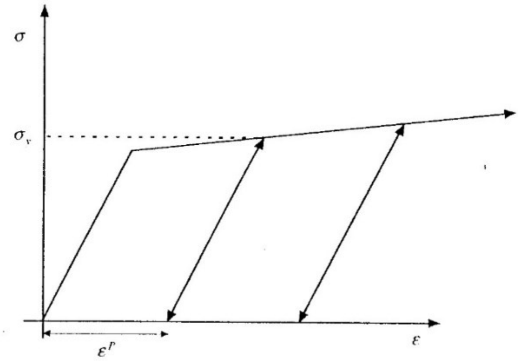

Figure 2.17: Mechanical behaviour of work hardened metals (Nova,2002)

According to ***Drucker, Gibson and Henkel***, the yield surface in the stresses space is the *Drucker-Prager cone* with a semispheric *cap*, which position increases with the isotropic components of the load (*isotropic hardening*) as shown in Figure 2.18. The cap is a yield surface which can expand or contract according to the volume changes of the material.

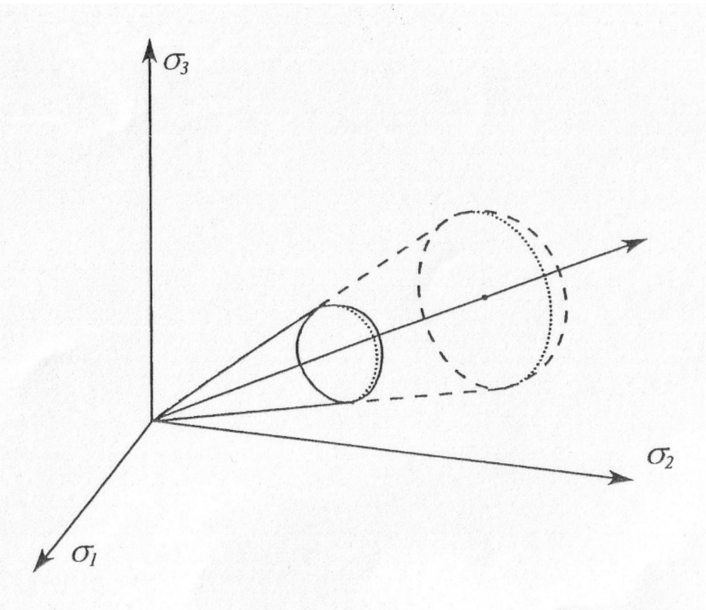

Figure 2.18: Yield surface according to Drucker et al. (1957), (Nova, 2002)

Inside the cone the behaviour is elastic; if the stress increment is towards the external region of the cap, plastic strains occur and an expansion of the cap occurs, too.

Analyzing the behaviour of the clays by means of triaxial tests, several constitutive models with hardening were developed, among which the two most known and utilised constitutive models are the ***Cam Clay*** model, created by Roscoe (Roscoe et al., 1963) and it developed by Schofield & Wroth (1968) and the ***modified Cam clay*** model developed by Roscoe & Burland (1968).

2.7 Constitutive models with isotropic and kinematic hardening

Several elastoplastic models with anisotropic hardening were developed (Mroz (1967), Iwan (1967), Prevost (1977; 1978 a-b), Dafalias &Popov (1975)), to describe the induced anisotropy. In the framework of the hardening plasticity, an anisotropic behaviour can be introduced in the formulation of the elastic constitutive model, or in the definition of the yield surface and of the plastic potential, by means a variable belonging to the internal variables. The anisotropy induced by the changes in the arrangements of the particles constituting the solid skeleton is described by means of hardening rules which associate the variation of anisotropy with the velocity of plastic strains.

For models with ***kinematic hardening***, the yield surface is defined by the following expression:

$$f(\boldsymbol{\sigma}, \boldsymbol{\alpha}, q_\kappa) = 0 \tag{2.26}$$

where $\boldsymbol{\alpha}$ is the anisotropic tensor. The yield surface moves rigidly with the $\boldsymbol{\alpha}$ changes in the stresses space (Figure 2.19). The internal scalar variables $\boldsymbol{q}_k$ control the size of the surface, as in the isotropic case.

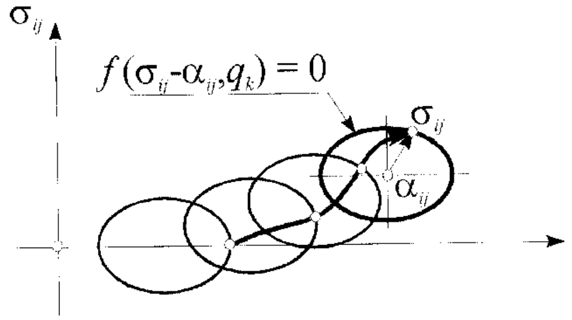

Figure 2.19: Kinematic hardening: rigid translation according to α *(Tamagnini,2002)*

Iwan (1967) and Mroz (1967) proposed a first model with kinematic hardening, in which several nested yield surfaces were proposed each of which translates independently from the others, according to the kinematic hardening rule, as shown in Figure 2.20.

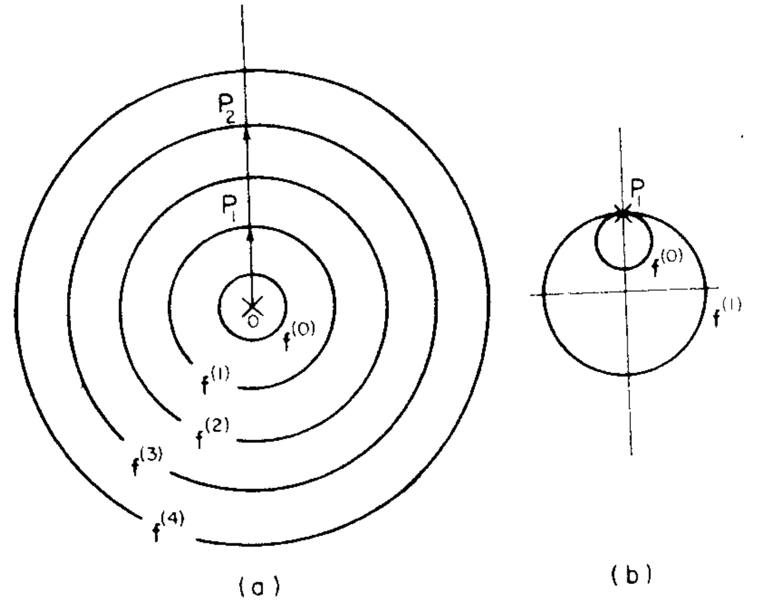

Figure 2.20: Yield surfaces according to Iwan-Mroz (1967)(Chen & *Baladi, 1985)*

In Figure 2.20a, the initial positions of the yield surfaces are indicated as $f^{(0)}$, $f^{(1)}$, $f^{(2)}$, $f^{(3)}$ ed $f^{(4)}$; when the stress state (in Figure 2.20a indicated with X) moves towards P_1, elastic strains occur; when the stress state reaches the $f^{(0)}$ surface, plastic strains occur and the $f^{(0)}$ surface moves towards the $f^{(1)}$ surface; when the $f^{(1)}$ is reached, both surfaces (Figure 2.20b) move towards the $f^{(2)}$ surface.

Prevost (1977; 1978 a-b) added to the model of Iwan/Mroz (1967) the isotropic hardening (Figure 2.21). When the stress state (point P) reaches the surface $f^{(m)}$, for a stress increment a translation of the surface $f^{(m)}$ towards the $f^{(m+1)}$ surface occurs along the PR path, where R is the conjugate point on the surface $f^{(m+1)}$, in which the normal direction to the surface is the same normal direction on the surface $f^{(m)}$.

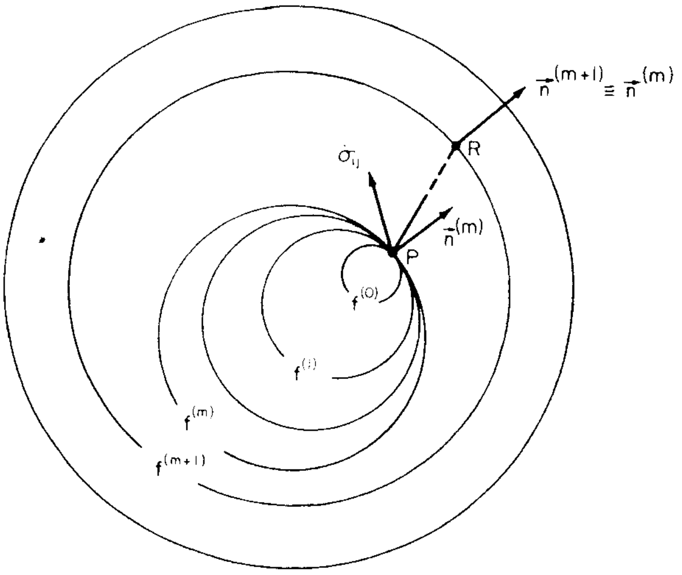

Figure 2.21: Yield surface according to Prevost (Chen & Baladi, 1985)

Afterwards, several models with isotropic and kinematic hardening were performed defining the evolution of the α variable by means of a "***bounding surface***" ((Dafalias & Popov,1975) in the stresses space, described by the equation (2.27) which delimits the possible states for the material (Figure 2.22):

$$F(\boldsymbol{\sigma}, q_{\kappa}) = 0 \tag{2.27}$$

The "***bounding surface***" can expand or contract isotropically, while the yield surface can translate, expand or contract within the domain defined by the "***bounding surface***". The translation of the yield surface is ruled by the same rules of the previously described models (i.e. f moves towards F, along the PR path shown in Figure 2.21). Moreover, the hardening modulus ***H*** depends on the distance δ between the stress state P, on the yield surface, and the conjugate point R, on the bounding surface.

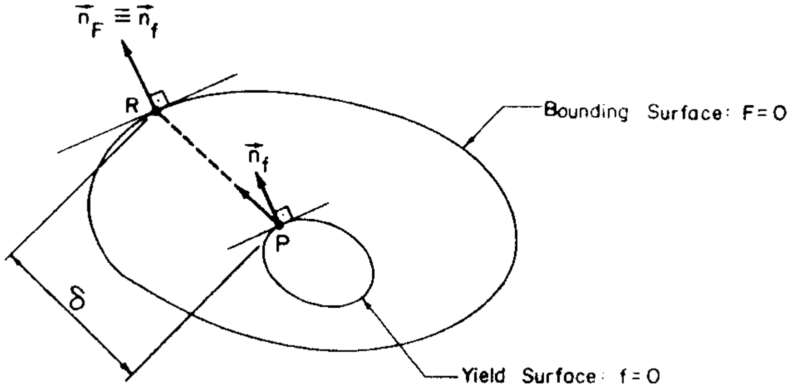

Figure 2.22: Yield surface and "bounding surface" (Chen & Baladi, 1985)

It has been stressed that the kinematic hardening is necessary to describe the behaviour of the soil subjected to loading-unloading cycle.

A better description of the behaviour of the soil can be achieved by the use of a rotational hardening, in which the yield surface changes not only its shape and size but also its orientation in the stress space.

Two different models with rotational hardening (Figure 2.23) exist:

1) Models with yield surfaces *open* along the hydrostatic axis, usually conic surfaces, useful to describe the behaviour of the coarse-grained soils (Ghaboussi & Momen, 1982; Gajo & Muir Wood, 1999 a-b);

2) Models with yield surfaces *close* along the hydrostatic axis, useful to describe the anisotropic behaviour of both coarse-grained soils and fine-grained ones (Hashiguchi, 1979; di Prisco, 1993; di Prisco et al., 1993).

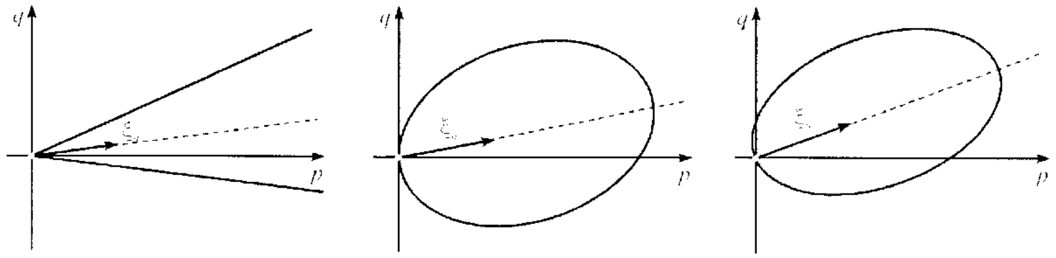

Figure 2.23: Models with rotational hardening (Tamagnini,2002)

The following section describes the mathematic formulation of the constitutive model characterized by isotropic and kinematic hardening, developed for sands by Gajo e Muir Wood (Muir Wood et al., 1994; Gajo & Muir Wood, 1999 a-b) and called ***Severn-Trent model***. It belongs to the first group of models, being characterized by an open yield surface along the hydrostatic axis.

Summing up, for the models with isotropic and kinematic hardening (Muir Wood et al., 1994; Gajo & Muir Wood, 1999; Rouainia & Muir Wood, 2001; di Prisco et al., 1993), the behaviour of the soil is elastic just inside a small domain, which moves in the stresses space maintaining the same size, according to the kinematic hardening, until to reaching the bounding surface, characterized by the isotropic hardening.

2.8 Severn-Trent constitutive model

2.8.1 Introduction

The constitutive model of ***Gajo & Muir Wood*** (1999a-b) describes the mechanical behaviour of granular soils, for any strain level and for any density value. It considers a first elastic phase followed by a plastic phase characterized by both isotropic and kinematic hardening. It requires ten parameters, two elastic and eight plastic, linked to clear physical features of the mechanical response. Moreover, the model is based on the state parameter ψ (Been & Jefferies, 1985), by means of both density-dependent (*pycnotropy*) and pressure-dependent (*barotropy*) of the behaviour of granular soils can be modelled.

2.8.2 Basic concepts of the constitutive model

The current strength of the sand is not constant but depends on the current specific volume and mean stress, through the state parameter ψ (Beem & Jefferies, 1985):

$$\psi = v - v_\lambda + \lambda \, ln \, p' \qquad (2.28)$$

where and are two constitutive parameters which define the local position of the critical-state line (2.29) in terms of the specific volume and mean effective stress p':

$$v = v_\lambda - \lambda \, ln \, p' \qquad (2.29)$$

So, the state parameter ψ represents the volumetric distance, for a constant mean stress, of the current state of the sand from the critical state line (Figure 2.24).

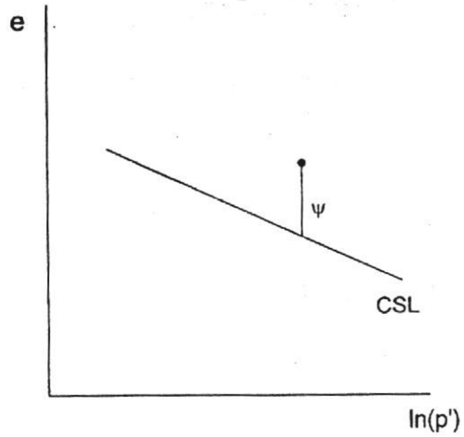

Figure 2.24: Parameter (Gajo & Muir Wood, 1999 – b)

The constitutive model is characterized by three surfaces shown in Figure 2.25:

1) ***Yield surface***;
2) ***Strength surface***;
3) ***Critical state surface***.

The ***yield surface*** (that is a cone) can extend or contract (*isotropic hardening*) and it can rotate (*kinematic hardening*). It always remains inside the strength surface tending asymptotically to it.

The ***strength surface*** can extend or contract and it tends to coincide with the critical state surface for infinite strains.

The ***critical state surface*** doesn't change its size or position and it depends on the void index and on the relativity density. Moreover, it can be inside or outside the strength surface. For dense sands, the strength surface tends to contract towards the critical state surface, which is so inside (*softening*); on the contrary, for loose sands, the critical state surface is outside the strength surface (*hardening*).

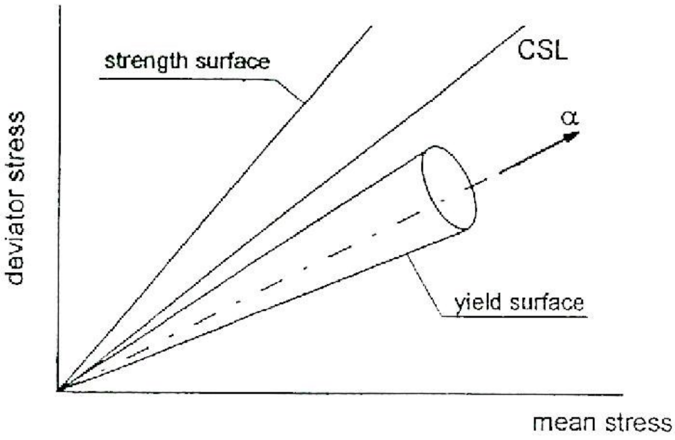

Figure 2.25: Strength, yield and critic state(CSL surface (Gajo & Muir Wood, 1999 – b)

The size of the strength surface is assumed to be related to the correspondent size of the critical state surface by means of a ratio “***r***” (2.30), which entirely contains, depending on $\boldsymbol{\psi}$, the effects induced by the density (*pycnotropy*) and mean stress (*barotropy*) on the strength and stress-strain response of the sand. It is equal to 1 when $\psi = 0$, i.e. the soil is at its critical-state conditions of mean stress and density (the strength surface coincides with the critical state surface):

$$r = (1 - k\psi) \tag{2.30}$$

where “***K***” is a constitutive parameter.

The size of the yield and the strength surface are linked by the constitutive parameter ***R***, which for ψ=0 is equal:

$$\boldsymbol{R} = \frac{sin\,\varphi_y}{sin\,\varphi_{cv}} \tag{2.31}$$

where and are angles of shear strenght for the yield surface and critical state surface, respectively.

For other values of ψ, the size of the yield surface changes, so that its size maintains a constant proportion ***R*** of the size of the strength surface and a constant proportion ***rR*** of the size of the critical state surface:

$$sin\,\varphi_y = rR\,sin\,\varphi_{cv} \tag{2.32}$$

The isotropic hardening is defined by "***r***": the yield and strength surfaces can change along elastic stress-paths starting from inside the yield surface, but then they can cross the yield surface (the strength surface can expand or contract according to the variation of ψ***)***.

And it is for this reason (ie to avoid numerical difficulties) that it is convenient to define the elastoplastic constitutive relationship in a normalized stress space in which all the deviatoric components of the stresses are divided by the term, so that the sizes of the strength and yield surfaces are constant and only kinematic hardening occurs.

Since the strength and yield surfaces must be independent of the reference system used to represent them, they are expressed through the stress invariants and their derivatives, defined in the next paragraph.

2.8.3 Stress and strain tensors and stress invariants

The deviatoric component "$\boldsymbol{s}$" of the stress tensor "$\boldsymbol{\sigma}$" is equal to:

$$\boldsymbol{s} = \boldsymbol{\sigma} - (\boldsymbol{\sigma}\colon\boldsymbol{\delta})\boldsymbol{\delta} \tag{2.33}$$

where $\boldsymbol{\delta}$ identifies the bisector of the first quadrant of the principal stress space ($\boldsymbol{\delta} = -\delta_{ij}/\sqrt{3}$, where δ_{ij} is the Kronecker's delta and the negative sign is because the compressions are assumed negative).

Moreover, $(\boldsymbol{\sigma}\colon\boldsymbol{\delta})$ is the isotropic component of the stress, linked to the mean stress *p'* (positive if it is compression stress) through $(\boldsymbol{\sigma}\colon\boldsymbol{\delta}) = \sqrt{3}p'$.

The "normalized stress is:

$$\bar{\boldsymbol{\sigma}} = \frac{\mathbf{1}}{(\mathbf{1}-\boldsymbol{k\psi})}\boldsymbol{s} + (\boldsymbol{\sigma}:\boldsymbol{\delta})\boldsymbol{\delta} \tag{2.34}$$

The deviatoric component of the "normalized" stress is:

$$\bar{\boldsymbol{s}} = \bar{\boldsymbol{\sigma}} - (\boldsymbol{\sigma}:\boldsymbol{\delta})\boldsymbol{\delta} = \frac{\mathbf{1}}{(\mathbf{1}-\boldsymbol{k\psi})}\boldsymbol{s} \tag{2.35}$$

The axis of the **yield surface** in the normalized space of the stress is a straight line and so just the unit tensor $\boldsymbol{\alpha}$ is necessary to define this surface. To define the **yield surface** is convenient to considerer the isotropic and deviatoric components of the normalized stress tensor respect to $\boldsymbol{\alpha}$ (Ghaboussi & Momen, 1982).

The deviatoric component of the normalized stress $\bar{\boldsymbol{\sigma}}$ respect to $\boldsymbol{\alpha}$ is defined as:

$$\boldsymbol{q} = \bar{\boldsymbol{\sigma}} - (\bar{\boldsymbol{\sigma}}:\boldsymbol{\alpha})\boldsymbol{\alpha} \tag{2.36}$$

where $(\bar{\boldsymbol{\sigma}}:\boldsymbol{\alpha})$ is the isotropic component of the stress $\bar{\boldsymbol{\sigma}}$ and $\boldsymbol{q}$ is the deviatoric component of $\bar{\boldsymbol{\sigma}}$ respect to $\boldsymbol{\alpha}$.

Before defining the stress invariants of the stress tensor $\bar{\boldsymbol{\sigma}}$ normalized respect to $\boldsymbol{\alpha}$, it is necessary to introduce the following tensor $\boldsymbol{k}_q$ e $\boldsymbol{k}_s$: :

$$\boldsymbol{k}_q = q_{ik}q_{kj} \qquad \boldsymbol{k}_s = s_{ik}s_{kj} \tag{2.37}$$

So, the above-mentioned invariants and the corresponding derivatives are expressed as:

$$\boldsymbol{I}_\alpha = -\sqrt{\mathbf{3}}\bar{\boldsymbol{\sigma}}:\boldsymbol{\alpha} \quad \boldsymbol{I}_{\alpha,\bar{\sigma}} = -\sqrt{\mathbf{3}}\boldsymbol{\alpha} \quad \boldsymbol{I}_{\alpha,\alpha} = -\sqrt{\mathbf{3}}\bar{\boldsymbol{\sigma}} \tag{2.38a}$$

$$\boldsymbol{J}_\alpha = \frac{\mathbf{1}}{\mathbf{2}}\boldsymbol{q}:\boldsymbol{q} \qquad \boldsymbol{J}_{\alpha,\bar{\sigma}} = \boldsymbol{q} \tag{2.38b}$$

$$\boldsymbol{J_{\alpha,\alpha}} = -(\bar{\boldsymbol{\sigma}} \otimes \boldsymbol{\alpha} + (\bar{\boldsymbol{\sigma}}:\boldsymbol{\alpha})\boldsymbol{I}):\boldsymbol{q} \tag{2.38c}$$

$$\boldsymbol{S_\alpha} = \frac{\mathbf{1}}{\mathbf{3}}\boldsymbol{k_q}:\boldsymbol{q}, \boldsymbol{S_{\alpha,\bar{\sigma}}} = (\boldsymbol{I} - \boldsymbol{\alpha} \otimes \boldsymbol{\alpha}):\boldsymbol{k_q} \tag{2.38d}$$

$$\boldsymbol{S_{\alpha,\alpha}} = -(\bar{\boldsymbol{\sigma}} \otimes \boldsymbol{\alpha} + (\bar{\boldsymbol{\sigma}}:\boldsymbol{\alpha})\boldsymbol{I}):\boldsymbol{k_q} \tag{2.38e}$$

Finally, the ***Lode's*** angle $\boldsymbol{\theta}$ and its derivatives are:

$$\boldsymbol{\theta} = \frac{\mathbf{1}}{\mathbf{3}} arcsin\left(-\frac{\mathbf{3}\sqrt{\mathbf{3}}}{\mathbf{2}}\frac{\boldsymbol{S}}{\boldsymbol{J}^{\frac{3}{2}}}\right) \tag{2.39a}$$

$$\boldsymbol{\theta}_{,\boldsymbol{\sigma}} = \frac{-\sqrt{\mathbf{3}}}{\mathbf{2}\,\boldsymbol{cos}(\mathbf{3}\boldsymbol{\theta})}\left(\frac{\mathbf{1}}{\boldsymbol{J}^{\frac{3}{2}}}\boldsymbol{S}_{,\boldsymbol{\sigma}} - \frac{\mathbf{3}\boldsymbol{S}}{\mathbf{2}\boldsymbol{J}^{\frac{5}{2}}}\boldsymbol{J}_{,\boldsymbol{\sigma}}\right) \tag{2.39b}$$

$$\boldsymbol{\theta}_{,\boldsymbol{\alpha}} = \frac{-\sqrt{\mathbf{3}}}{\mathbf{2}\,\boldsymbol{cos}(\mathbf{3}\boldsymbol{\theta})}\left(\frac{\mathbf{1}}{\boldsymbol{J}^{\frac{3}{2}}}\boldsymbol{S}_{,\boldsymbol{\alpha}} - \frac{\mathbf{3}\boldsymbol{S}}{\mathbf{2}\boldsymbol{J}^{\frac{5}{2}}}\boldsymbol{J}_{,\boldsymbol{\alpha}}\right) \tag{2.39c}$$

2.8.4 Yield and strength surfaces

The yield surface $\boldsymbol{f}$ and the strength surface $\boldsymbol{F}$ are in the following expressed through the invariants of the isotropic and deviatoric components of $\bar{\boldsymbol{\sigma}}$ respect to $\boldsymbol{\alpha}$ and $\boldsymbol{\delta}$:

$$\boldsymbol{f}(\bar{\boldsymbol{\sigma}}, \boldsymbol{\alpha}) = \boldsymbol{f}(\boldsymbol{I_\alpha}, \boldsymbol{J_\alpha}, \boldsymbol{S_\alpha}) = \mathbf{0} \tag{2.40}$$

$$\boldsymbol{F}(\bar{\boldsymbol{\sigma}}) = \boldsymbol{F}(\boldsymbol{I_\delta}, \boldsymbol{J_\delta}, \boldsymbol{S_\delta}) = \mathbf{0} \tag{2.41}$$

To evaluate the strain-stress relationships and to describe the consistency conditions, it is necessary to evaluate the following quantities:

$$\boldsymbol{n_{\bar{\sigma}}} = \boldsymbol{f}_{,\bar{\boldsymbol{\sigma}}}, \quad \boldsymbol{n_\alpha} = \boldsymbol{f}_{,\boldsymbol{\alpha}}, \quad \boldsymbol{F}_{,\bar{\boldsymbol{\sigma}}} \tag{2.42}$$

The tensors $\mathbf{n}_\sigma$ e $\mathbf{n}_\alpha$ can be computed through the following expression:

$$\boldsymbol{n}_{\bar{\sigma}} = \boldsymbol{f}_{,\bar{\sigma}} = \boldsymbol{f}_{,I}\boldsymbol{I}_{\alpha,\bar{\sigma}} + \boldsymbol{f}_{,J}\boldsymbol{J}_{\alpha,\bar{\sigma}} + \boldsymbol{f}_{,S}\boldsymbol{S}_{\alpha,\bar{\sigma}} \tag{2.43}$$

$$\boldsymbol{n}_{\alpha} = \boldsymbol{f}_{,\alpha} = \boldsymbol{f}_{,I}\boldsymbol{I}_{\alpha,\alpha} + \boldsymbol{f}_{,J}\boldsymbol{J}_{\alpha,\alpha} + \boldsymbol{f}_{,S}\boldsymbol{S}_{\alpha,\alpha} \tag{2.44}$$

Analogous expressions can be obtained for the strength surface ***F***.
In plasticity theory, the direction of loading is defined by a unit vector **n:**

$$\boldsymbol{n} = \frac{\boldsymbol{n}_{\bar{\sigma}}}{\sqrt{\boldsymbol{n}_{\bar{\sigma}}:\boldsymbol{n}_{\bar{\sigma}}}} \tag{2.45}$$

Gajo e Muir Wood (1999 a-b) proposed four different strength and yield surfaces: Drucker-Prager (1952), Matsuoka-Nakai (1974), Lade (1977) and Argyris (1973).

1. The ***Drucker-Prager*** surface is described by the following relationship:

$$\boldsymbol{F} = \boldsymbol{\alpha I} + \sqrt{\boldsymbol{J}} \tag{2.46}$$

where, if the Drucker-Prager circle coincides with the Mohr-Coulomb hexagon on the external vertexes, $\boldsymbol{\alpha}$ is:

$$\boldsymbol{\alpha} = \frac{\mathbf{2}\, \boldsymbol{sin}\, \boldsymbol{\varphi}}{\sqrt{\mathbf{3}}(\mathbf{3} - \boldsymbol{sin}\, \boldsymbol{\varphi})} \tag{2.47}$$

The derivatives respect to the invariants of stress are:

$$\boldsymbol{F}_{,I} = \boldsymbol{\alpha} \qquad \boldsymbol{F}_{,J} = \frac{\mathbf{1}}{\mathbf{2}\sqrt{\boldsymbol{J}}} \qquad \boldsymbol{F}_{,S} = \mathbf{0} \tag{2.48}$$

2. The ***Matsouka-Nakai*** (1974) surface is described by the following expression:

$$\frac{\boldsymbol{I}_1 \boldsymbol{I}_2}{\boldsymbol{I}_3} = \boldsymbol{\kappa} \tag{2.49}$$

where the invariants are defined:

$$I_1 = I \tag{2.50}$$

$$I_2 = \frac{1}{3}I^2 - J \tag{2.51}$$

$$I_3 = S - \frac{1}{3}IJ + \frac{1}{27}I^3 \tag{2.52}$$

So, the (2.49) become:

$$F = \kappa S + \left(1 - \frac{\kappa}{3}\right) IJ + \left(\frac{\kappa}{27} - \frac{1}{3}\right) I^3 \tag{2.53}$$

If, for each cross-section, the Matsuoka-Nakai surface coincides with the Mohr-Coulomb hexagon both on the external vertexes and on the internal ones:

$$\kappa = 9 + 8\,tan^2\,\varphi \tag{2.54}$$

The derivatives are:

$$F_{,I} = \left(1 - \frac{\kappa}{3}\right) J + 3\left(\frac{\kappa}{27} - \frac{1}{3}\right) I^2 \tag{2.55}$$

$$F_{,J} = \left(1 - \frac{\kappa}{3}\right) I \tag{2.56}$$

$$F_{,S} = \kappa \tag{2.57}$$

3. The **Lade** surface (1977) is described by the following expression:

$$\frac{{I_1}^3}{I_3} = \frac{1}{\kappa} \rightarrow \quad F = S - \frac{1}{3}IJ + \left(\frac{1}{27} - \kappa\right) I^3 \tag{2.58}$$

If the Lade surface coincides, for each cross-section, with the Mohr-Coulomb hexagon:

$$\boldsymbol{\kappa} = \frac{(1+sin\,\varphi)(1-sin\,\varphi)^2}{(3-sin\,\varphi)^3} \tag{2.59}$$

The derivatives are:

$$F_{,I} = -\frac{1}{3}J + 3\left(\frac{1}{27} - \kappa\right)I^2 \tag{2.60}$$

$$F_{,J} = -\frac{1}{3}I \tag{2.61}$$

$$F_{,S} = 1 \tag{2.62}$$

4. The **Argyris** surface is described by the following expression:

$$F = \kappa g(\theta)I + \sqrt{J} \tag{2.63}$$

The derivatives are:

$$F_{,I} = \kappa g(\theta) \tag{2.64}$$

$$F_{,J} = \frac{1}{2\sqrt{J}} + \frac{9\sqrt{3}}{4}kg(\theta)^2\frac{(1-m)}{2m}\frac{IS}{J^{\frac{5}{2}}} \tag{2.65}$$

$$F_{,S} = -\frac{3\sqrt{3}}{2}kg(\theta)^2\frac{(1-m)}{2m}\frac{I}{J^{\frac{3}{2}}} \tag{2.66}$$

2.8.5 Flow law

The flow law is not associated, or rather an associated flow law is defined on the deviatoric plane, so the unit direction of the plastic strain **m** must have the same deviatoric components of **n**.

It is possible to evaluate the unit direction **m** of the plastic flow, although the potential function is not defined explicitly:

$$m = \frac{\bar{m}}{\sqrt{\bar{m}\cdot\bar{m}}} \tag{2.67}$$

where

$$\bar{\boldsymbol{m}} = \frac{\sqrt{3}}{2\sqrt{J_\mu}}\boldsymbol{\mu} - \frac{d}{\sqrt{3}}\boldsymbol{\delta} \tag{2.68}$$

and where **μ** is the deviatoric component of **n** respect to **δ:**

$$\boldsymbol{\mu} = \boldsymbol{n} - (\boldsymbol{n}\colon\boldsymbol{\delta})\boldsymbol{\delta} \tag{2.69}$$

J_μ second invariant of **n** respect to **δ:**

$$J_\mu = 0.5\boldsymbol{\mu}\colon\boldsymbol{\mu} \tag{2.70}$$

d is the *dilatancy*, defined as the ratio between the plastic volumetric $\delta\varepsilon_v{}^p$ and deviatoric strain increments $\delta\varepsilon_s{}^p$:

$$d = \frac{\delta\varepsilon_v^p}{\delta\varepsilon_s^p} = -A[(1 + k_d\psi)G(\varphi_{cv}) - G(\varphi_m)] \tag{2.71}$$

where A and k_d are two constitutive parameters and $\boldsymbol{\phi_m}$ is an angle of shear strength depending on the first and the second invariants by means of a relationship correlated to the assumed critical state surface. For example, assuming the *Drucker-Prager* surface:

$$\sin\phi_m = \frac{-3\sqrt{3}\sqrt{J_\delta}}{2I_\delta - \sqrt{3}\sqrt{J_\delta}} \tag{2.72}$$

The function $\boldsymbol{G(\phi)}$ is essentially arbitrary, and it is assumed based on the original Cam-Clay model:

$$G(\varphi) = \frac{6\sin\varphi}{3 - \sin\varphi} \tag{2.73}$$

The plastic strain increments, deduced by $\bar{\mathbf{m}}$, are:

$$\delta\varepsilon_s^p = \frac{2}{\sqrt{3}}\sqrt{J_{\bar{m}}} = 1 \quad \text{and} \quad \delta\varepsilon_v^p = -\sqrt{3}\bar{\boldsymbol{m}}:\boldsymbol{\delta} = d \tag{2.74}$$

2.8.6 Hardening rule

In the normalized space, only the kinematic hardening occurs through the rotation of the unit tensor $\boldsymbol{\alpha}$, which is the direction of yield surface axis in the normalized space of the stresses.

In particular, the following translation law is assumed:

$$\delta\boldsymbol{\alpha} = \tau(\bar{\boldsymbol{\sigma}}_c - \bar{\boldsymbol{\sigma}}) \tag{2.75}$$

where τ is a coefficient scalar that it can be evaluated by the consistency condition; $\bar{\boldsymbol{\sigma}}_c$ is the normalized stress corresponding to the “imagine” stress on the strength surface.

The position of $\bar{\boldsymbol{\sigma}}_c$ in the normalized stress space is defined considering that the deviatoric component of the normal direction to the strength surface at the $\bar{\boldsymbol{\sigma}}_c$ coincides with the deviatoric component of the normal direction to the yield surface at the $\bar{\boldsymbol{\sigma}}$ (Figure 2.26). An expression for $\bar{\boldsymbol{\sigma}}_c$ does not exist, so it must be evaluated through an iterative procedure.

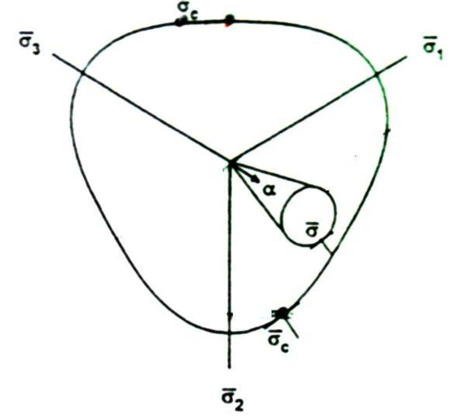

Figure 2.26: Conjugated stress on the strength surface (Gajo & Muir Wood, 1999 – b)

2.8.7 Consistent condition

The consistency condition ensures that during yielding the stress state remains on the yield surface. As a result, since the yield surface moves asymptotically towards the strength surface, the consistency condition also ensures that the stress state will never be outside the strength surface.

It is convenient to consider the consistency condition in the normalized stress space, where neither the strength surface nor the yield surface changes in size and the yield surface is only subjected to a kinematic hardening.

If *f* is the yield surface, the consistency condition is:

$$\delta f = \boldsymbol{f}_{,\bar{\sigma}}\colon \delta\bar{\boldsymbol{\sigma}} + \boldsymbol{f}_{,\alpha}\colon \delta\boldsymbol{\alpha} = 0 \tag{2.76}$$

And using the tensor $\mathbf{n}_{\sigma}$ and $\mathbf{n}_{\alpha}$ the consistency condition becomes:

$$\boldsymbol{n}_{\bar{\sigma}}\colon \delta\bar{\boldsymbol{\sigma}} + \boldsymbol{n}_{\alpha}\colon \delta\boldsymbol{\alpha} = 0 \tag{2.77}$$

As mentioned above, τ, is a coefficient scalar that it can be evaluated by the consistency condition (2.75).

Moreover, since the updated tensor $\boldsymbol{\alpha}+\delta\boldsymbol{\alpha}$ must have a unitary norm, it is necessary to consider only the component of $\tau\left(\bar{\boldsymbol{\sigma}}_c-\bar{\boldsymbol{\sigma}}\right)$ which is normal to $\boldsymbol{\alpha}$ that is:

$$\delta\boldsymbol{\alpha}=\tau\left(\bar{\boldsymbol{\sigma}}_c-\bar{\boldsymbol{\sigma}}\right)-\left[\left(\bar{\boldsymbol{\sigma}}_c-\bar{\boldsymbol{\sigma}}\right):\boldsymbol{\alpha}\right]\boldsymbol{\alpha} \tag{2.78}$$

So, τ can be evaluated according to the following expression:

$$\tau=\frac{\mathbf{n}_{\dot{\sigma}}:\delta\bar{\boldsymbol{\sigma}}}{\mathbf{n}_{\alpha}\left(\bar{\boldsymbol{\sigma}}_c-\bar{\boldsymbol{\sigma}}\right)-\left[\left(\bar{\boldsymbol{\sigma}}_c-\bar{\boldsymbol{\sigma}}\right):\boldsymbol{\alpha}\right]\left(\mathbf{n}_{\alpha}:\boldsymbol{\alpha}\right)} \tag{2.79}$$

2.8.8 The hypoelastic constitutive relation

The hypoelastic constitutive relation is given in terms of the "real" effective stress $\delta\boldsymbol{\sigma}$ and elastic strain increment $\delta\boldsymbol{\varepsilon}^e$:

$$\delta\boldsymbol{\sigma}=\boldsymbol{D}^e:\delta\boldsymbol{\varepsilon}^e \tag{2.80}$$

For isotropic hypoelasticity:

$$\boldsymbol{D}^e=2G\boldsymbol{I}+(3K-2G)\boldsymbol{\delta}\otimes\boldsymbol{\delta} \tag{2.81}$$

where $\boldsymbol{K}$ and $\boldsymbol{G}$ are the elastic bulk and shear moduli, respectively, which are assumed dependent on the square root of the mean stress.
It is necessary to evaluate the hypoelastic relationship in terms of "normalized" effective stress increments $\delta\bar{\boldsymbol{\sigma}}$ and elastic-strain increments $\delta\boldsymbol{\varepsilon}^e$.
Differentiating (2.34):

$$\delta\bar{\boldsymbol{\sigma}}=\frac{1}{(1-\kappa\psi)}\cdot\delta\boldsymbol{s}+\frac{\kappa\delta\psi}{(1-\kappa\psi)}\cdot\boldsymbol{s}+\sqrt{3}\cdot\delta p'\boldsymbol{\delta} \tag{2.82}$$

where:

$$\delta\psi = \lambda\frac{\delta p'}{p'} + v\delta\varepsilon_v \tag{2.83}$$

where $\delta\boldsymbol{\varepsilon}_v$ is the volumetric strain increment:

$$\delta\boldsymbol{\varepsilon}_v = -\sqrt{3(\delta\boldsymbol{\varepsilon}:\boldsymbol{\delta})} \tag{2.84}$$

After substituting (2.83) and (2.84) into (2.82) and rearranging:

$$\delta\bar{\boldsymbol{\sigma}} = \left[\frac{1}{(1-\kappa\psi)}\boldsymbol{I} - \frac{\kappa\psi}{(1-\kappa\psi)}\boldsymbol{\delta}\otimes\boldsymbol{\delta} + \frac{\kappa\lambda}{\sqrt{3}(1-\kappa\psi)^2}\boldsymbol{s}\otimes\boldsymbol{\delta}\right]:\delta\boldsymbol{\sigma}$$

$$-\left[\frac{\sqrt{3}\cdot\kappa v}{(1-\kappa\psi)^2}\boldsymbol{s}\otimes\boldsymbol{\delta}\right]:\delta\boldsymbol{\varepsilon} \tag{2.85}$$

The relationship can be written:

$$\delta\bar{\boldsymbol{\sigma}} = \left\{\left[\frac{1}{(1-\kappa\psi)}\boldsymbol{I} - \frac{\kappa\psi}{(1-\kappa\psi)}\boldsymbol{\delta}\otimes\boldsymbol{\delta} + \frac{\kappa\lambda}{\sqrt{3}(1-\kappa\psi)^2}\boldsymbol{s}\otimes\boldsymbol{\delta}\right]:\boldsymbol{D}^e - \left[\frac{\sqrt{3}\cdot\kappa v}{(1-\kappa\psi)^2}\boldsymbol{s}\otimes\boldsymbol{\delta}\right]\right\}:\delta\boldsymbol{\varepsilon}^e \tag{2.86}$$

Obviously, if the behaviour is elastic, , $\delta\boldsymbol{\varepsilon}^p = 0$.
The (2.86) can be written as:

$$\delta\bar{\boldsymbol{\sigma}} = \bar{\boldsymbol{D}}^e:\delta\boldsymbol{\varepsilon}^e - \left(\frac{\sqrt{3}\cdot\kappa v}{(1-\kappa\psi)^2}\right)[\boldsymbol{s}\otimes\boldsymbol{\delta}]:\delta\boldsymbol{\varepsilon}^p \tag{2.87}$$

The equivalent elastic stiffness tensor $\bar{\boldsymbol{D}}^e$ provides the looked for relationship between the "normalized" effective stress increments $\delta\overline{\boldsymbol{\sigma}}$ and the elastic strain increments $\delta\boldsymbol{\varepsilon}^e$ (when the yielding is not reached).

2.8.9 The elastoplastic constitutive relations

As usual, the strain increment can be decomposed into an elastic component and a plastic one:

$$\delta\boldsymbol{\varepsilon} = \delta\boldsymbol{\varepsilon}^e + \delta\boldsymbol{\varepsilon}^p \tag{2.88}$$

According to (2.85):

$$\delta\bar{\boldsymbol{\varepsilon}}^e = \bar{\mathbf{D}}^e : \delta\bar{\boldsymbol{\sigma}} - \left(\frac{\sqrt{3}\cdot\kappa\nu}{(1-\kappa\psi)^2}\right)\bar{\mathbf{D}}^{e-1} : [\mathbf{s}\otimes\boldsymbol{\delta}] : \delta\boldsymbol{\varepsilon}^p \tag{2.89}$$

where $\bar{\boldsymbol{D}}^{e-1}$ is the fourth-order tensor such that $\bar{\boldsymbol{D}}^{e-1}{:}\,\bar{\boldsymbol{D}}^{e} = \bar{\boldsymbol{D}}^{e}{:}\,\bar{\boldsymbol{D}}^{e-1} = \boldsymbol{I}.$ The following expression defines the plastic strain increments:

$$\delta\boldsymbol{\varepsilon}^p = \frac{B\beta_{\max}}{\beta^2}\left(\mathbf{n} : \delta\bar{\boldsymbol{\sigma}}\right)\mathbf{m} \tag{2.90}$$

where $\boldsymbol{B}$ is a constitutive parameter, $\beta = \mathbf{n} : (\bar{\boldsymbol{\sigma}}_c - \bar{\boldsymbol{\sigma}})$ and $\beta_{\max}$ is the maximum value of β, achieved when the yield surface is close to the strength surface at the point diametrically opposite to $\bar{\boldsymbol{\sigma}}_c$:

$$\beta_{\max} = (1-R)\,\mathbf{n} : \left(\hat{\bar{\boldsymbol{\sigma}}}_c - \bar{\boldsymbol{\sigma}}\right) \tag{2.91}$$

where $\hat{\bar{\boldsymbol{\sigma}}}_c$ is the stress state at the strength surface at the point diametrically opposite to $\bar{\boldsymbol{\sigma}}_c$. The term (1-*R*) takes into account that, when $\beta = \beta_{\max}$, a part of $\boldsymbol{n}{:}\,(\hat{\bar{\boldsymbol{\sigma}}}_c - \bar{\boldsymbol{\sigma}})$ is inside to the yield surface.

Substituting, the strain increments can be written:

$$\delta\boldsymbol{\varepsilon} = \left[\bar{\boldsymbol{D}}^{e-1} + \frac{1}{H}\boldsymbol{m}^* \otimes \boldsymbol{m}\right] : \delta\bar{\boldsymbol{\sigma}} \tag{2.92}$$

where:

$$\frac{1}{H} = \frac{B\beta_{max}}{\beta^2} \tag{2.93}$$

$$\boldsymbol{m}^* = \boldsymbol{m} + \left(\frac{\sqrt{3}\kappa v}{(1-\kappa\psi)^2}\right)(\boldsymbol{\delta}: \boldsymbol{m})[\bar{\boldsymbol{D}}^{e-1}: \boldsymbol{s}] \tag{2.94}$$

In other words, passing from the real to the "normalized" stress space, the unit direction of the plastic flow $\boldsymbol{m}$ changes to $\boldsymbol{m^*}$, adding a small deviatoric component

The (2.92) can be inverted obtaining:

$$\delta\bar{\boldsymbol{\sigma}} = \left[\bar{\boldsymbol{D}}^e - \frac{(\bar{\boldsymbol{D}}^e{:}\boldsymbol{m}*)\otimes(\boldsymbol{n}{:}\bar{\boldsymbol{D}}^e)}{H+\boldsymbol{n}{:}(\bar{\boldsymbol{D}}^e{:}\boldsymbol{m}*)}\right] : \delta\boldsymbol{\varepsilon} \;\rightarrow\; \delta\bar{\boldsymbol{\sigma}} = \bar{\boldsymbol{D}}^{ep}: \delta\boldsymbol{\varepsilon} \tag{2.95}$$

The real stress is linked to the normalized stress through the following expression:

$$\boldsymbol{\sigma} = (1 - \kappa\psi)\bar{\boldsymbol{s}} + \sqrt{3}\bar{p}'\boldsymbol{\delta} \tag{2.96}$$

Where $\bar{\boldsymbol{p}}' = \boldsymbol{p}'$, because the normalization concerns only the deviatoric stress tensor.

Differentiating (2.96):

$$\delta\boldsymbol{\sigma} = (1 - \kappa\psi)\delta\bar{\boldsymbol{s}} - \kappa\delta\psi\bar{\boldsymbol{s}} + \sqrt{3}\delta\bar{p}'\boldsymbol{\delta} \tag{2.97}$$

After several substitutions:

$$\delta\boldsymbol{\sigma} = \left[(1-\kappa\psi)\mathbf{I} + (\kappa\psi)\boldsymbol{\delta}\otimes\boldsymbol{\delta} - \frac{\kappa\lambda}{\sqrt{3p}}\bar{\mathbf{s}}\otimes\boldsymbol{\delta} \right] : \delta\bar{\boldsymbol{\sigma}} + \left[\sqrt{3}\kappa\nu\bar{\mathbf{s}}\otimes\boldsymbol{\delta} \right] : \delta\boldsymbol{\varepsilon}$$

(2.98)

The rearranged expression becomes:

$$\delta\boldsymbol{\sigma} = \left\{ \left[(1-\kappa\psi)\mathbf{I} + (\kappa\psi)\boldsymbol{\delta}\otimes\boldsymbol{\delta} - \frac{\kappa\lambda}{\sqrt{3p}}\bar{\mathbf{s}}\otimes\boldsymbol{\delta} \right] : \bar{\mathbf{D}}^{ep} + \left[\sqrt{3}\kappa\nu\bar{\mathbf{s}}\otimes\boldsymbol{\delta} \right] \right\} : \delta\boldsymbol{\varepsilon}$$

(2.99)

That in compact form is:

$$\delta\boldsymbol{\sigma} = \mathbf{D}^{ep} : \delta\boldsymbol{\varepsilon} \tag{2.100}$$

So, the equivalent elastoplastic stiffness tensor $\bar{\mathbf{D}}^{ep}$ provides the relationship between the stress increments and the strain increments, which characterizes the Severn-Trent model.

2.8.10 Parameters of the model

The constitutive parameters are ten (table 1): two elastic parameter (G and ν) and eight plastic parameters: λ, v_λ, ϕ_{cv}, *k*, *R*, *A*, k_d e *B*.

The triaxial tests are the only tests useful to evaluate these parameters. By means of triaxial tests, the Severn-Trent constitutive model has been validated by the Authors (Gajo & Muir,1999). It has been stressed that the parameters *A, B, k* and k_d are estimated according to iterative procedures (trial and error procedures).As for the elastic parameter *G*, it is related to G_0 by means of a scale factor *C*:

$$G_0 = C\,G \qquad (2.101)$$

where the value of G_0 can be achieved by the formula proposed by Hardin and Black (1966), according to which G_0 depends on the specific volume v and the mean stress p':

$$G_0 = 3230 \cdot \frac{(3.97-v)^2}{v} \cdot \sqrt{p'} \qquad (2.102)$$

Table 2.1 -Parameters of the model (Gajo & Muir Wood, 1999)

Parameters	***Description***
G	shear modulus
ν	Poisson's coefficient
ϕ_{cv}	critical state angle of friction
λ	slope of the critical state line in the plane *v-lnp*
v_λ	intercept for the critical state line in the *v-lnp* plane at p=1 kPa
k	effect of state parameter on strength
R	size of kinematic yield surface
A	dilatancy parameter
k_d	effect of state parameter on dilatancy
B	distortional strain hardening parameter

Chapter 3

FEM MODEL VALIDATION

3.1 Introduction

The main purpose of the present thesis is studying the seismic behaviour of a tunnel-soil-aboveground structure system and evaluating the effects of the tunnel on the response of the aboveground building and vice versa employing FEM analyses.

The results of the performed FEM analyses will be discussed in chapter 4: the analyses have initially concerned with a cross-section of the underground network case-history of Catania (Italy); then, numerous parametric analyses were performed, varying the main characteristics of the system in order to study their effects on the dynamic tunnel-soil-aboveground structure interaction.

This chapter shows the validation of the developed FEM model, briefly described in the following paragraph. For a detailed description of the model and all the assumptions that led to it, please refer to chapter 4.

In order to validate the FEM model, several seismic response analyses were carried out. In the first phases, one-dimensional (1D) and two-dimensional (2D) seismic response analyses were performed, using the same soil profile but different inputs characterized by several *Peak Ground Acceleration (PGA)*. Moreover, several soils characterized by different stiffnesses were analysed.

Finally, soil-tunnel dynamic interaction analyses and a centrifugal test simulation by means a FEM model were performed.

The goals of these analyses were to evaluate the correct application of the boundary conditions, to test the correct use of the dashpots at the bedrock to simulate the bedrock.

The one-dimensional analyses were conducted in the frequency domain ~~with~~ by the following codes: *EERA* (Bardet et al., 2000), *STRATA* (Kottke & Rathje, 2008) and *DEEPSOIL* (Hashash et al., 2018). Moreover, a soil column soil 1-meter wide was analysing in the time domain employing the *ADINA* code (2008). For the soil-tunnel dynamic interaction analyses and the centrifugal test simulation, the software *ADINA* was used to comparing the obtained results with those obtained through the *ABAQUS* (2012) code by other Authors (Argyroudis et al. 2017; Mentrey & Willam, 1995; Lanzano et al.,2010,2012). The results are compared in terms of: a) acceleration time history at different depths; b) shear strain and stress time history at the different depths; c) amplification function; d) peak ground acceleration with the depth; e) bending moment and axial force on the underground structure.

So, all the performed analyses are:

1) Visco-elastic-linear analysis of a layered undamped soil on elastic rock characterized by high stiffness values through 1D analyses ("*Stiff Soil*");
2) Visco-elastic-linear analysis of a layered undamped soil on elastic rock characterized by low stiffness values through 1D analyses ("*Soft Soil*");
3) Visco-elastic-linear analysis of a tunnel-soil coupled system through 2D analyses. The results were compared with those obtained by Argyroudis et al. (2017);
4) Visco-elastoplastic analysis of the tunnel-soil coupled system. The same FEM model of the previous step was analysed, using a different constitutive model

for the soil. In particular, a perfectly plastic elastic model was used (Mohr-Coulomb) for the soil;

5) Numerical analysis of the centrifuge test performed using a visco-elastoplastic model (Mohr-Coulomb) for the soil (Mentrey & Willam, 1995; Lanzano et al.,2010,2012).

In the following sections, general settings about of the 1D and 2D numerical analyses are shown and the main characteristics of the FEM model developed for the analysis of the behaviour of a tunnel-soil-aboveground structure system are summarized. After that, the results obtained by the above-mentioned analyses are discussed.

3.2 General settings: numerical models for 1D and 2D analyses

Figure 3.1 shows the FEM model developed for the analysis of the behaviour of a tunnel-soil-aboveground structure system. For a detailed description of the model and all the assumptions that led to its development, please refer to chapter 4. Here, just the main characteristics concerning the boundary conditions, the material's viscosity and the mesh density are summarized, because they are the object of the validation described in the following sections.

For the validation of the numerical model, a great contribution was made by the PhD student Zhongkai Huang of the Tonji University (China), during the period of study spent at the Aristotle University of Thessaloniki (Greece), which provided me results achieved through the *ABAQUS* and *EERA* codes. In particular, the results for the above-mentioned steps 1 and 2 were compared with the results obtained by the undersigned through the *STRATA* and *DEEPSOIL* codes*,* for the 1D analyses, and through the *ADINA* code for the 2D analyses.

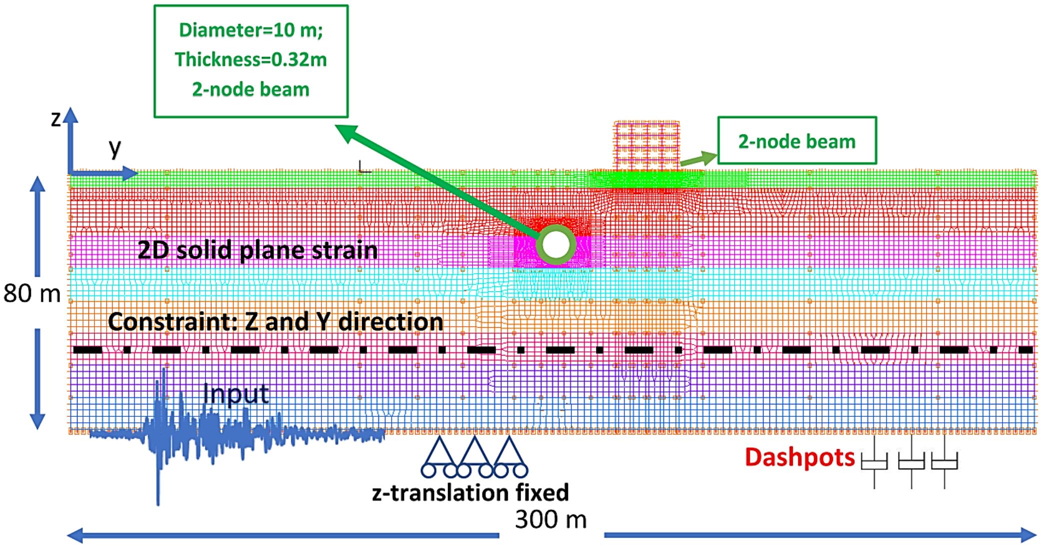

Figure 3.1: FEM model of the tunnel-soil-aboveground building system analysed in Chapter 4.

The general settings that concern with the numerical models are summarised in this section. In particular, the stratigraphy used for the validation of the numerical model is described.

The soil, for both the used FEM codes (*ADINA* and *ABAQUS*) was modelled by 2D solid elements in plane-strain conditions and four nodes, using two different constitutive models: 1) a viscoelastic constitutive model; 2) a visco-elastoplastic model (Mohr-Coulomb).

As for the boundary conditions, for an initial geostatic analysis, the bottom of the numerical models was fixed in both horizontal and vertical directions, and the vertical boundaries were fixed in the horizontal direction allowing the vertical displacements. For the subsequent dynamic analysis, the nodes of the soil vertical boundaries were linked by "constraint equations" that imposed the same displacements, both horizontally and vertically, at the same depths (Abate & Massimino, 2016), imitating in this way a desirable 'shear beam' response and to reproduce the free field seismic response; the effectiveness of the "constraint equations" imposed at the vertical lateral boundaries are independent on the model width. About that, for a numerical model with a width equal to 1 m or 400 m (see STEP 1 section 3.3), without the presence of a building, the results obtained were similar for the two models analysed. Moreover, for the numerical model with a width equal to 400 m, without the presence of a building, the results were independent on the alignment analysed. Preliminary analyses to detect the minimum width of the numerical model able to minimizing (or to avoid) reflection of outward propagating waves back into the model were carried out, obtaining a width of the numerical model equal to around four times of the depth of the model. By the use of the "constraint equations" at the vertical boundaries and a width of the model able to avoid reflection phenomena of the propagating waves, a free field condition was ensured in the region close to the vertical boundaries; moreover, the nodes at the base of the mesh were constrained only in the vertical direction.

Moreover, as shown in Figure 3.1 to the base of the numerical model the dashpots were implemented, only in the same direction of the input motion (horizontal direction), to simulate the elastic bedrock according to Lysmer and Kuhlemeyer (1969). The viscous boundary by Lysmer & Kuhlemeyer (1969), consisting of independent dashpots in the normal and shear direction at the model boundaries. For the numerical models analysed and described in the following sections, a "shear beam" response was reproduced through the use of the constraint equations at the vertical lateral boundaries. For this reason, the viscous boundary was used only in the shear direction. The dashpot coefficients, c, were defined as the product of the mass density, ρ, and the shear wave velocity, V_S, of the bedrock and the 'effect' area, A, of each dashpot, to maintain proportional results for any horizontal element size:

$$c = \rho \cdot V_s \cdot A \tag{3.1}$$

In the case of quite/absorbing boundaries, in most of the available codes, the input motion is introduced as a displacement or velocity or acceleration time history. In the FEM models analysed by the following presented studies, the input motion was applied through the above dashpots, located to the bottom of the model, as an acceleration time history.

As for the materials' viscosity, it was modelled according to the Rayleigh damping. According to this formulation, the damping matrix [C], was defined as a combination of the mass [M] matrix and the stiffness [K] matrix (Chopra, 2007):

$$[C] = \alpha[M] + \beta[K] \tag{3.2}$$

Considering the modal damping ratios for a system with mass-proportional damping to the coefficient α, the generalized damping for the nth mode is:

$$C_n = \alpha M_n \tag{3.3}$$

And the modal damping ratio is:

$$\zeta_n = \frac{\alpha}{2\omega_n} \tag{3.4}$$

The damping ratio is inversely proportional to the natural frequency (see Figure 3.2). Similarly, the modal damping ratios for a system with stiffness-proportional damping can be related to the coefficient β. In this case:

$$C_n = \beta K_n = \beta(\omega_n^2 M_n) \tag{3.5}$$

$$\zeta_n = \frac{\beta}{2}\omega_n \tag{3.6}$$

The damping ratio increases linearly with the natural frequency (see Figure 3.2). Neither of the damping matrices defined by Eq. 3.3 and 3.5 are appropriate for practical numerical analysis. For this reason, a Rayleigh damping was modelled according to the following equation (3.7). The damping ratio for the n^{th} mode is:

$$\zeta_n = \frac{\alpha}{2\omega_n} + \frac{\beta}{2}\omega_n \tag{3.7}$$

The coefficients α and β can be evaluated from specified damping ratios ζ_i and ζ_j for the i^{th} and j^{th} modes, respectively. Expressing Eq. (3.7) for these two modes in matrix form leads to:

$$\frac{1}{2}\begin{bmatrix} \frac{1}{\omega_i} & \omega_i \\ \frac{1}{\omega_j} & \omega_j \end{bmatrix} \begin{Bmatrix} \alpha \\ \beta \end{Bmatrix} = \begin{Bmatrix} \zeta_i \\ \zeta_j \end{Bmatrix} \tag{3.8}$$

These two algebraic equations can be solved to determine the coefficients α and β. If both modes are assumed to have the same damping ratio ζ, the coefficients can be evaluated through the following expressions:

$$\alpha = 2 \cdot \frac{D \cdot \omega_i \cdot \omega_j}{\omega_i + \omega_j}; \qquad \beta = 2 \cdot \frac{D}{\omega_i + \omega_j} \tag{3.9}$$

in which D is the damping ratio of the material $\omega_\mathrm{i} = \omega_1 = \frac{V_S}{4H} 2\pi$ the first angular frequency of the soil and $\omega_\mathrm{j} = \mathrm{n} \cdot \omega_1$. The value of "n" is usually chosen to obtain the damping within a period range essentially constant. The value of "n" is usually between 3÷6. In this way, the damping is essentially constant within the frequencies range between the first frequency of the soil and the fourth or sixth frequency.

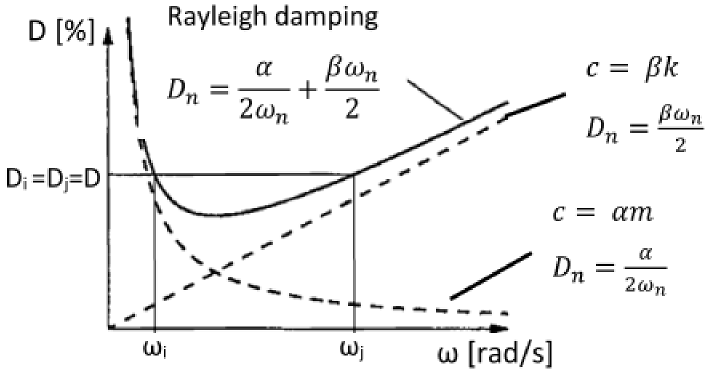

Figure 3.2: Variation of modal damping ratios with natural frequency (Chopra, 2007)

As for the mesh density, the accuracy of the numerical solution depends on the number and the size of elements introduced into the FEM model, whose however growth affects calculation times. A good rule to optimize discretization is to provide at least 3-4 points to describe the generic semi wavelength of the vibration of an element of thickness h and velocity V_S. So, the maximum element size of the mesh was chosen in a way that guarantees the efficient reproduction of the waveforms of the frequency range considered useful for a better seismic response analysis, according to the following expression (Lanzo & Silvestri, 1999, Kuhlemeyer & Lysmer, 1973):

$$H_{max,Adopted} < \frac{V_{S,min}}{(6\div 8)\cdot f_{\max}} \tag{3.10}$$

where f_{max} is the maximum significant frequency of the seismic input (15 Hz) and $V_{S,min}$ is the minimum shear waves velocity of the soil, in the present analyses.

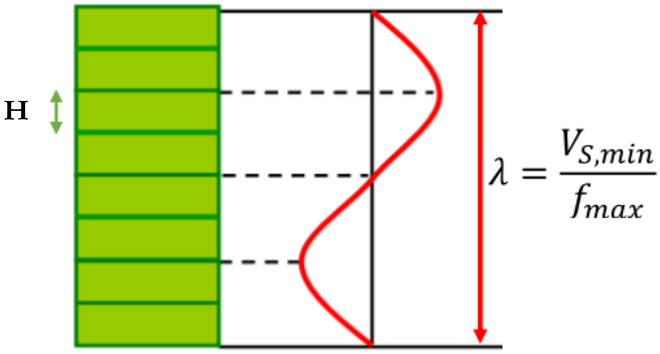

Figure 3.3 maximum size of the elements

Moreover, the element shape was chosen to have a regular shape, with aspect ratio H/B not exceeding 3÷5, according to the following expression (3.11):

$$\frac{H}{B} < 3 \div 5 \tag{3.11}$$

being H and B the two dimensions of the element.

3.3 STEP 1: Visco-elastic-linear analyses of a stiff layered undamped soil on an elastic rock ("*Stiff Soil*")

Initially, a seismic response analysis of a layered undamped soil was reproduced, comparing the results achieved by PhD Huang through *ABAQUS* and *EERA* codes with the results achieved using *DEEPSOIL*, *STRATA* and *ADINA* codes. The soil was characterized by high values of the shear waves velocity and therefore characterized by high values of stiffness, on an elastic rock. In particular, the shear waves velocity grows with a linear trend.

3.3.1 Mechanical parameters of the soil and the elastic rock

A stiffness of about 100 MPa (which corresponds to a value of V_S of about 200 m/s) for the first layers until the depth of about 46.5 meters, was considered.

For subsequent layers, to obtain a soil characterized by high values of stiffness, the shear waves velocities, V_S, grow with the depth according to a linear trend, reaching a value of V_S equal to 750 m/s to the depth of 142.5m.

Figures 3.4a and 3.4b show the shear waves velocity and the shear modulus with the depth of the hypothesized stiff soil.

The soil was divided into 8 layers according to the stratigraphy shown in Table 3.1. The bedrock is located to the depth of 142.5m and it is characterised by the same geotechnical parameters of layer No. 8.

The natural frequency of the soil, "f_n", was initially evaluated through the well-known expression (3.12) (Kramer, 1996):

$$f_n = \frac{V_s}{4H}(2n-1) \qquad n = 1 \rightarrow f_1 = \frac{550}{4(142.5)} = 1.1\,Hz \tag{3.12}$$

being V_S and H, respectively, the shear wave velocity and the height of the deformable geological formations.

Table 3.1: Geotechnical parameters of the stiff soil: STEP 1

Geotechnical Parameters of *STIFF SOIL*							
layer	Depth (m)	Vs (m/s)	ρ (kg/m^3)	γ (kN/m^3)	G (MPa)	ν	E (MPa)
1	5.5	231	1937	19	103.211	0.3	268.349
2	14.5	200	1886	18.5	75.433	0.3	196.127
3	46.5	250	2141	21	133.792	0.3	347.859
4	66.5	550	2141	21	647.553	0.3	1683.639
5	86.5	600	2141	21	770.642	0.3	2003.670
6	110.5	650	2141	21	904.434	0.3	2351.529
7	138.5	700	2141	21	1048.930	0.3	2727.217
8	142.5	750	2141	21	1204.128	0.3	3130.734

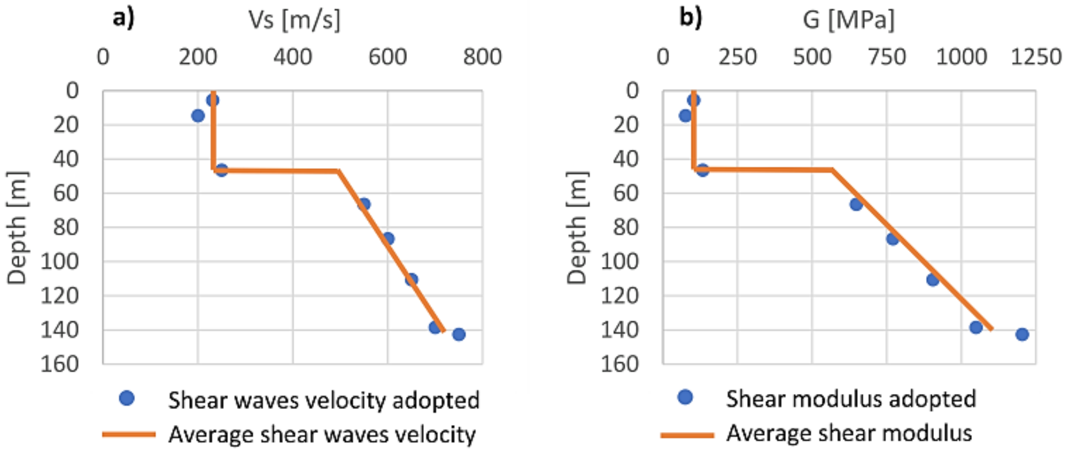

Figure 3.4: a) Shear waves velocity adopted for "stiff soil"; b) Shear modulus adopted for "stiff soil"

3.3.2 Numerical modelling: loading and boundary conditions

Figure 3.5a shows the adopted 1D mesh, including the geometry, boundary and loading conditions. The width of the soil deposit is 1 meter. From the shear waves velocity shown in Table 3.1, an average value was obtained equal to about 550 m/s, achieving a value of the first frequency equal to 1.1 Hz (this result was also confirmed by the amplification function shown in Figure 3.7), according to the expression 3.12:

$$f_1 = \frac{V_S}{4H}(2 \cdot 1 - 1) = \frac{520}{4 \cdot 142.5} \approx 1.1\ Hz$$

Moreover, for n=2, the second frequency:

$$f_2 = \frac{V_S}{4H}(2 \cdot 2 - 1) = \frac{520}{4 \cdot 142.5} \cdot 3 \approx 3.3\ Hz$$

So, to reproduce resonance phenomena, an input motion with the predominant frequency of about 4 Hz was chosen (frequency close to the second frequency of the soil). Figure 3.5b shows the earthquake used to the bottom of the model for the seismic response. The input motion was recorded in Ano Liosia, a city located to the north of Athens (Greece) on 7 September 1999. The earthquake, with a magnitude of 5.9 Richter and epicentre less than 50 km from the centre of Athens, caused the collapse of several buildings. The PGA registered on outcropping rock was equal to 0.267g with a fundamental frequency about 4Hz. As regards the maximum size of each element, according to the expression (3.10), it was:

$$H_{max} < \frac{200}{8 \cdot 15} = 1.66\, m; \tag{3.13}$$

Then it was adopted:

$$H_{adopted} = 1\, m; \tag{3.14}$$

For this analysis, two values of the dashpot coefficients were used according to expression (3.1):

$$c_1 = \frac{21000 \frac{N}{m^3}}{9.81 \frac{m}{s^2}} \cdot 750 \frac{m}{s} \cdot 0.5m \cdot 1m = 802752 \frac{N \cdot s}{m}\ ; \tag{3.15a}$$

$$c_2 = \frac{21000 \frac{N}{m^3}}{9.81 \frac{m}{s^2}} \cdot 750 \frac{m}{s} \cdot 0.25m \cdot 1m = 401376 \frac{N \cdot s}{m}; \tag{3.15b}$$

in which, c_1 and c_2 regard the “effect” area equal to 0.5 m for the central node of the mesh bottom and 0.25 m for the lateral nodes of the mesh bottom, respectively. Figure 3.5c shows a magnification of the bottom of the FEM model. Then, tree dashpot elements were used, one for each partition of the mesh bottom, using the value c_1 for the central dashpot, while the value c_2 was used for the lateral dashpots.

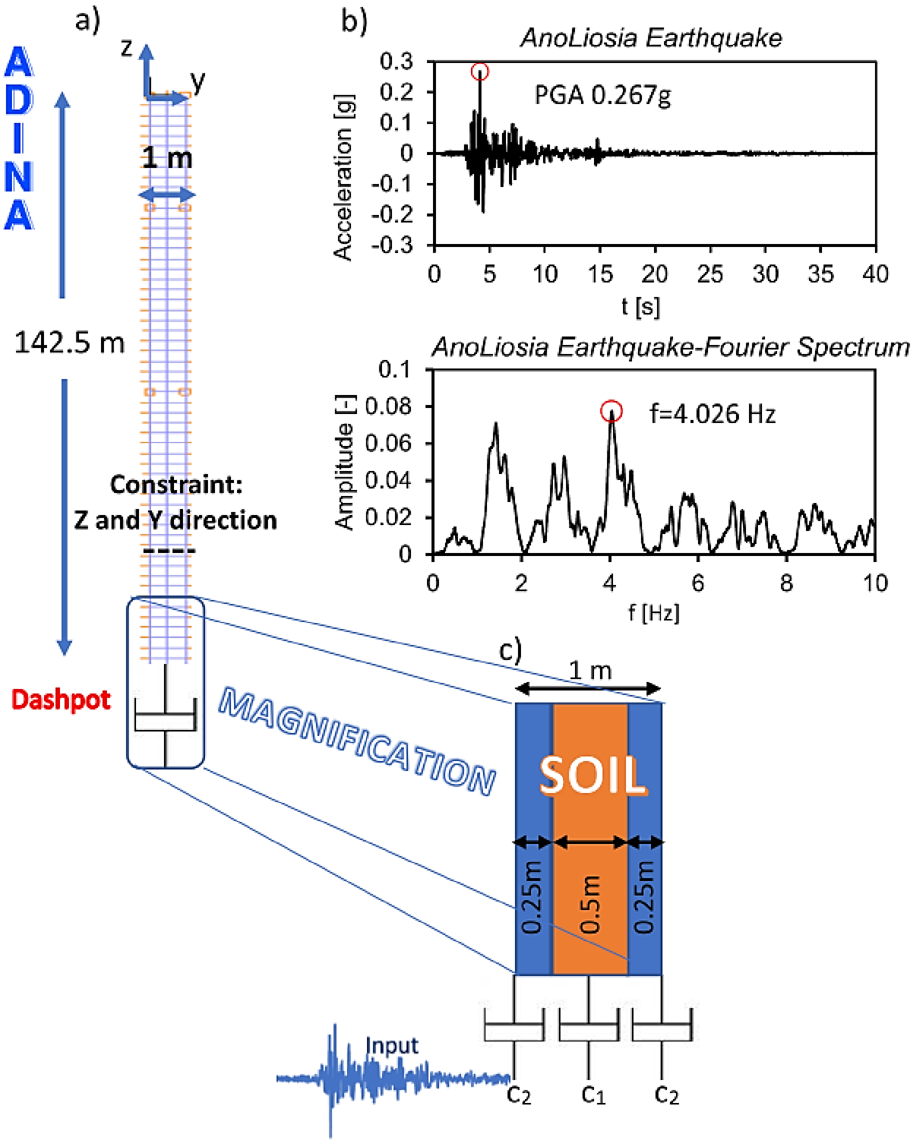

Figure 3.5: Numerical modelling for step 1: a) 1D FEM Model of a column of the soil 1 meter wide; b) adopted input motion; c) magnification of the bottom of the model

The same stratigraphy was used for the two-dimensional (2D) seismic response analysis. The size of the 2D FEM model, shown in Figure 3.6, is equal to 142.5mx400m. As regards the size of each element, the boundary and the loading conditions are the same as described previously for the one-dimensional seismic response analysis. In Figure 3.6, four alignments were chosen to compare the results. At first, only the soil was modelled and therefore the results for any alignment must be very similar.

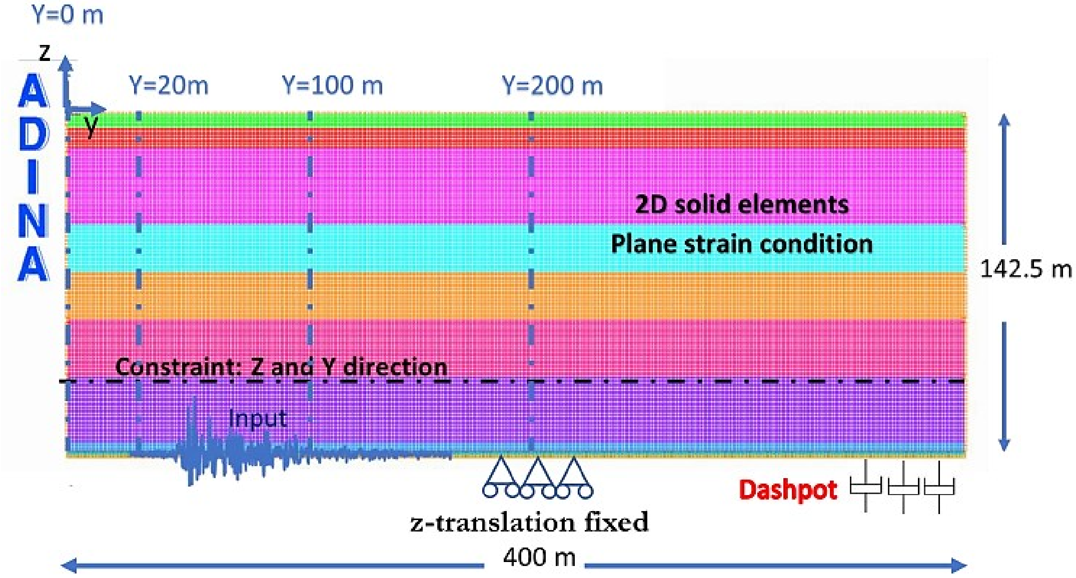

Figure 3.6 Numerical modelling for step 1: 2D FEM Model

3.3.3 Results STEP 1

The following Figure 3.7 shows the comparison between the results achieved with the different software used: a)*ABAQUS* and *DEEPSOIL* used by PhD student Huang and b)*ADINA, STRATA* and *DEEPSOIL*. The results were shown in terms of: 1) acceleration time history on the surface; 2) amplification function; 3) peak ground acceleration with the depth. Furthermore, the results for the four different alignments shown in Figure 3.6 were reported. In particular, the graphs in the left column display the results achieved through 1D analyses using different software. The graphs on the right column show the comparison between the results achieved employing the 2D analyses and those obtained through 1D analyses.

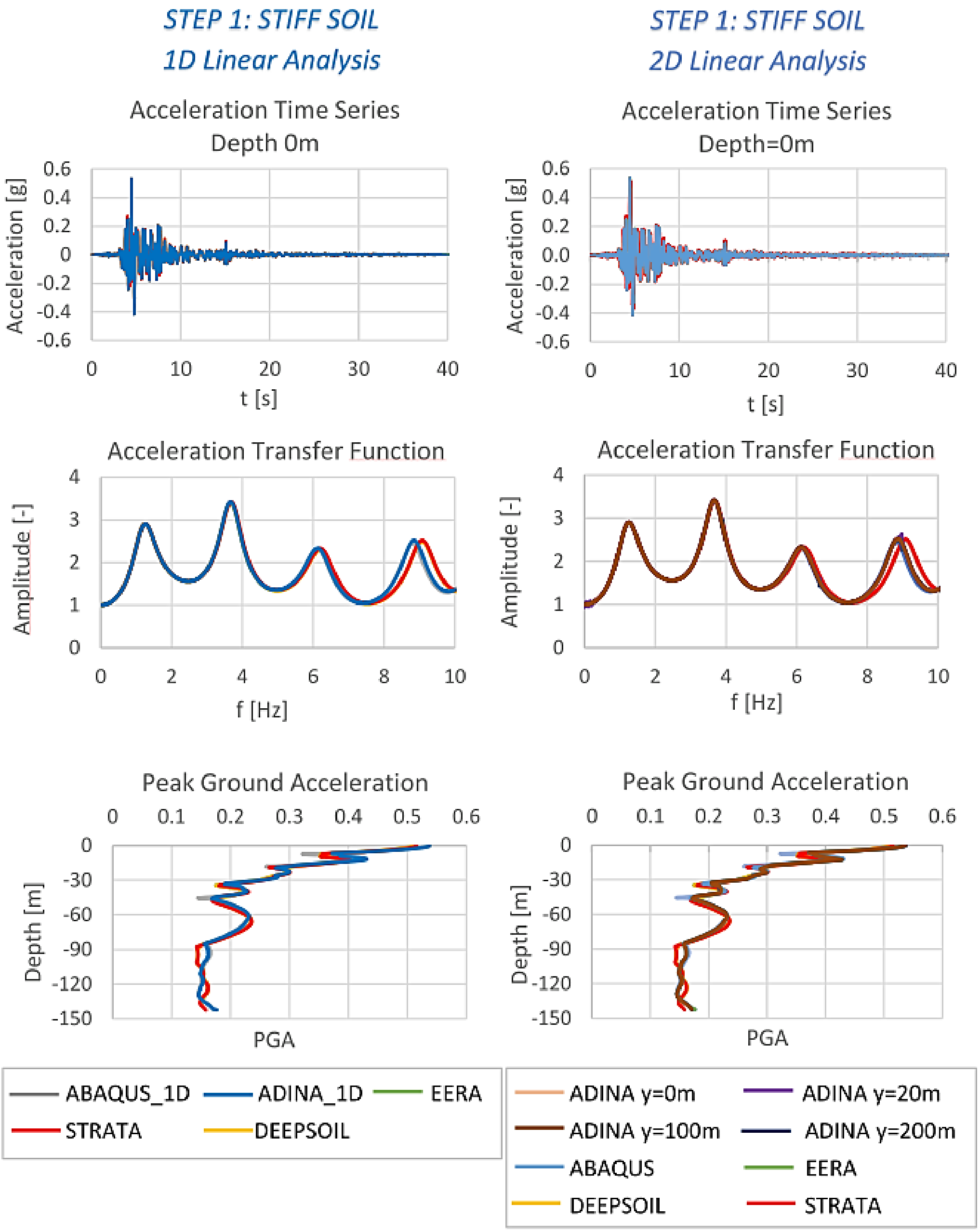

Figure 3.7: Results for STEP 1: 1D and 2D seismic response analyses

From Figure 3.7, it is possible to highlight the perfect agreement between the results obtained by employing the different software and the different numerical models (1D and 2D analysis).

The matching of the results shown in Figure 3.7, reveals the correct approach used here with the *ADINA* code. Thus the general settings described in this section, have been will be used for the other numerical analyses described in the following.

3.4 STEP 2: Visco-elastic-linear analyses of a soft layered undamped soil on an elastic rock ("*Soft Soil")*

Completed the first step, similar analyses were carried out for a layered undamped soil, characterized by low values of the shear waves velocity and therefore characterized by low values of stiffness, on the elastic rock. Also for step 2, the results achieved by PhD Huang through *ABAQUS* and *EERA* codes were reproduced using *DEEPSOIL, STRATA* and *ADINA* codes.

3.4.1 Mechanical parameters of the soil and the elastic rock

The shear wave velocity grows with a parabolic trend (Figure 3.8). Approaching the surface, the soil has values very low of the shear wave velocity, equal about 100 m/s. To obtain a soil characterized by low values of stiffness, the shear waves velocities grow gradually with the depth according to a parabolic trend, reaching a value of V_S equal to 580 m/s to the depth of 280m. Therefore, several layers were considered to obtain a stratigraphy compliant with the description above.

The soil was divided into 14 layers, with a thickness of about 10÷15 meters everyone, according to the stratigraphy shown in Table 3.2. The bedrock is located at the depth of 280 m and it is characterised by $V_S = 1000$ m/s and $\rho = 2390$ kg/m^3.

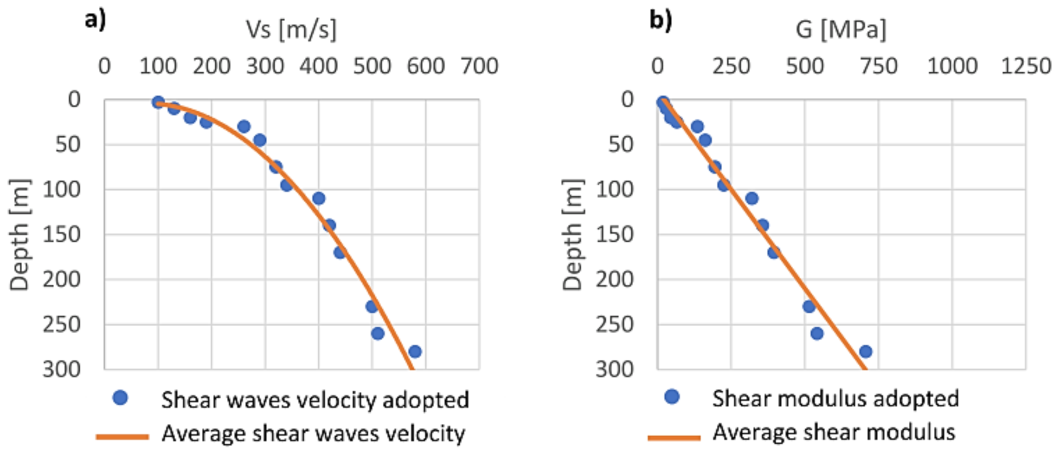

Figure 3.8: a) Shear waves velocity adopted for "soft soil"; b) Shear modulus adopted for "soft soil"

Table 3.2: Geotechnical parameters of the soft soil: STEP 2

Geotechnical Parameters of SOFT SOIL								
layer	Soil Type	Depth (m)	Vs (m/s)	ϱ (kg/m^3)	γ (kN/m^3)	G (MPa)	v	E (MPa)
1	Clay	3	100	1900	18.63	19.000	0.3	49.400
2	Muddy silty clay	10	130	1750	17.17	29.575	0.34	79.261
3	Muddy clay	20	160	1750	17.17	44.800	0.3	116.480
4	Clay	25	190	1820	17.85	65.702	0.3	170.825
5	Clay	30	260	2000	19.62	135.200	0.3	351.520
6	Sand	45	290	1920	18.83	161.472	0.33	429.516
7	silty clay	75	320	1900	18.4	194.560	0.34	521.421
8	Sand	95	340	1950	19.13	225.420	0.33	599.617
9	Clay	110	400	2000	19.62	320.000	0.3	832.000
10	Sand	140	420	2020	19.82	356.328	0.33	947.832
11	Clay	170	440	2040	20.01	394.944	0.3	1026.854
12	Sand	230	500	2060	20.21	515.000	0.33	1369.900
13	Clay	260	510	2080	20.40	541.008	0.3	1406.621
14	Sand	280	580	2100	20.60	706.440	0.33	1879.130

3.4.2 Numerical modelling: loading and boundary conditions

Figure 3.9a shows the adopted 1D mesh for STEP 2, including the geometry, boundary and loading conditions. A width of the soil deposit once more equal 1 meter was used. Figure 3.9b shows three earthquakes, used at the bottom of the model for the seismic response, scaled to the same peak horizontal accelerations equal to 0.1g and to 0.3g.

Following the same reasoning explained above, the input motions were chosen to reproduce any resonance phenomena. From the shear waves velocity shown in Table 3.2, an average value was obtained equal to about 330 m/s, achieving a value of the first frequency equal to 0.3 Hz (this result was also confirmed by the amplification function shown in Figure 3.11), according to the expression 3.12:

$$f_1 = \frac{V_S}{4H}(2 \cdot 1 - 1) = \frac{330}{4 \cdot 280} \approx 0.3\ Hz$$

$$f_2 = \frac{V_S}{4H}(2 \cdot 2 - 1) = \frac{330}{4 \cdot 280} \cdot 3 \approx 0.9\ Hz$$

$$f_3 = \frac{V_S}{4H}(3 \cdot 2 - 1) = \frac{330}{4 \cdot 280} \cdot 5 \approx 1.5\ Hz$$

Therefore, the first three natural frequencies of the soil were evaluated between 0.3 and 1.5. So, to reproduce possible resonance phenomena, three input motions with the fundamental frequency of about 0.5÷1.5 Hz were chosen.

In particular, the first input motion was an artificial motion (named Shanghai earthquake). The other two input motions were registered input motions. The first one was registered in Loma Prieta on 17 October 1989 It was characterised by a magnitude M_W of 6.9 and the epicentre on the Santa Cruz Mountains, in a section of the great fault system of Sant 'Andrea. The second one in Kobe occurred on 17 January 1995. The earthquake was characterised by a magnitude M_W of 5.9 and the epicentre less than 20 km from the city of Kobe in Japan.

Moreover, Figure 3.9b shows the fundamental frequency of each earthquake used.

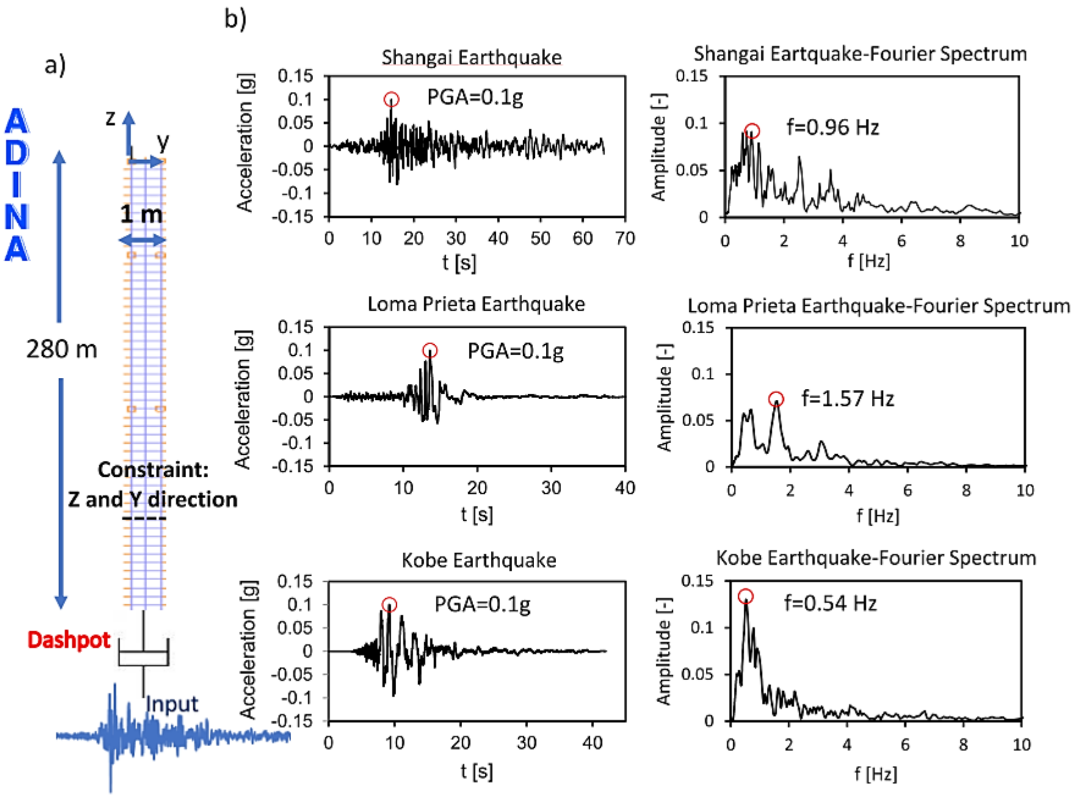

Figure 3.9: Numerical modelling for step 2: a) 1D FEM Model of a column of the soil 1 meter wide; b) Adopted input motions

3.4.3 Results STEP 2

The following Figures 3.10-3.15 show the comparison between the results achieved using different numerical codes (mentioned in the previous section) and considering the two different peak ground accelerations at the bottom of the model, 0.1g and 0.3g in terms of: a) peak ground acceleration with the depth, shown in Figure 3.10; b) amplification function, shown in Figure 3.11; c) acceleration time history at the depth of 0m, 90m, 180, 270m, shown in the

Figures 3.12 and 3.13 ; d) shear strain and shear stress time history at the depth of 70m and 140m, shown in the Figures 3.14 and 3.15.

To decrease the calculation times, for STEP 2 only 1D numerical model using *ADINA* code was employed to compare the results with these achieved through the 1D analyses conducted in the frequency domain by PhD student Huang (*EERA)* and 1D analyses performed using *STRATA* and *DEEPSOIL*.

A good agreement occurs for the peak ground acceleration with the depth obtained with the different numerical codes.

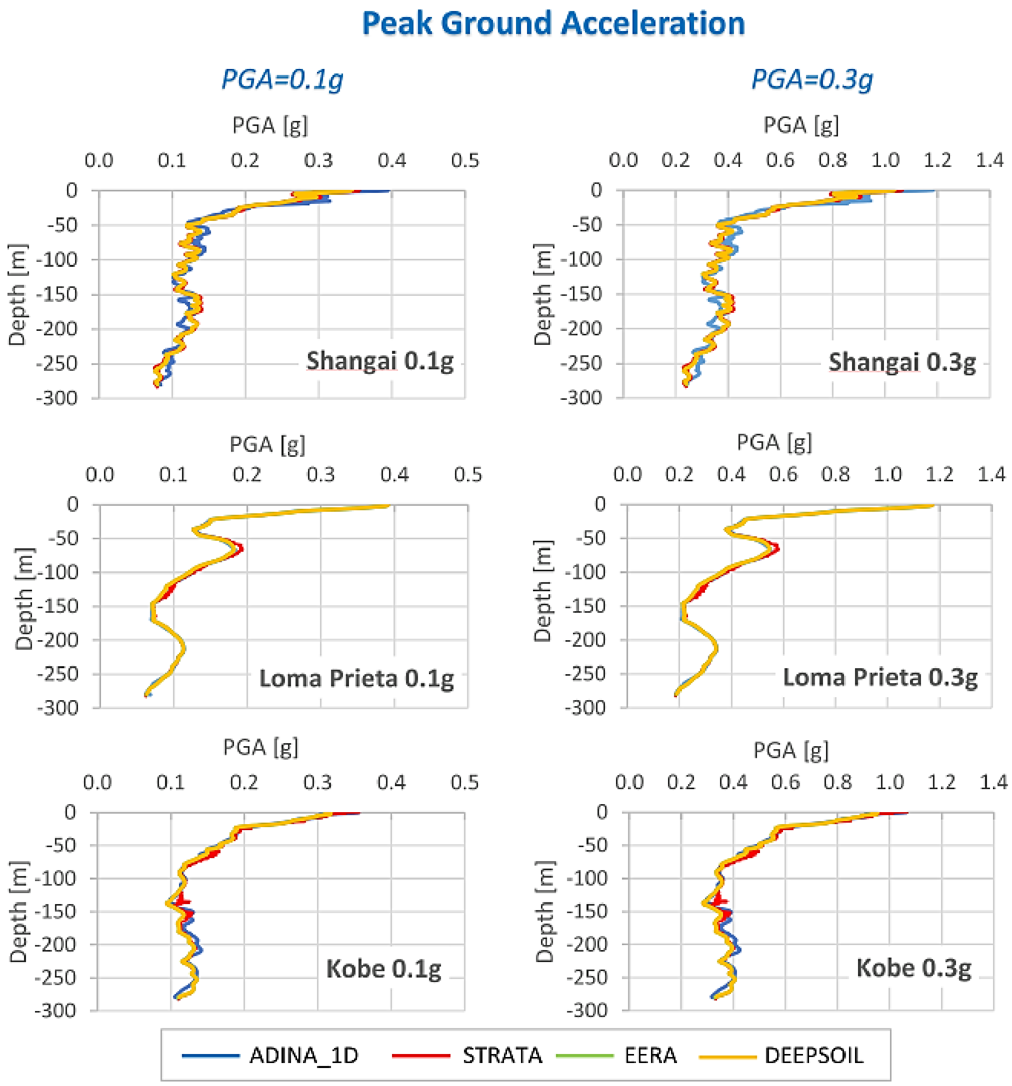

Figure 3.10: Results in terms of PGA for "Soft Soil"

From Figure 3.11, it is possible to observe a perfect overlap of the amplification function curves with the different numerical codes used and for all input motions. This occurrence attests the correct approach of the numerical model used.

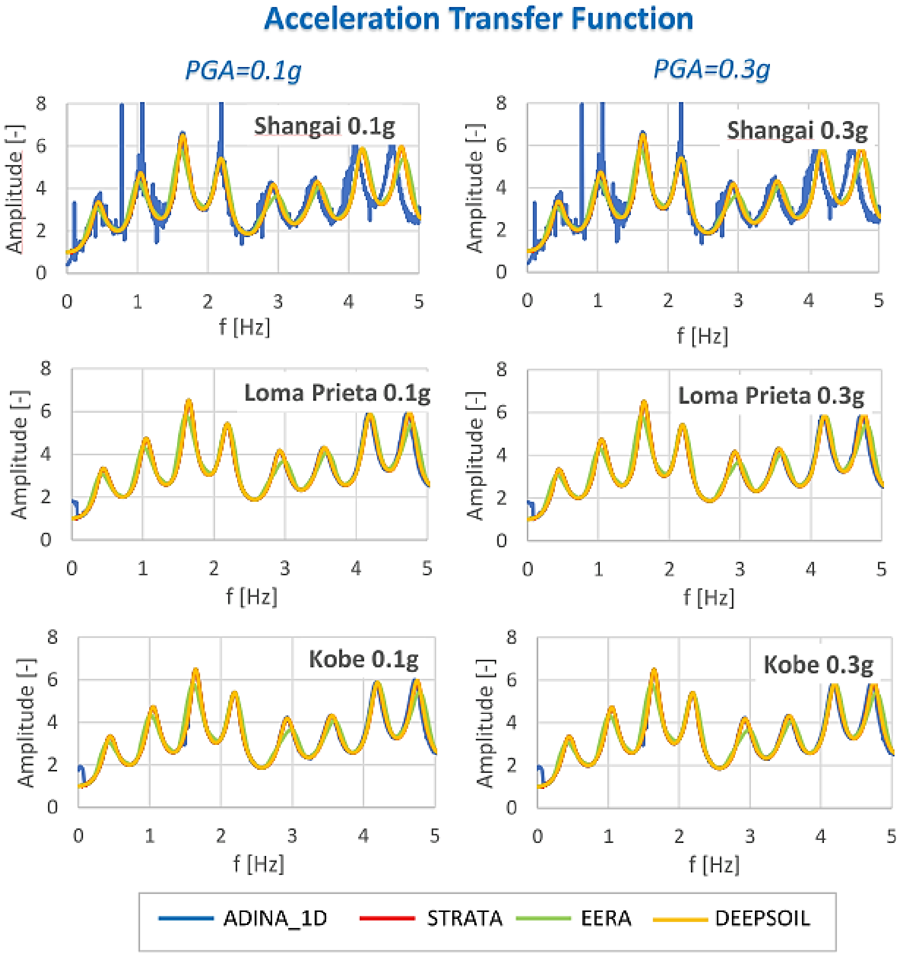

Figure 3.11: Results in terms of Amplification Function for "Soft Soil"

Analysing the fundamental frequencies of the soil obtained utilizing the numerical modelling (Figure 3.11), they are very similar to the values of natural frequencies for the nth vibration shape, "f_n", achieved by the well-known expression 3.12 and showed in the previous section.

A good agreement was also achieved for the different numerical codes and PGAs used, in terms of: a) acceleration time history at the different depths of 0m, 90m, 180m,270m (Figures 3.12 and 3.13); b) shear strain and stress time history at the depth of 70m and 140m (Figures 3.14 and 3.15).

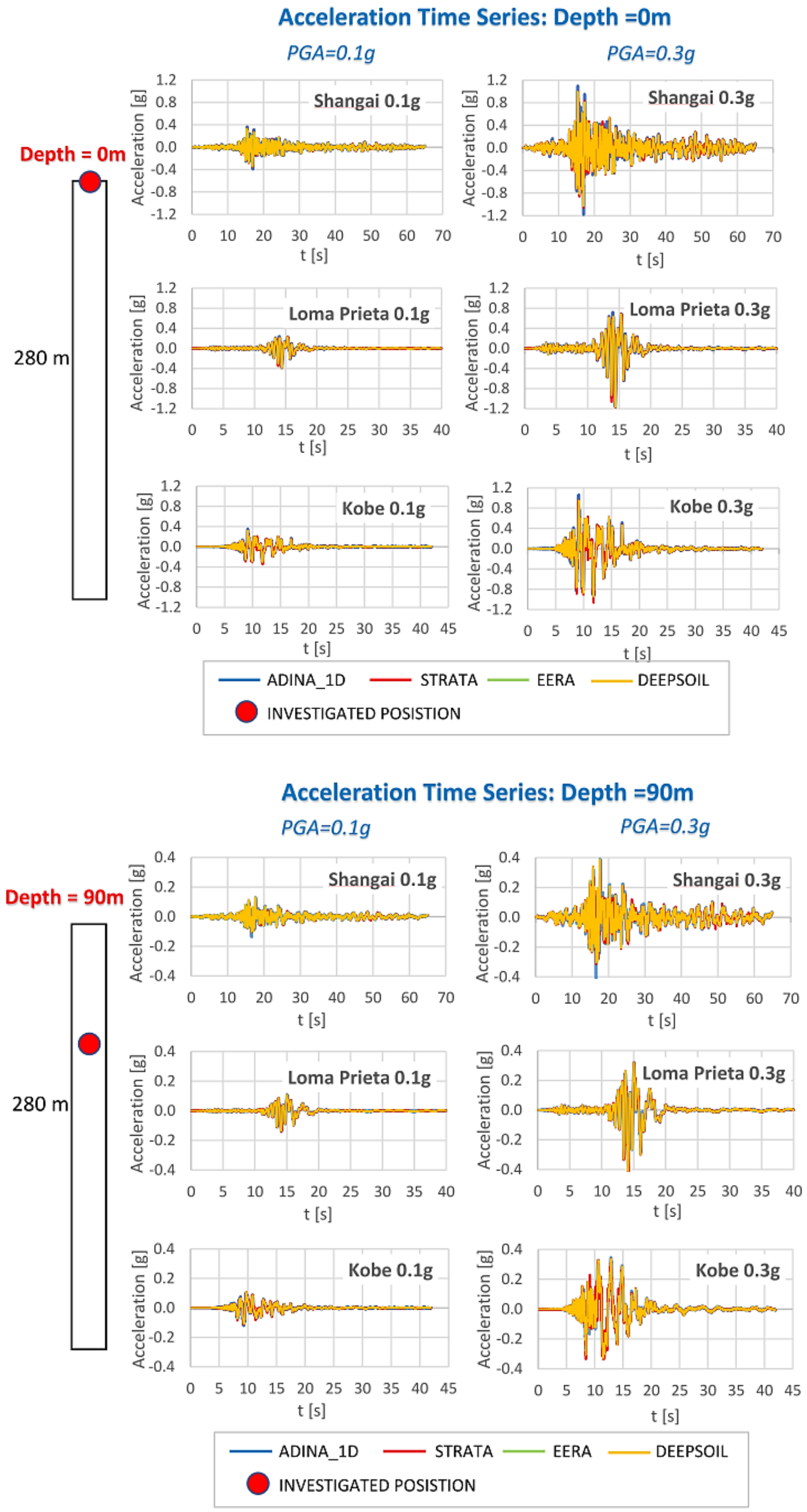

Figure 3.12: Results in terms of acceleration time series for "Soft Soil"

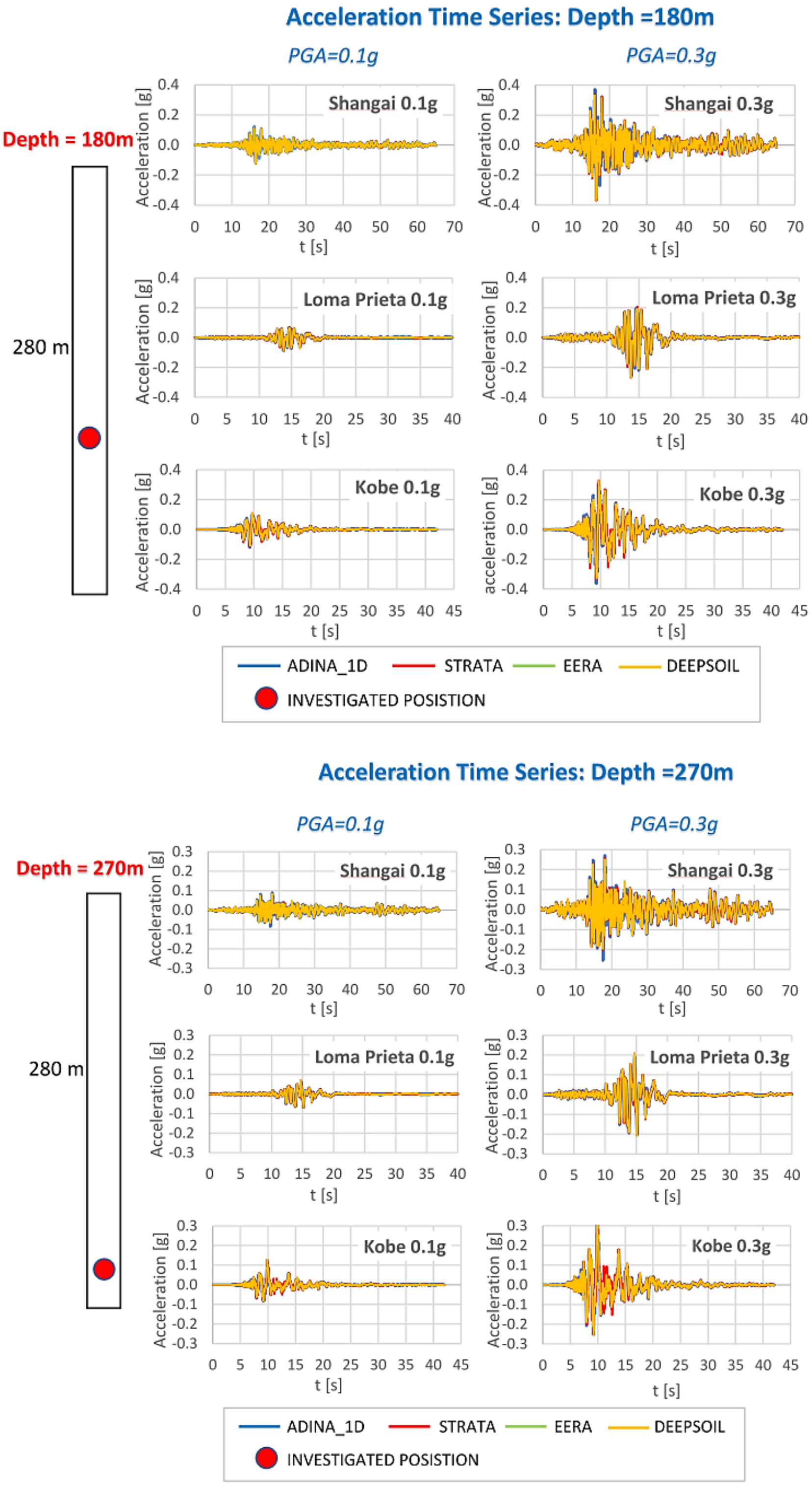

Figure 3.13: Results in terms of acceleration time series for "Soft Soil"

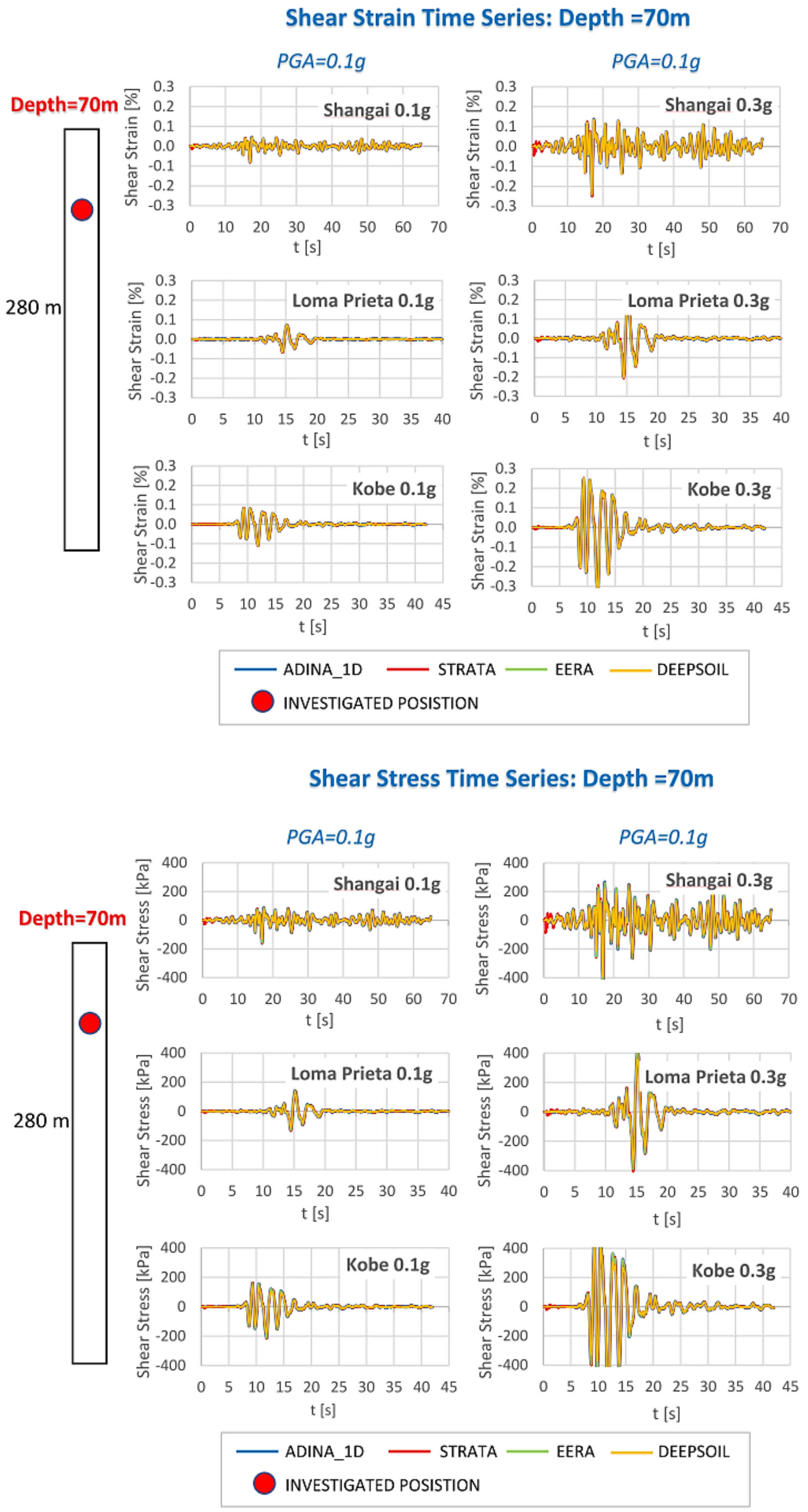

Figure 3.14: Results in terms of shear strain and stress time series for "Soft Soil"

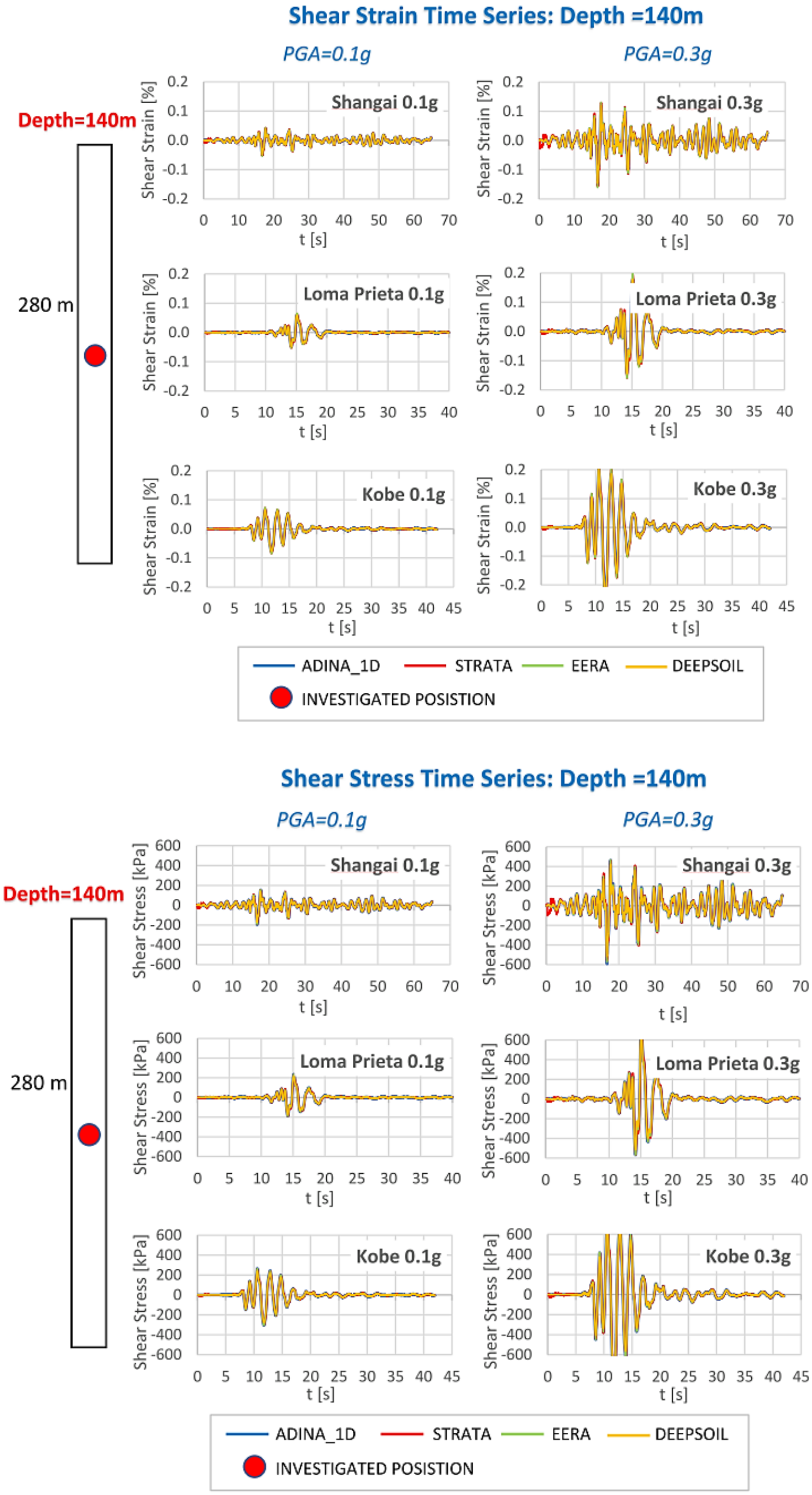

Figure 3.15: Results in terms of shear strain and stress time series for "Soft Soil"

Summing up the analyses described in Section 3.3 and in this Section 3.4, two different soil profiles were analysed: the first one characterized by high values of the shear waves velocity and the bedrock at the depth of 142.5m (“Stiff Soil”); the second one characterized by low values of the shear waves velocity and the bedrock at the depth of 280 m (“Soft soil”). The first two steps (STEP 1 and STEP2) previously described were helpful to validate the numerical models developed with the *ADINA* code, which will be used in the following part of this thesis.

A good agreement was found between the results achieved with the *ADINA* code and those achieved with other numerical codes by PhD Huang, for different soil profiles, different input motions and different peak ground accelerations. These preliminary analyses were useful to verify the correct use of the dashpot elements modelled at the bottom of the model, to simulate the elastic bedrock. The use of dashpot elements is fundamental to avoid phenomena of reflection of the waves that could influence the response of the system by amplifying its effects.

In conclusion, the FEM model created as specified in the previous section is adapted for seismic response analysis of the soil.

So, to sum it up, to achieve the same results for 1D and 2D seismic analysis, without structures, the numerical model must have the following properties:

1) As regards the boundary conditions, the nodes of the soil vertical boundaries have to be linked by “constraint equations” that imposed the same displacements, both horizontally and vertically, at the same depths; the nodes at the base of the mesh have to be constrained only in the vertical direction. Moreover, at the base of the numerical model, the dashpots have to be implemented, in the horizontal direction, to simulate the elastic bedrock according to Lysmer and Kuhlemeyer (1969);

2) The soil must be modelled with 2D solid elements in plane strain conditions;
3) The input motion must be applied to the models through the dashpots, located at the bottom of the model.

3.5 STEP 3: Equivalent Visco-elastic-linear analysis of a coupled system soil-tunnel

In the previous sections, seismic response analyses of the only heterogeneous soil were performed. The third phase concerns the seismic response analysis of a coupled soil-tunnel system. The results achieved by means the software Adina were compared with those obtained by other authors through Abaqus code (Argyroudis et al., 2017).

3.5.1 Mechanical parameters of the soil and the tunnel

The shear Modulus G and the damping D, in the low to medium shear strains, were evaluated by a series of 1D equivalent linear site response analyses for representative ground motions, scaled up to 0.1 g.

The analyses were performed by Argyroudis et al., (2017). The analyses were carried out using the code *EERA* (Bardet et al., 2000), using the G-γ-D curves, proposed by Darendeli (2001), as a function of plasticity index (PI) and effective stress. In particular, curves corresponding to an average PI =30% for various effective stresses were used by Argyroudis et al., (2017). The equivalent soil properties thus obtained, shown in Table 3.3, were adopted in the 2D numerical model of the coupled soil-tunnel system shown in Figure 3.16.

Table 3.3: Geotechnical Equivalent parameters of soil: STEP 3

Geotechnical Parameters of SOIL (Visco-Elastic-Linear)					
layer	Depth (m)	ϱ (kg/m^3)	G (equivalent) (MPa)	ν	E (equivalent) (MPa)
1	2.5	1925	34.73	0.35	93.8
2	5.0	1925	34.73	0.35	93.8
3	7.5	1925	67.60	0.35	182.5
4	10.0	1925	67.60	0.35	182.5
5	12.5	1925	84.04	0.35	226.9
6	15.0	1925	84.04	0.35	226.9
7	17.5	1925	100.81	0.35	272.2
8	20.0	1925	100.81	0.35	272.2
9	25.0	1925	117.53	0.35	317.3
10	30.0	1925	137.35	0.35	370.8
11	35.0	1925	154.25	0.35	416.5
12	40.0	1925	171.17	0.35	462.2
13	45.0	1925	188.97	0.35	510.2
14	50.0	1925	205.53	0.35	554.9

As described in Section 3.2, the materials' viscosity was modelled according to the Rayleigh damping formulation. According to this formulation:

$$\alpha = 2 \cdot \frac{D \cdot \omega_1 \cdot \omega_2}{\omega_1 + \omega_2} = 0.7475 \; ; \qquad \beta = 2 \cdot \frac{D}{\omega_1 + \omega_2} = 0.0032$$

In which D is the damping ratio of the soil, estimated 0.057, $\omega_1 = 8.796\, rad/s$ the first angular frequency of the soil and $\omega_2 = 3 \cdot \omega_1 = 26.389\, rad/s$.

For the lining tunnel, a Young Modulus, E, equal to 29 GPa and a Poisson coefficient, ν, equal to 0.2 were used.

3.5.2 Numerical Modelling: loading and boundary conditions

The FEM model of the soil was created using the same elements, boundary and loading conditions used for the previous analysis. It consists of a stratified soil 50 m deep and has a wide equal to 200 m, equal to 4 times the depth of the soil. The side boundaries were located in an adequate distance from the tunnel to reduce potential interaction effects between the soil and the tunnel, ensuring a free field response far enough from the tunnel.

The soil was meshed with 4-node elements in plane strain conditions, while the tunnel lining was modelled with 2-node linear beam elements. The tunnel, with a diameter equal to 3m and a thickness 0.3m, was located at the depth of 10m. The cross-section used for the tunnel was 0.3x1m. In order to ensure a working well simulation of the circular tunnel, a finer discretization was used around the tunnel. Therefore, the element shape was chosen to have a regular shape, with aspect ratio H/B not exceeding 3÷5, according to the expression (3.11) and it is shown below:

$$\frac{H}{B} < 3 \div 5$$

According to expression 3.11:

$$H_{max,adopted} = 1m < \frac{134}{(6 \div 8) \cdot 15} = 1.12m$$

Initially, a geostatic step was performed, whereby the bottom of the numerical model, was fixed in both horizontal and vertical directions. After the preliminary geostatic phase, the dynamic step was performed, during which, the bottom was constrained in the vertical direction, leaving free the horizontal displacements. Moreover, to assure “quasi transparent” conditions, proper dashpots were implemented in the horizontal direction, following the Lysmer and Kuhlemeyer (1969). The dashpots coefficients, C, were defined as shown in the expression (3.1) of the 3..2 section. In this case, a value equal to 2200 kg/m^3 and 1000 m/s, were used for the mass density and the shear waves velocity.

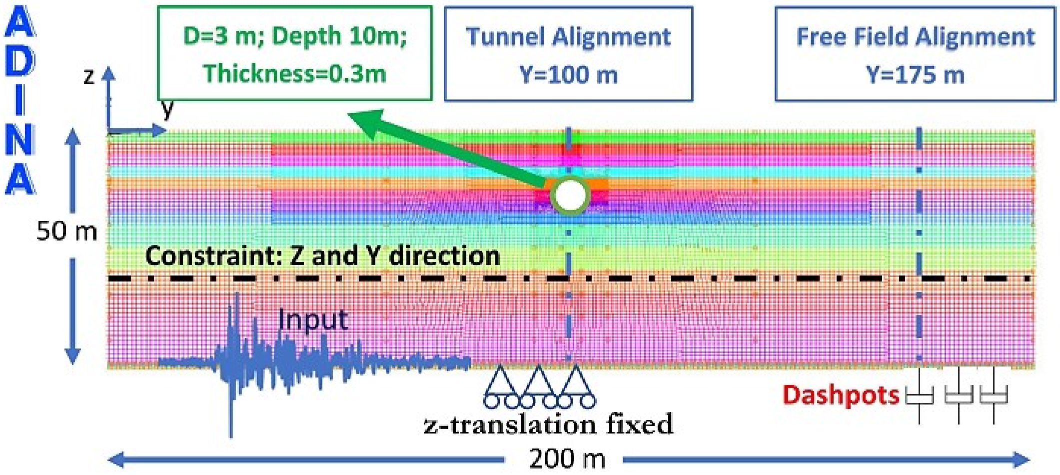

Figure 3.16: Numerical model for step 3 and for the following step 4

The soil-tunnel interface was modelled using a finite sliding contact model. The Coulomb friction coefficient was set at 0.5.

The input motion shown in Figure 3.17, was applied at the base of the model. It was recorded in Montenegro at the accelerometric station called Hercegnovi Novi on 15 April 1979. The Mw reached by the earthquake was equal to 6.9 and the PGA 0.256g. In the present application, the PGA was scaled to 0.15g.

The results were evaluated for the two alignments, “Tunnel Alignment” and “Free Field Alignment” shown in Figure 3.16.

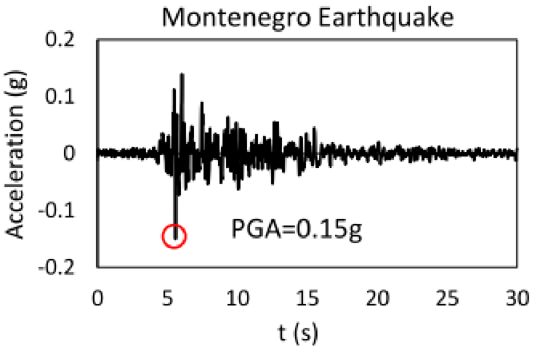

Figure 3.17: Input motion, recorded in Montenegro and scaled to a PGA of 0.15g

3.5.3 Results STEP 3

In this section, the results of the coupled system tunnel-soil described above will be shown.

The following Figures 3.18 and 3.19 show the results in terms of: a) bending moment time history computed at a crucial lining section (θ=45 degree); b) acceleration time history on the surface; c) peak ground acceleration with the depth for the two alignments shown in Figure 16; d) maximum (ABAQUS_MAX and ADINA_MAX) and minimum (ABAQUS_MIN and ADINA_MIN) bending moment distribution in the tunnel and bending moment distribution for the geostatic step (ABAQUS_GEOSTATIC and ADINA_GEOSTATIC).

Figure 3.18 shows the bending moment history at 45 degrees on the lining tunnel, as indicated in the figure, the acceleration time history on the surface and the peak ground acceleration with the depth.

Figure 3.19 shows the bending moment distribution on the lining tunnel. The estimated value of the maximum and minimum bending moment tend to coincide at 0, 90, 180 and 270 degrees, showing a growing gap for the remaining part of the tunnel lining. In particular, the maximum gap was found at 45, 135, 225 and 315 degrees.

The perfect agreement achieved by the comparison between the results obtained by means *ADINA* code and the results evaluated through *ABAQUS* code (PhD student Huang) ensures a good simulation of the seismic response of a coupled tunnel-soil system with the *ADINA* code, which will be then used by the writer in the following.

So, the numerical modelling performed as described in the previous sections produces good results in terms of the soil seismic response and lining force on the tunnel.

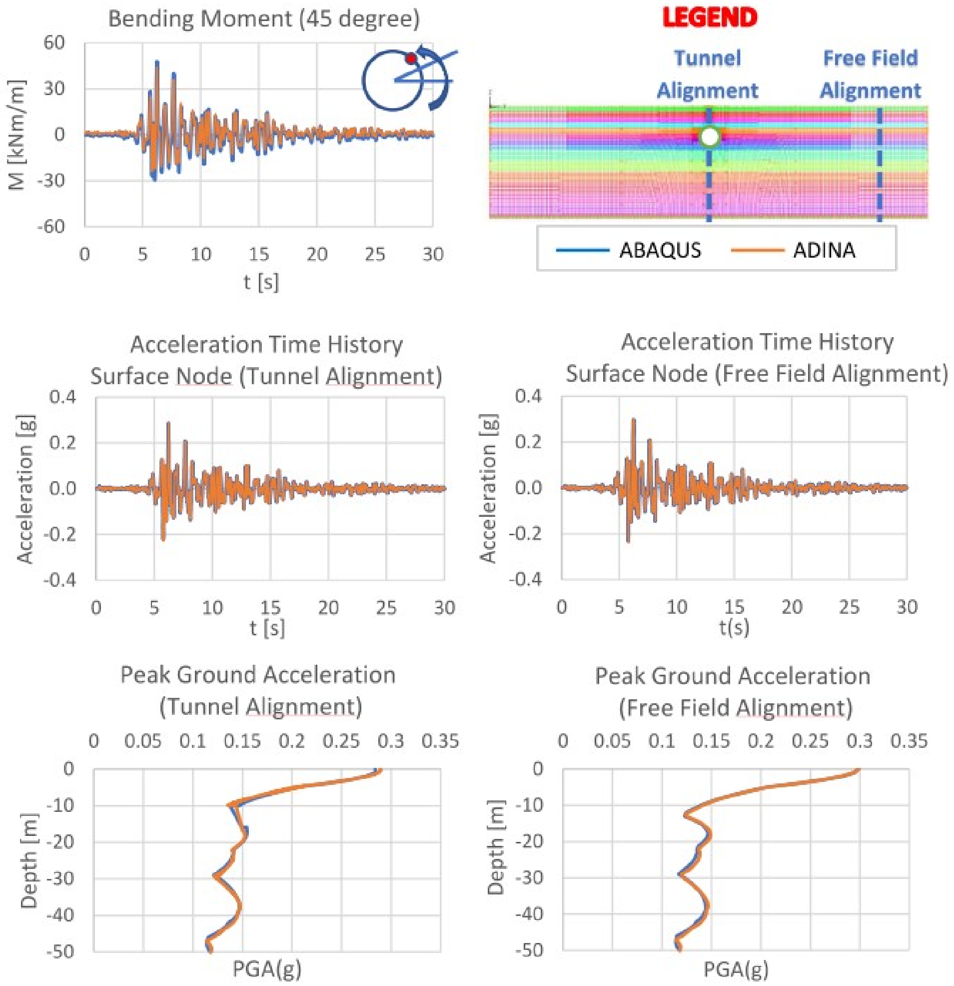

Figure 3.18: Results for the visco-elastic-linear analysis of the tunnel soil system (STEP 3)

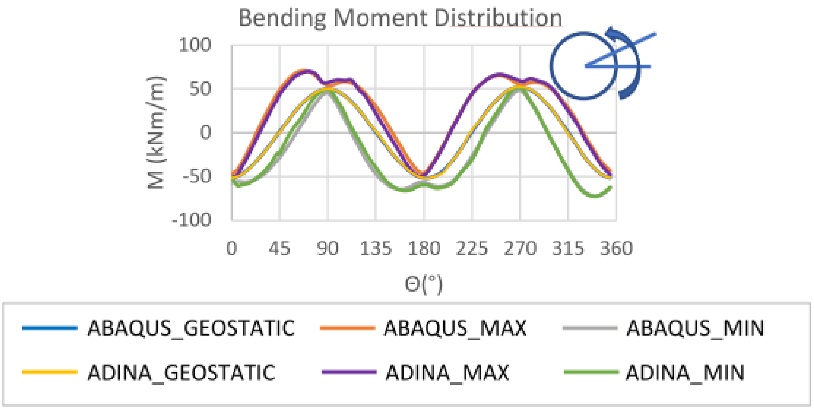

Figure 3.19: Results for the visco-elastic-linear analysis of the tunnel soil system (STEP 3): Bending Moment Distribution on the lining tunnel

3.6 STEP 4: Perfectly plastic analysis of the coupled tunnel-soil system

The next step consisted of the numerical analysis of the same FEM model before described (see Figure 3.16) modifying the constitutive model used for the soil: a perfectly plastic elastic model was used (Tresca).

3.6.1 Mechanical parameters of the soil

The soil stratigraphy used for step 4 was shown in section 3.5.1 with the bedrock located at the depth of 50 meters. Table 3.4 shows the geotechnical parameters of the soil used for the perfect plastic analysis.

Table 3.4: Geotechnical parameters of soil: STEP 4

Geotechnical Parameters of SOIL (Tresca analysis)							
layer	Depth (m)	ϱ (kg/m^3)	G (equivalent) (MPa)	ν	E (equivalent) (MPa)	c_u (kPa)	φ (°)
1	2.5	1925	34.73	0.35	93.8	50.00	0
2	5.0	1925	34.73	0.35	93.8	73.80	0
3	7.5	1925	67.60	0.35	182.5	85.60	0
4	10.0	1925	67.60	0.35	182.5	97.50	0
5	12.5	1925	84.04	0.35	226.9	109.40	0
6	15.0	1925	84.04	0.35	226.9	121.30	0
7	17.5	1925	100.81	0.35	272.2	133.10	0
8	20.0	1925	100.81	0.35	272.2	145.00	0
9	25.0	1925	117.53	0.35	317.3	168.80	0
10	30.0	1925	137.35	0.35	370.8	192.50	0
11	35.0	1925	154.25	0.35	416.5	216.30	0
12	40.0	1925	171.17	0.35	462.2	240.00	0
13	45.0	1925	188.97	0.35	510.2	263.80	0
14	50.0	1925	205.53	0.35	554.9	287.50	0

3.6.2 Numerical modelling: loading and boundary conditions

The FEM model used for step 4 was the same as that used previously and described in section 3.5.2. The only difference respect to the previous numerical model is the constitutive model used for the soil. So, the possible differences in the seismic response of the FEM model are to be attributed to the constitutive model used for the soil.

3.6.3 Results STEP 4

The following Figures 3.20 and 3.21 show the results achieved in terms of: a) bending moment time history computed at a crucial lining section (θ=45 degree); b) acceleration time history on the surface; c) peak ground acceleration with the depth for the two alignments shown in Figure 3.16; d) maximum (ABAQUS_MAX and ADINA_MAX) and minimum (ABAQUS_MIN and ADINA_MIN) bending moment distribution in the tunnel and bending moment distribution for the geostatic step (ABAQUS_GEOSTATIC and ADINA_GEOSTATIC).

In this case, there is not a good agreement between the results achieved by means the two numerical code used for the seismic analysis (*ADINA* and *ABAQUS* codes). The disagreement is most evident for the peak ground acceleration with the depth.

Regarding the bending moment on the lining tunnel, the disagreement is less clear as shown in Figure 3.21.

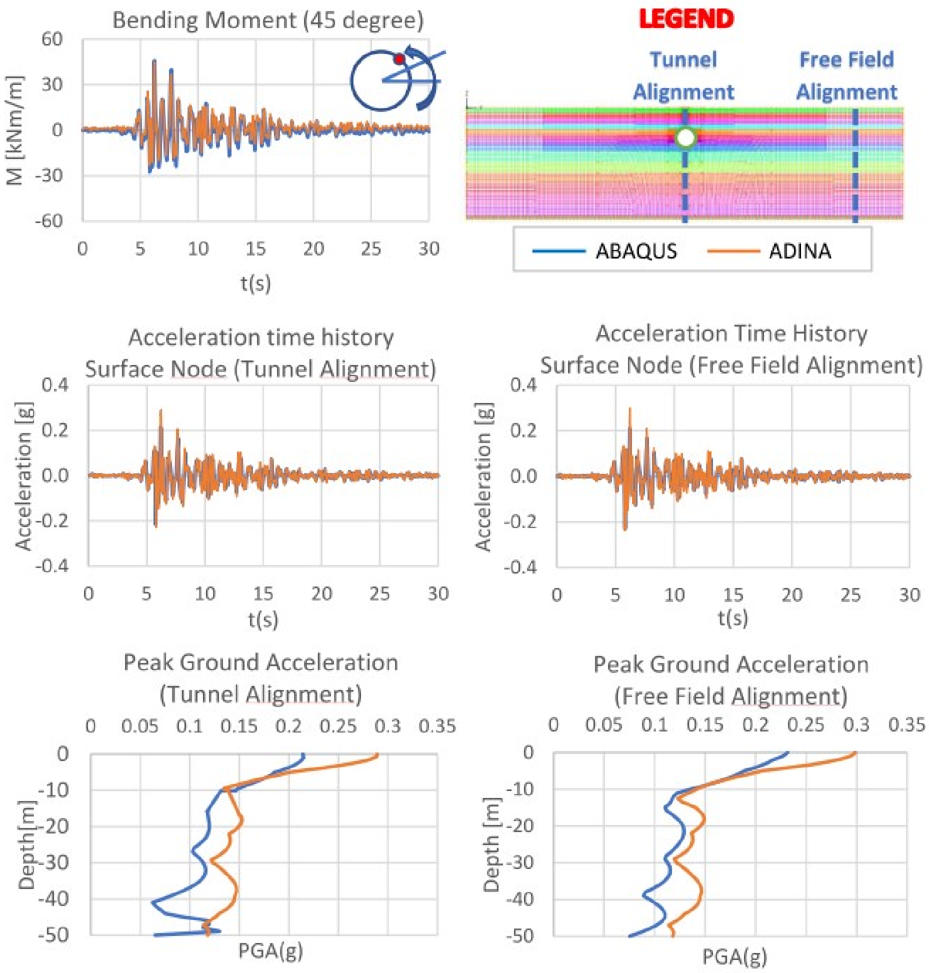

Figure 3.20: Results for the non-linear analysis of the tunnel soil system (STEP 4)

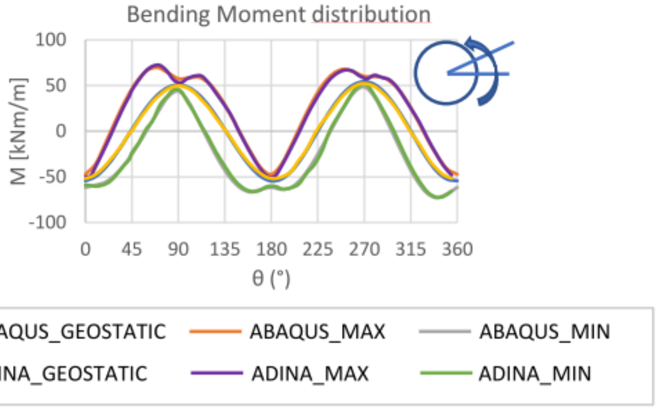

Figure 3.21: Results for the non-linear analysis of the tunnel soil system (STEP 4): Bending Moment Distribution on the lining tunnel

The strong differences between the two FEM code used, Adina and Abaqus, in terms of peak ground acceleration, were due to the constitutive model used for the soil.

The Tresca model, in *ADINA*, is based on:

- a non-associative flow rule and then a potential function defined by the Drucker-Prager criterion.

The Mohr-Coulomb model, in *ABAQUS*, is based on:

- a non-associative flow rule and then a potential function defined by a hyperbolic function in the meridional stress plane and the smooth elliptic function proposed by Menétrey and Willam (1995) in the deviatoric stress plane.

The Tresca model used in *ADINA* and in *ABAQUS* differs in the potential function. This causes a remarkable alteration of the dynamic response of the coupled tunnel-soil system. Moreover, in Figure 3.18, when a linear elastic constitutive model was used, the same PGA values at the bedrock were obtained for the two used different numerical codes, while the PGA values achieved at the bedrock by a perfectly plastic analysis were in disagreement for the two used numerical codes, being they actually computed and therefore dependent on the adopted constitutive model of the soil.

So, to sum it up, to perform an efficient seismic response analysis of a coupled tunnel-soil system, the following conditions must be respected, in addition to the condition described in 3.4.3:

1) The tunnel must be modelled with a 2-node beam;
2) The viscous damping must be modelled according to the Rayleigh damping;

3) In order to ensure a working well simulation of the circular tunnel, a finer discretization must be used around the tunnel;
4) The element shape must be chosen to have a regular shape, with aspect ratio H/B not exceeding 3÷5;
5) In order to avoid numerical problems, the maximum element size of the soil must be chosen in a way that guarantees the efficient reproduction of the waveforms of the frequency range considered useful for better seismic response analysis.

3.7 STEP 5: Numerical analysis of a centrifuge test

Finally, to validate the developed *ADINA* models a centrifuge test was modelled through Adina code. The numerical results were compared with the results recorded during the centrifugal tests. A series of dynamic centrifuge tests were carried out on a circular model tunnel embedded in dry sand. The tests were performed at the centrifuge facility of the University of Cambridge (Lanzano et al., 2012), while representative experimental data were provided to the scientific community through the so-called Round Robin Tunnel Test (RRTT) organization (Bilotta et al., 2014a; Bilotta et al., 2014b). The main goal was the validation of numerical models and codes that are often used in the seismic analysis of tunnels, using the experimental data as a benchmark.

The geotechnical centrifuge test is often used to study geotechnical structures, the response of which is highly related to the in-situ stress state (Madabhushi, 2014). The method allows for the reproduction of the in-situ stress-strain behaviour in small scale models, by increasing the body forces through the application of high centrifugal acceleration.

Several research projects have actually been concentrated on the efficiency of the method to analyse dynamic soil-structure interaction problems comparing the experimental data with actual case studies and results of numerical simulations (El Nahas et al., 2006; Anastasopoulos et al., 2007b; Kirtas et al., 2009, Pitilakis et al., 2010)

Assuming that a model is scaled down N times (compared to the prototype), the following relations are worth, for length, area and volume, respectively:

$$L_{Model} = \frac{L_{Prototype}}{N} \qquad A_{Model} = \frac{A_{Prototype}}{N^2} \qquad V_{Model} = \frac{V_{Prototype}}{N^3} \tag{3.25}$$

To achieve similar stresses between the model and the corresponding prototype, the acceleration field on the model should be multiplied $N_{gravity}$ times. So, the vertical stress, $\sigma_{z(Model)}$, at generical depth z_{Model} will be given by the following expression:

$$\sigma_{z(Model)} = z_{Model} \cdot \rho \cdot N_{gravity} \cdot g \tag{3.26}$$

Similarly, the vertical stress, $\sigma_{z(Prototype)}$, at the same depth, $z_{Model}=z_{Prototype}$, of the prototype model will be:

$$\sigma_{z(Prototype)} = z_{Prototype} \cdot \rho \cdot g \tag{3.27}$$

To achieve the stresses compliance between the model and the prototype the stress equivalence requires:

$$\sigma_{Prototype} = \sigma_{Model} \rightarrow L_{Prototype} \cdot \rho \cdot g = L_{Model} \cdot \rho \cdot N_{gravity} \cdot g \rightarrow$$
$$N_{gravity} = \frac{L_{Prototype}}{L_{Model}} \rightarrow N_{gravity} = N \tag{3.28}$$

Therefore, to achieve the same results between a scaled-down model by N times and the prototype, the gravitational acceleration of the scaled model must be increased N times. Table 3.5 summarizes scaling laws for other quantities, derived through simple dimensional analysis.

Table 3.5: Scaling laws for geotechnical centrifuge tests (Schofield, 1981)

Parameter	Dimension (*)	Model/Prototype
Length	L	1/N
Mass	M	$1/N^3$
Stress	$ML^{-1}T^{-2}$	1
Strai	1	1
Force	MLT^{-2}	$1/N^2$
Time (dynamic loading)	T	1/N
Frequency	1/T	N
Acceleration	LT^{-2}	N
Velocity	LT^{-1}	1
Displacement	L	1/N

* where: L is the length, T is the time, M is the mass and N is the scaling factor

The centrifuge tests were performed under centrifugal accelerations of 80g and 40g (Lanzano et al., 2010; Lanzano et al., 2012). A small laminar box ($500\times250\times300mm^3$) was used.

The mechanical properties of the specific aluminium are: unit weight $\gamma=27kN/m^3$, elastic modulus E=70 GPa and coefficient of Poisson $\nu=0.33$.

Several centrifuge tests, according to Lanzano et al., 2012, were performed at the University of Cambridge. The burial depth of the tunnel was set equal to two times the diameter of the tunnel according to Lanzano et al., 2012.

In particular, the soil models were made using dry Leighton Buzzard sand (fraction E), reconstituted at two different relative densities: about 40% for test T4 and 75% for test T3 (Lanzano et al., 2012). To validate the numerical model and the Adina code, the test with the test T3 with a centrifugal acceleration equal to 80g was used.

Figure 3.22 shows the circular model tunnel composed by an aluminium tube, having an external diameter D=75mm and a thickness t=0.5mm

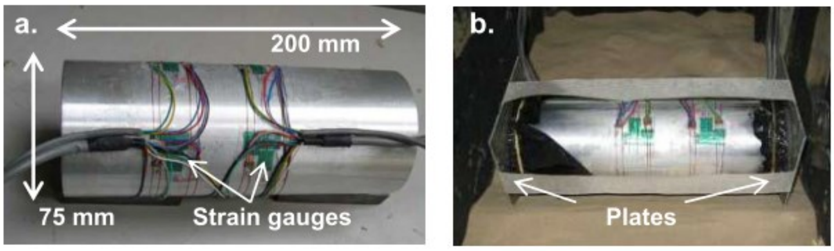

Figure 3.22: Model tunnel instrumented with strain gauges, (b) placement of the model tunnel in the laminar box (after Lanzano et al., 2012)

Accelerometers were used to record the horizontal and the vertical acceleration at several locations in the soil and on the laminar box. Also, the tunnel was instrumented with strain gauges, to record the bending moment and the axial force of the lining at four locations. Two linear variable differential transducers (LVDTs) were attached on gantries running above the model, to measure the soil surface settlements.

The position of the devices of the case studied herein is presented in Figure 3.23.

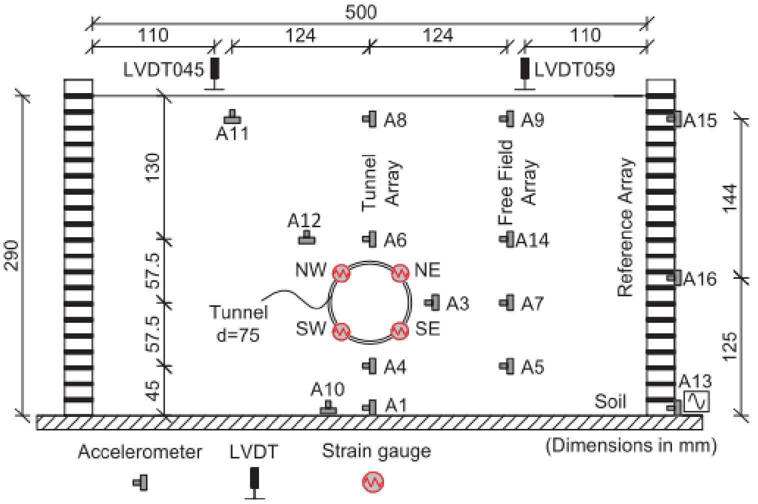

Figure 3.23: Models layout, instrumentation scheme for the T3 test case (A12, A13 are reversed for T4), modified after Lanzano et al. (2012)

3.7.1 Mechanical parameters of the soil and the tunnel

Table 3.6 shows the geotechnical parameters of the soil used for the numerical analysis according to the test T3 (Lanzano et al.,2012).

Table 3.6: Geotechnical parameters of the soil (Test T3)

V_S [m/s]	ϱ [t/m^3]	ν	φ [°]	c [MPa]
116	1.55	0.33	33.4	0.002

More details regarding the geotechnical characterization of the soil were shown in (Bilotta et al., 2014a, b)

3.7.2 Numerical modelling: loading and boundary conditions

Four input motions were applied to the bottom of the model for the test T3. To validate the developed *ADINA* FEM model, only the input motion EQ1 and the centrifugal acceleration 80g was used. The main characteristics of the input motions are tabulated in Table 3.7, highlighting in bold the input used (EQ1). More details regarding the testing procedure may be found in Lanzano et al. (2012).

Table 3.7: Input motions used (Lanzano et al., 2012)

Input	Gravity level [g]	Frequency [Hz]	Nominal duration [s]	Nominal amplitude [g]
EQ1	**80**	**30**	**0.4**	**4**
EQ2		40		8
EQ3		50		9.6
EQ4		60		12

The FEM analyses through the Adina code was performed under plane strain conditions on prototype scale models (see Figure 3.24)

The soil was modelled with the 2D solid element in plane strain conditions and four nodes, using a visco-elastoplastic model (Mohr-Coulomb), while the tunnel was modelled with 2-node beam elements,

As regards the boundary conditions, the bottom of the model was fixed in the vertical translation, simulating a rigid bedrock. Side boundaries kinematic tie constraints were introduced, forcing the opposite vertical sides to move simultaneously, simulating the laminar box.

The viscous damping was modelled according to the Rayleigh damping:

$$\alpha = 2 \cdot \frac{D \cdot \omega_1 \cdot \omega_2}{\omega_1 + \omega_2} = 0.7345 \; ; \qquad \beta = 2 \cdot \frac{D}{\omega_1 + \omega_2} = 0.0085$$

In which D is the damping ratio of the soil, estimated at 0.1, $\omega_1 = 4.561\, rad/s$ the first angular frequency of the soil and $\omega_2 = 4 \cdot \omega_1 = 18.849\, rad/s$.

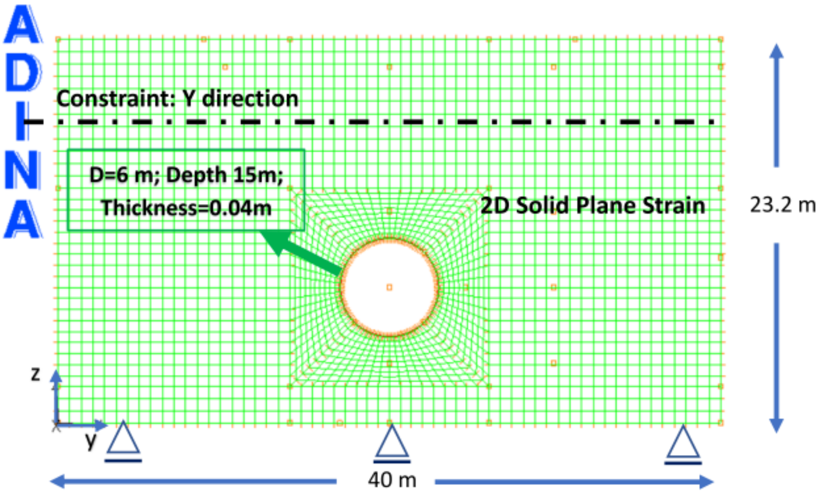

Figure 3.24: Numerical FEM model for step 5

The following Figures (Figs. 3.25, 3.26, 3.27) show the comparisons between the results achieved by the numerical analysis and these recorded during the centrifugal test T3.

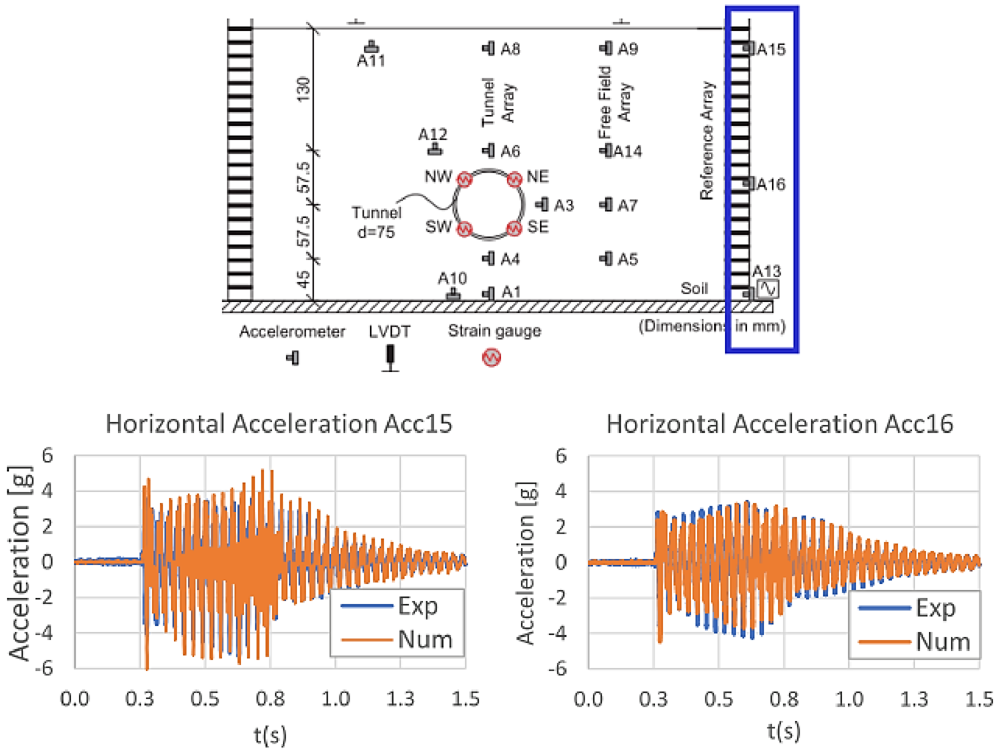

Figure 3.25: Comparisons between the results achieved by the numerical analysis and these recorded during the centrifugal test in terms of horizontal accelerations

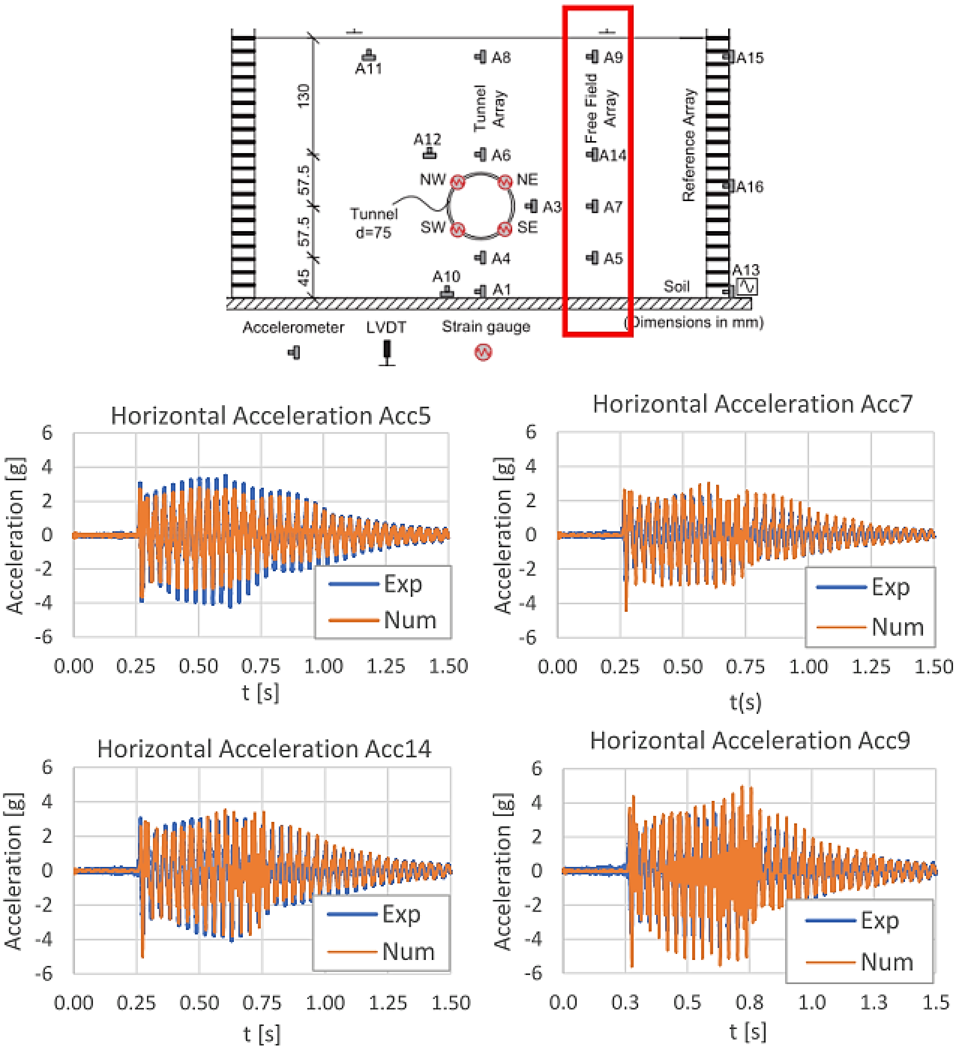

Figure 3.26: Comparisons between the results achieved by the numerical analysis and these recorded during the centrifugal test in terms of horizontal accelerations

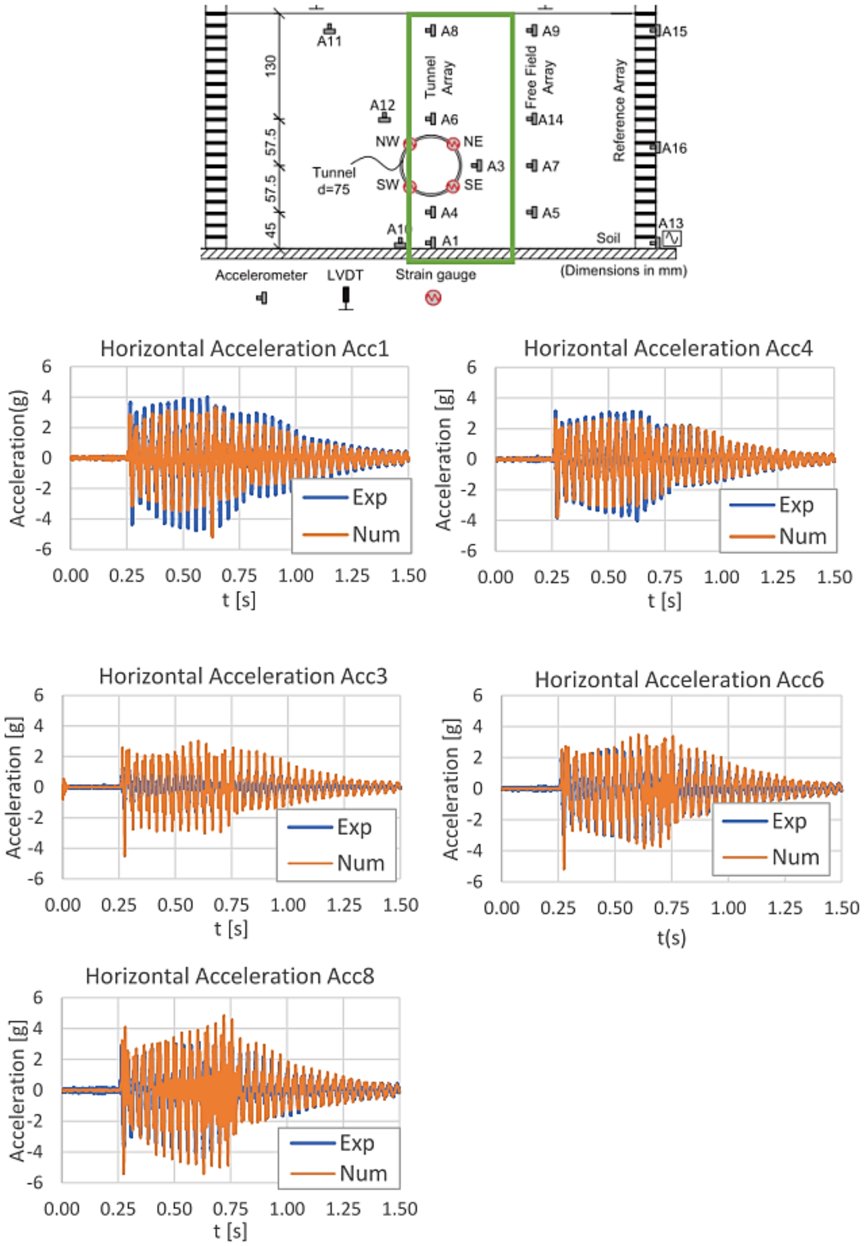

Figure 3.27: Comparisons between the results achieved by the numerical analysis and these recorded during the centrifugal test in terms of horizontal accelerations

The numerical results achieved in terms of horizontal accelerations are similar to the results recorded during the centrifuge tests described previously, along the different alignments analysed.

Thus, the FEM model that will be used to analyse the seismic response of the coupled system tunnel-soil-aboveground structure will have the characteristics showed in 3.4.3 and 3.6.3 sections.

In the next chapter 4, a parametric analysis of the system was analysed to study several aspects of dynamic interaction phenomena.

Chapter 4

THE RAILWAY NETWORK OF CATANIA (ITALY): FROM A CASE-HISTORY TO PARAMETRIC ANALYSES

4.1 Introduction

The existing underground line in the urban area of the city of Catania (Italy) is being extended in two directions; towards the main towns in the hinterland and also towards the "Vincenzo Bellini" airport (Abate et al. 2016; 2019; Abate and Massimino 2017). The tunnel is being dug using a Dual Mode TBM (Herrenknecht S454.1, Diameter 10.6 m). During my stage in the CMC (Cooperativa Muratori e Cementisti) of Ravenna, that is the company committed in the building of the underground in Catania, geological and geotechnical reports were studied to achieve the geotechnical parameters of the soil.

In the following sections, the seismicity of the area and the geotechnical parameters will be shown for the Nesima-Misterbianco segment. As will be possible to see, the soil profile is mainly formed by volcanic soil, due to the different lava flows caused by volcanic eruptions of Mount Etna in Catania (Banna et al. 2015; Capilleri and Massimino 2019; Abate et al. 2006; 2016; Caruso et al. 2016; Castelli et al. 2016; 2018; Massimino et al. 2019).

4.2 The railway network in Catania and the investigated segment

The design of the new railway network in Catania is part of the programme to upgrade and modernize the current narrow-gauge monorail. Two different railway lines (currently in operation) were built in 1999: an underground double-track railway in the centre of the city (1.8 km long), and a surface monorail track (2.0 km long). The goal is now extending the existing railway line, that is at present confined exclusively to the urban area of Catania, towards the sub-metropolitan area of Misterbianco and Paternò villages in the north-west direction, and towards the "Vincenzo Bellini" airport in the south-east direction. It will serve an estimated population of about one million inhabitants, covering an urban and suburban area of about 44 km, including 18 km in tunnels and 26 km on the surface as well as 117 km of extra-urban surface track.

Figure 4.1 shows the whole designed network: the red line indicates the two lines built in 1999 and currently in operation; the light blue lines indicate the two new lines at present under construction (Nesima-Misterbianco and Stesicoro-Palestro). The dark blue lines indicate the planned lines, which are not yet under construction. The present research project regards the blue lines between the stations of Nesima and Misterbianco (Figures 4.1 and 4.2).

Figure 4.1: The underground network in Catania

Figure 4.2: The Nesima-Misterbianco segment analysed.

The Nesima-Misterbianco railway line is 3940 m long. The underground segment covers a length of 1748 m. A TBM has been used to realise this railway segment. Due to the strong heterogeneity of the geological profile of this area, the digging has proceeded in both the OF (Open Face) and EPB (Earth Pressure Balance) modes, switching frequently from one to the other.

The main technical characteristics of the TBM are (Figure 4.3): digging diameter = 10.65 m; shield length ≈ 9.35 m; shield thickness = 0.07 m; excavation chamber length = 1.00 m; total force of jacks = 100370 KN; maximum torque = 26026 kNm; head rotation speed = 0-3 rpm. Moreover, the TBM presents No. 6 back-up wagons for a length of about 100 m. The digging average depth is equal to about 20.00÷25.00 m. The final tunnel lining consists of a precast reinforced concrete ring with a thickness of 0.32 m and a width of 1.50 m.

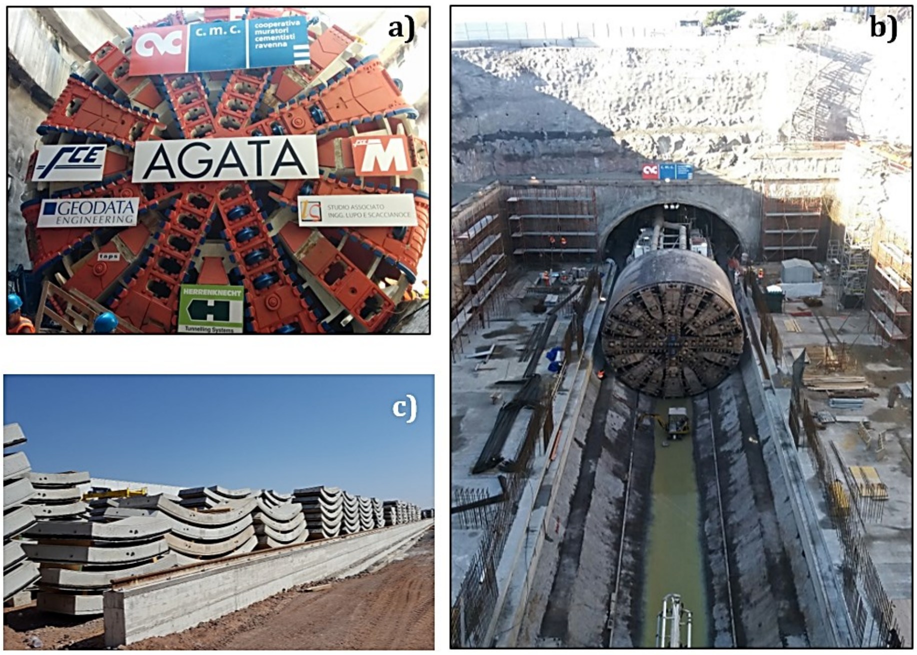

Figure 4.3: TBM utilised along the Nesima-Misterbianco segment: a) front view of the TBM; b) TBM across Fontana station; c) precast concrete segments.

Each ring consists of 7 segments (see Figure 4.4) installed by an appropriate erector inside the TBM. The outside ring diameter is equal to 10.24 m.

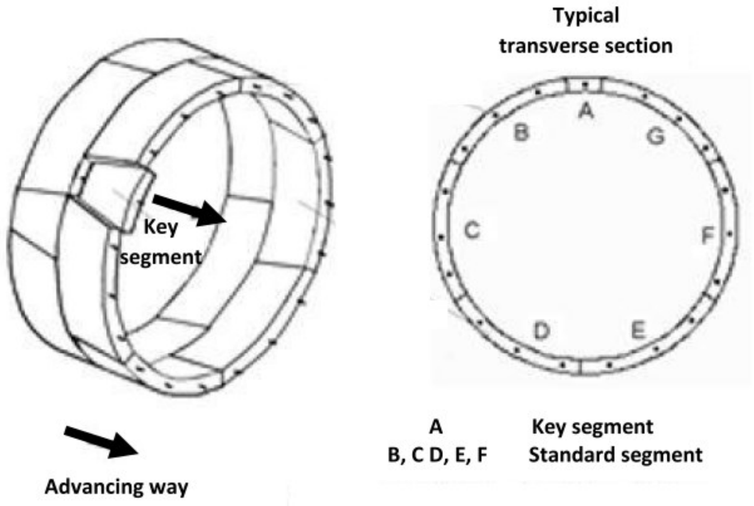

Figure 4.4: Ring of the line tunnel consisting of seven segments.

Figure 4.5 shows a longitudinal section of a tunnel boring machine. The TBM is equipped with a rotating cutter head through which it digs the front excavation; behind the rotating head, there is the soil cutting chamber inside which the excavated soil, maintained as a highly viscous fluid through the addition of chemical additives, is used to keep the pressure to guarantee the stability of the excavation front (EPB mode). Hydraulic rams push against newly placed concrete segments to drive the machine forward; a rotating arm adds pre-cast concrete tunnel segments to form a ring. Each ring is composed of 7 segments. The excavated soil is removed by a conveyor belt and it is transported to the tanks and is left to decant.

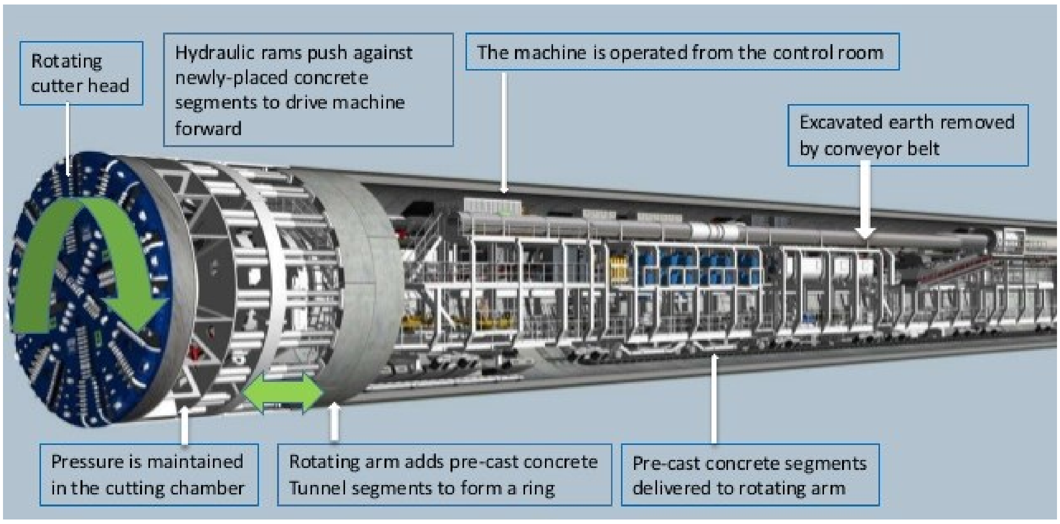

Figure 4.5: Longitudinal section of a Tunnel Boring Machine

4.3 Geotechnical characterization of the Nesima-Misterbianco segment

Many geotechnical characterizations of the soil have been performed in this city, due to its high seismic risk (Castelli et al., 2016; Castelli and Maugeri, 2008; Castelli et al., 2008a, 2008b; Castelli and Lentini, 2013; Castelli and Lentini, 2016; Castelli et al., 2017; Cavallaro, 2006b, 2008a, 2008b).

In order to define the geological profile and the geotechnical parameters of the soils and rocks along the Nesima-Misterbianco segment, two different geotechnical investigations were performed: the first one in 2004 during the preliminary design of the underground and the second one in 2015 for the executive design. Furthermore, the investigations carried out for the construction of a parking area around the Monte Po station and those performed in 1996 as part of the "The Catania Project" (Faccioli E. and Pessina V. 2000) were also considered.

During the geotechnical investigation survey carried out in 2004, 15 boreholes, 5 samples Q1 (UNI ENV 1997-2:2002) and 3 Down-Hole tests were carried out. The most significant 3 boreholes, named S2, S3 and S4 (in green in Figure 4.6), were considered for the characterization of the analysed Nesima-Misterbianco segment. During the investigation survey carried out in 2015, 17 boreholes (Si1, Si2, Si3, Si4, Si4bis, Si5, Si6, Si7, Si8, Si9, Si9bis, Si10, Si11, Si12, Si13, Si14, Si15) were performed (in red lines in Figure 4.6). Besides, the boreholes designated as 1, 2, 3, 4, 5 (in black in Figure 4.6) performed for the construction of the parking area around Monte Po station and the boreholes numbered as 140, 1242 and 1068 (in violet in Figure 4.6) performed as part of the "The Catania Project" were used to define the soil profile.

Generally, an anthropic layer is found in the most superficial portion; then, lava rock layers are observed at greater depths. The geological formations directly involved in the digging process are essentially: Volcanoclastic breccia and sand dating from 1669 from Si1 to Si8; Lava of Quartalaro from Si8 to Si10; Volcanoclastic breccia dating from 1669 from Si10 to shortly after more than Si11; finally, Lava of Quartalaro up to Si13.

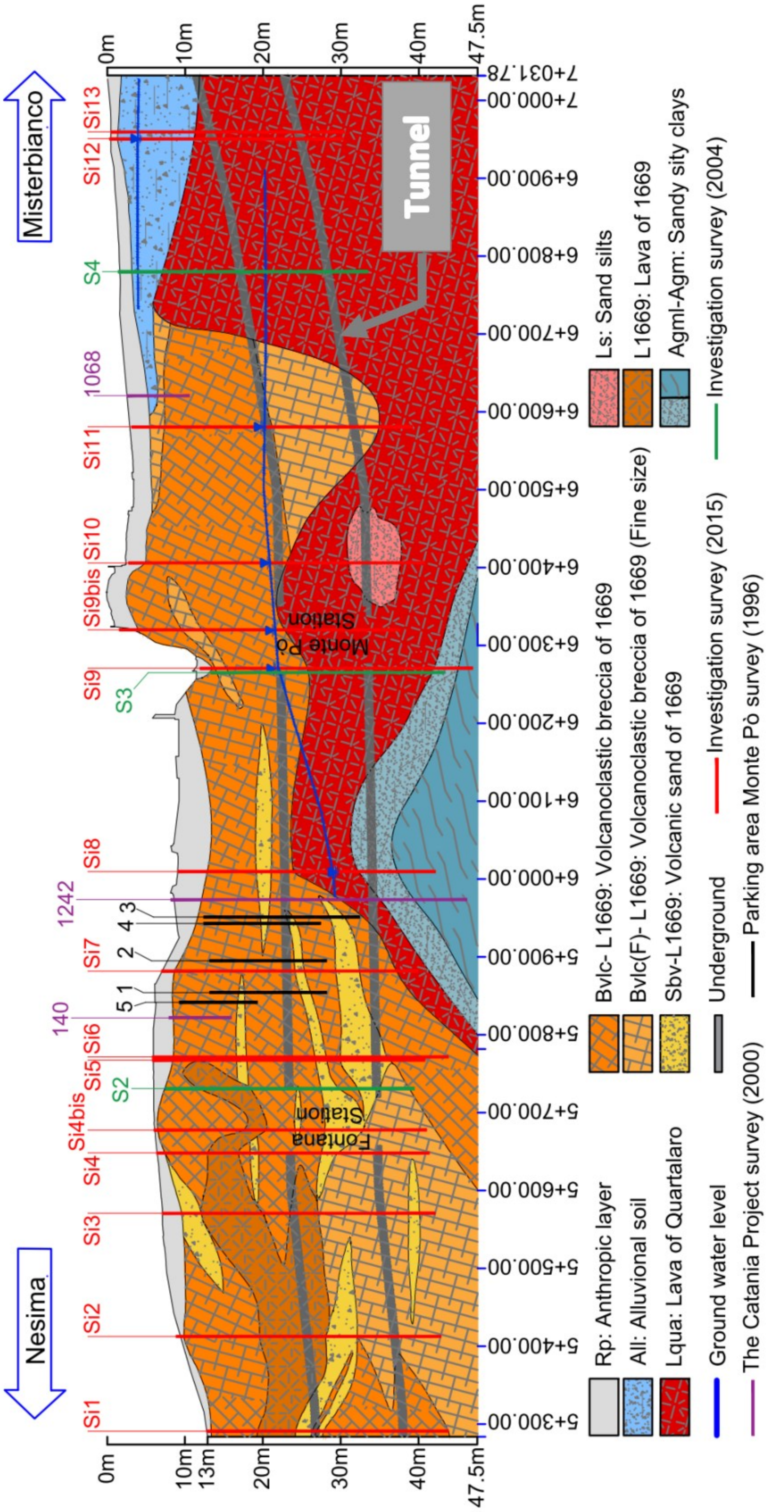

Figure 4.6: Soil profile and positions of the boreholes along the Nesima-Misterbianco segment at the design phase.

The following in-situ tests were also performed in 2015 inside several boreholes shown in Figure 4.6: 2 Dilatometric Tests; 15 Standard Penetration Tests; 7 Permeability Lefranc Tests; 6 absorption Lugeon Tests; 2 Dac-Tests and 6 Pocket Penetrometer Tests. Furthermore, 15 Open Piezometer Tests were performed to evaluate the depth of the groundwater. Finally, to define the shear wave velocity V_S, Down-Hole tests (Figure 4.7) and traditional Horizontal-to-Vertical Spectral Ratio (HVSR) tests (Figure 4.8) were performed. In Figure 4.8, the analysed cross section, Si3, was highlighted. Moreover, many samples were collected during the investigation survey and the undisturbed samples were subjected to the following laboratory tests: a) classification tests; b) tests to determine the resistance and deformability characteristics of the soil: oedometric tests, direct shear tests, triaxial tests; c) tests to determine the resistance and deformability characteristics of the rock: uniaxial compression tests, point load tests, triaxial compression strength tests, indirect tensile strength tests and measurement of sonic waves.

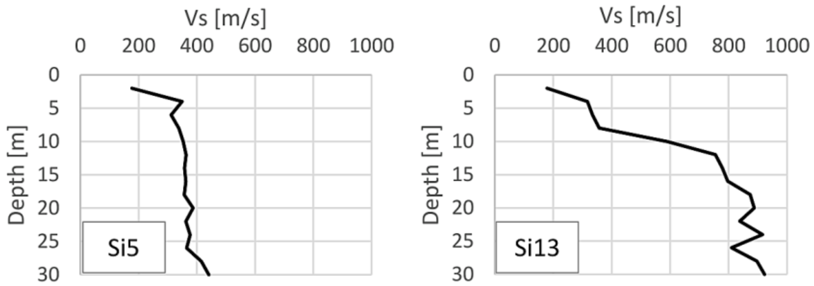

Figure 4.7: Shear waves velocity by Down-Hole Tests

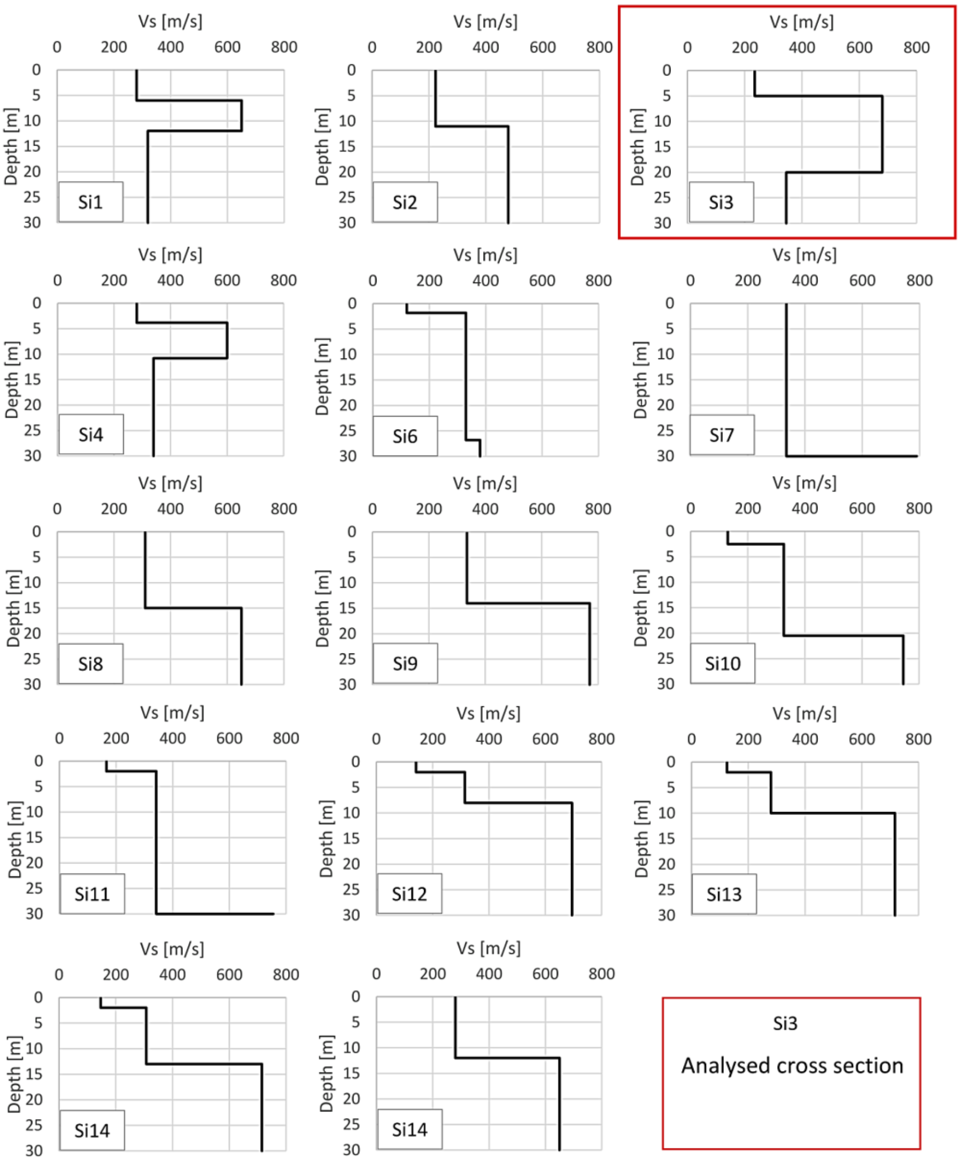

Figure 4.8: Shear waves velocity by HVSR Tests

Table 4.1 shows all the geotechnical parameters obtained per each geological formation reported in Figure 4.6, being: γ the unit weight; φ' the angle of shear strength and c' the cohesion obtained by the direct shear test; c_u the undrained cohesion obtained by the U-U triaxial tests and by the SPT and PPT tests; E_0 the Young modulus at very small strains obtained by the V_S values; E_u the undrained modulus of elasticity obtained by the U-U triaxial tests; k the coefficient of permeability obtained by the LE and LU tests and by the oedometric tests. Since geotechnical investigations were not sufficient to evaluate depth- dependent (or stress-dependent) mechanical parameters, average values were estimate and used for each layer. Moreover, the thickness of the soil layers (described in Table 4.1 and Figure 4.6) was considered enough small (about 10 meters) to allow us the use of constant properties for each layer.

Table 4.1: Geotechnical parameters per each geological formation

Geological Formation								
↓	γ [kN/m^3]	φ' [°]	c' [kPa]	c_u [kPa]	V_S [m/s]	E_0 [MPa]	E_u [MPa]	k [m/s]
Rp	18÷19	30÷35	0÷10		120÷180	70÷125		
All	18÷21	20÷23	0÷10	70÷150	200÷350		20÷45	
Sbv-L1669	18÷21	32÷40	0÷20		200÷350	200÷400		10^{-5}
Agm	20÷21	18÷27	5÷30	100÷300	400÷550	1000		
Agml	20	18÷27	0÷15	200÷400	400÷550		55÷75	
Ls	19÷20	30÷35	0÷30	200÷400				10^{-5}
Bvlc-Bvlc(F)-L1669	18÷21	38÷45	0÷20		200÷350	250÷750		10^{-6}÷10^{-5}
Lqua -L1669	25÷27	50÷65	100÷1000		550÷800	2000÷5000		10^{-5}÷10^{-3}

4.4 Analysis of the vibrations induced on the surface by the TBM

4.4.1 HVSR method

The HVSR method was introduced by Nogoshi and Igarashi (1971) and first applied by Nakamura (1989) and it is useful to estimate the fundamental frequency of the soil. According to this method, it is possible to estimate the dynamic characteristic of surface layers by measuring the microtremor of the surface. The surface layers are normally exposed to tremor by natural forces (storm, sea waves) and artificial forces (plant, train etc.). Sea waves induce a tremor of a relatively long period (2-3 seconds or more), the so-called microseisms, while the storm and artificial forces do a tremor of short period, the so-called micro-tremor.

In this section, the basic concept of the HVSR method is reported (Nakamura, 1989).

Figure 4.9 shows the ratio (A_H/A_V) of maxima values between horizontal and vertical motions of a dynamic input for each observation point. Evidently, the A_H/A_V value of the dynamic inputs is related to the soil conditions of the observation point and the ratio is close to 1 for stiff soil. Consequently, no amplitude in a specific direction prevails on the stiff soil.

Considering the horizontal component of the tremor, they may be considered to be amplified through multi-reflection of the S wave, while the vertical component is amplified through multi-reflection of the P wave. The P wave velocity is generally higher than 1000 m/s and the tremor around 10 Hz or less may not be amplified so much through multi-reflection within surface layers of several ten meters at most in thickness.

The effect of the Rayleigh wave, on the other hand, is remarkable in the vertical component of the tremors. This effect may be known by determining the ratio of vertical tremor between the surface and the substrate. So, the effect of the Rayleigh wave is nearly zero when the ratio is about 1.

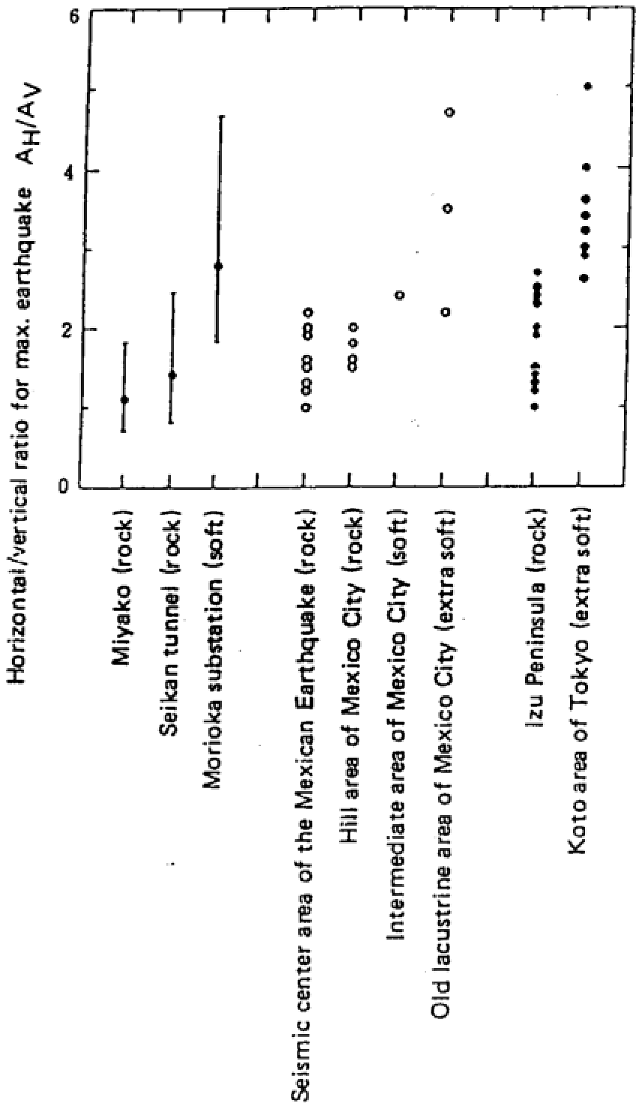

Figure 4.9 Ratio of maximum values between horizontal and vertical components of some dynamic inputs (Nakamura, 1989)

The transfer function S_T of surface layers is defined as follows:

$$S_T = \frac{S_{HS}}{S_{HB}} \tag{4.1}$$

Where S_{HS} and S_{HB} are the horizontal tremor spectrum on the surface and the horizontal tremor spectrum on the substrate, respectively.

S_{HS} is affected by the surface wave. Since the artificial noise is mostly propagated as Rayleigh wave, the horizontal tremor spectrum on the surface may possibly be affected by the Rayleigh wave. The effect of the Rayleigh wave should be included in the vertical tremor spectrum on the surface, S_{VS}, but not in the vertical tremor spectrum at bottom of the soil, S_{VB}. Assuming that the vertical tremor is not amplified by the surface layers, the E_S defined by the following expression should represent the effect of the Rayleigh wave on the vertical tremor:

$$E_S = \frac{S_{VS}}{S_{VB}} \tag{4.2}$$

The Rayleigh wave effect is nearly zero when the ratio E_S is about equal to 1. E_S value will be larger than 1 with increasing effect of the Rayleigh wave.

Assuming that the effect of the Rayleigh wave is equal for vertical and horizontal components, the ratio S_T/E_S may be considered:

$$S_{TT} = \frac{S_T}{E_S} = \frac{R_S}{R_B} \quad \text{with } R_S = \frac{S_{HS}}{S_{VS}} \text{ and } R_B = \frac{S_{HB}}{S_{VB}} \tag{4.3}$$

As shown in Figure 4.10, R_B value is about 1 for a relatively wide frequency range. So, on the stiff substrate, the wave propagation occurs in all directions. Being $R_B \approx 1$, S_{TT} is equal to R_S ($S_{TT}=R_S$). In the following sections, the horizontal (S_{HS}) and vertical (S_{VS}) spectrum will be indicated with "H" to indicate the horizontal spectrum on the surface and with "V" to indicate the vertical spectrum. This means that the transfer function of surface layers may be estimated from the tremor on the surface only. So, the vertical tremor on the surface conserves the characteristics of horizontal tremor at the substrate therewith substituting it.

The Rayleigh wave effect annuls the substitution. But R_S value becomes about 1 in the frequency range where the Rayleigh prevail and thus it is not remarkable in the estimated transfer function.

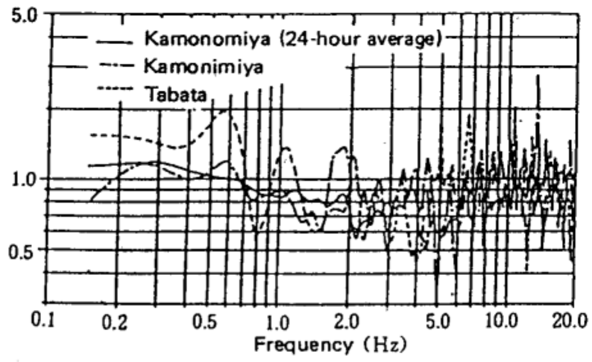

Figure 4.10: Spectrum ratio of horizontal and vertical components in the substrate (Microtremor: Kamanomiya, Tabata) (Nakamura, 1989)

Definitely, this method is based on the assumption that the ratio of horizontal and vertical spectra of surface tremor can be considered a transfer function, where the peak of the curve reveals the fundamental frequency of the soil.

The HVSR was applied in the present work on the vibrations induced by the TBM during the excavation to evaluate the soil profile during the digging, in order to refine the soil profile established in the design phase. In the next section, the method applied to the vibrations induced by the TBM will be explained in detail.

4.4.2 A new low-cost procedure for refining the soil profile during TBM tunnelling

As mentioned earlier, the tunnel is being dug using a Dual Mode TBM, which can dig in two ways: in Open Face (OF) mode for the lava rock formations; in Earth Pressure Balance (EPB) mode for cohesive and/or incoherent soil. In OF mode the TBM excavates rock using disc cutters mounted in the cutter head. In EPB mode the TBM balances the soil/water pressure at the tunnel face. The pressure is maintained in the cutter head by controlling the rate of extraction of spoil through the Archimedes screw and the advance rate. Additives such as bentonite, polymers, and foam are injected ahead of the face to increase soil stability.

In this section, a simple and useful procedure was proposed to validate or not the soil profile established in the tunnels' design phase through the comparison between data obtained from the geotechnical survey at the design phase and data coming from HVSR method applied here on the microtremors induced on the soil surface layers by TBM during tunnelling. This is a new application of well-known HVSR methods. In particular, the first natural frequency of the soil deposit computed applying the well-known theoretical linear approach for ground response analysis (f_n) was steadily compared with that derived from the HVSR method on TBM microtremors (f_n*) involving a soil area 30 m far from the TBM digging front. The agreement between theoretically evaluated frequency and experimentally evaluated frequency confirms the previously defined soil profile; the disagreement between the aforementioned frequencies suggests a disagreement between the profile defined in the previous design phase and the actual soil profile that the TBM will encounter in the next 30 m. The disagreement should be solved by additional investigations.

The recording of the microtremors induced by TBM is prescribed by technical regulations (UNI9916 - DIN 4150) to avoid damage to existing structures and/or infrastructures; thus, this approach was proposed to use these prescribed records also as an early warning system devoted to validating and/or refining the soil profile.

Geological and geotechnical information about the rocks and soils at the digging front is fundamental, firstly to define the appropriate digging mode and, consequently, to choose the correct front pressure to guarantee stability at the digging front (Mohammadi 2010; Anagnostou and Kovari 1994; 1996; Carranza-Torres et al. 2013.) An error in the estimation of the front pressure can cause subsidence or uplift problems with disastrous effects in urban areas (Broere 2002; Atkinson and Potts 1977; Attewell 1978; Attewell and Taylor 1984; Burland 1995).

Using geophones, which are instrumented by electrodynamics velocimeters, can it is possible to carry out the measurements of microtremors. Two velocimeters were horizontally oriented, one was vertically oriented. In the H/V vs f diagram (being f the frequency), a peak indicates the amplification value of the horizontal components of the soil motion with respect to the vertical component relative to the natural frequency of the surface layers, f_n*. Thus, this non-invasive, rapid and low-cost method, allows us to easily estimate f_n* for the soil surface layers.

According to the HVSR method, an H/V vs f diagram deriving by the microtremors due to TBM was developed day by day and it was used to estimate the daily f_n* for the Nesima-Misterbianco segment. Thus, the value of f_n* was compared day by day with the value of the natural frequency f_n obtained by the well-known following expression (Kramer, 1996):

$$f_n = \frac{V_S}{4h} \tag{4.4}$$

being V_S and h, respectively, the shear wave velocity and the height of the deformable geological formations over the bedrock, estimated in the design phase. Two different conditions are possible:

1) $f_n^* \approx f_n$, so the soil profile established during the design phase can be confirmed;
2) $f_n^* \neq f_n$, so the soil profile established during the design phase cannot be confirmed and it will be necessary to carry out further geotechnical surveys to establish the “real” profile; because, according to equation (4.4), if $f_n^* \neq f_n$ the initially estimated V_S and/or h could be wrong (Figure 4.11).

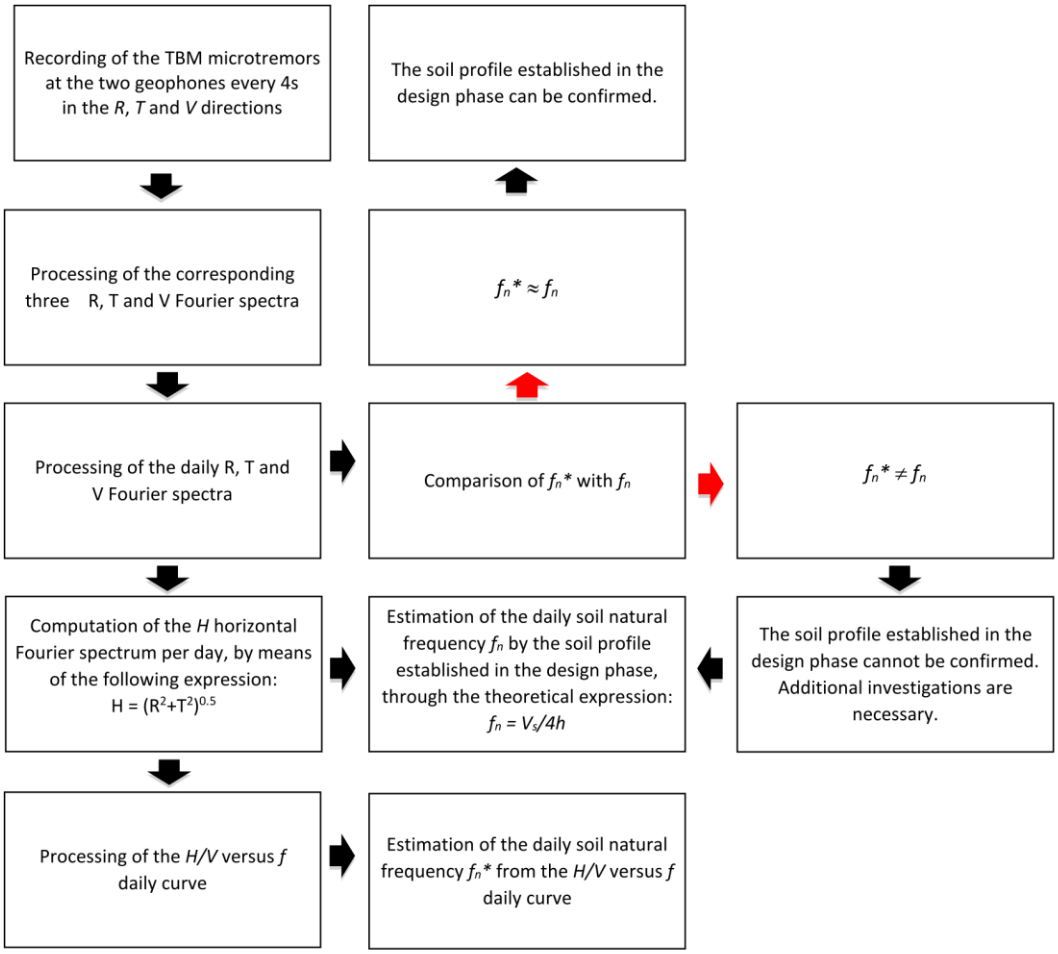

Figure 4.11: Flow chart of the proposed procedure based on the HVSR method for refining the soil profile during TBM digging

In the considered case-history, while the tunnel was being dug, two geophones (Figure 4.12) were located at the soil surface. These geophones recorded day by day a great quantity of velocity-time histories in the following three directions: Radial (*R*), Transversal (*T*) and Vertical (*V*). Each time history was 4s long. The time histories recorded between March 2017 and November 2017 were analysed.

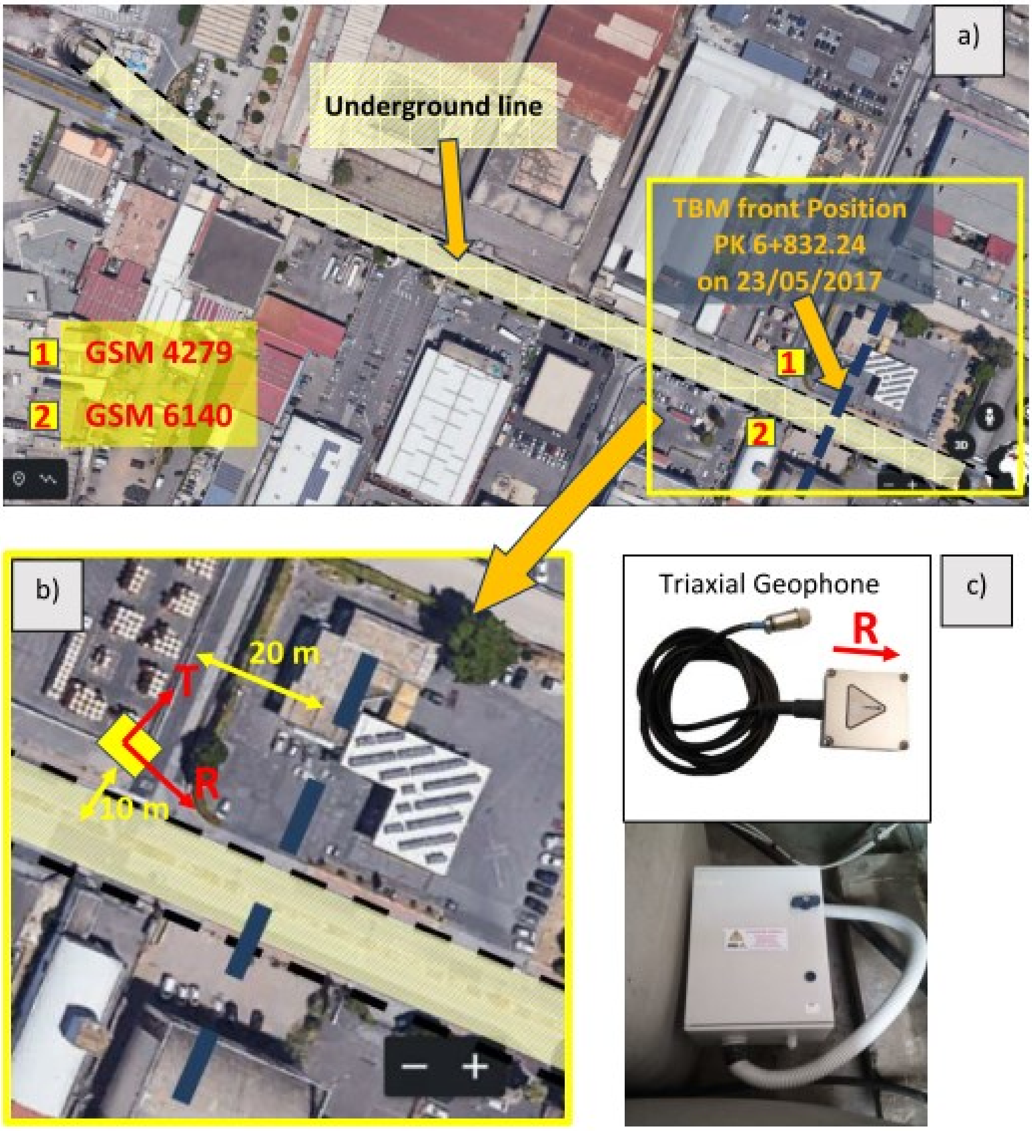

Figure 4.12: Layout of the geophones at the soil surface

Figure 4.13 reports the typically recorded velocity time histories. In particular, Figure 4.13 shows one of the 101 sets of registrations recorded on May 23th, 2017 at the geophone labelled GSM4279 (see Figure 4.12).

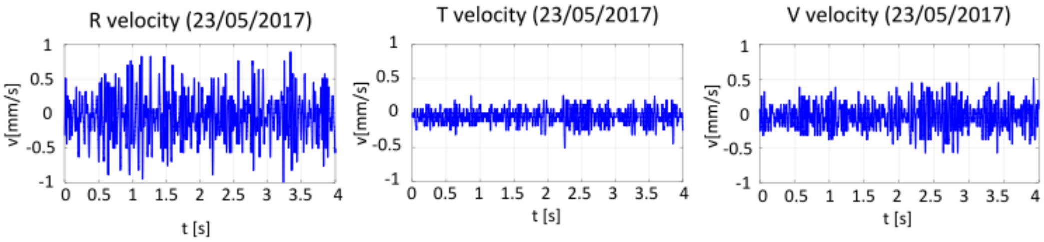

Figure 4.13: Radial (R), Transversal (T) and Vertical (V) velocity time-histories recorded by geophone "GSM 4279" during TBM tunnelling at 00:39 (Italian time) of May 23th, 2017 (see Figure 4.12).

Using these data, it was possible to compute the related acceleration time-histories (Figure 4.14) and in turn the corresponding Fourier spectra. This process was repeated for all the data recorded in one day.

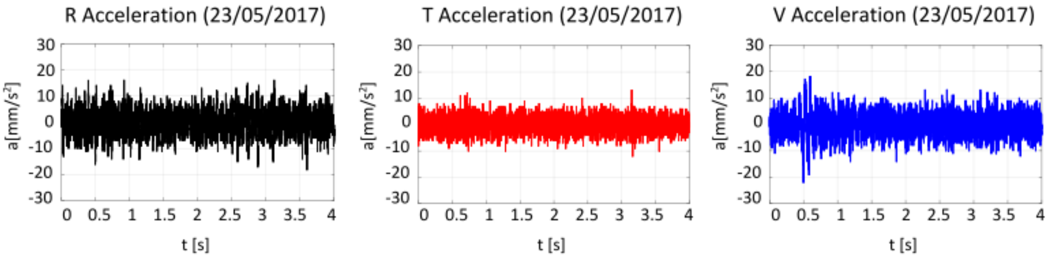

Figure 4.14: Radial (R), Transversal (T) and Vertical (V) average acceleration time histories derived from the velocity-time histories shown in Figure 4.13.

Then, firstly the average *R*, *T* and *V* Fourier spectra per day were computed (Figure 4.15); secondly, the horizontal Fourier spectra (*H*) were computed considering the *R* and *T* Fourier spectra, according to the following expression:

$$H = \sqrt{R^2 + T^2} \tag{4.5}$$

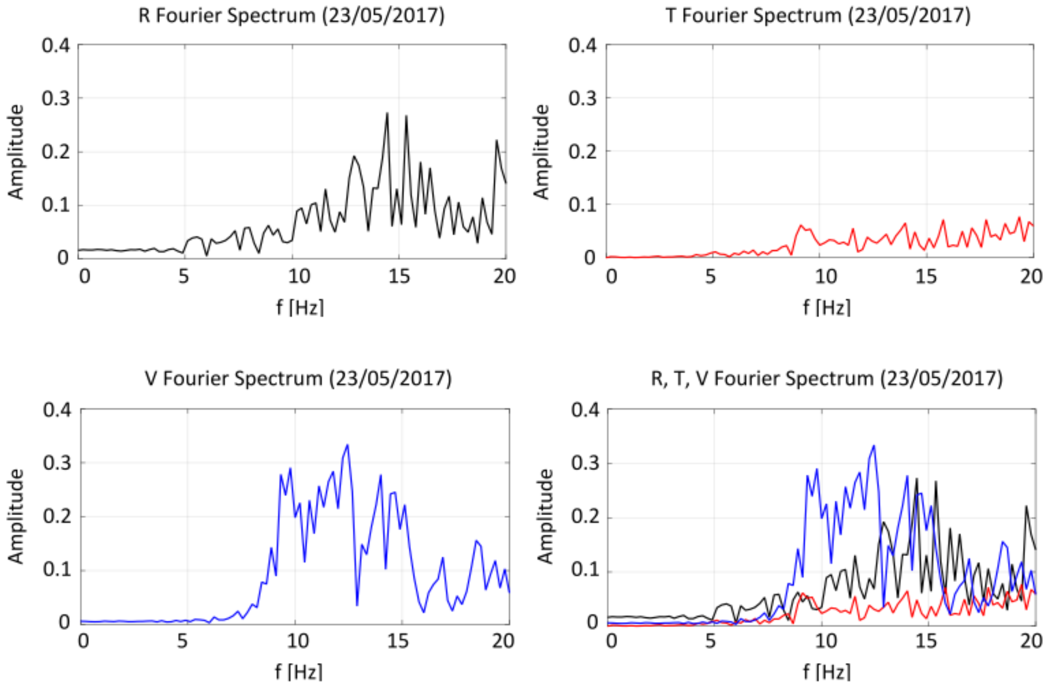

Figure 4.15: Fourier spectra derived by the acceleration time histories coming from all the recording of May 23th, 2017.

Finally, the ratio H/V between the horizontal H and vertical V Fourier spectra was evaluated. So, Figure 4.16 shows the corresponding H/V vs f curve. The frequency at which the H/V ratio reaches the peak represents the first natural frequency of the subsoil involved in the TBM microtremors.

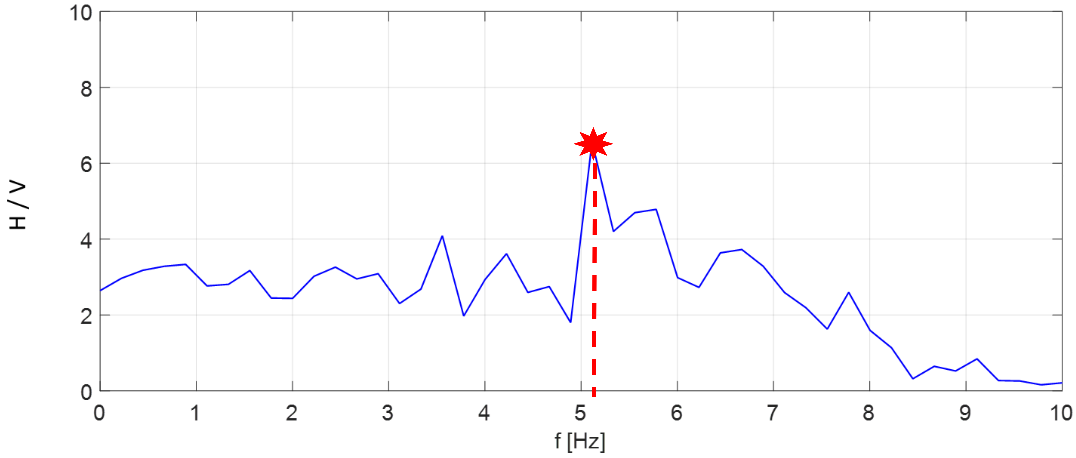

Figure 4.16: H/V vs f curves obtained by the Fourier spectra (May 23th, 2017).

Furthermore, the same procedure was repeated for all the days from March 2017 to November 2017. Figure 4.17 shows the results achieved for the period: May 14th, 2017 - July 12th, 2017.

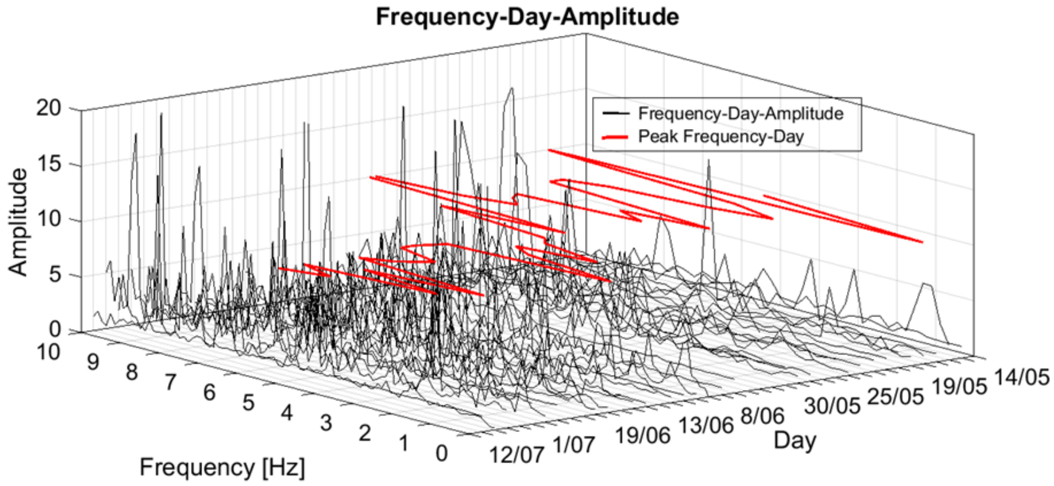

Figure 4.17: Frequency-day-amplitude curves obtained by the new procedure in the period May 14th, 2017 – July 12th, 2017.

Thus, following the above-described procedure for the whole period March-November 2017, Figure 4.18a shows the natural frequency f_n* of the soil deposit day by day (red line), and the corresponding average values (blue line). From Figure 4.18a it is possible to detect five average values of f_n*: going from March 2017 to November 2017 (from the right side to left one), the first one (from section 7+000.00 to section 6+870.00) is equal to 6.5 Hz; the second one (from section 6+870.00 to section 6+440.00) is equal to 3.5 Hz. After Monte Po Station other three average values can be distinguished: the first one is 8 Hz (from section 6+200.00 to section 6+100.00); the second one is 4 Hz (from section 6+100.00 to 5.970.00); the third one is 7.5 Hz (from section 5+970.00 to section 5+870.00). Figure 4.18a below reports also the values of the natural frequencies f_n obtained by expression (4.4).

Figure 4.18b and 4.18c show also the track of the tunnel. Figure 4.18b shows the original soil profile already reported in Figure 4.6 and Figure 4.18c shows the soil profile updated during the tunnel digging, on the base of the TBM spoil and on the base of the proposed procedure.

From Figure 4.18a it is possible to notice a generally good agreement between f_n* and f_n. Only in two segments between section 6+150.00 and section 5+9200.00, which are highlighted by the green box in Figure 4.18, it is possible to notice a disagreement between f_n* and f_n. In particular, between section 6+150.00 and section 5+970.00 f_n* is equal to 4 Hz while f_n is equal to 7.5 Hz; this is due to the presence of sandy silty clays (Agml-Agm) at lower depths (Figure 4.18c), differently from the assumed soil profile in the design phase (Figure 4.18b). Between section 5+970.00 and section 5+9200.00 f_n* is equal to 7.5 Hz, while f_n is equal to 4 Hz; this disagreement is due to the presence of rock (Lava of Quartalaro) at a depth actual lower than that expected in the design phase. The TBM spoil confirms the estimation of f_n*.

Finally, the values of f_n* were compared with the natural frequencies obtained by the traditional HVSR tests performed during the design phase, i.e. before the tunnel digging. In particular, the natural frequencies obtained at boreholes Si11 (section 6+580.00) and Si12 (section 6+950.00) through the traditional HVSR tests performed in the design phase were about 4.5 Hz and 6 Hz respectively. These frequencies are in agreement with the values of f_n* obtained through the proposed HVSR application to TBM microtremors, reaching 4 Hz and 7 Hz around boreholes Si11 and Si12, respectively.

Unfortunately, the traditional HVSR tests performed in the design phase did not cover all the segments investigated, so other comparisons cannot be performed.

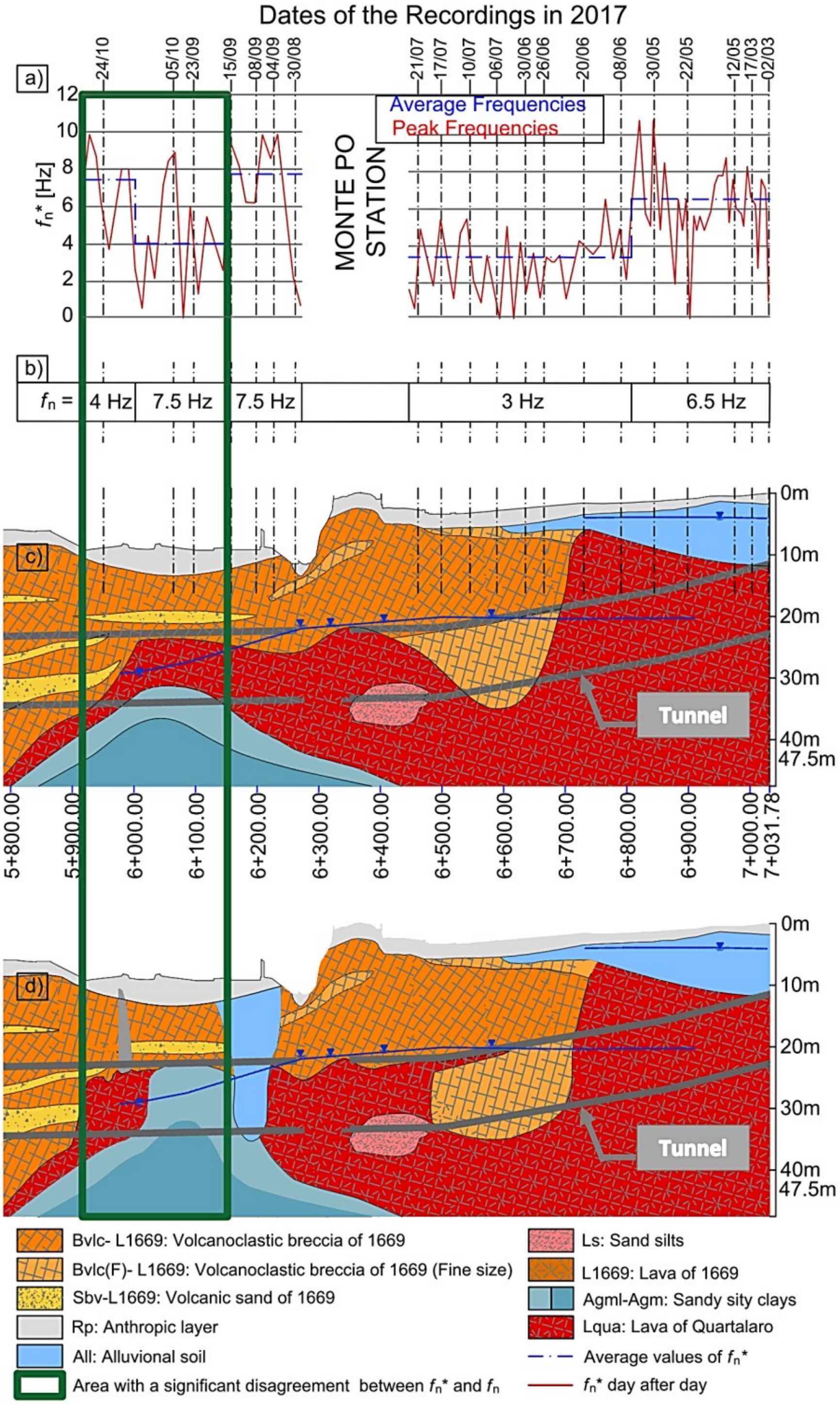

Figure 4.18: Results of the new proposed HVSR application: a) achieved fundamental frequency f_n^* *of the soil deposit in red line and corresponding average values in blue line and comparison with the theoretical expression* $f_n = V_s/4h$*; b) soil profile at the design phase; c) soil profile updated during the tunnelling, on the base of the TBM spoil and the new proposed procedure.*

Figure 4.19a shows the zoom of the soil profile established before the tunnel digging (see also Figure 4.6), and Figure 4.19b shows the zoom of the soil profile updated during the tunnel digging, on the base of the TBM spoil and according to the proposed procedure (Figure 4.18c). As previously said, in this section the two soil profiles appeared quite different. This led to a drastic slowing of the tunnel digging and it required additional tests to be carried out to clarify the real nature of the soil.

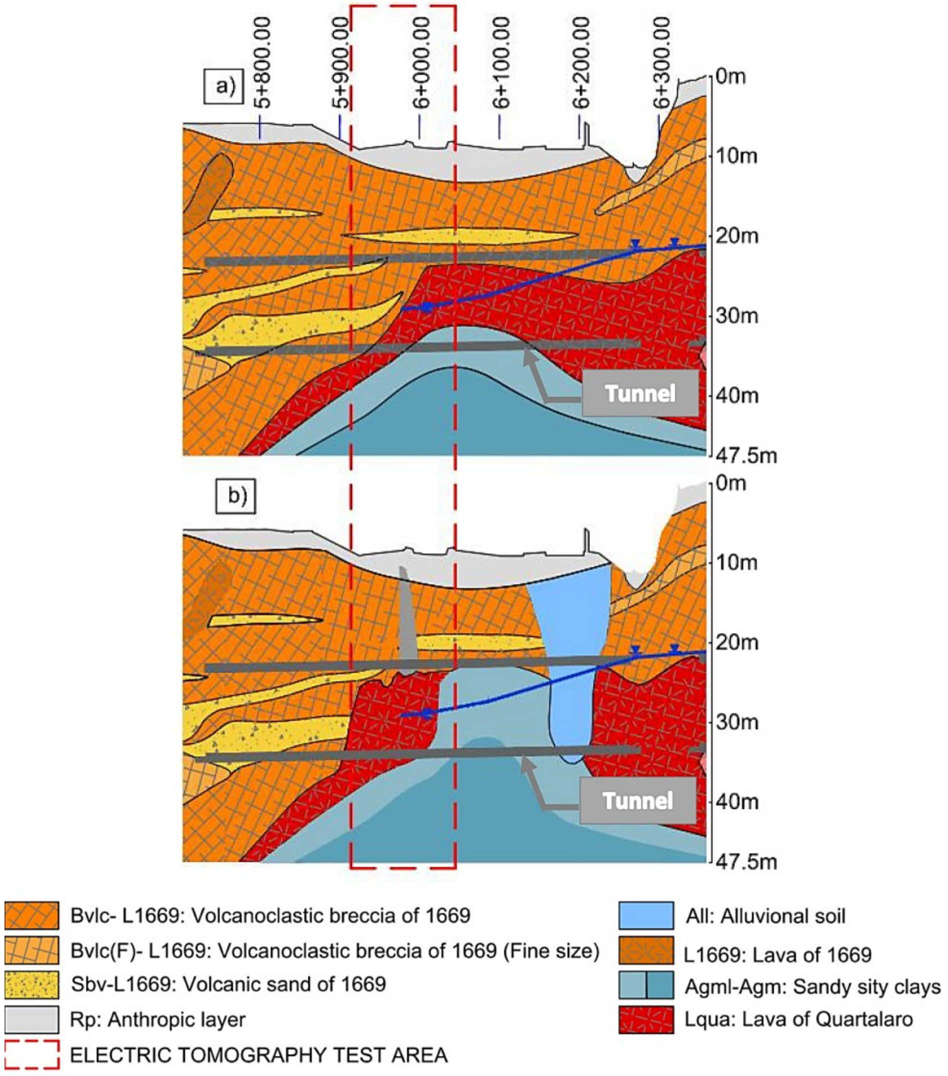

Figure 4.19: Zoom of the soil profile established during the design phase (Figure 4.18b) and the soil profile updated during the tunnelling (Figure 4.18c).

An Electric Tomographic Test (ETT) and new boreholes (S1T, S2T, S3T, S4T and S7T) were performed in October 2017. The red box in Figure 4.19 shows the segment of the soil profile in which these supplementary tests were carried out. Figure 4.20 shows the exact location of these tests.

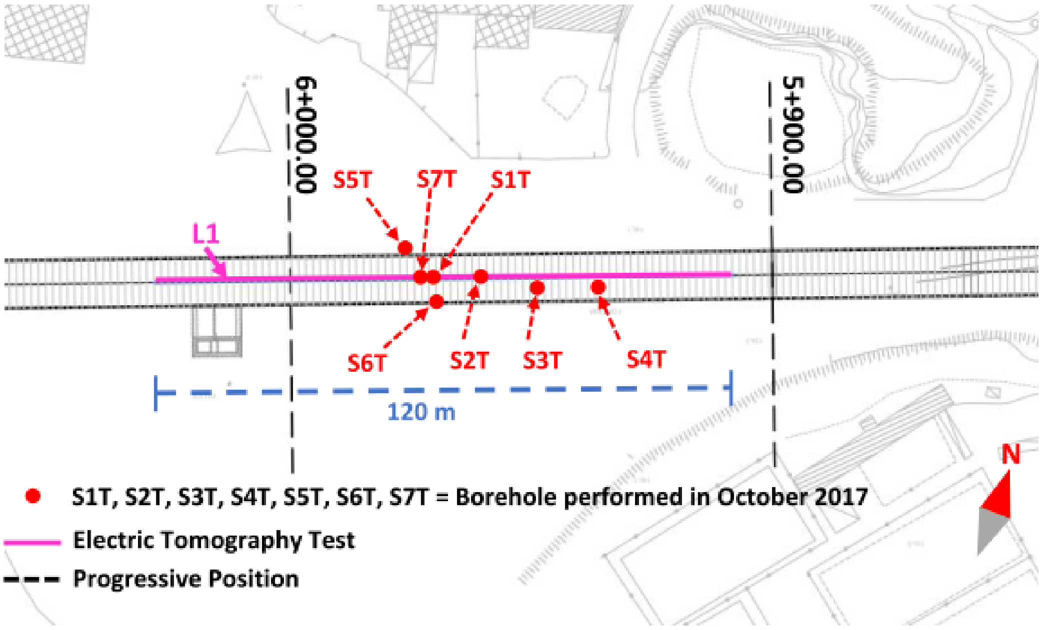

Figure 4.20: Layout of the Electric Tomography Test and the new boreholes performed in October 2017.

Figure 4.21 shows the results of the ETT. Figure 4.22 shows the typical resistivity ranges of rocks, soils and minerals according to Loke (2013). Figures 4.21 and 4.22, as well as the results of the new boreholes, confirm the presence of rock at a depth lower than that expected in the design phase, giving a natural frequency $f_n = 8$ Hz according to equation (4.4). The latter is very close to the value $f_n^* = 7.5$ Hz found by the proposed procedure.

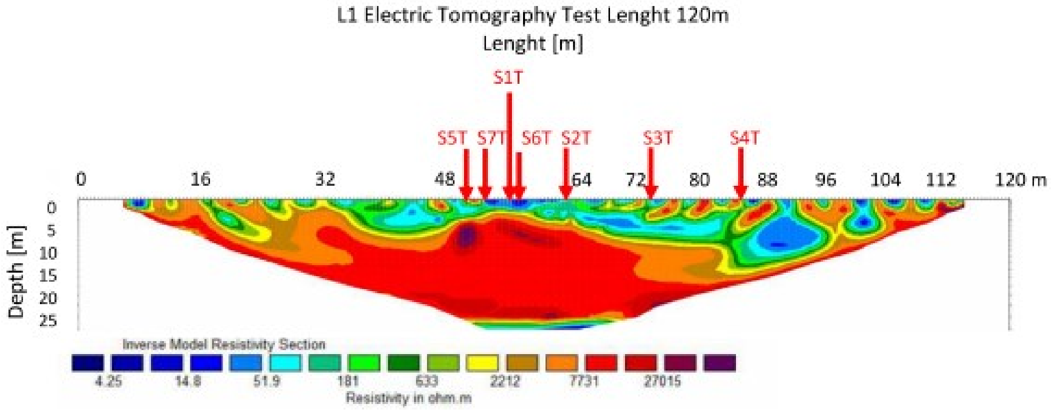

Figure 4.21: Results of the Electric Tomography Test performed in October 2017.

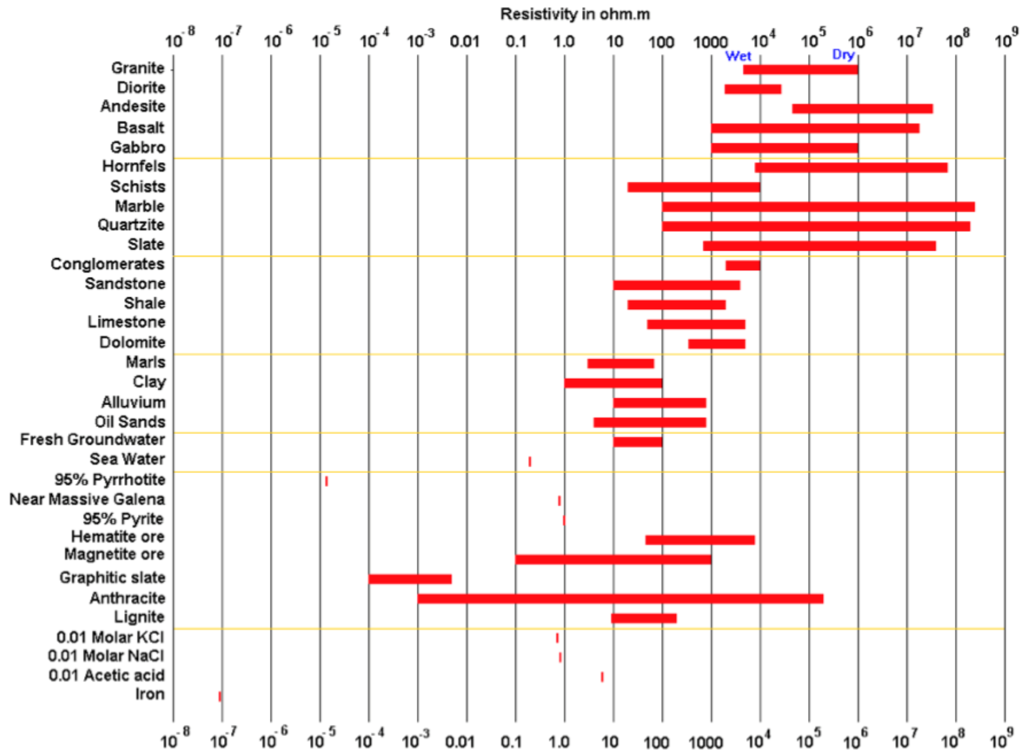

Figure 4.22: The resistivity of rocks, soils and minerals (after Loke, 2013).

The new proposed procedure was successfully applied in a long segment of the Catania under-construction underground. The agreement between f_n* and f_n confirmed the soil profile established at the design phase for the majority of the investigated segment; nevertheless, in a long part, f_n* was deeply different from f_n. The TBM spoil, additional boreholes and an electric tomographic test confirmed the values of f_n* obtained by the proposed procedure. The latter, therefore, can be considered an interesting early warning system devoted to confirming and/or refining the soil profile during tunnel digging.

4.5 Seismicity of the area

Because the strong earthquakes that occurred in Sicily in the past years and the importance of the seismic effects suffered in past times, the city of Catania, located on the eastern zone of Sicily, is considered one of the most high-risk seismic areas in Italy.

In the last centuries the east coast of Sicily was affected by several disastrous earthquakes. In particular, the seismic event of January 11, 1693, with an estimated magnitude between 7.0 and 7.4 (Boschi et al., 1995; Gizzi, 2006), destroyed the city of Catania and much more cities of eastern Sicily. The seismic event caused the partial, and in many cases total, destruction of 57 cities/villages and 40,000 victims. Another seismic event, with an estimated magnitude of 6, on February 20, 1818 (Barbano et al., 2010) caused a lot of victims. Other important seismic events which struck the city of Catania, but with less destructive effects, occurred in March 1536, April 1698, December 1716 and December 1990. The last earthquake struck Eastern Sicily with a local Richter Magnitude ML= 5.6 and caused 19 victims and severe damages to buildings and infrastructures (De Rubeis et al., 1991). Seismicity is mainly distributed in two sectors: along the coast, where the events have also reached a Richter Magnitude MS≥ 7.0, and inland with earthquakes with MS≤ 5.5 (Panzera et al., 2011).

4.5.1 Basic seismic hazard for the city of Catania

The basic seismic hazard for the city of Catania was evaluated according to the Ministerial decree of January 17, 2018 (NTC018). The class of use to which belongs the analysed structure (i.e. the underground) is the IV, according to NTC 2018 because it is a structure with important and strategic public services. Seismic actions on the underground construction were evaluated concerning a reference period V_R that is obtained multiplying the nominal life V_N for the use coefficient $C_U = 2$ corresponding to the class of use IV, according to NTC 2018. So, for the analysed structure ($V_N = 100$ years):

$$V_R = V_N \times C_U = 100 * 2 = 200 \text{ years} \tag{4.6}$$

The seismic hazard must be evaluated through the time of return (T_R) estimated in years:

$$T_R = -\frac{V_R}{\ln(1-P_{VR})} \tag{4.7}$$

in which P_{VR} is the probability of exceeding in the period of reference V_R (Table 4.2). In the studied case, the maximum amplitude of all the accelerograms was appropriately scaled to the value equal to 0.383g, that is the average expected value at the bedrock in Catania, considering the SLV.

4.5.2 Utilised input motions

Three accelerograms (Figure 4.23), scaled up to PGA of 0.383g, were applied at the bedrock of the soil deposit. Due to the few records of earthquakes, only one input recorded during the 1990 earthquake at the Sortino station (EW direction) was used; moreover, two synthetic accelerograms were used. The synthetic seismograms were obtained using a source mechanism modelling, assuming the source to be under the sea along the Hyblean-Maltese fault, for the 1693 and 1818 earthquakes (Azzaro et al., 1999; Azzaro and Barbano, 2000).

Table 4.2: Seismic parameters for the city of Catania

	T_R [years]	a_g [g]	M	F_0 [-]	T^*_c [s]	C_c [-]
SLO (P_{VR}=81%)	120	0.111g	4.3	2.489	0.290	1.98
SLD (P_{VR}=63%)	200	0.140g	4.5	2.461	0.313	1.92
SLV (P_{VR}=10%)	**1900**	**0.383g**	**6.2**	**2.395**	**0.503**	**1.65**
SLC (P_{VR}=5%)	2475	0.440g	6.4	2.382	0.529	1.55

As shown in Figure 4.23, the three inputs differ for the frequency content, in order to study the importance of the input frequency on the seismic response of the system. In particular, the 1693 input motion was characterized by a frequency content (4 Hz) similar to the frequency of the aboveground structure (f=3.7 Hz); the 1818 and 1990 inputs were characterized by a frequency content (1-2 Hz) similar to the first frequency range of the soil deposit (f=1.6 Hz). In the following sections, the importance of the frequency content on the seismic response of the system will be shown in terms of acceleration spectral, of seismic forces on the aboveground structure and in terms of peak ground acceleration achieved on the surface.

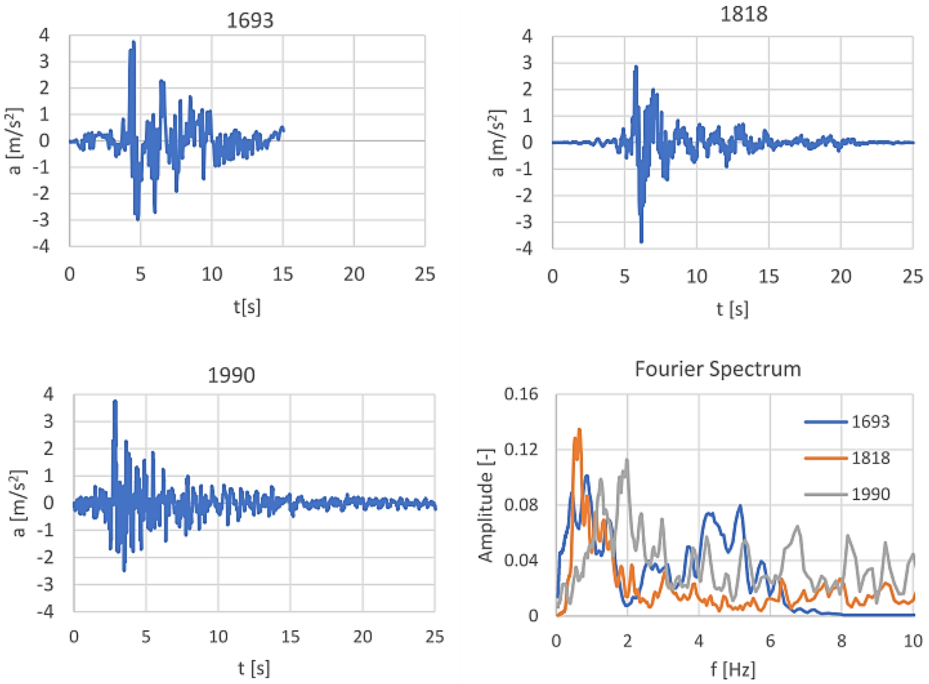

Figure 4.23: Input motions used for the numerical analyses and their Fourier spectra

4.6 Numerical modelling of a cross section of the railway in Catania

After several numerical analyses shown in the previous Chapter 3 to validate the adopted FEM modelling of tunnel-soil-aboveground structures, a cross-section of the railway in Catania (Italy) was analysed, in which several aboveground structures there were to allow the study of the dynamic interaction of coupled systems.

4.6.1 Geotechnical characterization of the analysed cross section (Si3)

In order to define the stratigraphy of the cross section analysed (Si3, see Figures 4.6 and 4.24) and the geotechnical parameters, data achieved by the several geotechnical investigation surveys, described in the previous sections, were taken into consideration.

Laboratory tests on the following samples extracts from the borehole Si3 were performed during the investigation survey of 2015:

- 3 reworked samples called S_{rew};
- 9 samples taken from the Standard Penetration Test and indicate with the S(SPT) abbreviation;
- 2 lava rock samples called S(R);

Figure 4.24: Nesima-Misterbianco segment with cross section Si3 highlighted by a quadrangular shape

Table 4.3 shows the laboratory tests performed on samples (see Figures 4.6 and 4.24). At the Si3 borehole, the following in situ tests were also performed during the investigation survey of 2015:

- Standard Penetration Standard (SPT)
- Lefranc Permeability Test;
- Lugeon Permeability Test;

Finally, an open tube piezometer was installed to estimate the depth of the water table.

Table 4.3: Laboratory tests performed on samples taken from Si3 borehole

Sample Name	**Depth [m]**	**Lithology**	**Laboratory tests performed during the investigation survey of 2015**
S (SPT1)	3.00÷3.15	Sbv	Visual description
S(R1)	6.30÷7.30	LV	Visual description; Point Load Test; Indirect Tensile Strength test
S(R2)	10.00÷11.00	LV	Visual description; Point Load Test; Indirect Tensile Strength test; Abrasion Index; Drop Test;
S(SPT2)	15.00÷15.30	Bvlc	Visual description
$S_{rew}1$	20.00÷20.50	Bvlc-F	Determination of physical quantities (weight per volume unit, natural water content, grain weight per volume unit), particle size analysis
S(SPT3)	21.00÷21.45	Bvlc-F	Determination of physical quantities (weight per volume unit, natural water content, grain weight per volume unit), particle size analysis, direct shear test
S(SPT4)	23.00÷23.45	Bvlc-F	Visual description
$S_{rew}2$	24.50÷25.00	Bvlc-F	Determination of physical quantities (weight per volume unit, natural water content, grain weight per volume unit), particle size analysis, direct shear test
S(SPT5)	25.00÷25.45	Bvlc-F	Visual description
S(SPT6)	28.00÷28.40	Bvlc-F	Visual description
$S_{rew}3$	29.50÷30.00	Bvlc-F	Visual description
S(SPT7)	30.00÷30.37	Bvlc-F	Visual description
S(SPT8)	32.00÷32.45	Sbv	Determination of physical quantities (weight per volume unit, natural water content, grain weight per volume unit), particle size analysis
S(SPT9)	34.00÷34.45	Bvlc-F	Visual description

Moreover, the HVSR test was carried out at the Si3 borehole. Figure 4.25 shows the H/V curve, highlighting the frequency at the peak of the curve.

As written in Section 4.4.1., the HVSR method (Nakamura, 1989) is based on the assumption that the ratio of the horizontal (H) and vertical (V) Fourier spectra of surface microtremors is an approximate transfer function for the horizontal motion of surface layers. In the H/V vs f diagram (being f the frequency), the peak indicates the amplification value of the horizontal components of the soil motion concerning the vertical component relative to the natural frequency of the surface layers. Through the HVSR test, the shear waves velocity, the thickness and the Poisson coefficient of each layer were estimated, as shown in Table 4.4.

Moreover, from the in-situ investigations carried out on the city of Catania in Monterosso street, located near to the Nesima-Misterbianco railway segment to evaluate the geotechnical characteristics for the volcanic soil within the "Catania Project" (Maugeri et al., 2006), the estimated Poisson coefficient through Down-Hole test was once more estimated equal to about 0.4, as shown in Figure 4.26.

To sum it up, the geotechnical parameters for the soil at the cross-section analysed (Si3) are shown in the following Table 4.5, being: γ the unit weight; φ' the angle of shear strength and c' the cohesion obtained by the direct shear test; E_0 the Young modulus at very small strains obtained by the shear waves velocity V_S values; Poisson coefficient ν.

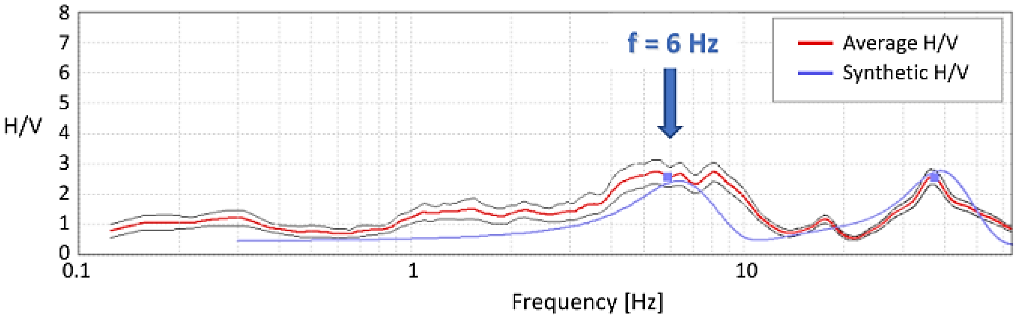

Figure 4.25: H/V vs f diagram at the borehole Si3

Table 4.4: estimated parameters through the HVSR Test at the borehole Si3

Layer depth [m]	Thickness [m]	V_S [m/s]	Poisson Coefficient
0.00÷5.00	5.00	235	0.4
5.00÷20.00	15.00	680	0.4
20.00÷30.00	10	345	0.4

Table 4.5: Geotechnical parameters for the geological formations found at the borehole Si3

Geological Formation	Depth [m]	γ [kN/m³]	φ' [°]	c' [kPa]	V_S [m/s]	E_0 [MPa]	ν
Rp	0÷5	18÷19	30÷35	0÷10	120÷180	70÷125	0.4
Lqua -L1669	5÷20	25÷27	50÷65	100÷1000	550÷800	2000÷5000	0.4
Bvlc-Bvlc(F)-L1669	20÷80	18÷21	38÷45	0÷20	200÷350	250÷750	0.4

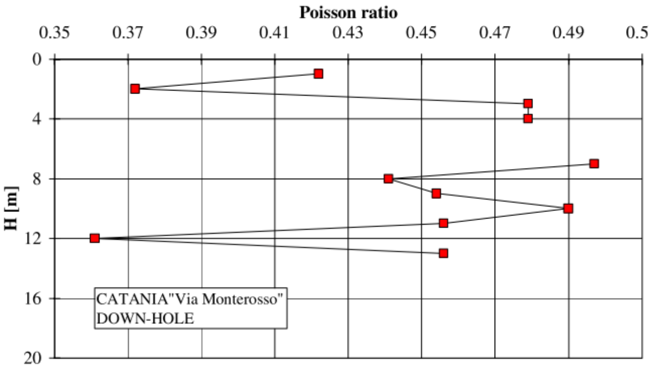

Figure 4.26: Poisson ratio for soil volcanic in the city of Catania in Monterosso street, located near to the Nesima-Misterbianco railway segment (Maugeri et al. 2006)

Unfortunately, the investigation survey concerned up to the depth of about 30 m. The shear waves velocity achieved at the depth greater than 20 m, was equal to 345 m/s (see Table 4.4). This value is very far from the value of 800 m/s, minimum value to consider the rock soil type A, according to the technical regulations NTC18. For this reason, a Gibson model for the soil was supposed, keeping constant the value of the Poisson coefficient, ν=0.4:

$$E(z) = E_0 + mz = E_0 + \frac{998.99 - 283.72}{15}(z) = E_0 + 47.685z \tag{4.8}$$

In which: E_0 is the value of the Young modulus at the surface, "m=47.685" is the gradient of increase with the depth and "z" is the generic depth. In this way, neglecting the rock soil layer between the depth of 5 and 20 m, the depth of the bedrock was estimated at the 80 m from the surface. At this depth, a value of the shear waves velocity equal to 800 m/s was achieved, according to the technical regulations.

Definitely, the elastic geotechnical parameters for the soil, according to the investigation surveys described above, are shown in the following Table 4.6.

Table 4.6: Elastic geotechnical parameters for the soil profile used for the FEM model

Geotechnical parameters at the Si3 borehole					
Depth [m]	γ [kN/m^3]	V_S [m/s]	ν	G_0 [MPa]	E_0 [MPa]
0÷5	18	235	0.4	101.33	283.72
5÷20	26	680	0.4	1225.52	3431.47
20÷30	20	418	0.4	356.78	998.99
30÷40	20	492	0.4	492.83	1379.94
40÷50	20	565	0.4	650.81	1822.28
50÷60	20	638	0.4	830.72	2326.02
60÷70	20	712	0.4	1032.55	2891.16
70÷80	20	800	0.4	1256.32	3517.70
Bedrock	22	1000			

4.6.2 Equivalent visco-elastic-linear analysis of a coupled tunnel – soil – aboveground structure

The cross section of the Nesima-Misterbianco segment located at the Si3 borehole (see Figure 4.6) was analysed. In the first time, for the seismic response of the coupled tunnel-soil-aboveground structure, an equivalent-visco-elastic linear model for the soil was used as discussed in this section; then, advanced visco-elasto-plastic analysis was performed.

4.6.2.1 G-γ-D curves

The equivalent soil stiffness and damping ratio, with the shear strain level achieved, were evaluated by a series of 1D equivalent linear site response analyses for representative ground motions, using *STRATA* Code. Typical curves G-γ-D, for Catania soil, were used. The most important results about the dynamic characterization for the soil of Catania are collected within of "The Project of Catania" (Pastore & Turello, 2000).

Resonant Column and Torsional shear tests (Lo Presti et al. 1993) were carried out on undisturbed samples retrieved with a 86 mm diameter Shelby sampler; In particular, the investigations that were carried out to determine the soil dynamic characteristics in the site of "Via Monterosso" in the city of Catania were used (Maugeri et al., 2006)

The site of "Via Monterosso, located near the Nesima-Miserbianco segment (see Figure 4.24, highlighted in red), mainly consists of an alternance of lava in blocks, coriaceous lava, grey-black pyroclastic sand and red volcanic rocks. The soil of the city of Catania consists of an alternance of stiff soil and softer soil materials, typically found in a volcanic zone like Catania, which lies at the foot of the Mt. Etna volcano and was affected by many eruptions in historical and prehistoric times. The most important lava flow dates back to 1669.

The laboratory tests, mentioned above, were performed to characterize the non-linear soil behaviour, which may occur during strong earthquakes, such as the 1693 and the 1818 scenario earthquakes. In the present research, the results of the Resonant Column test were used. The damping ratio was determined using the steady-state method. Moreover, the laboratory test results at small strain were compared with in situ seismic tests and in particular with a Down Hole test.

Figure 4.27 shows the results of RCTs normalised by dividing the shear modulus G(γ) for the initial value G_0 at very low strain. The experimental results were used to determine the empirical parameters of the eq. proposed by Yokota et al. (1981) to describe the shear modulus decay with shear strain level (Maugeri et al., 2006):

$$\frac{G(\gamma)}{G_0} = \frac{1}{1+\alpha\gamma(\%)^{\beta}} \tag{4.9}$$

in which:

G(γ) = strain dependent shear modulus.

γ = shear strain (in percent).

α , β = soil constants.

The values of α = 7.5 and β = 0.897 were obtained (Maugeri et al., 2006).

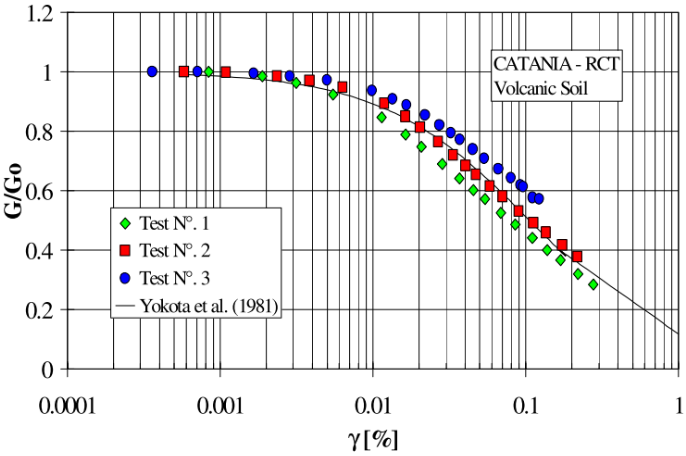

Figure 4.27: Soil profile and positions of the boreholes along the Nesima-Misterbianco segment at the design phase (Maugeri et al.,2006).

As suggested by Yokota et al. (1981), the variation of damping ratio with respect to the normalised shear modulus (Figure 4.28) can be described by the following equation:

$$D(\gamma)(\%) = \eta \cdot \exp\left[-\lambda \cdot \frac{G(\gamma)}{G_0}\right] \tag{4.10}$$

in which:

$D(\gamma)$ = strain dependent damping ratio;

γ = shear strain;

η , λ = soil constants.

The values of η= 90 and λ=4.5 were obtained.

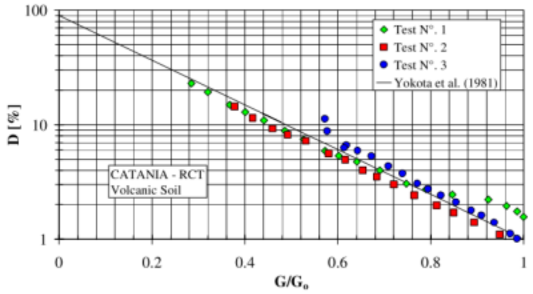

(b)

Figure 4.28: D- G/Go curves from RCTs for Monterosso volcanic soil (Maugeri et al.,2006)

4.6.2.2 1D Equivalent linear site response analyses to evaluate the equivalent shear modulus G and damping ratio D

The equivalent shear modulus G and the damping D, to be used in the following 2D FEM model of the fully coupled tunnel-soil-aboveground structure system, were evaluated by a series of 1D equivalent linear site response analyses for all the selected input motions. The analyses were performed through the *STRATA* code, using G-γ-D curves described in the previous section. Three accelerograms, shown in Figure 4.23, were used for the seismic response.

STRATA performs equivalent linear site response analysis in the frequency domain using time domain input motions or random vibration theory (RVT) methods. STRATA computes the dynamic site response of a one-dimensional soil column using linear wave propagation with strain dependent dynamic soil properties. This is commonly referred to as an equivalent linear analysis method, which was firstly used in the computer program SHAKE (Idriss and Sun, 1992;

Schnabel et al., 1972). Similar to SHAKE, STRATA only computes the response for vertically propagating, horizontally polarized shear waves propagated through a site with horizontal layers. For linear elastic, one-dimensional wave propagation, the soil is assumed to behave as a Kelvin-Voigt solid, in which the dynamic response is described using a purely elastic spring and a purely viscous dashpot (Kramer, 1996).

The behaviour of the soil is nonlinear, such that the dynamic properties of soil (shear modulus, G, and damping ratio, D) vary with shear strain, and thus with the intensity of shaking. In equivalent-linear site response analysis, the nonlinear response of the soil is approximated by modifying the linear elastic properties of the soil based on the induced strain level. Because the induced strains depend on the soil properties, the strain compatible shear modulus and damping ratio values are iteratively calculated based on the computed strain.

Equivalent-linear site response analysis requires that the strain dependent nonlinear properties (i.e. G and D) are defined. The initial (at small strain) shear modulus (G_0) is calculated by:

$$G_0 = \rho \cdot V_s^2 \tag{4.11}$$

where ϱ is the mass density and V_S is the measured shear wave velocity. Using the initial dynamic properties of the soil, equivalent-linear site response analysis involves the following steps:

- Initially, the shear modulus G_0 and the damping D_0 at low tangential strain are used for the first iteration;
- After the first iteration, for each layer, the effective shear strain (γ_{eff}) is estimated like a rate of the maximum strain within each layer. Usually, an effective shear strain estimated with the following expression is used:

$$\gamma_{eff} = 0.65\gamma_{max} \tag{4.12}$$

- By the use of the G-γ-D curves, new values of G and D are estimated within each layer;
- The new nonlinear properties (G and D) are compared to those of the previous iteration and an error is calculated. If the error for all layers is below a defined threshold the calculation stops. If not, new values of G and D are recalculated.

The G-γ-D curves used for the equivalent linear analysis are shown in Figure 4.29. For the second layer, consisting of rock soil (Lqua-L1669) due to the lava flow of 1669, a minor degradation was used. In particular, a maximum degradation of 10% is used for the rock soil.

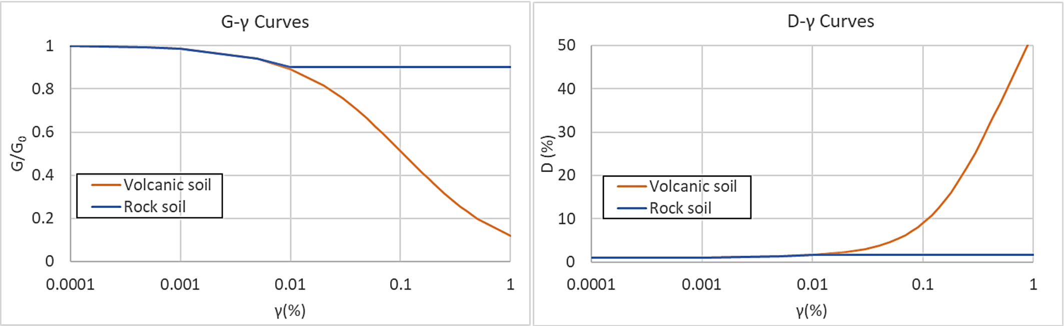

Figure 4.29: G-γ-D curves used for the equivalent linear analysis according to the eq. proposed by Yokota et al. (1981)

4.6.2.3 Equivalent properties of the soil used for the FEM analyses

Figure 4.30a shows the damping ratio obtained with the shear strain achieved by the 1D equivalent elastic linear analysis performed using *STRATA* code. The blue line represents the trend of the obtained damping ratio with the depth, while the orange line is the assumed average value. Figure 4.30b shows the peak ground acceleration profiles achieved by the 1D equivalent elastic linear analysis and by 1D elastic linear analysis using a single value of damping for the soil deposit. A single damping value was used for each analysis performed in which way that similar peak ground acceleration profiles were obtained to the ones achieved with the 1D equivalent analysis.

In Tables 4.7, 4.8 and 4.9 the dynamic properties (G and D) used in the numerical modelling of the fully coupled tunnel-soil-aboveground structure system are shown in bold.

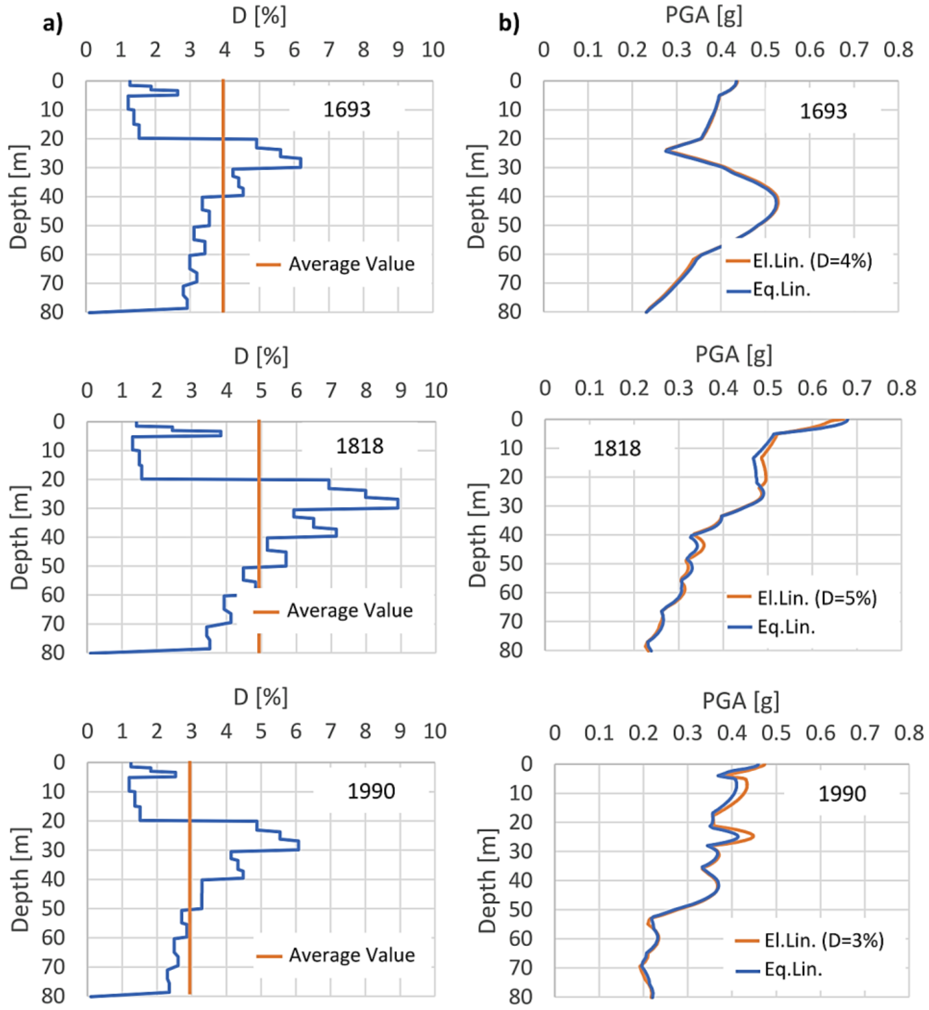

Figure 4.30: a) Damping ratio obtained with the shear strain achieved by the 1D equivalent elastic linear analysis for each input motion used; b) Peak Ground Acceleration achieved by the 1D equivalent elastic linear analysis and by 1D elastic linear analysis using a single value of damping

Table 4.7: Equivalent dynamic parameters for the soil profile used for the FEM model for the input 1693

1693 seismic event								
Depth [m]	γ [kN/m^3]	ν	G_0 [MPa]	E_0 [MPa]	Degradation [%]	**G [MPa]**	**E [MPa]**	**D [%]**
0÷5	18	0.4	101.33	283.72	0.79	**79.69**	**223.16**	**4**
5÷20	26	0.4	1225.52	3431.47	0.91	**1110.56**	**3109.58**	**4**
20÷30	20	0.4	356.78	998.99	0.60	**212.43**	**594.81**	**4**
30÷40	20	0.4	492.83	1379.94	0.66	**327.68**	**917.49**	**4**
40÷50	20	0.4	650.81	1822.28	0.72	**468.19**	**1310.93**	**4**
50÷60	20	0.4	830.72	2326.02	0.73	**604.63**	**1692.98**	**4**
60÷70	20	0.4	1032.55	2891.16	0.74	**767.33**	**2148.52**	**4**
70÷80	20	0.4	1256.32	3517.70	0.76	**958.26**	**2683.12**	**4**

Table 4.8: Equivalent dynamic parameters for the soil profile used for the FEM model for the input 1818

1818 seismic event								
Depth [m]	γ [kN/m^3]	ν	G_0 [MPa]	E_0 [MPa]	Degradation [%]	**G [MPa]**	**E [MPa]**	**D [%]**
0÷5	18	0.4	101.33	283.72	0.70	**71.14**	**199.20**	**5**
5÷20	26	0.4	1225.52	3431.47	0.90	**1103.35**	**3089.37**	**5**
20÷30	20	0.4	356.78	998.99	0.51	**183.42**	**513.59**	**5**
30÷40	20	0.4	492.83	1379.94	0.56	**277.56**	**777.18**	**5**
40÷50	20	0.4	650.81	1822.28	0.61	**399.45**	**1118.47**	**5**
50÷60	20	0.4	830.72	2326.02	0.65	**540.76**	**1514.12**	**5**
60÷70	20	0.4	1032.55	2891.16	0.69	**708.89**	**1984.91**	**5**
70÷80	20	0.4	1256.32	3517.70	0.72	**906.69**	**2538.75**	**5**

Table 4.9: Equivalent dynamic parameters for the soil profile used for the FEM model for the input 1990

1990 seismic event								
Depth [m]	γ [kN/m^3]	ν	G_0 [MPa]	E_0 [MPa]	Degradation [%]	**G [MPa]**	**E [MPa]**	**D [%]**
0÷5	18	0.4	101.33	283.72	0.80	**80.61**	**225.72**	**3**
5÷20	26	0.4	1225.52	3431.47	0.91	**1112.88**	**3116.09**	**3**
20÷30	20	0.4	356.78	998.99	0.60	**213.96**	**599.08**	**3**
30÷40	20	0.4	492.83	1379.94	0.67	**328.83**	**920.72**	**3**
40÷50	20	0.4	650.81	1822.28	0.74	**479.15**	**1341.61**	**3**
50÷60	20	0.4	830.72	2326.02	0.77	**637.47**	**1784.91**	**3**
60÷70	20	0.4	1032.55	2891.16	0.79	**815.09**	**2282.25**	**3**
70÷80	20	0.4	1256.32	3517.70	0.81	**1018.79**	**2852.63**	**3**

4.6.3 General settings of the FEM model

The FEM model of the selected cross-section was created according to the FEM validation Model described in the previous Chapter 3.

- ***Geometry and mesh elements of the FEM model***

The FEM model consists of a stratified soil 80 m deep (i.e. up to the conventional bedrock) and 300 m wide (≈ 4 times the depth of the soil) to reduce the boundary effects. The cross-section of the underground of Catania at the Si3 borehole (see Figure 4.6) including one real aboveground structure was modelled through *ADINA* code. Figure 4.31 shows the position of the building respect to the tunnel line.

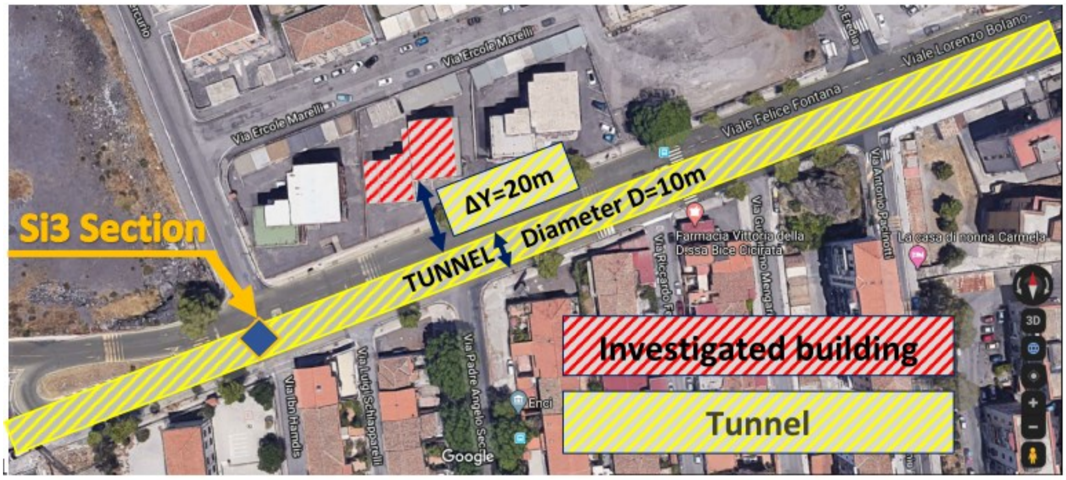

Figure 4.31: Position of the building and the tunnel modelled by means ADINA code

The soil was meshed by 4-node elements in plane strain conditions, while the tunnel lining was modelled by 2-node linear beam elements, as well as the aboveground structure. The cross section used for the tunnel was 0.32x1m. The cross section of the columns and the beams of the building were hypothesized equal to 0.3x0.6. Figure 4.32 shows in detail the analysed cross-section with E(z) profile and mesh size, the cross section used in the numerical model for the beams, the columns and the foundation of the building and of the tunnel.

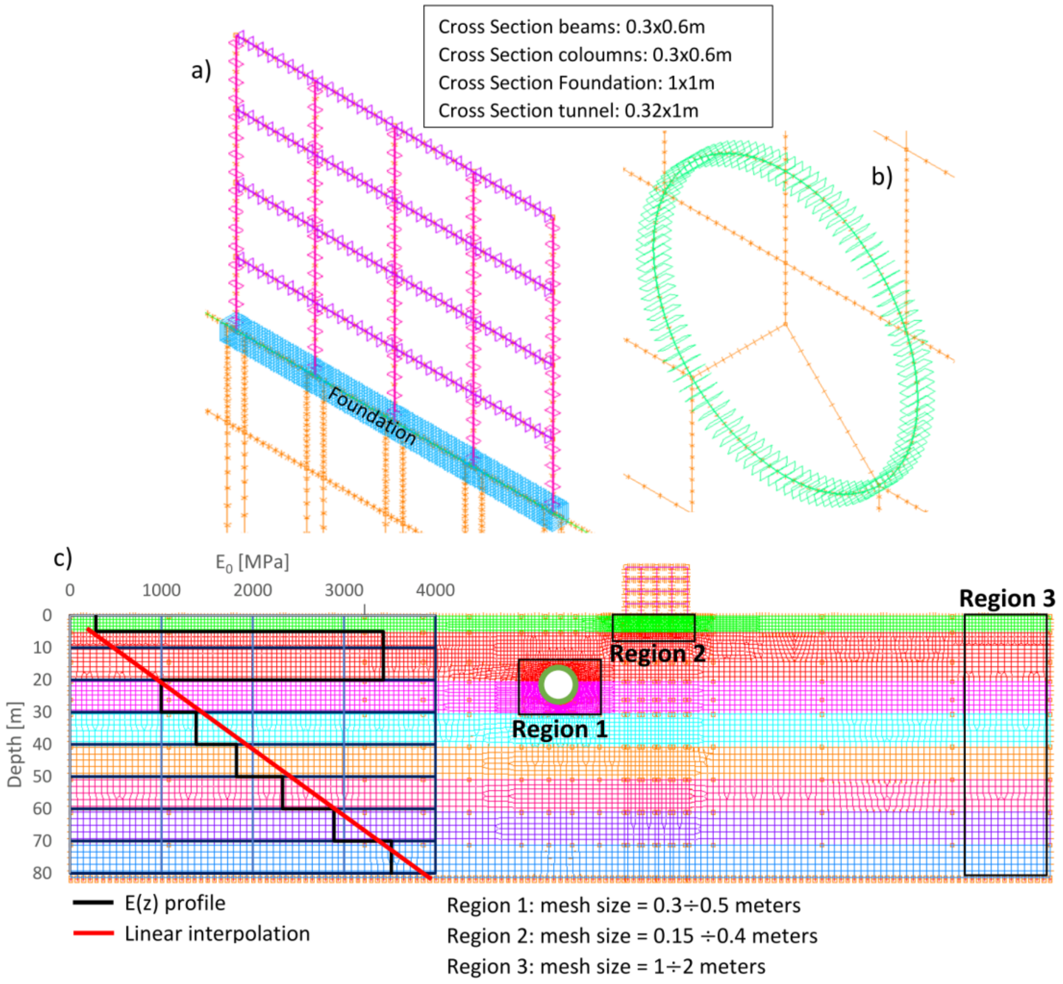

Figure 4.32: a) Plot of the element beams used for the above-ground structure; b) plot of the element beams used for the tunnel: c) analysed cross-section with E(z) profile and mesh size

The tunnel, with a diameter equal to 10 m was located at three different depths:

- ΔZ =17 m (original location of the tunnel);
- ΔZ =12 m;
- ΔZ =7 m;

The building was located at three different distances from the tunnel axis (Tunnel Alignment in Figure 4.35):

- ΔY =20 m (original location of the structure, see Figure 4.31);
- ΔY =5 m;
- aboveground structure located at the axis of the tunnel.

Moreover, a FEM model with the only tunnel and a FEM model with only the aboveground structure were carried out to evaluate the influence of each structure in the seismic response of the system.

The material viscosity was modelled according to the Rayleigh damping. For the calibration of the Rayleigh parameters, once more the double frequency approach was used (Hashash & Park, 2002), obtaining the results shown in Figure 4.33 for all the selected inputs.

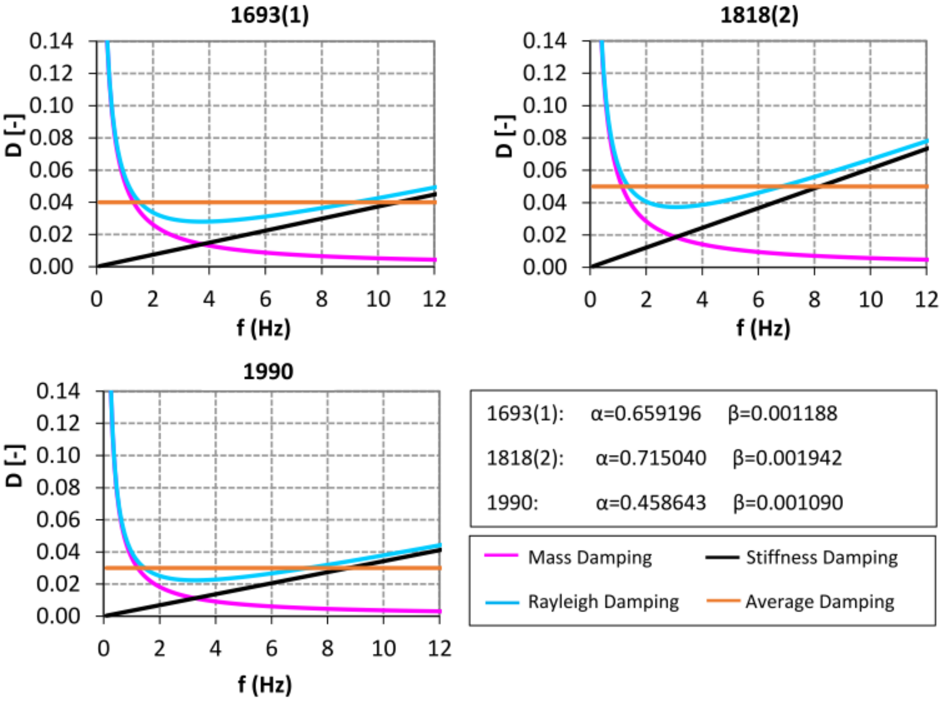

Figure 4.33: Rayleigh damping curves used for each input motion; Rayleigh coefficient used in the FEM modelling.

For the tunnel, a Young Modulus, E, equal to 36283 MPa and a Poisson coefficient, ν, equal to 0.2 were used. For the building, a Young Modulus, E, equal to 30000 MPa and a Poisson coefficient, ν, equal to 0.2 were used.Unit weight of 25 kN/m^3 was used for both the structure.

To ensure a working well simulation of the circular tunnel, a finer discretization was used around the tunnel. Therefore, the element shape was chosen to have a regular shape, with aspect ratio H/B not exceeding 3÷5, according to expression 3.11 of Chapter 3. To avoid numerical problems, the maximum element size of the soil was chosen according to expression 3.10 of Chapter 3.

- ***Boundary and loading conditions***

According to the validation process described in the previous chapter, for an initial geostatic analysis, the bottom of the numerical models was fixed in both horizontal and vertical directions, and the vertical boundaries were fixed in horizontal direction allowing the vertical displacements. In this first phase, the excavation of the tunnel was simulated, providing initially the absence of the tunnel and establishing the geostatic conditions achieved after the digging.

For the subsequent dynamic analysis, the nodes of the soil vertical boundaries were linked by "constraint equations" that imposed the same displacements, both horizontally, both vertically, at the same depths (Abate & Massimino, 2016), imitating in this way a desirable 'shear beam' response, typical of 1D seismic response analyses; the nodes at the base of the mesh were constrained only in the vertical direction. Moreover, at the base of the numerical model, dashpots were implemented, in the horizontal direction, to simulate the elastic bedrock according to Lysmer and Kuhlemeyer (1969). The dashpot coefficients, c, were defined as the product of the mass density, ρ, shear wave velocity, V_S, of the bedrock and the 'effective' area, A, of each dashpot, to maintain proportional results for any horizontal element size. In this case, it was ϱ = 2200 kg/m^3 and V_S = 1000 m/s. The input motions were applied on the models through the above dashpots, located to the bottom of the model, as described in the previous chapter.

Moreover, a "mass proportional load" was applied to the whole model, that it is the weight of the FEM model. A distributed load on the beams was used to represent the load of the slab on the beam. In particular, a distributed load of 20 kN/m was applied on each beam.

- ***Contact conditions***

The soil-structure interface was modelled using a finite sliding contact model. The model constrains the two media when attached, while it allows for separation. The tangential behaviour of the interface was modelled introducing the classical Coulomb friction model. The friction coefficient μ was evaluated equal to 0.4, computed as tg(2/3φ'). According to table 4.1, the angle of shear strength φ' for the Anthropic layer (Rp) was estimated equal to 30°÷35°. The contact element between the soil and the aboveground structure was important to allow their possible detachment and to simulate a better seismic response of the system. Without the contact element, a probable uplift of the foundation during a seismic event would cause the lifting of the soil which would tend to follow the movement of the foundation. This lifting of the soil is not possible because the soil has not tensile strength. To allow a behaviour not correct of the soil could lead to the results non-compliant to the real case.

Regarding the contact surface between the soil and the tunnel, the No-Slip condition, the Full-Slip condition and a Partial-Slip condition were compared.

In order to simulate the No-Slip condition between the soil and the tunnel, a nodal coincidence between the beam element of the tunnel and the 2D solid element of the soil was expected. In this case, the finite sliding contact model was not modelled, therefore not allowing detachment or sliding between the tunnel and the soil. In order to simulate the Full-Slip condition between the soil and the tunnel, the finite sliding contact was modelled using a friction coefficient μ equal to 0 allowing the perfect sliding between the beam element of the tunnel and the 2D solid element of the soil. Finally, an intermediate condition of the contact condition between the tunnel and the soil was modelled using a friction coefficient μ equal to 0.4.

As it will see in the following sections, the results in terms of bending moment on the tunnel line were similar in the different soil-tunnel slip conditions. Small differences were evaluated in terms of dynamic axial force.

In particular, the dynamic axial forces achieved by the "No-Slip condition" were higher than those by the "Full-Slip condition", ensuring greater safety in the evaluation of the stress on the tunnel line ignoring soil-tunnel slipping. Moreover, a No-Slip condition requires a lower calculation time. For this reason, a "No-Slip condition" was chosen for the contact surface between the soil and the tunnel in the majority of the performed numerical analyses.

Contact in ADINA is modelled using contact groups, contact surfaces, contact segments and contact pairs. Contact groups (and their contact surfaces) in ADINA can be either 2-D or 3-D. The contact surfaces should be defined as regions that are initially in contact or that are anticipated to come into contact during the solution. A contact pair consists of the two contact surfaces that may come into contact during the solution. One of the contact surfaces in the pair is selected to be the contactor surface and the other contact surface to be the target surface. Within a contact pair, the nodes of the contactor surface are prevented from penetrating the segments of the target surface, and not vice versa. Figure 4.34 shows the effect of contactor and target selection on the different contact configurations. Therefore, the foundation and the soil were modelled as Target surface and contactor surface, respectively.

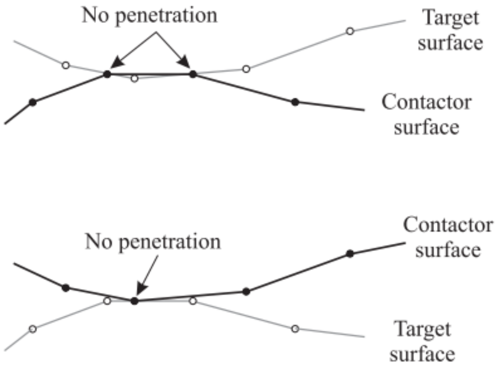

Figure 4.34: Contactor and target selection (ADINA, 2008)

The normal contact conditions can ideally be expressed as:

$$g \geq 0; \qquad \lambda \geq 0; \qquad g \cdot \lambda = 0 \tag{4.13}$$

where g is a gap, and λ is the normal contact force.

For friction, a nondimensional friction variable τ can be defined as:

$$\tau = \frac{F_T}{\mu\lambda} \tag{4.14}$$

where F_T is the tangential force and λ is the normal contact force.

Figure 4.35 shows the FEM model created through Adina code with the geometry, loading and boundary conditions.

The results were achieved at three alignments like shown in Figure 4.35: tunnel alignment at the axis of the tunnel; structure alignment at the axis of the structure; free field alignment at a distance far enough from the building.

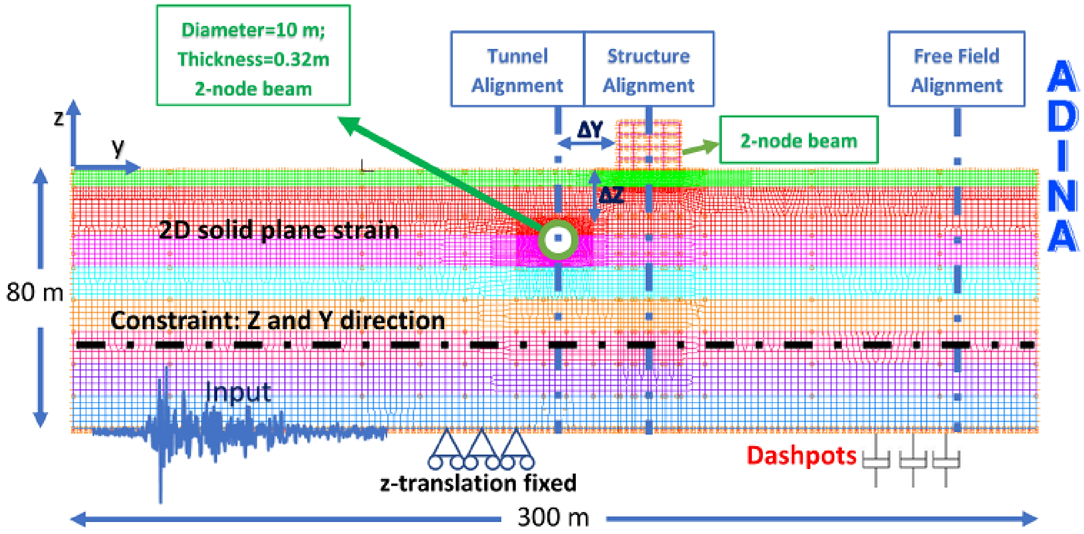

Figure 4.35: FEM Model used for the cross section at Si3 borehole

4.7 Parametric analyses

4.7.1 Bending moments and axial forces in the tunnel for a heterogeneous soil: different contact conditions between tunnel and soil

Representative results of the numerical analysis of the soil-tunnel system are presented in this section, highlighting the importance of soil heterogeneity and soil-structure interface conditions on the tunnel response.

Usually, dynamic analyses of a coupled soil-tunnel system with a homogeneous soil at the depth of the tunnel were performed (Argyroudis et al., 2017). The present work deals with numerous parametric analyses carried out using different values of the impedance ratio, I, according to the following expression:

$$I = \frac{\rho_1 \cdot V_{S1}}{\rho_2 \cdot V_{S2}} \tag{4.15}$$

where ρ_1 and V_{S1} stand for the density and shear waves velocity for the soil interacting with the upper part of the tunnel, while ρ_2 and V_{S2} stand for the density and shear waves velocity for the soil interacting with the bottom part of the tunnel, shown in Figure 4.36.

To analyse the influence of the soil-tunnel interface conditions and the impedance ratio on the dynamic response of the tunnel, a 2D soil-tunnel system was modelled. The loading and boundary conditions of the FEM model are shown in Figure 4.36a.

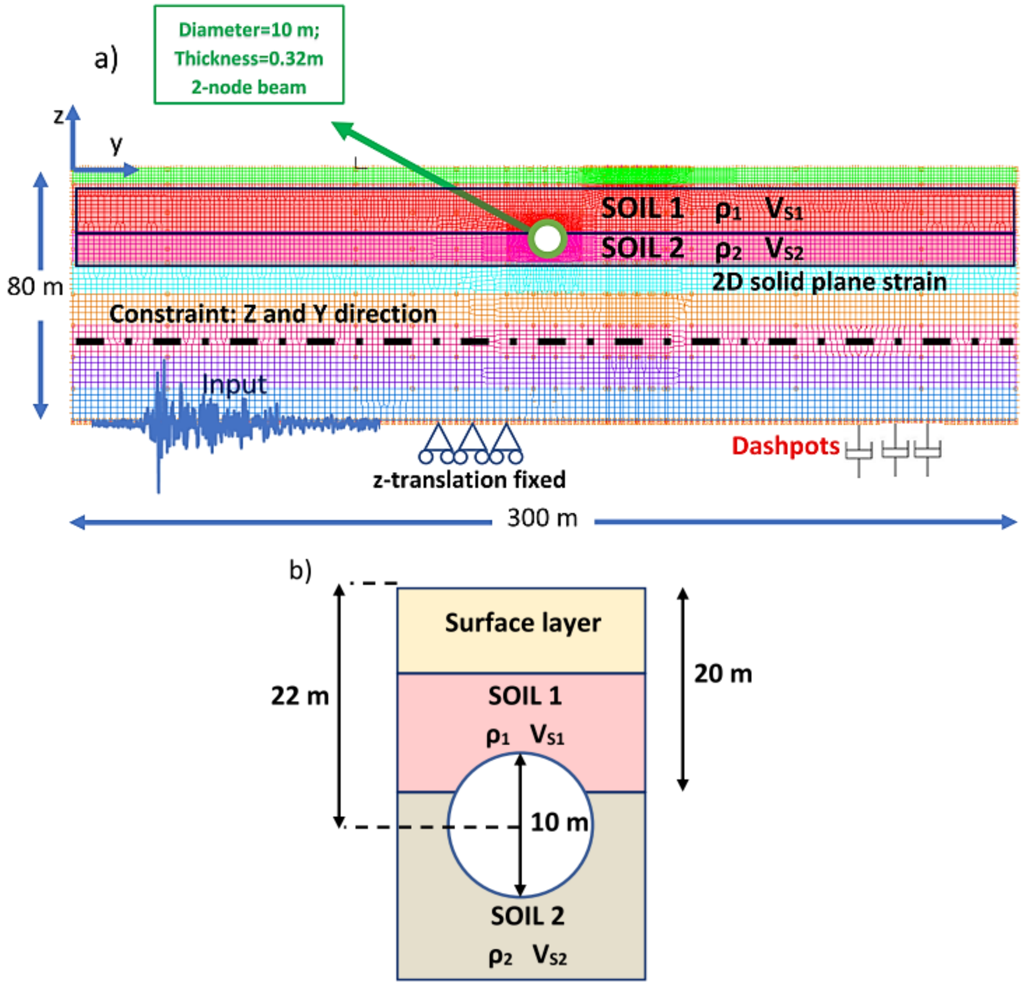

Figure 4.36: a) FEM model to investigate the influence of soil heterogeneity and soil-tunnel interface conditions; b) Zoon of the stratified soil at the depth of the tunnel

In particular, the centre of the tunnel, having a diameter of 10 m, was located at the depth of 22 m from the surface. The depth at which there was a strong difference in soil stiffness was at the 20 m (Figure 4.36b). The equivalent geotechnical parameters showed in Table 4.7 for the 1693 input motion were used. In order to perform parametric analyses, geotechnical parameters of the second and third layer were changed to obtain different values of the impedance ratio, I. Initially, four values of I were used, shown in Table 4.10, performing four different models 1-4. Model 3, characterized by an impedance ratio I = 2.6, represents the real condition at the borehole Si3 (see Figure 4.32c); Model 1, characterized by an impedance ratio I = 1, represents a homogeneous soil at the depth of the tunnel. Moreover, per each impedance ratio, three different interface conditions were used: a) Full-Slip condition; b) No-Slip condition; c) sliding contact with a friction coefficient μ equal to 0.4.

A fixed value of Poisson coefficient, $\nu = 0.4$, and a value of damping ratio D = 4% were used according to the results of the 1D equivalent visco-elastic analysis previously described (see Table 4.7, Figure 4.30).

In a second phase of the analysis, totally ten different impedance ratios were used for the two layers located at the depth of the tunnel, and just the No-Slip tunnel-soil interface condition was modelled, for reasons which will be explained in the following.

Table 4.10: Soil parameters for the FEM model related to the fixed impedance ratios I

			Model 1 I=1			**Model 2 I=2**		
Depth [m]	ν	D [%]	ϱ [kg/m^3]	V_S [m/s]	E [MPa]	ϱ [kg/m^3]	V_S [m/s]	E [MPa]
5÷20	0.4	4	2038	342	669.33	2650	496	1831.14
20÷30	0.4	4	2038	342	669.33	2038	323	594.82
			Model 3 I=2.6			**Model 4 I=3.5**		
Depth [m]	ν	D [%]	ϱ [kg/m^3]	ϱ [kg/m^3]	ϱ [kg/m^3]	ϱ [kg/m^3]	V_S [m/s]	E [MPa]
5÷20	0.4	4	2650	2650	2650	2650	647	1790.40
20÷30	0.4	4	2038	2038	2038	2038	280	448.88

Figure 4.37 shows the numerical dynamic bending moment ΔM computed along the tunnel for all the tunnel-soil interface conditions and the four impedance ratios previously explained. These numerical dynamic bending moments were computed as the maximum values of the semi-amplitude of the cycles in the bending moment time histories, according to the following expression:

$$\Delta M = \frac{M_{Max} - M_{Min}}{2} \tag{4.16}$$

Two different colours highlight the two different layers (1 and 2) at the depth of the tunnel. In particular, the pink colour refers to the soil 1 interacting with the upper part of the tunnel, while the yellow colour refers to the soil 2 interacting with the bottom part of the tunnel. The strong influence of the soil heterogeneity of the soil at the depth of the tunnel can be observed. For higher values of the impedance ratio (i.e. from Model 1 to Model 4), higher values of bending moments were evaluated, achieving a bad bending moment distribution along the tunnel. As a matter of fact, very small bending moments were achieved at the depth of soil 1 (stiff soil), while higher values were obtained at the depth of soil 2 (soft soil), achieving the peak of bending moment at the depth of the stiffness discontinuity (20 m). The achieved peaks of bending moment increased with the impedance ratio. As expected, the better distribution of the bending moment was obtained for Model 1, i.e. I=1 (homogeneous soil). For this reason, it is advisable to build the underground structures far enough from a possible stiffness discontinuity, in which a concentration of stress and strain could occur, recording high values of internal forces along the tunnel.

As for the three different tunnel-soil interface conditions, represented by three different coloured lines, very similar results to each other were achieved.

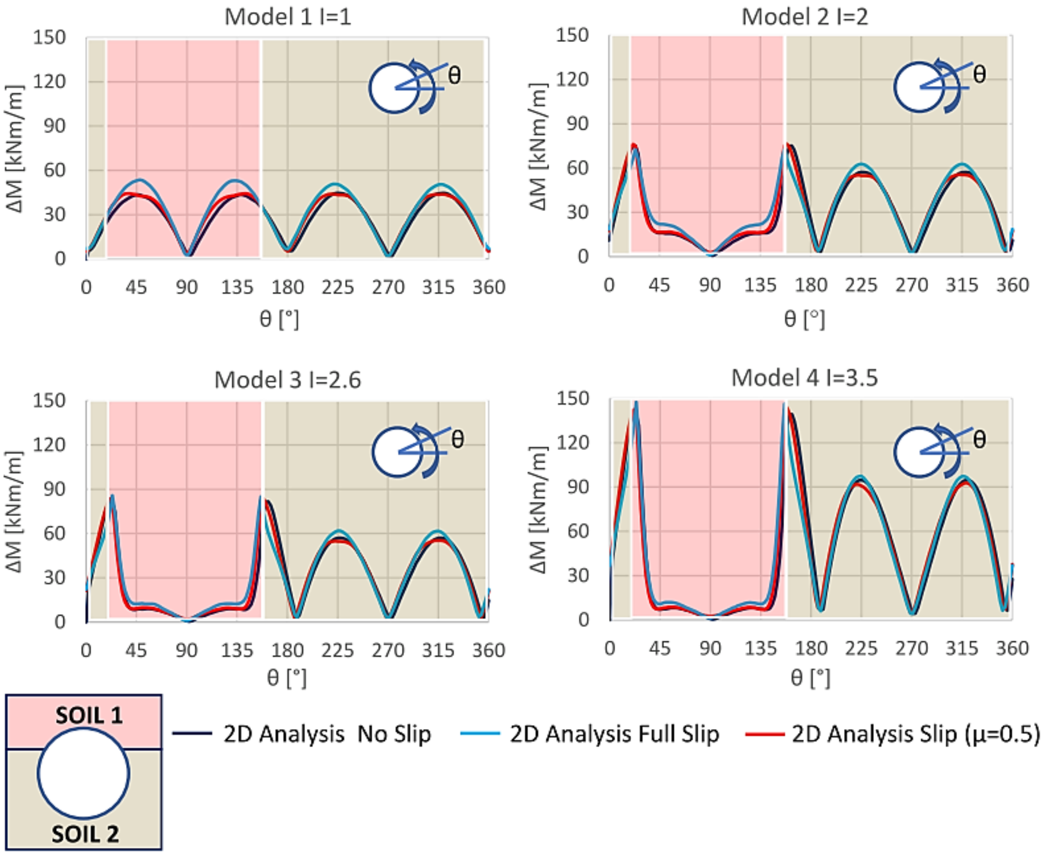

Figure 4.37: Numerical dynamic bending moments for all the four analysed models

Similarly, Figure 4.35 shows the dynamic axial forces N computed along the tunnel, for all the tunnel-soil interface conditions and the four impedance ratios previously explained; the same two different colours were used for highlighting the two different layers (1 and 2) at the depth of the tunnel. Unlike the bending moments, the obtained dynamic axial forces did not vary much along the tunnel, achieving an average value of dynamic axial forces around 800-1000 kN/m. Regarding the three different soil-tunnel interfaces (represented by the same three different coloured lines of Figure 4.37) by the “No-Slip” condition, higher values of dynamic axial forces were achieved due to the higher concentration of stress along the perimeter of the tunnel, generated by the lack of relative sliding between the soil and the tunnel. For the sliding contact having a tangential behaviour of the interface according to the classical Coulomb friction model, lower values of around 20% were achieved. Instead, for Full-Slip condition, constant values (about 200kN/m) along the perimeter of the tunnel were achieved.

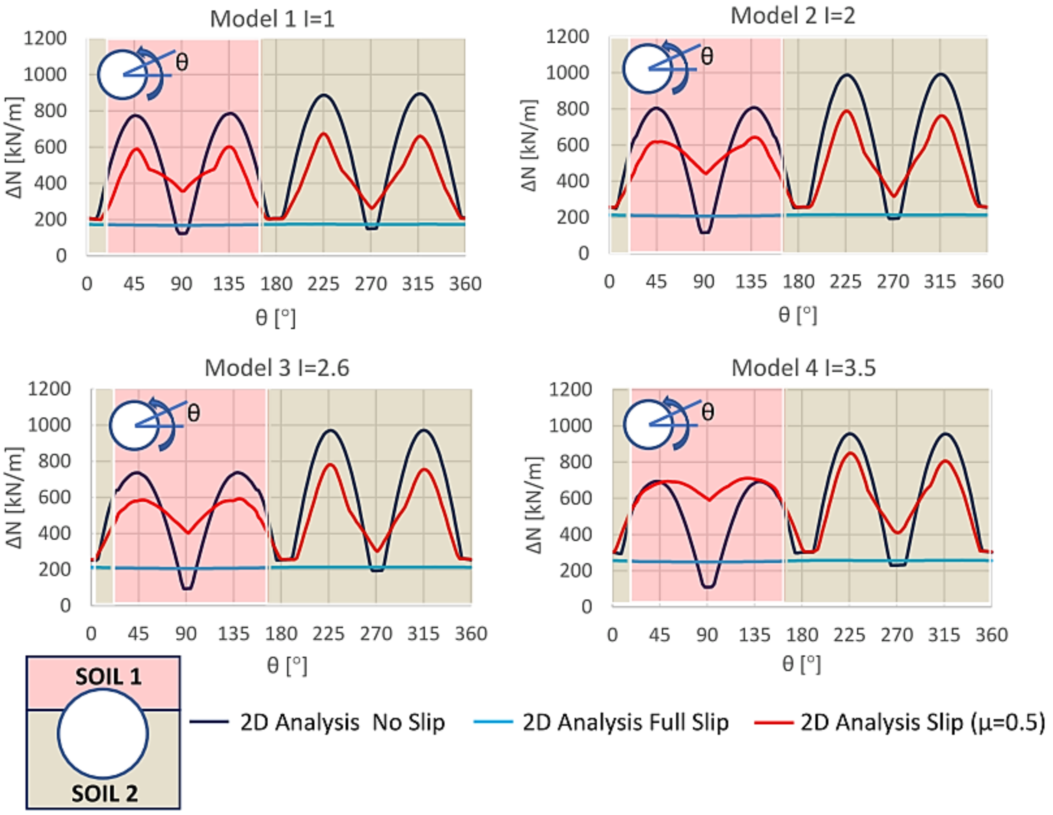

Figure 4.38: Numerical dynamic axial forces for all the four analysed models.

So, from the achieved numerical results, the following conclusions can be deduced:

- building underground structures that cross soil discontinuities is not advisable; this could cause strong concentrations of stress and strain at the discontinuity depth, generating peaks of bending moments and a bad bending moment distribution along the tunnel;

- to guarantees greater safety, the No-Slip condition between the soil and the tunnel is advisable to use.

After a first numerical evaluation of the dynamic response of the tunnel, the results were compared with the analytical solutions developed for both No-Slip and full-Slip conditions (Wang, 1993; Penzien, 2000), as described at Chapter 1. For the analytical solutions, it is necessary to estimate the average of the maximum shear strain values of the soil along the tunnel. It was evaluated using the results of the 2D numerical analyses of the soil-tunnel system. In particular, the shear strain was computed far from the tunnel at "free-field" conditions, whose shear strain values are very similar to the values achieved with a 1D seismic response analysis.

Figure 4.39 shows the comparisons between the analytical and the numerical dynamic bending moments for the four different models analysed and for all the tunnel-soil interface conditions. The numerical results achieved by Model 1 (I = 1) were very similar to the analytical solutions for both interface conditions ("No-Slip" and "Full-Slip" conditions). For impedance ratios I > 1 a disagreement between the analytical and numerical results was obtained; in particular, the analytical solution underestimated the tunnel forces for heterogeneous soil.

Similarly, Figure 4.40 shows the comparison between the numerical and the analytical dynamic axial forces. A great disagreement was obtained. As well as for the bending moments, better results were achieved for Model 1, in which numerical and analytical (Wang, 1993) results were very similar to each other, revealing a good prediction for the No-Slip interface condition. Very low values were achieved by the Penzien solutions (Penzien, 2000), as found by other studies (Argyroudis et al., 2017).

The increasing of the impedance ratios I leads to a greater disagreement between the analytical and numerical results, and the strongest disagreement was achieved for the Full-Slip interface condition, for which very small analytical values were found. The complete sliding did not allow the increase of the stress on the interface, recording very low numerical values of dynamic axial forces. Moreover, the numerical results remain constant along the perimeter of the tunnel, against a "real" evidence.

So, from the comparisons it was deduced that the No-Slip condition is advisable to evaluate the dynamic response along the tunnel.

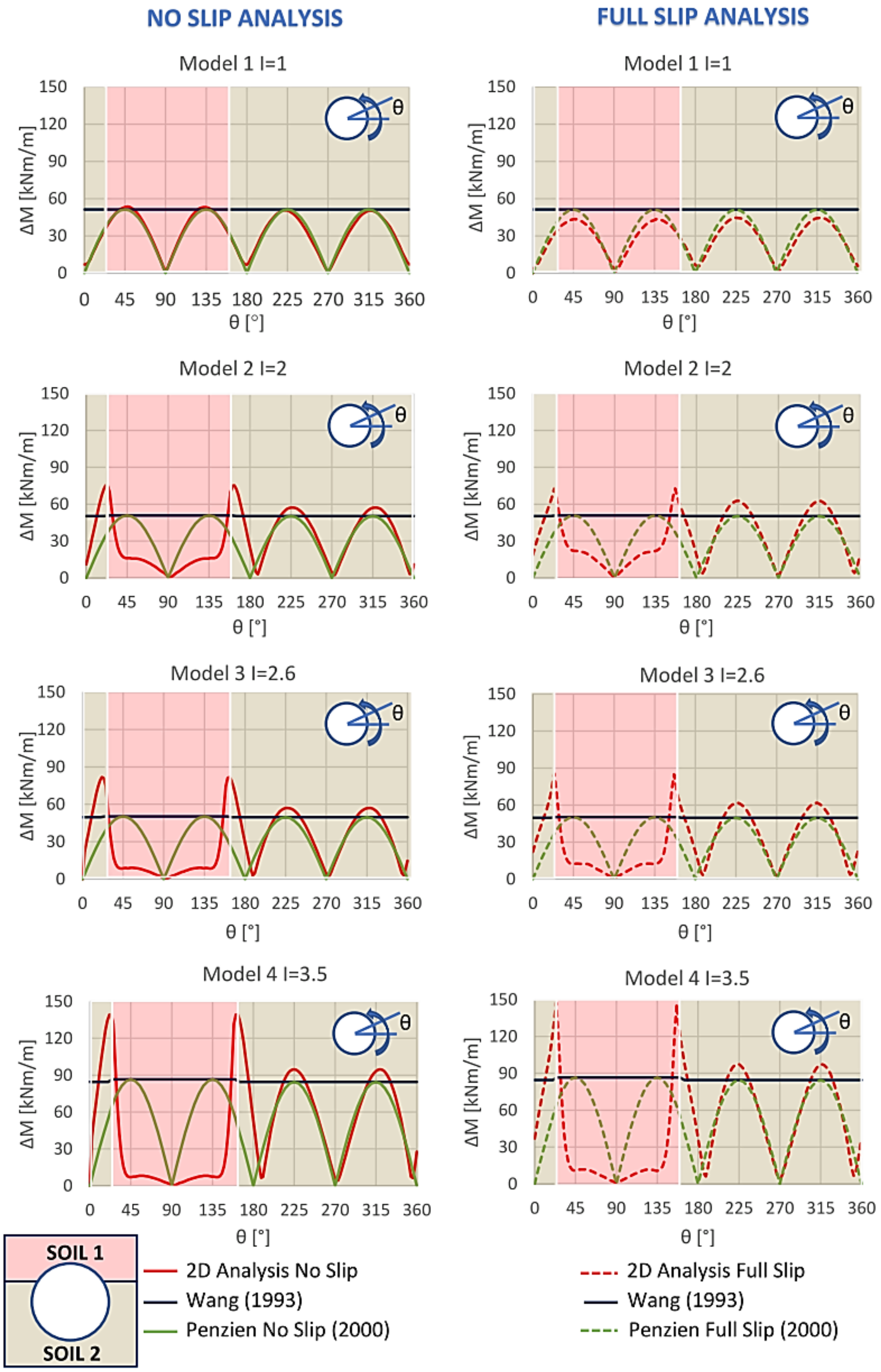

Figure 4.39: Comparison between analytical and numerical results in terms of dynamic bending moments.

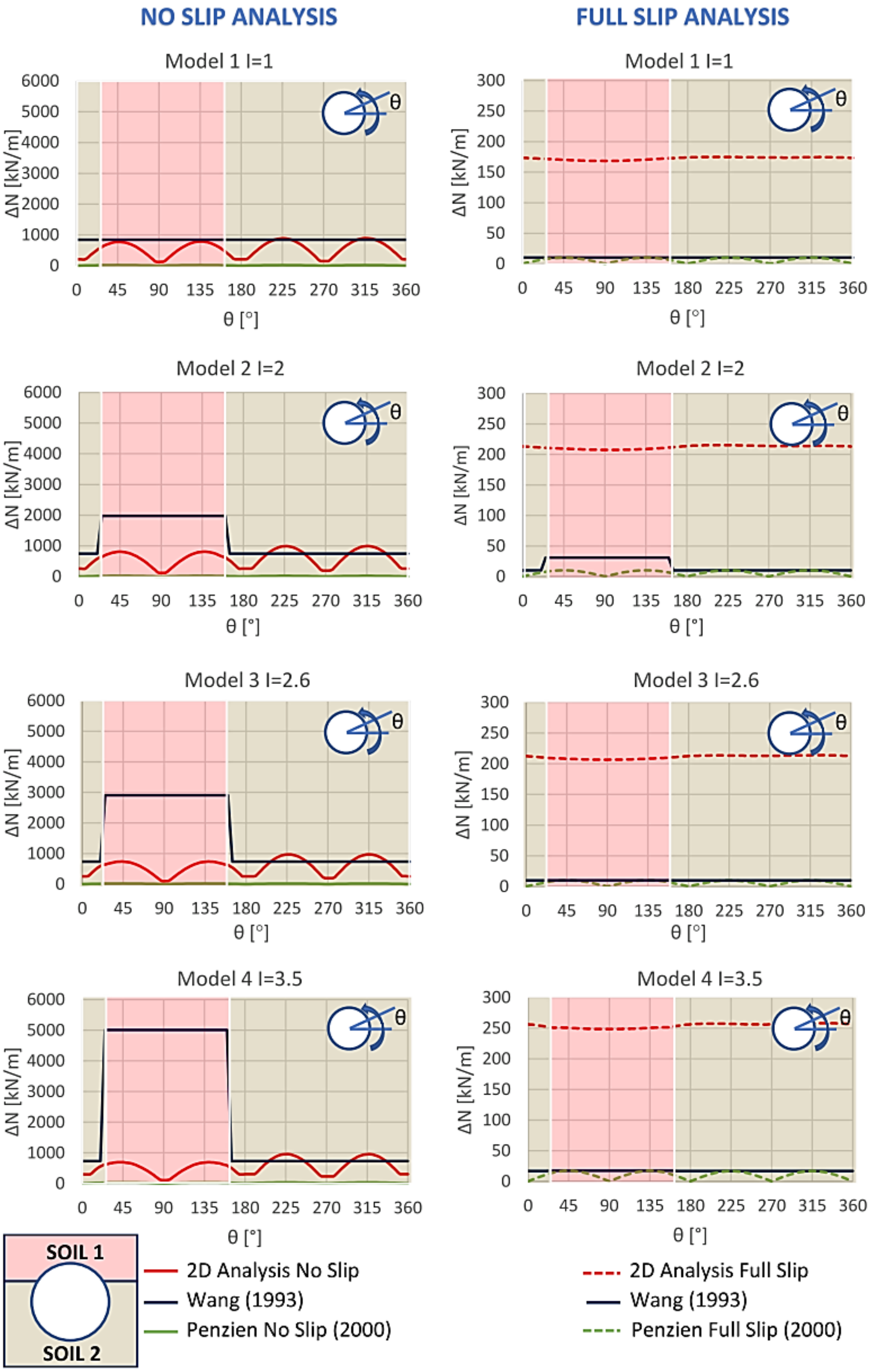

Figure 4.40: Comparison between analytical and numerical results in terms of dynamic axial forces

It was stressed that for the analytical solutions the average of the maximum soil shear strains occurred at the tunnel depth was used. Obviously, the strong stiffness discontinuity caused a strong difference in shear strains for the two involved soils (soil 1 and soil 2 in Figure 4.36a and 4.36b). So, for I>1, a strong difference of the dynamic axial forces along the tunnel was achieved, obtaining the highest values for the tunnel part interacting with the soil 1(stiffer soil).

For this reason, in a second step of the analysis, the average values of the maximum shear strains per each layer (Soil 1 and Soil 2) interacting with the tunnel were computed.

Figure 4.41a shows the maximum shear strain profile with the depth for Model 3 with I=2.6 (real profile); the two layers interacting with the tunnel were highlighted by the pink colour for Soil 1 and by the yellow colour for Soil 2. Figure 4.41.b is a zoomed figure at the tunnel depth (17-27m). The dashed blue line shows the average of the maximum strains for both soils, equal to 0.117%. This value was used for the computation of the analytical results shown in Figure 4.40. The dashed green line shows the average values of the maximum strains for each single layer: 0.054% for Soil 1 and 0.165% for Soil 2, respectively. By these values, the results shown in Figure 4.42 were achieved.

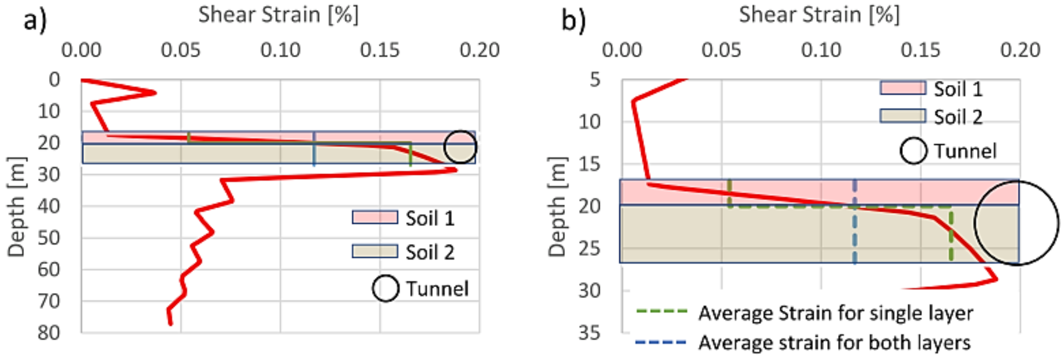

Figure 4.41: Maximum soil shear strain profile for Model 3 (I=2.6, real condition)

From Figure 4.42 it is possible to observe a better agreement between the numerical and analytical results.

Consequently, for strong soil stiffness discontinuity at the tunnel depth, different values of mean shear strain, one per each layer, are advisable to use to evaluate the internal forces along the tunnel. However, the shear strain values to be conveniently used in the analytical solutions will be deeper investigated in the following.

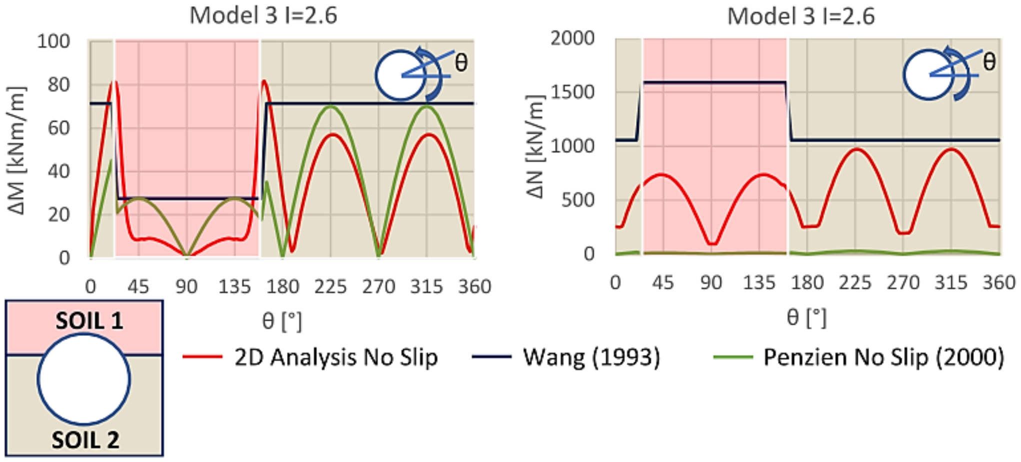

Figure 4.42: Comparison between analytical and numerical results in terms of dynamic axial force and bending moment, considering the green profile of the soil shear strain reported in Figure 4.41 for the analytical approaches (Model 3 I=2.6).

Considering the results obtained so far, in order to study the dynamic internal forces along the tunnel line with the impedance ratio I, other ten models were analysed, characterized by ten different impedance ratios varying between 0.285 and 4, as shown in Table 4.11

The analytical results were achieved using the average value of the shear strains for each layer, as shown in Figure 4.41 and 4.42. Just the No-Slip soil-tunnel interface condition was adopted, for the reasons above discussed, briefly here summarized: the dynamic axial forces achieved by the No-Slip condition were higher than those achieved by the Full-Slip condition, ensuring greater safety in the evaluation of the stress on the tunnel line ignoring soil-tunnel slipping. Moreover, a No-Slip condition requires a lower calculation time.

Table 4.11: Soil parameters of the two layers at the depth of the tunnel

			Model 1 I=1			**Model 2 I=2**		
Depth [m]	ν	D [%]	ϱ $[kg/m^3]$	V_S [m/s]	E [MPa]	ϱ $[kg/m^3]$	V_S [m/s]	E [MPa]
5÷20	0.4	4	2038	342	669.33	2650	496	1831.14
20÷30	0.4	4	2038	342	669.33	2038	323	594.82
			Model 3 I=2.6			**Model 4 I=3.5**		
Depth [m]	ν	D [%]	ϱ $[kg/m^3]$	V_S [m/s]	E [MPa]	ϱ $[kg/m^3]$	V_S [m/s]	E [MPa]
5÷20	0.4	4	2650	647	3109.58	2650	647	3109.58
20÷30	0.4	4	2038	323	594.82	2038	240	329.82
			Model 5 I=1.5			**Model 6 I=1.5**		
Depth [m]	ν	D [%]	ϱ $[kg/m^3]$	V_S [m/s]	E [MPa]	ϱ $[kg/m^3]$	V_S [m/s]	E [MPa]
5÷20	0.4	4	2650	647	3109.58	2650	647	3109.58
20÷30	0.4	4	2038	560	1790.40	2650	431	1381.55
			Model 7 I=3			**Model 8 I=0.5**		
Depth [m]	ν	D [%]	ϱ $[kg/m^3]$	V_S [m/s]	E [MPa]	ϱ $[kg/m^3]$	V_S [m/s]	E [MPa]
5÷20	0.4	4	2650	647	3109.58	2038	323	594.82
20÷30	0.4	4	2038	280	448.88	2650	496	1831.14
			Model 9 I=0.285			**Model 10 I=4**		
Depth [m]	ν	D [%]	ϱ $[kg/m^3]$	V_S [m/s]	E [MPa]	ϱ $[kg/m^3]$	V_S [m/s]	E [MPa]
5÷20	0.4	4	2038	240	329.82	2650	647	3109.58
20÷30	0.4	4	2650	647	3109.58	2038	210	252.54

Figure 4.43 shows the comparison between analytical (Wang,1993 and Penzien,2000) and numerical results for all the ten performed models (represented by the ten different indicators). Analytical results were computed using: 1) the average shear strain evaluated for single layer (Figures 4.43a and 4.43b); 2) the average shear strain computed for both layers crossed by the tunnel (Figure 4.43c and 4.43d). In particular, Figures 4.43a and 4.43c show the results in terms of dynamic bending moments ΔM and Figures 4.43b and 4.43d show the results in terms of dynamic axial forces ΔN. The analytical results were

represented on the horizontal axis, while the numerical results were displayed on the vertical axis. The black line reveals the perfect agreement between the analytical and numerical results.

Regarding the dynamic bending moments, the numerical results were very similar to the analytical ones, for both the two criteria adopted in the choice of the average shear strains (1. only one value for the two layers crossed by the tunnel; 2. two values, one per each layer crossed by the tunnel). However, the analytical approaches underestimate the dynamic bending moments compared to the numerical results, especially if the average value of the shear strains for both layers was used (Figure 4.43c). The Penzien (2000) approach provided slightly lower values than Wang (1993) approach. This result has been also recently obtained by Kontoe et al. (2014).

As for the dynamic axial forces, the Penzien (2000) approach underestimated significantly the dynamic axial force compared with the Wang (1993) approach. Similar observations may be found in the literature (Hashash et al., 2005; Kontoe et al., 2014). Unfortunately, a no-good agreement between analytical and numerical results is observed.

Similarly, Figure 4.44 reports the ΔM vs I and the ΔN vs I trends obtained for all the ten models, adopting the same previous different approaches for the computation of the soil shear strains. Regarding the dynamic bending moments, it is possible to observe that they strongly depend on I and the minimum value of ΔM is reached for I = 1 (homogeneous soil); while the further I is away from 1, the higher the value of ΔM. Numerical and experimental results were essentially in good agreement, even if the numerical values were slightly higher than the analytical ones. The best agreement between numerical and experimental results is obtained for I = 1, by the increase of I the gap between numerical and analytical results increases, because analytical approaches deal only with homogeneous soil. As for the dynamic axial forces, it is possible to observe that ΔN does not vary with I according to the numerical modelling and Penzien (2000) approach; instead it strongly increases with I according to Wang, 1993 approach.

It is also important to stress that the numerical results were achieved by a FEM modelling characterised by a seismic input, differently from the analytical approaches. For these reasons, differences observed between the numerical and the analytical results are unavoidable.

However, the showed gap between the numerical and analytical results revealed the need to increase numerical analyses to estimate lining forces more consistent with the real behaviour of the soil-tunnel system.

Average Shear Strain for single layer

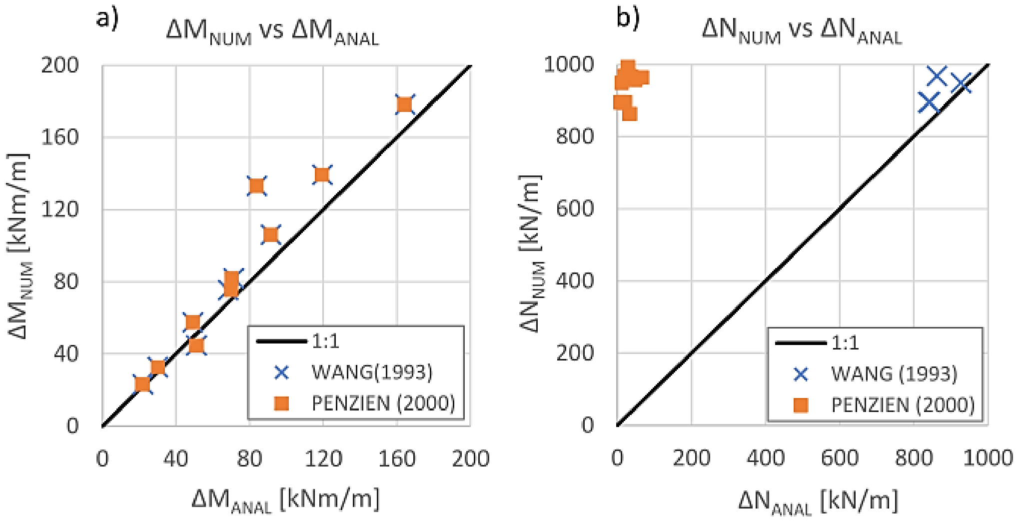

Average Shear Strain for both layers

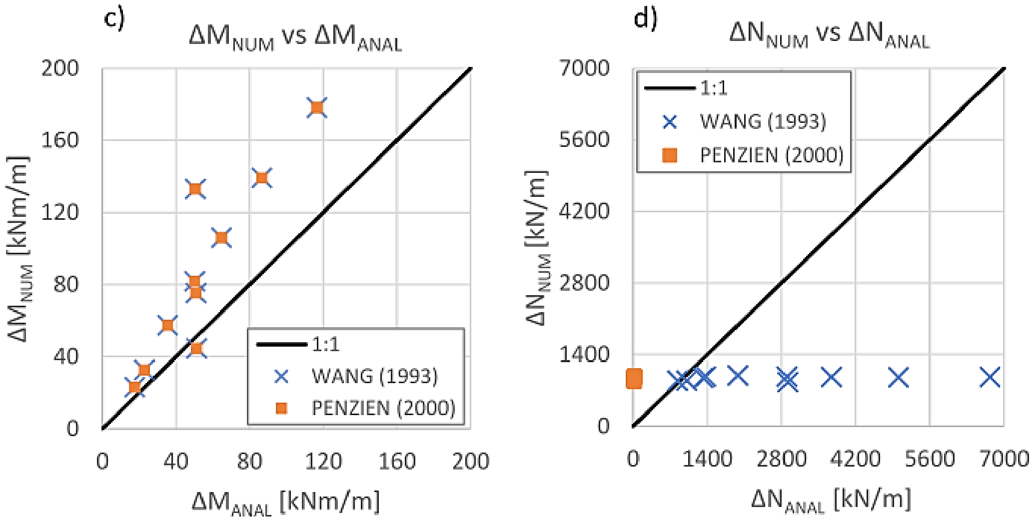

Figure 4.43: Comparison between numerical and analytical results for all the ten performed models

Average Shear Strain for single layer

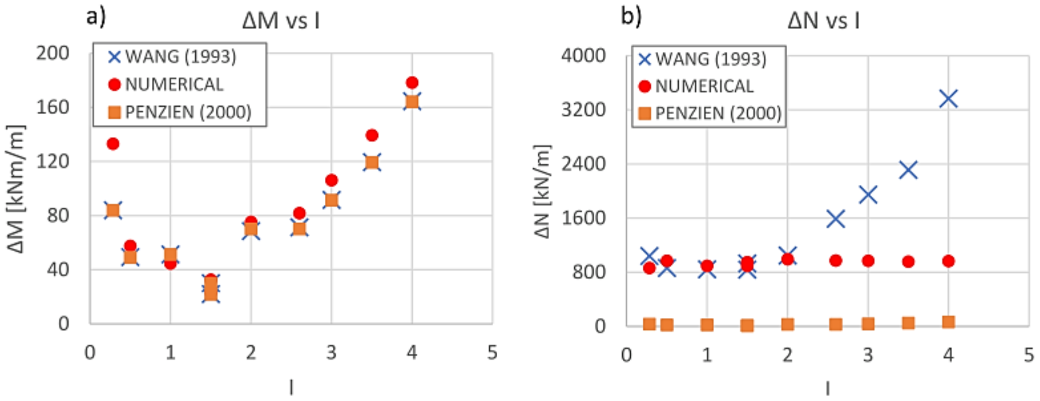

Average Shear Strain for both layers

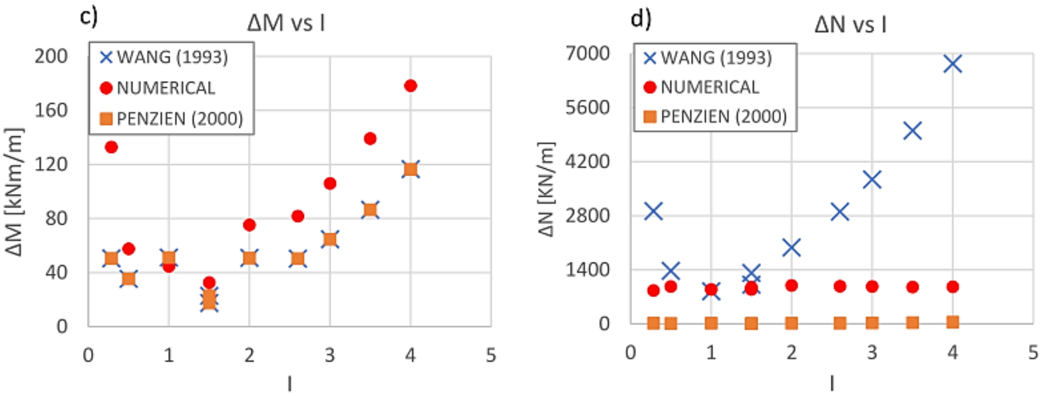

Figure 4.44: Comparison between numerical and analytical results with the impedance ratio I for all the ten performed models

4.7.2 Influence of the aboveground structure location, tunnel depth and input motions in terms of lining forces on the tunnel

Several numerical analyses were performed modifying the positions of the structure on the surface and the depth of the tunnel to study the seismic response of the coupled system soil-tunnel-structure. According to Figure 4.45, three different positions of the structure, ΔY (25m, 5m and 0m), and three different depths of the tunnel, Δz (17m,12m and 7 m), were used. ΔY=0 was used to indicate the position of the structure at the axis of the tunnel.

	ΔY	Δz
Model 12	25m	17m
Model 13	5m	17m
Model 14	0m	17m
Model 15	25m	12m
Model 16	5m	12m
Model 17	0m	12m
Model 18	25m	7m
Model 19	5m	7m
Model 20	0m	7m

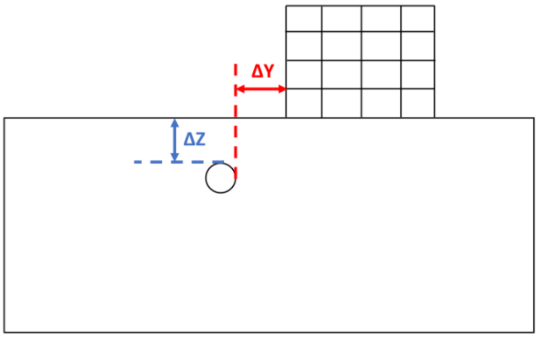

Figure 4.45: Aboveground structure positions and tunnel depths investigated through FEM modelling

The other aspects of the numerical modelling were not modified and only the “No-Slip” tunnel-soil contact condition is taken into account.

Figure 4.46 shows the comparison between the analytical and numerical dynamic bending moments, ΔM. In particular, each histogram shows the influence of the depth of the tunnel on the dynamic bending moment along the tunnel line for a fixed position of the aboveground structure. The lowest values of ΔM were obtained for Δz = 7 m. This occurred because for Δz = 7 m the tunnel was completely inside in a single layer (rock soil between 5 m and 20 m). Due to the lack of the strong impedance ratio at the depth of the tunnel, strong strains and stresses did not occur, and so low values of dynamic bending moments occur. Moreover, for Δz = 7 m the lowest values of ΔM were obtained because in this case, the tunnel is totally in the middle of a very stiff soil, in which small shear strains occur. As seen in the previous sections, the strong impedance ratio at the depth of the tunnel causes high values of the line force along the tunnel due to the concentration of strains and stresses. For this reason, at the tunnel depth equal to 17 m and 12 m, higher values of ΔM were obtained. This highlights the importance to build the tunnel inside a homogeneous soil, avoiding strong concentrations of line forces. Otherwise, careful attention has to be devoted to the effect of a great impedance ratio.

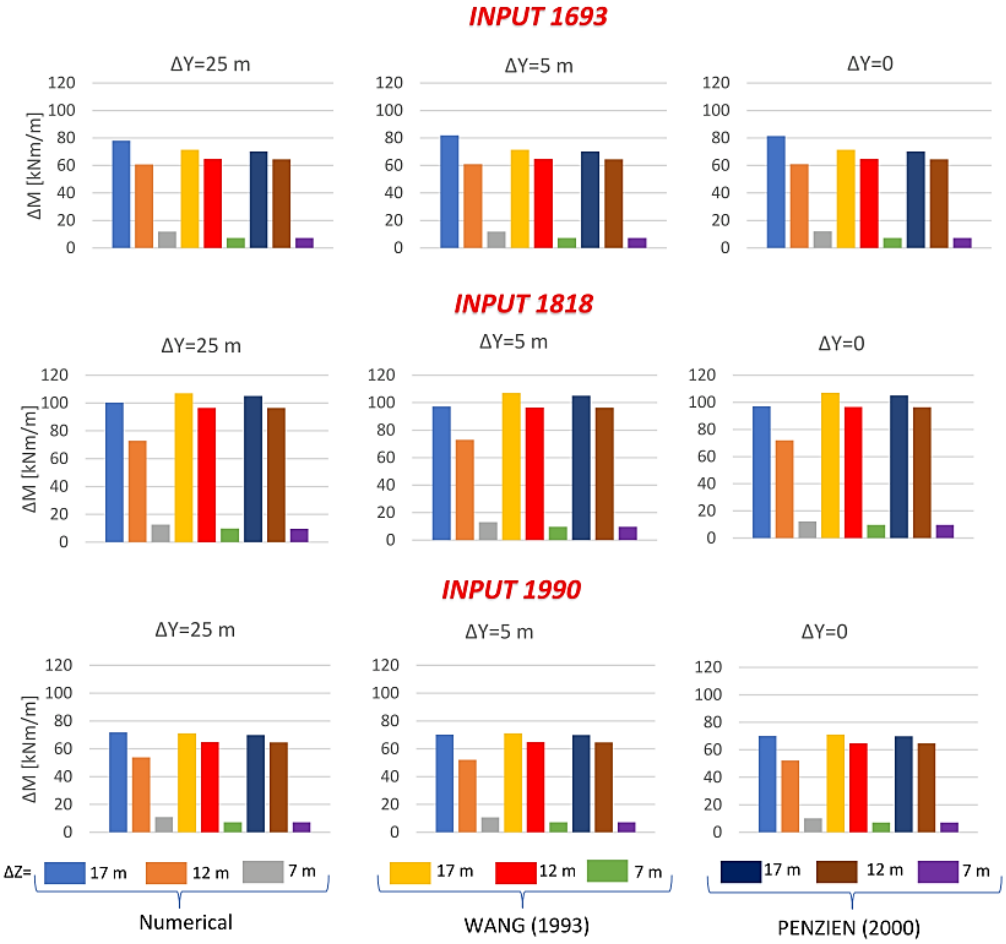

Figure 4.46: Influence of the aboveground structure position (ΔY) and tunnel depth (Δz) on the tunnel dynamic bending moments – first kind of histograms.

On the contrary, Figure 4.46 shows a low influence of the position of the aboveground structure on the dynamic bending moments along the tunnel. Finally, the analytical results were very similar to the numerical ones.

The same results of Figure 4.46 are reported in Figure 4.47 highlighting more clearly the poor influence of aboveground structure position ΔY on ΔM.

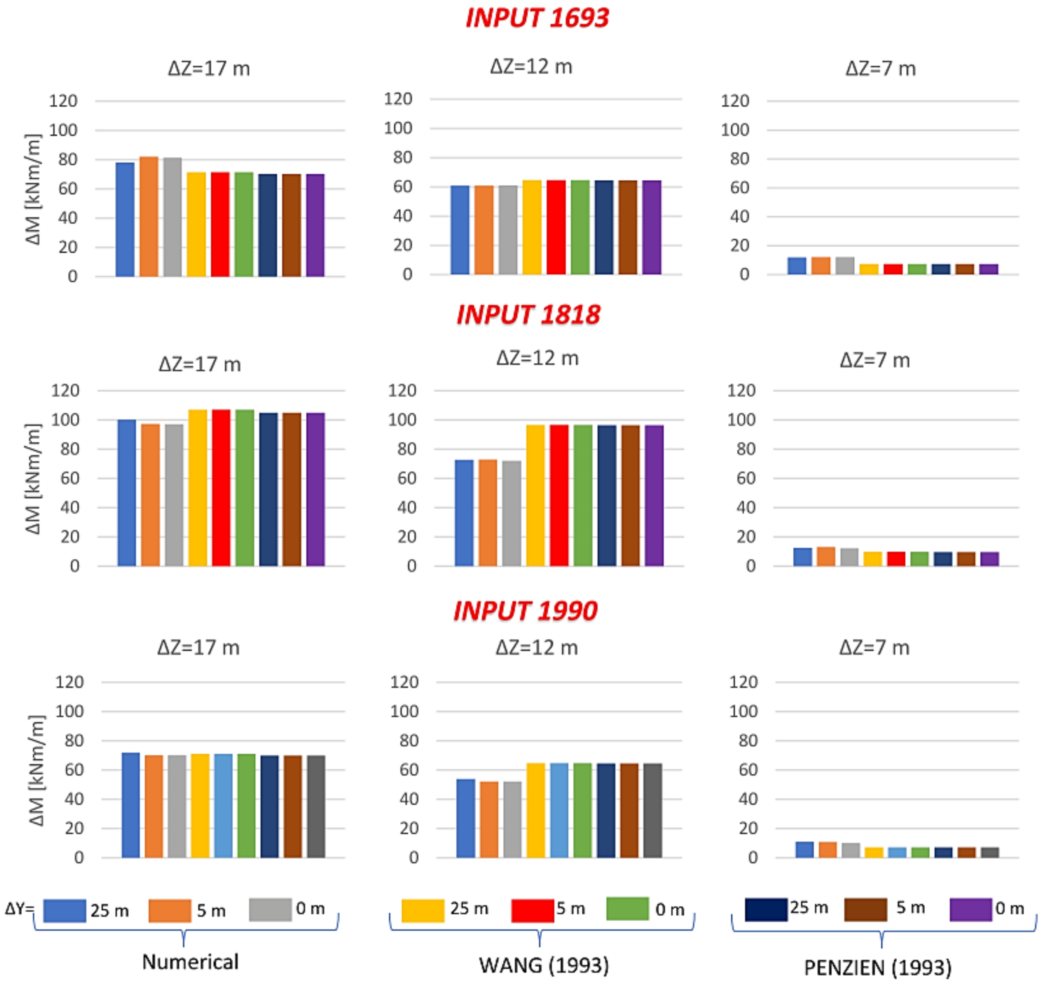

Figure 4.47: Influence of the aboveground structure position (ΔY) and tunnel depth (Δz) on the tunnel dynamic bending moments – second kind of histograms.

As for the dynamic bending moments, similar figures were made for the dynamic axial forces (Figures 4.48, 4.49).

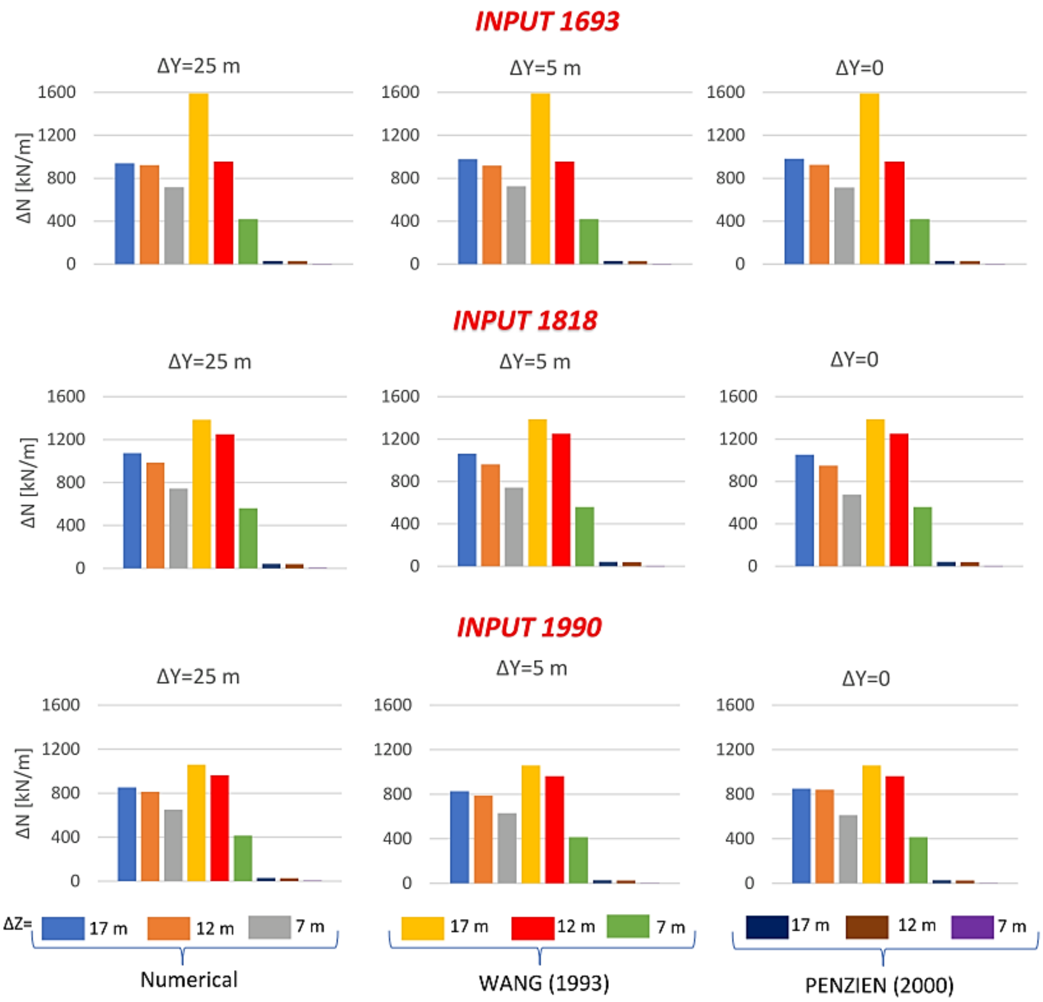

Figure 4.48: Influence of the aboveground structure position (ΔY) and tunnel depth (Δz) on the tunnel dynamic axial forces – first kind of histograms.

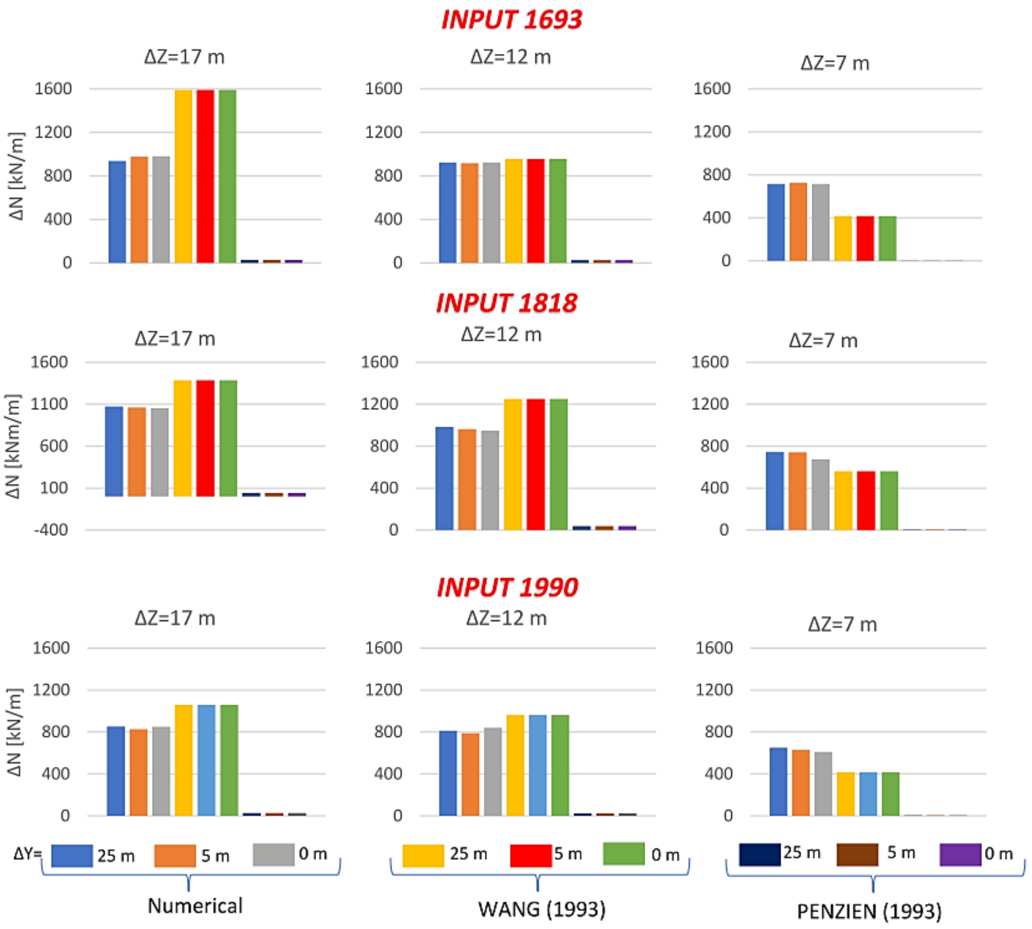

Figure 4.49: Influence of the aboveground structure position (ΔY) and tunnel depth (Δz) on the tunnel dynamic axial forces – second kind of histograms.

Definitely, ΔN were not strongly influenced by the depth of the tunnel and the position of the aboveground structure. ΔN strongly depends on the shear strains induced by the input motion on the soil around the tunnel. If at the depth of the tunnel soil stiffness discontinuity does not exist (see $\Delta z = 7$ m), low values of ΔN are obtained. Wang (1993) reproduced quite well the numerical results; on the contrary Penzien (2000) drastically underestimate ΔN This important result was also highlighted by Argyroudis (2017)

The above-discussed comparison between analytical and numerical results is more clearly shown in Figure 4.50. Figure 4.50 shows the comparison between the numerical and analytical results for the several models analysed and for the three different input motions used in terms of ΔM and ΔN. In particular, on the horizontal axis, the analytical results were shown, while on the vertical axis, the numerical results were displayed. The black line reveals the perfect agreement between the analytical and numerical results.

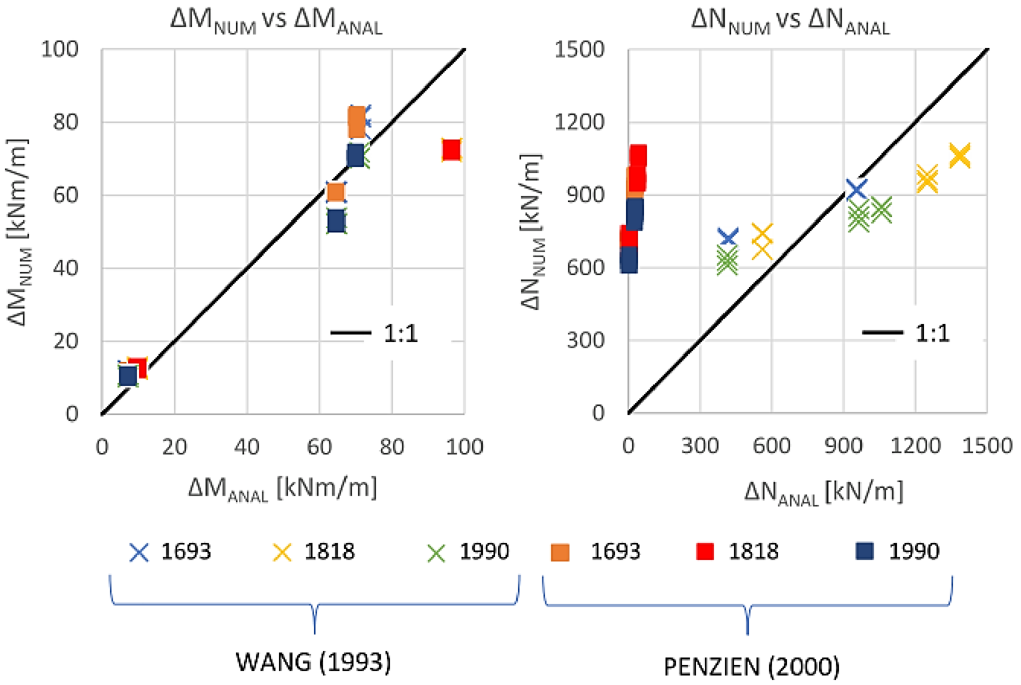

Figure 4.50: Comparison between numerical and analytical results for the several models analysed and the three different input motions used

4.7.3 Influence of the aboveground structure location, tunnel depth and input motions in terms of acceleration response spectra

The response of the coupled system soil-tunnel-structure in terms of acceleration response spectra was also investigated. The numerical results were compared with the response spectra suggested by the Italian Technical Regulation (NTC18), considering a structure damping ratio equal to 5%. According to NTC18, the elastic acceleration response spectrum for the horizontal direction of the input motion, S_e, is defined by the following expressions (4.17):

$$0 \leq T < T_B \qquad S_e(T) = a_g \cdot S \cdot \eta \cdot F_0 \cdot \left[\frac{T}{T_B} + \frac{1}{\eta \cdot F_0}\left(1 - \frac{T}{T_B}\right)\right] \tag{4.17.a}$$

$$T_B \leq T < T_C \qquad S_e(T) = a_g \cdot S \cdot \eta \cdot F_0 \tag{4.17.b}$$

$$T_C \leq T < T_D \qquad S_e(T) = a_g \cdot S \cdot \eta \cdot F_0 \cdot \left(\frac{T_C}{T}\right) \tag{4.17.c}$$

$$T_D \leq T \qquad S_e(T) = a_g \cdot S \cdot \eta \cdot F_0 \cdot \left(\frac{T_C \cdot T_D}{T^2}\right) \tag{4.17.d}$$

where:

- T is the vibration period measured in seconds;
- S is the product between the stratigraphic (S_S) and topographic (S_T) amplification coefficient: $S = S_S \cdot S_T$;
- $\eta = \sqrt{\frac{10}{5+\xi}} \geq 0.55$; η=1 for a structure damping ratio ξ=5%;
- F_0 is the maximum spectral amplification, on horizontal bedrock, with a minimum value is equal to 2.2;
- $T_C = C_C \cdot T_C^*$;
- $T_B = \frac{T_C}{3}$;
- $T_D = 4 \cdot \frac{a_g}{g} + 1.6$.

To estimate the stratigraphic amplification coefficient S_S a local response analysis could be done. Alternatively, S_S can be estimated according to Table 4.12 based on the soil category (NTC, 2018).

Table 4.12: S_S *and* C_C *according to NTC18*

Soil Category	S_S	C_C
A	1.00	1.00
B	$1.00 \leq 1.40 - 0.40 \cdot F_0 \cdot \frac{a_g}{g} \leq 1.20$	$1.10 \cdot (T_C^*)^{-0.20}$
C	$1.00 \leq 1.70 - 0.60 \cdot F_0 \cdot \frac{a_g}{g} \leq 1.50$	$1.05 \cdot (T_C^*)^{-0.33}$
D	$0.90 \leq 2.40 - 1.50 \cdot F_0 \cdot \frac{a_g}{g} \leq 1.80$	$1.25 \cdot (T_C^*)^{-0.50}$
E	$1.00 \leq 2.00 - 1.10 \cdot F_0 \cdot \frac{a_g}{g} \leq 1.60$	$1.15 \cdot (T_C^*)^{-0.40}$

The soil category has to be defined, computing an equivalent shear waves velocity according to the following expression:

$$V_{S,eq} = \frac{H}{\sum_{i=1}^{N} \frac{h_i}{V_{S,i}}} \tag{4.18}$$

where:

- H is the depth of the bedrock characterized by a shear waves velocity V_S>800 m/s;
- h_i is the thickness of each layer;
- $V_{S,i}$ is the shear wave velocity of each layer;
- N is the number of layers.

According to expression 4.18 and the shear waves velocity value shown in Table 4.6, $V_{S,eq}$ was estimated equal to 540 m/s. According to the soil categories reported in the NTC18, the soil category of the analysed tunnel-soil-aboveground structure cross section was B. Then, according to Table 4.12, the applied procedure gives:

$$1.00 \leq 1.40 - 0.40 \cdot 2.395 \cdot \frac{3.75}{g} \leq 1.20 \qquad S_S = 1.033$$

Then, the first natural period of the aboveground structure resting on the soil including the tunnel was estimated by the amplification function curve evaluated as the ratio between the Fourier spectrum computed at the top and the Fourier spectrum computed at the bottom of the aboveground structure, as shown in Figure 4.51.

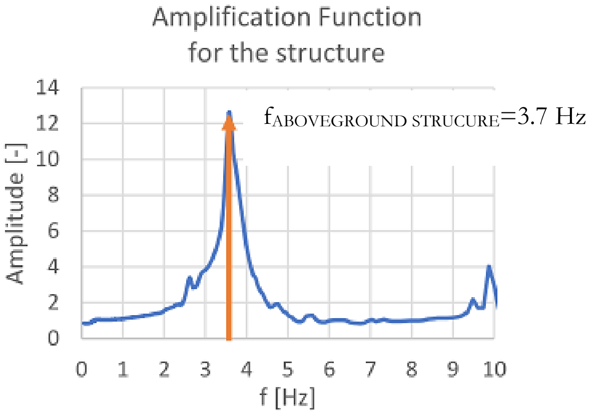

Figure 4.51: Amplification Function curve for the aboveground structure

Figure 4.52, 4.53 and 4.54 show the elastic response acceleration spectra along the tunnel alignment (T.A.) and the free filed alignment (F.F.A.) on the soil surface and along the structure alignment (S.A.) at the foundation level, obtained by the FEM modelling compared with the design spectrum provided by the NTC18. For the investigated models the spectral accelerations at T = 0.27s achieved numerically along the different alignments and provided by NTC18 are very similar for the 1693 and 1990 inputs, clearly lower for the 1818 input.

For the analysed models, in the range of periods equal to 0.8–1.5s the FEM spectral acceleration was generally much larger than that provided by NTC18 and the FEM response spectra obtained for the three different alignments were very similar.

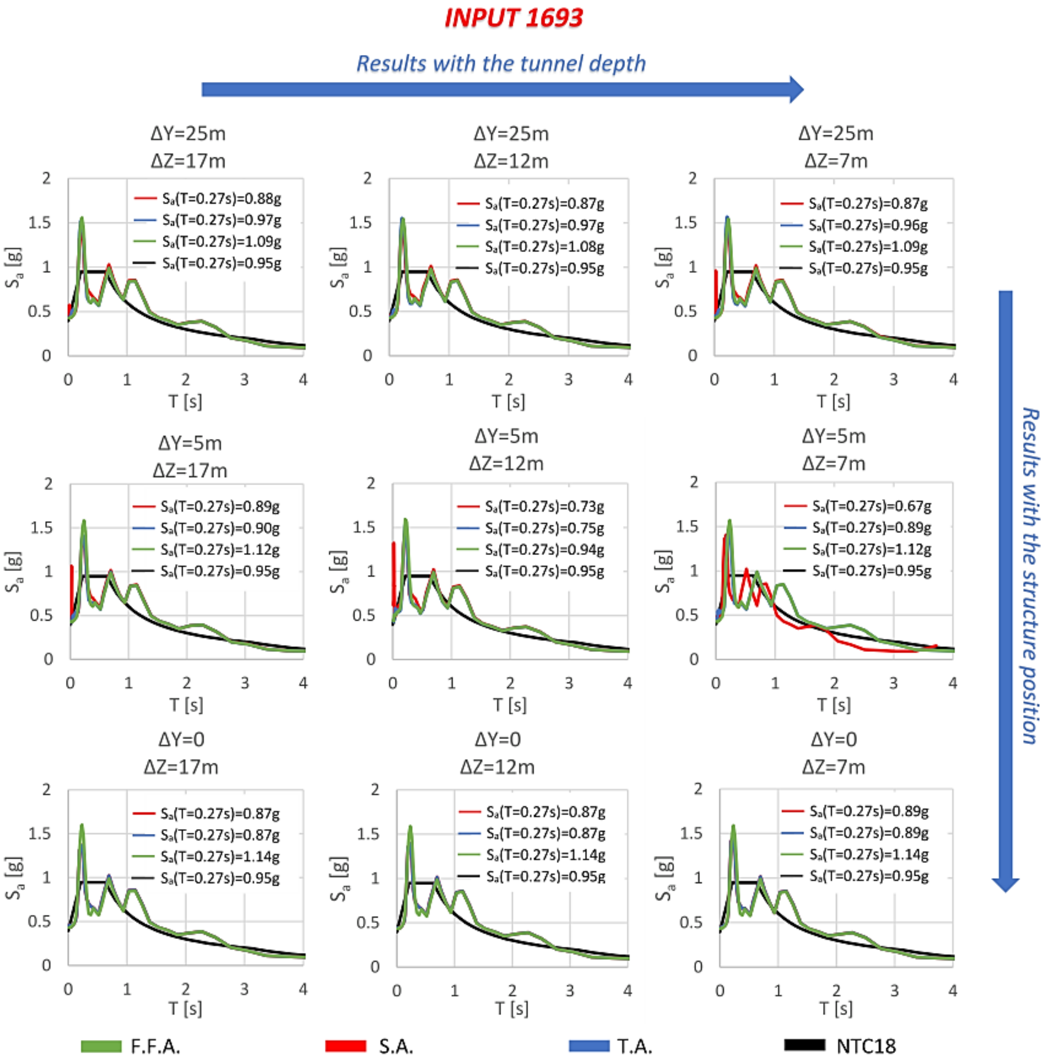

Figure 4.52: Acceleration response spectra for 1693 input motion: comparison between the analysed alignments

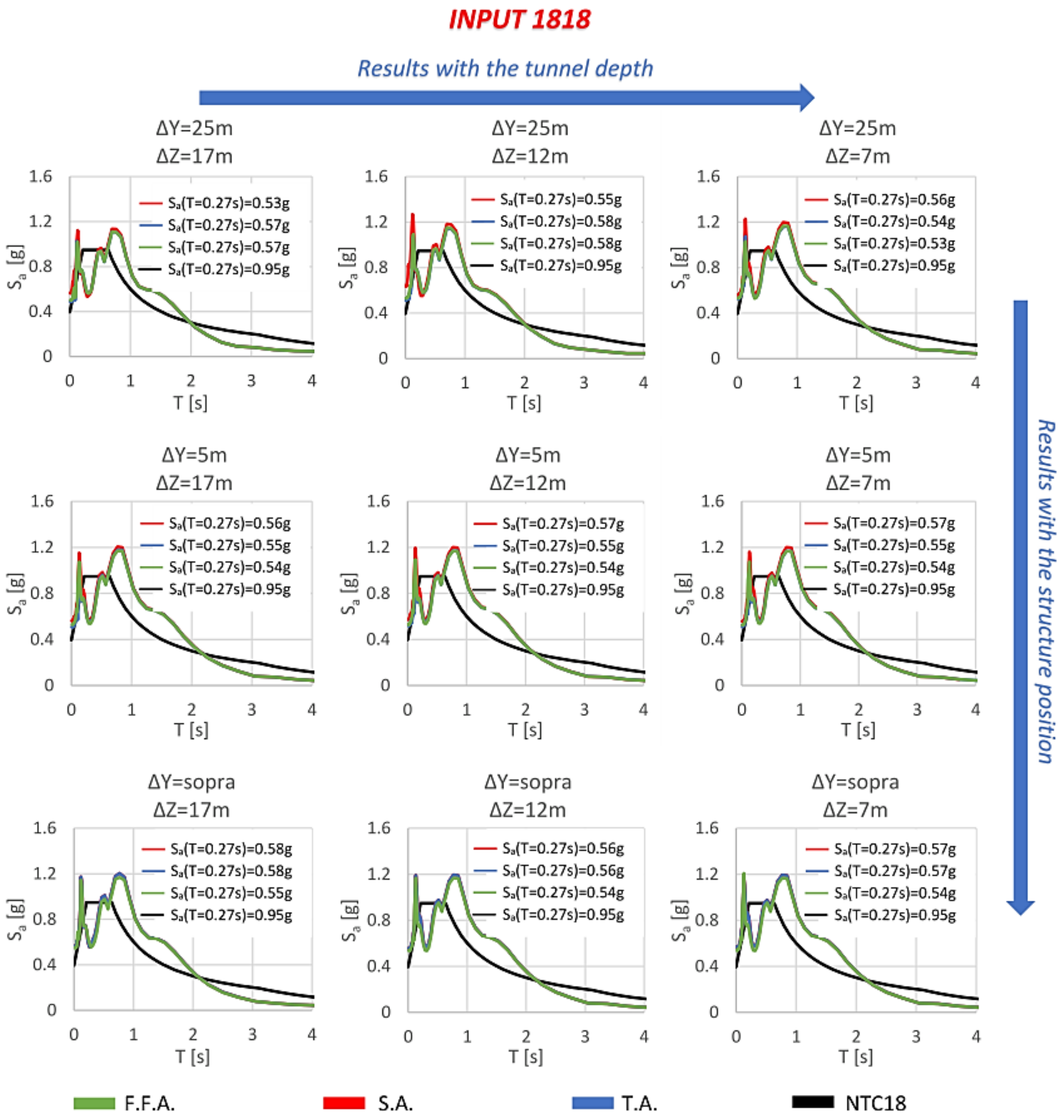

Figure 4.53: Acceleration response spectra for 1818 input motion: comparison between the analysed alignments

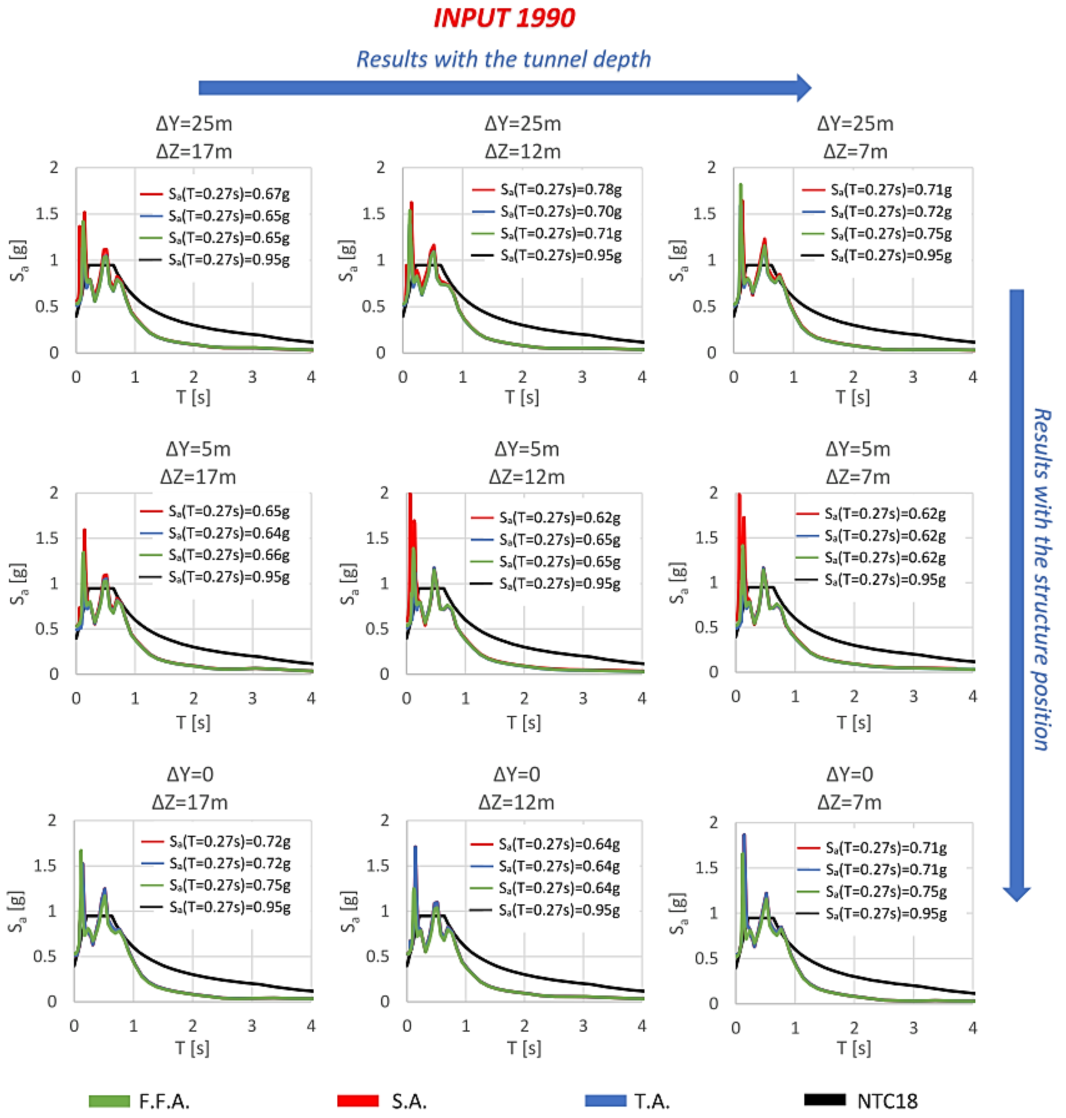

Figure 4.54: Acceleration response spectra for 1990 input motion: comparison between the analysed alignments

Figures 4.55 and 4.56 show more clearly the differences obtained in terms of S_a(T=0.27s) considering the different input motions and alignments.

In particular, starting to analyse the results obtained along the free field alignment (F.F.A.), the highest value achieved was about 1.1g, obtained for 1693 input motion. Then, the following values were obtained: S_a = 0.95g for NTC18, S_a = 0.75g for 1990 input motion, S_a = 0.56g for 1818 input motion. Thus, strong differences, along the F.F.A., were achieved in terms of spectral acceleration for the several input motions used. This is due to the different frequency content of each input motion: of course, the closer the predominant frequency of the input is to the natural frequency of the tunnel-soil-aboveground structure system, the higher the value of Sa.

Analysing the structure alignment (S.A.) and the tunnel alignment (T.A.), slight differences were achieved comparing the numerical value of $S_a(T=0.27s)$ achieved for the 1693 input motion and the value suggested by. The presence of the tunnel and the structure reduce the spectral acceleration for the 1693 input motion.

Applying the 1818 and 1990 input motions similar values of $S_a(T=0.27s)$ were achieved along the different alignments and these values are lower than that suggested by NTC18.

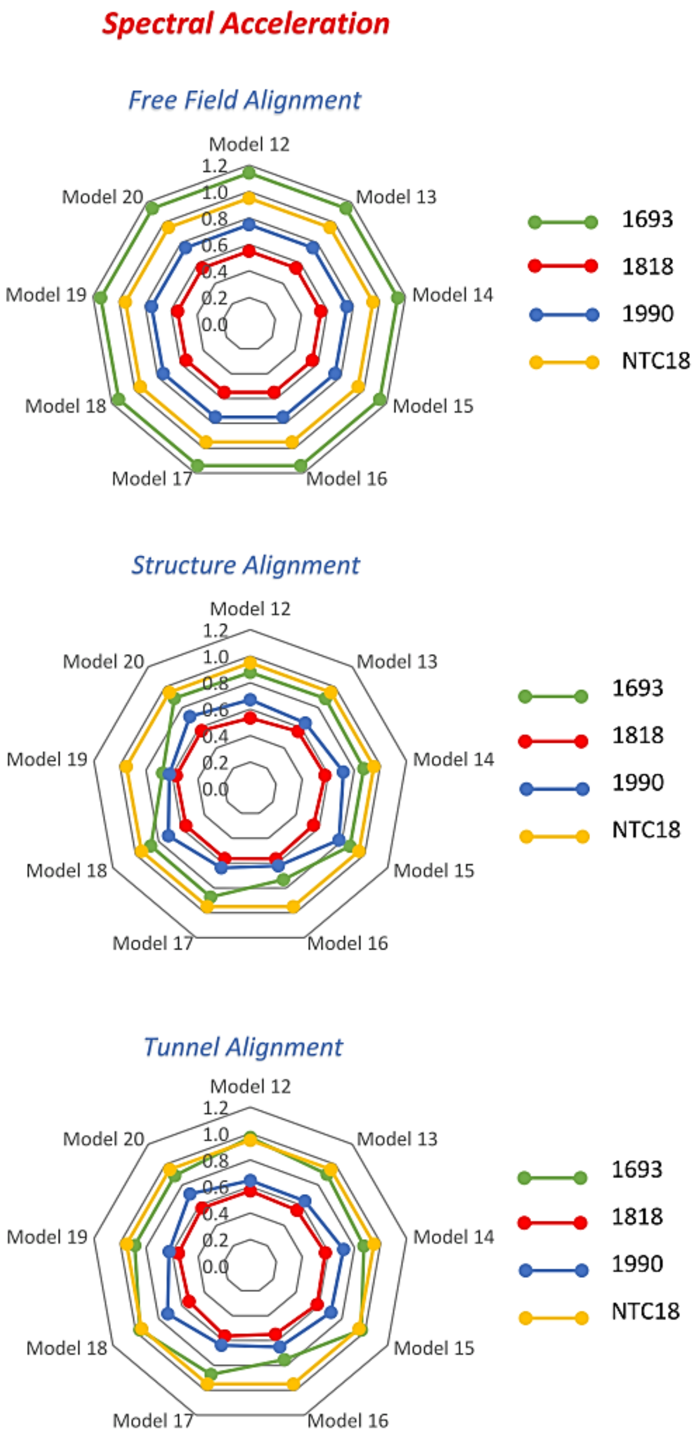

Figure 4.55: Comparison between the input motion used and the several models analysed in terms of the spectral acceleration $S_a(T=0.27s)$

Figure 4.56 shows a comparison of the results achieved along the three alignments. In particular, in the first line, the results achieved along the free field alignment (green line) were compared with the results obtained along the structure alignment (red line); in the second line, the results achieved along the free field alignment were compared with the results obtained along the tunnel alignment (blue line); in the last line, the results achieved along the structure alignment (red line) were compared with the results obtained along the tunnel alignment (blue line).

Concerning the first line, for the 1693 input motion, a strong disagreement between the free field and aboveground structure alignment results was achieved, obtaining lower values for the aboveground structure alignment. A disagreement between the free field alignment and aboveground structure alignment results also occurred with the input motion, recording values along the aboveground structure alignment of about 6÷7 per cent lower than the values obtained along the free filed alignment. For the 1818 input, the spectral acceleration values were very similar for both the alignments. Similar considerations can be made for the second line (comparison between the free field and tunnel alignment). Considering the last line of Figure 4.56 a good agreement between the aboveground building alignment and the tunnel alignment can be observed.

Finally, Figure 4.57 shows the same comparisons previously described in another configuration. The black line revealed the agreement between the results showed.

The results obtained according to the Technical Regulation (NTC18) cannot describe dynamic interaction phenomena. As it was possible to see, the structure on the surface and the tunnel modified the signal that hits the foundations. About the numerical results, important disagreements were obtained between the results achieved along the free field alignment and those achieved along the aboveground structure or tunnel alignment. These results revealed the importance to analyse a coupled system that takes into account the presence of aboveground structures and tunnels.

Moreover, the results obtained clearly show the importance of an accurate evaluation of the natural period of the structure. Important peaks of Sa were obtained with the FEM analyses, so a very small variation in the evaluation of the natural period of the structure could increase significantly the disagreement between the numerical results and that achieved according to NTC18.

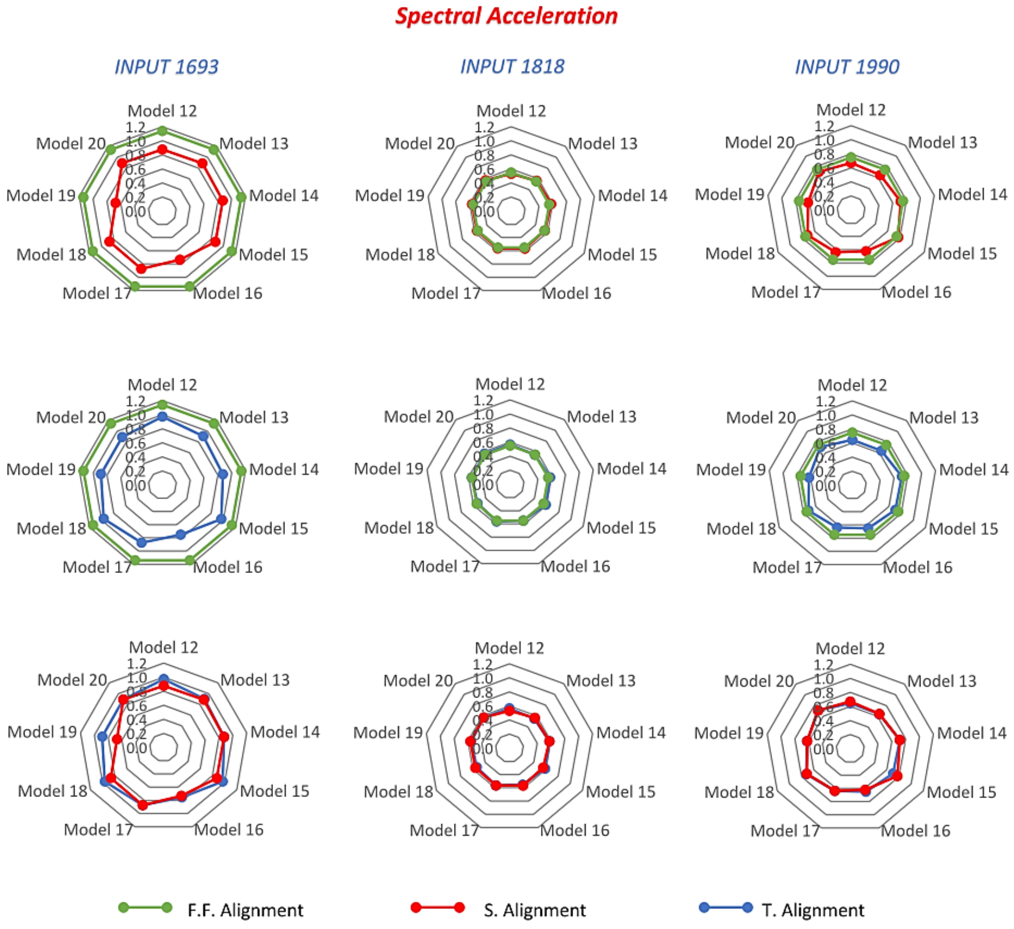

Figure 4.56: Comparison between the several alignments analysed in terms of the spectral acceleration $S_a(T=0.27s)$ *for each input motion used*

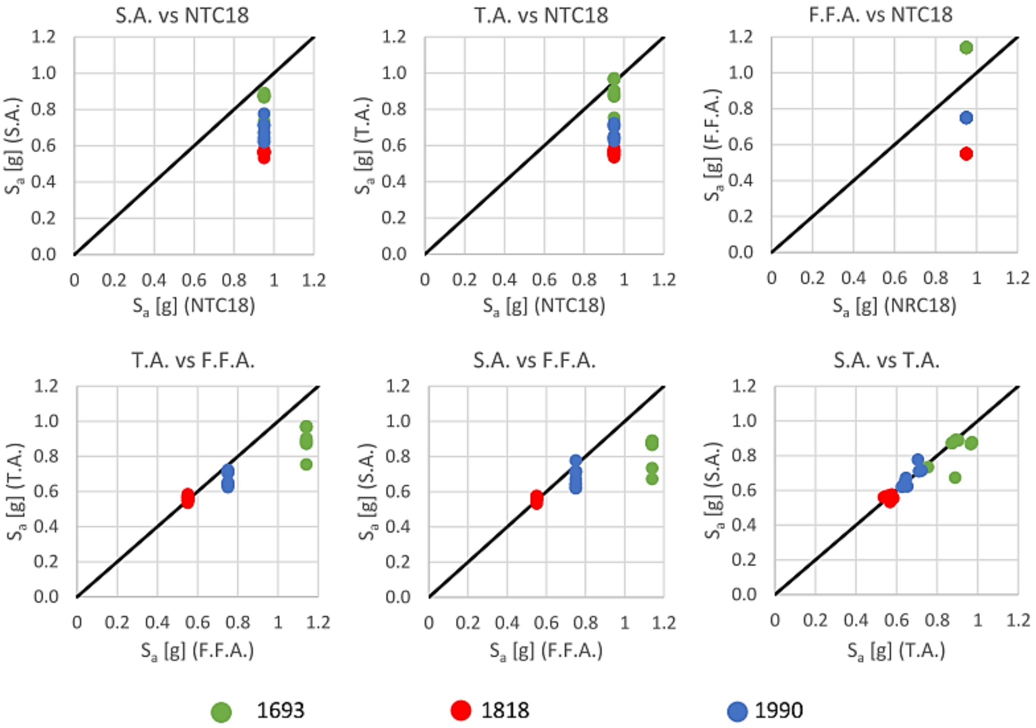

Figure 4.57: Spectral acceleration for the three input motion: comparison between the numerical results and the results suggested by NTC18

4.7.4 Influence of the aboveground structure location, tunnel depth and input motions in terms of seismic horizontal forces on the aboveground structures

The spectral acceleration values were useful to estimate the seismic horizontal forces to be applied to each floor of the aboveground structure, as showed in Figure 4.58. The NTC18 allows performing a linear static analysis for buildings with a natural period of vibration less than 2.5T_C or T_D (for the values of T_C and T_D see the previous section). For the investigated soil profile:

$$2.5 \cdot T_C = 2.5 \cdot (C_c \cdot T_C^*) = 2.5 \cdot (1.262 \cdot 0.503) = 1.59s$$

$$T_D = 4 \cdot \frac{a_g}{g} + 1.6 = 4 \cdot 0.383 + 1.6 = 3.13s$$

Both values were greater than the natural period of vibration estimated equal to 0.27s. Then the horizontal seismic load F_{hi} to apply to each floor were computed through the following expression, according to the NTC18:

$$F_{hi} = F_h \cdot z_i \cdot \frac{w_i}{\sum_j z_j w_j} \tag{4.19}$$

where:

- $F_h = S_e(T_1) \cdot W \cdot \frac{\lambda}{g}$;
- w_i and w_j are the weights of i^{th} and j^{th} floors, respectively;
- z_i and z_j are the heights of the masses from the foundation level;
- $S_e(T_1)$ is the spectral acceleration value at the natural period of the structure;
- W is the weight of the whole aboveground structure;
- λ is a coefficient equal to 0.85 if $T_1<2T_C$ and the aboveground structure has more than three floors. In this case $\lambda=0.85$;
- g is the gravity acceleration equal to $9.81 m/s^2$.

According to expression (4.19), the seismic force to apply to each floor of the aboveground structure were:

$F_{h1}=148$ kN for the first floor;
$F_{h2}=296$ kN for the second floor;
$F_{h3}=445$ kN for the third floor;
$F_{h4}=593$ kN for the fourth floor;

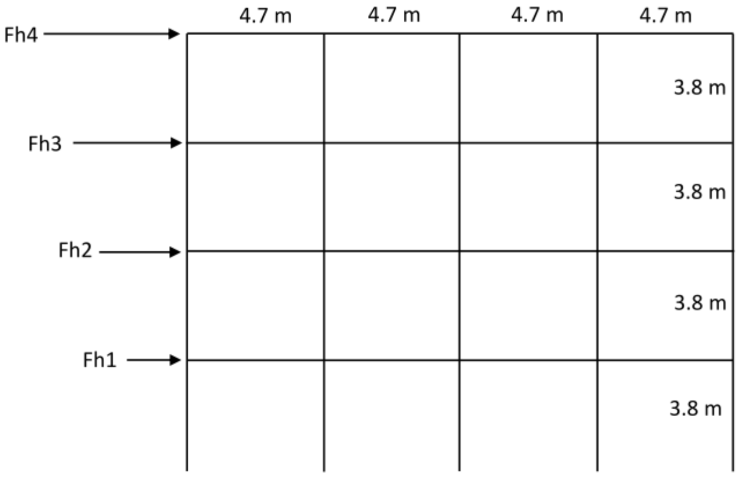

Figure 4.58: Analysed frame with the horizontal seismic force per each floor

Figure 4.59 shows the comparison between the seismic forces achieved according to NTC18 and the numerical seismic forces for all the input motions and FEM models analysed. NTC18 gives horizontal seismic forces 3 times higher than the numerical ones. In this case, a structural design according to the NTC18 could be too expensive. Numerical analyses are recommended, for analysing dynamic interaction phenomena and non-linearities.

Significant differences were also found for the three input motions used, showing the importance of accurate numerical analyses using many input motions with different natural frequencies. Figure 4.60 shows the ratios between the first two fundamental frequencies of the input motions, $f_{input}(1)$ and $f_{input}(2)$, and the frequency of the aboveground structure in the fully-coupled tunnel-soil-aboveground structure system (Figure 4.51). If the above-mentioned frequency ratio is between 0.5 and 1.5, resonance phenomena could occur.

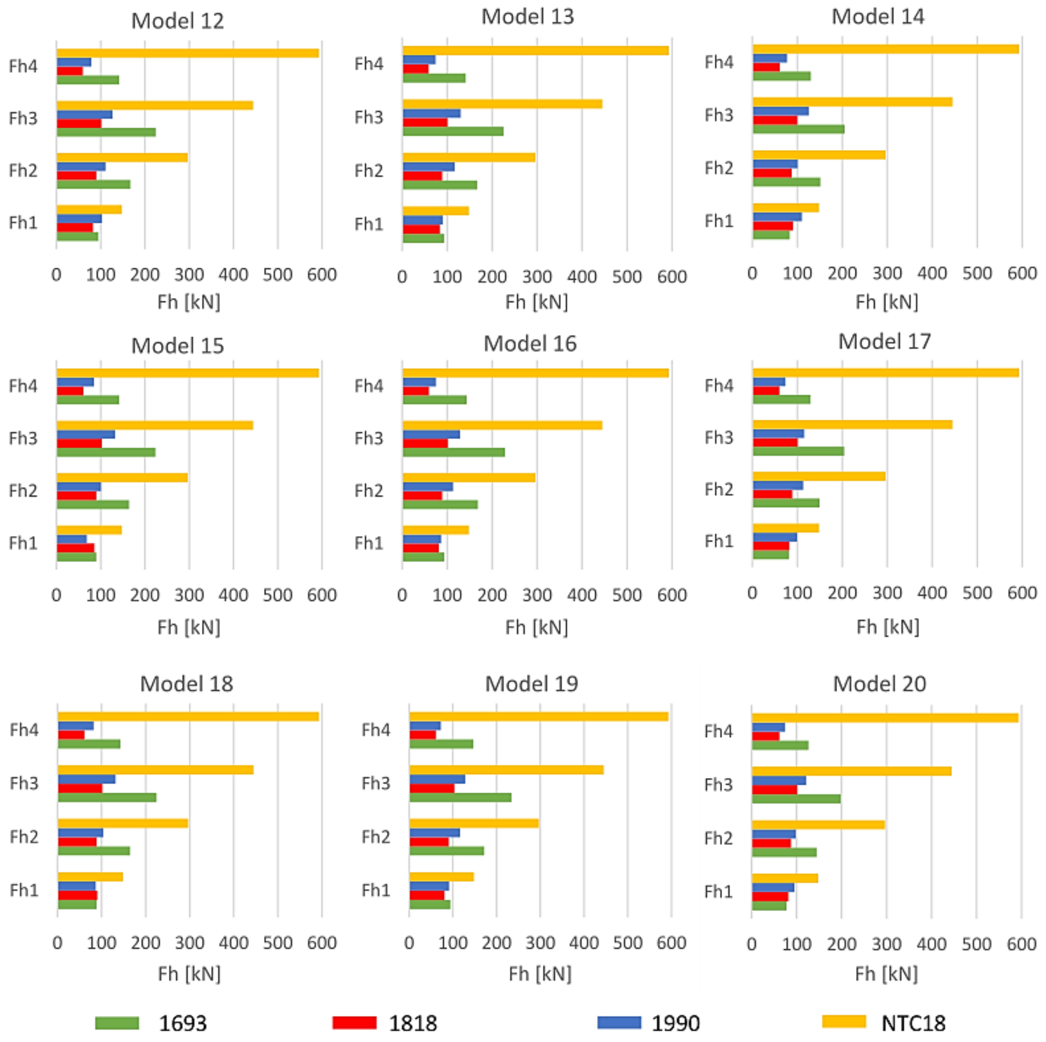

Figure 4.59: Comparison between the horizontal seismic forces for the analysed models and for the three input motion used

The greater severity in terms of horizontal seismic forces for the 1693 input motion can be noted because the ratio $f_{input}/f_{structure}$ evaluated was in the range of probable resonance and in particular the value was very close to one (perfect resonance).

The second input motion for severity was the 1990 one, with slightly lower values of forces, because the ratio $f_{input}/ f_{structure}$ evaluated was in the range of probable resonance, but further away from the unit value, achieving a value of about 0.55. The lowest horizontal seismic forces were obtained for the 1818 input motion; as expected, this occurred because the ratio $f_{input}/ f_{structure}$ evaluated was enough far from the range of probable resonance.

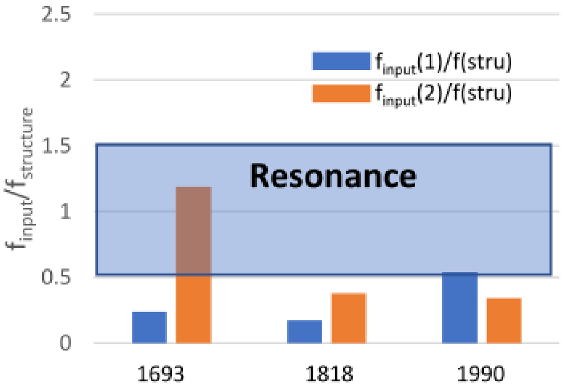

Figure 4.60: Ratios between the first two frequencies of the input motion and the natural frequency of the structure

The following Figure 4.61 shows the seismic forces on the aboveground structure for the same position of the aboveground structure, ΔY, and varying the depth of the tunnel Δz, for each input motion used. The depth of the tunnel did not produce significant differences in terms of horizontal seismic forces.

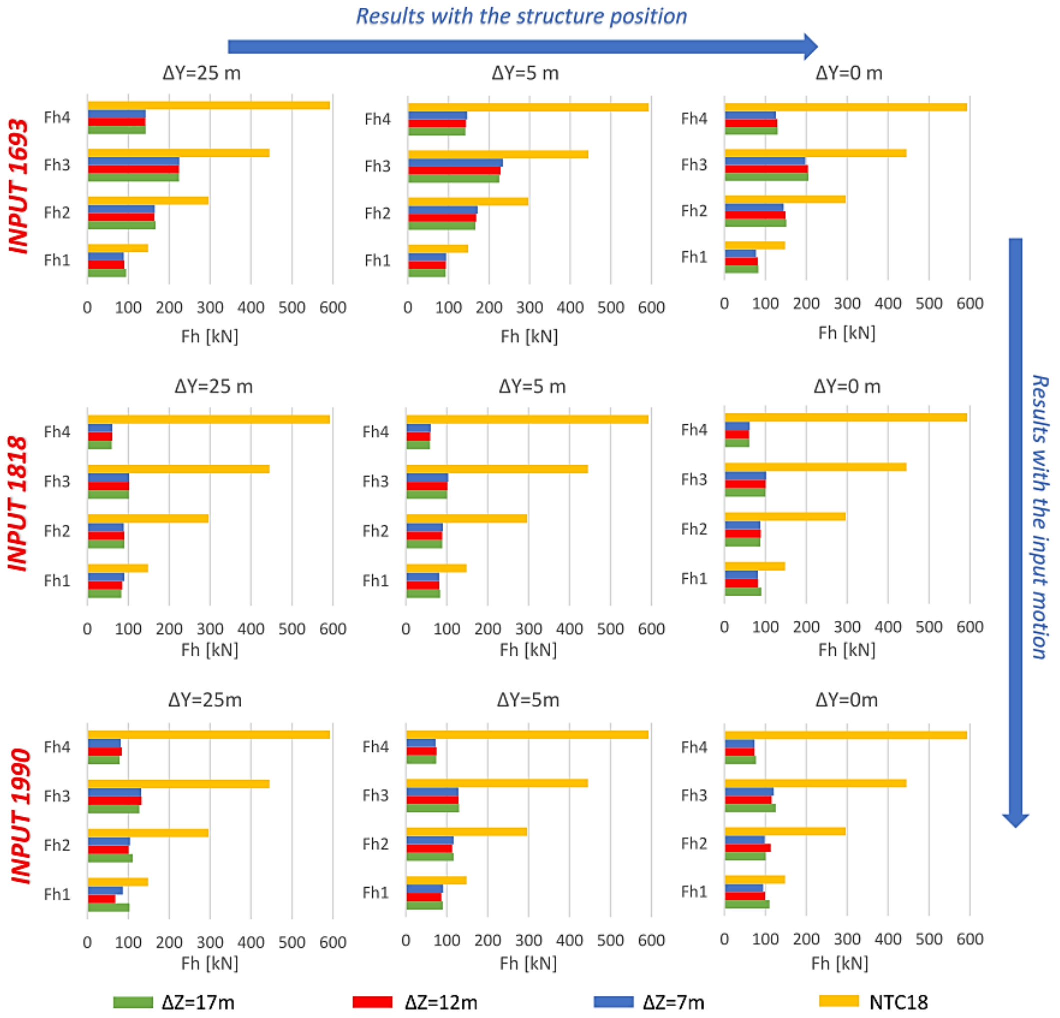

Figure 4.61: Zorizontal seismic forces on the frame with the same position of the aboveground structure on the surface, ⊿Y, on varying the depth of the tunnel ⊿Z, for each input motion used

Figure 4.62 shows the seismic forces on the aboveground structure with the same position of the tunnel, Δz, and varying the position of the aboveground structure, ΔY, for each input motion used. Generally, slightly lower values of seismic force were found for ΔY=0, i.e. when the aboveground structure is along the axis of the tunnel. Consequently, the seismic response of the building varied with the relative position between the tunnel and the aboveground structure, recording a slight improvement of the seismic response when the aboveground building was along the axis of the tunnel and the tunnel is closer to the soil surface. These results can be explained because the seismic waves can not propagate through empty space, such as the tunnel.

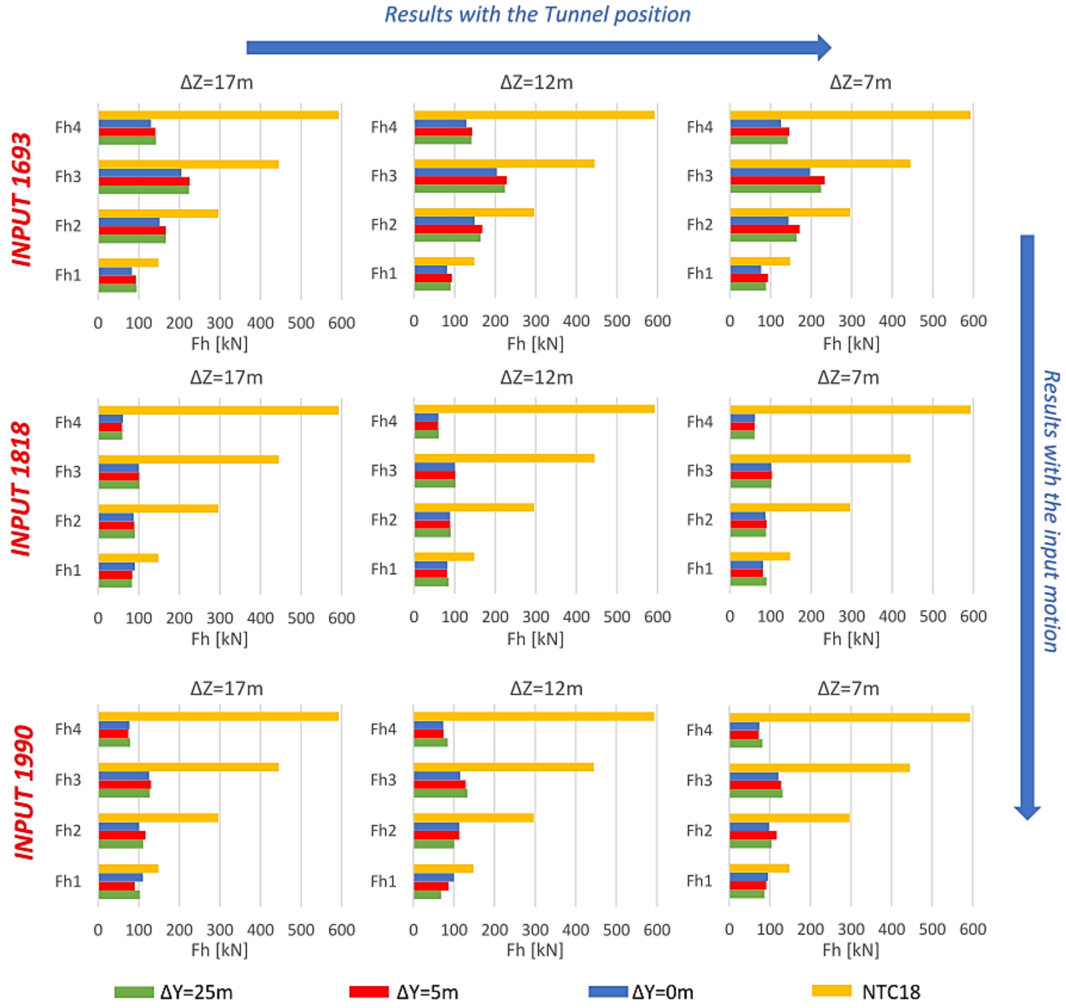

Figure 4.62: Horizontal seismic forces on the frame with the same position of the tunnel, ⊿Z, on varying the position of the aboveground structure on the surface, ⊿Y, for each input motion used.

In conclusion, the horizontal seismic force, F_{hi}, depended mainly by the ratio $f_{input}/ f_{structure}$. Less effect had the position of the aboveground structure on the surface and the depth of the tunnel. A considerable influence on the seismic response of the aboveground building in terms of seismic forces occurred for a depth of the tunnel equal to 7 m; on the contrary, no significant changes for greater depths of the tunnel were observed.

4.7.5 Influence of the aboveground structure location, tunnel depth and input motions in terms of peak ground acceleration at the soil surface level

Figure 4.63 shows the results in terms of peak ground acceleration, PGA, achieved at the soil surface level for all the models analysed. The yellow histograms point at the value suggested by NTC18, equal to 0.396g according to the following expression:

$$a_g \cdot S_s = 0.383g \cdot 1.033 = 0.396g$$

The numerical results achieved were generally 30÷35% higher than the value suggested by the NTC18. The peak ground acceleration values varied with the input motion used. In particular, the results obtained with 1818 and 1990 input motions revealed a major amplification of the signals in terms of accelerations.

So, a study of the frequencies was performed. Figure 4.64 shows the ratios between the first two fundamental frequencies of the input $f_{input}(1)$ and $f_{input}(2)$ and the first three natural frequencies of the soil $f_{soil}(1)$, $f_{soil}(2)$ and $f_{soil}(3)$. The soil frequencies were achieved by the peaks of the amplification functions showed in Figure 4.65. These amplification function curves were computed as the ratios between the Fourier spectra achieved at the soil surface level and the Fourier spectra of the input motion. The greatest severity in terms of peak ground acceleration for 1818 and 1990 input motions can be noted because the ratio f_{input}/f_{soil} was in the range of probable resonance and in particular often was very close to one (perfect resonance). The lowest peak ground acceleration values were obtained for 1693 input motion with values of about 0.45, very close to the value suggested by the NTC18. As expected, this occurred because the ratio f_{input}/f_{soil} evaluated was enough far from the range of probable resonance.

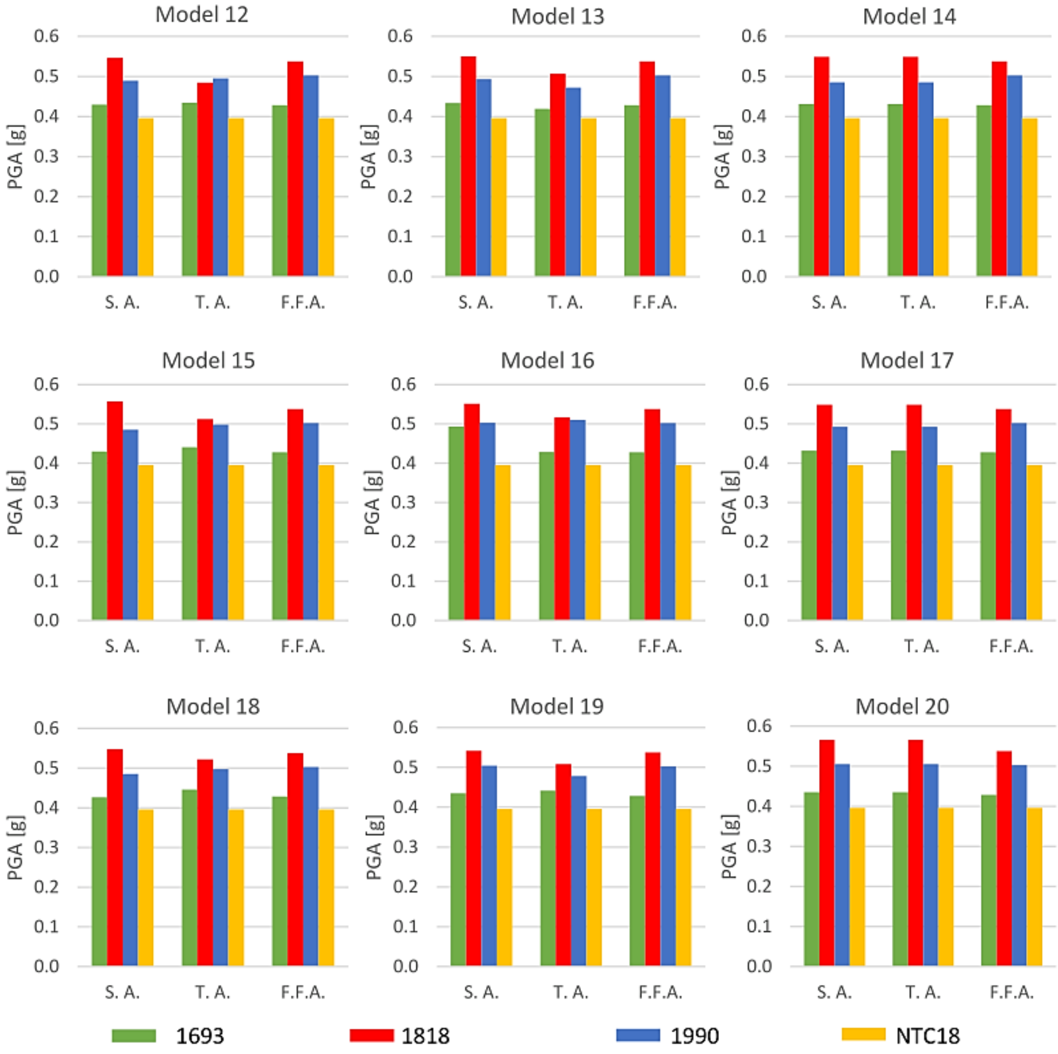

Figure 4.63: Peak ground acceleration at the soil surface level for each analysed model, varying the alignment and the input motion used

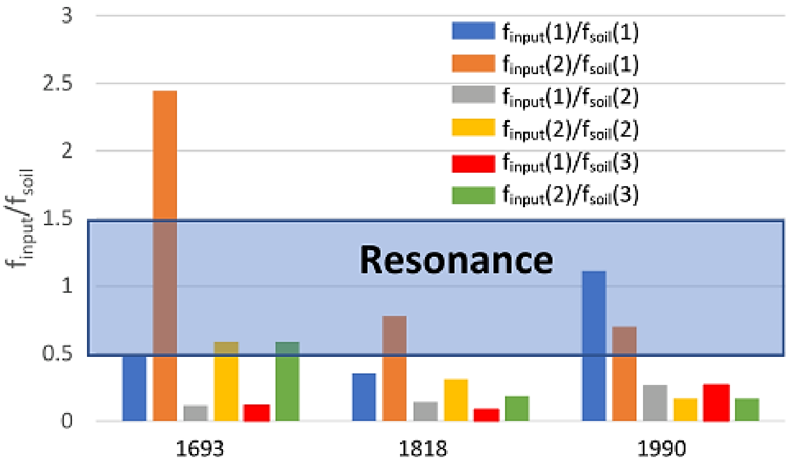

Figure 4.64: Ratios between the first two frequencies of the input motion and the three natural frequencies of the soil

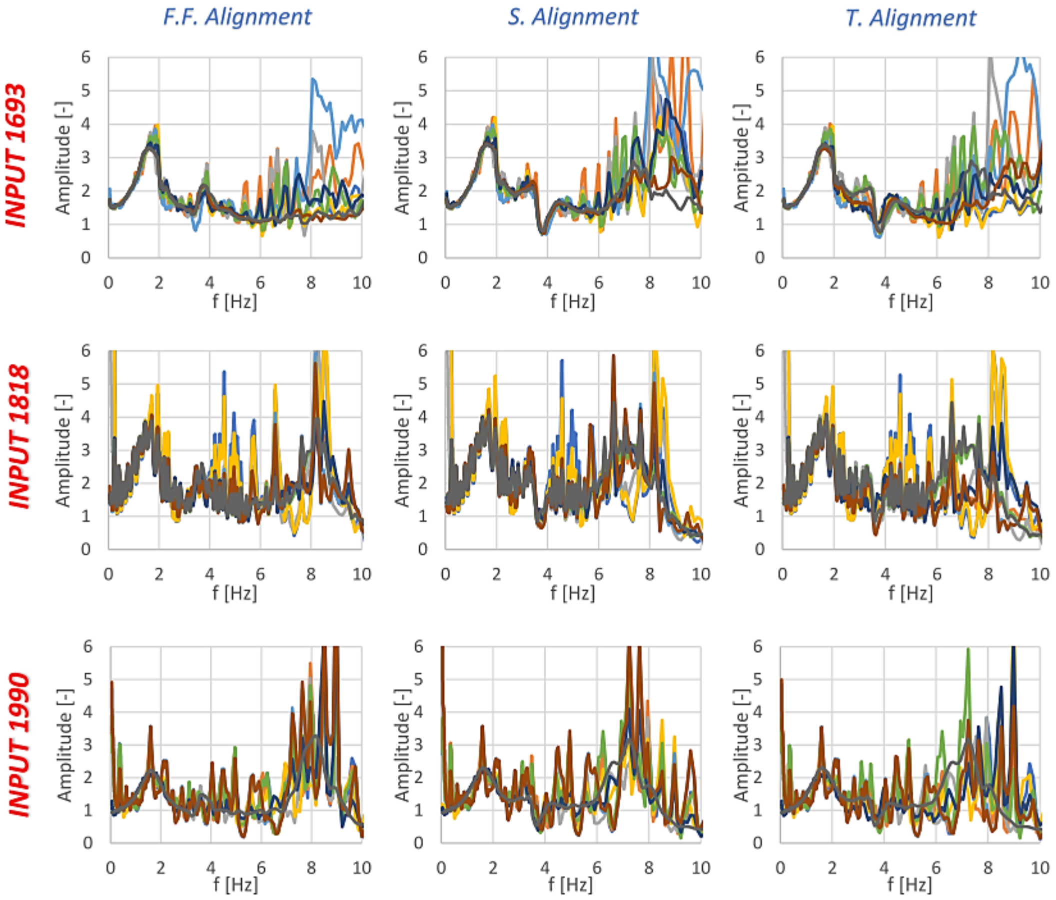

Figure 4.65: Amplification function for each input and for each analysed alignment, varying the analysed FEM models

Figure 4.66 shows the comparison in terms of numerical peak ground acceleration on the surface for the three different alignments analysed: free field alignment (F.F.A.), structure alignment (S.A.) and tunnel alignment (T.A.). It is evident that the results generally suffered an irrelevant change with the presence of the structure and of the tunnel. Only in some cases, small decreases in terms of peak ground acceleration occurred along the tunnel axis.

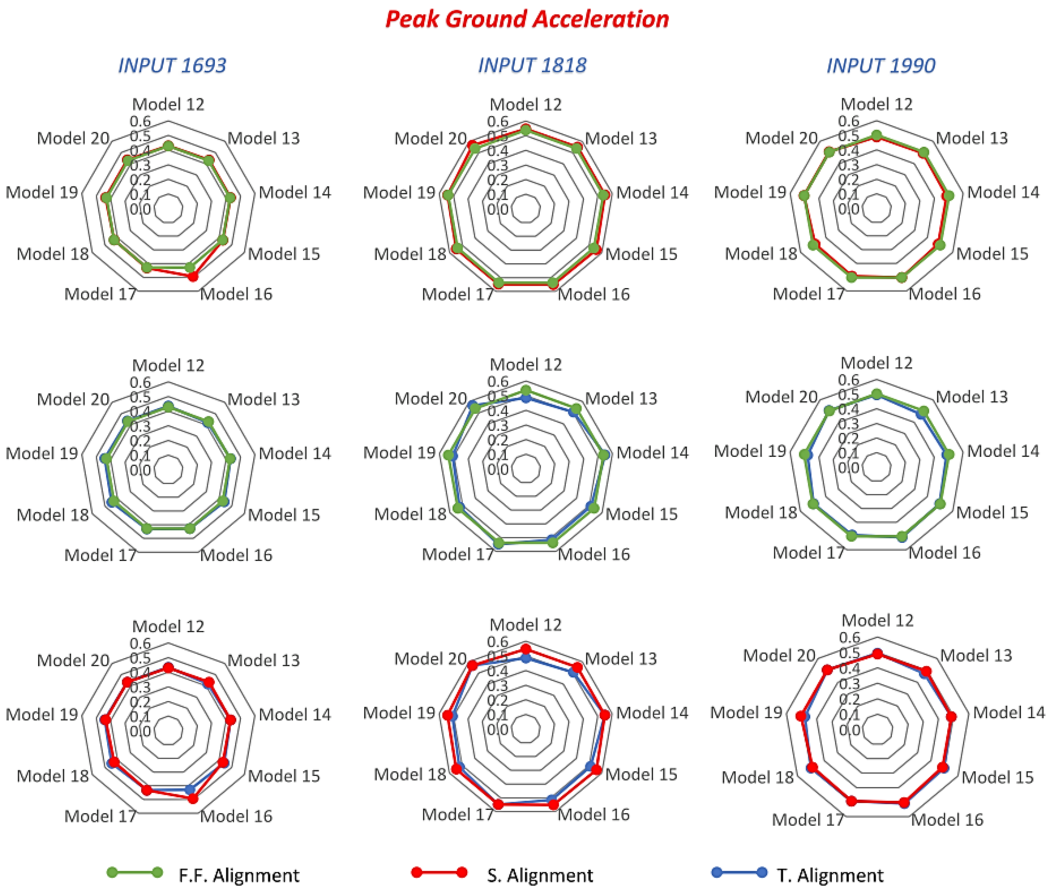

Figure 4.66: Comparison between the three analysed alignments in terms of peak ground acceleration at the soil surface level.

In conclusion, the peak ground accelerations on the surface depended mainly by the ratio $f_{input}/\ f_{soil}$. When the frequency ratio was between 0.5 and 1.5, probable resonance phenomena can occur, amplifying the amplitude of the seismic waves that propagate through the soil, from the bedrock to the surface. Small changes were obtained along the several alignments, obtaining only for some cases lower values for the tunnel axis alignment. Probably, this result was due to the empty space created by the tunnel, through which the seismic waves cannot propagate, decreasing the signal on the surface. Finally, there was an underestimation of signal amplification recorded on the surface according to the Italian Technical Regulation.

4.7.6 Non-linear analysis of the coupled tunnel-soil-aboveground structure: effects of the soil constitutive model

In the previous sections, an equivalent visco-elastic linear constitutive model was used to describe the behaviour of the soil. In this section, a parametric analysis of the coupled tunnel-soil-aboveground structure was analysed, comparing three different constitutive models, and using two different values of peak ground acceleration at the bedrock (0.383g and 0.2g):

- Visco-elastic linear model;
- Equivalent visco-elastic linear model;
- Visco-elastoplastic constitutive model (Severn-Trent model).

The aboveground building was fixed along the axis of the tunnel; while once more the following three tunnel depths were considered (Figure 4.67).

- Δz =17 m;
- Δz =12 m;
- Δz =7 m;

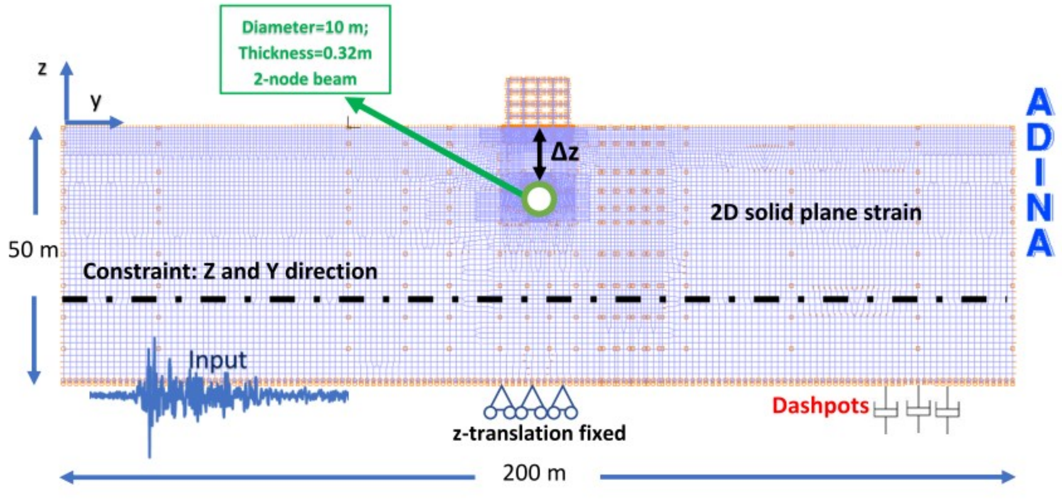

Figure 4.67: Geometry characteristics of the FEM model used in the non-linear analyses.

The configuration with the structure located along the axis of the tunnel was chosen because, by the results described in the previous sections, this configuration was the one with the greatest seismic response. For the soils of the real section of the underground investigated not all the necessary laboratory tests were carried out to characterize their plastic behaviour; thus in this section, the "Plaja beach" soil, in Catania (Italy), was chosen, because several laboratory and in situ tests allowed us to characterise the visco-elastoplastic behaviour of this sand (Faccioli E. and Pessina V. 2000; Pastore and Turello 2000). For the "Plaja beach" soil, a Young's Modulus E=80000 kPa, a density ϱ=1800 kg/m^3 and a Poisson's coefficient ν=0.3, a damping ratio D=1% (small strain) were used to analyse the seismic response with a visco-elastic linear analysis.

As regards the equivalent visco-elastic linear analysis, the equivalent soil stiffness and damping ratio were evaluated according to the shear strains along the soil profile obtained by several 1D equivalent visco-linear site response analyses, using the *STRATA* code.

Figure 4.68 shows the G vs γ and D vs γ curves furnished by RCT tests. The RCT results were used to determine the empirical parameters of the equation

(4.9) proposed by Yokota et al. (1981) to describe the shear modulus decay with the shear strain increase (Cavallaro & Maugeri, 2005, Maugeri et al., 2006).

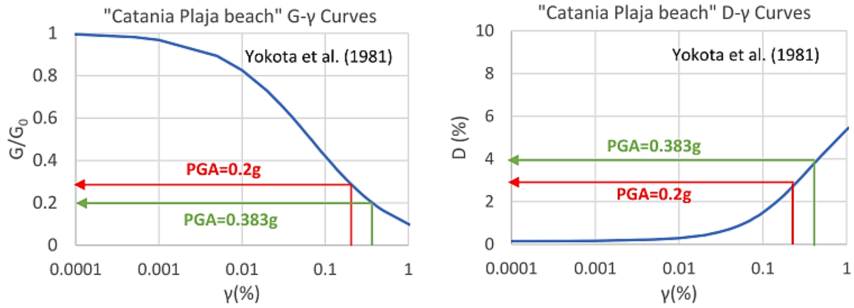

Figure 4.68: G/Go -γ curves and D-G/Go curves from RCT for "Plaja beach" site. (Cavallaro & Maugeri, 2005)

The RCT results were also used to determine the empirical parameters of the equation (4.10) proposed by Yokota et al. (1981) to describe the damping ratio increase with the shear strain increase (Cavallaro & Maugeri, 2005; Maugeri et al., 2006).

The input motion used for the parametric analysis was the 1693 input motion. The equivalent properties, computed for both the peak ground acceleration used (0.383g and 0.2g) are showed in Table 4.13:

Table 4.13: Equivalent soil parameters for the nonlinear analysis

PGA	V_s [m/s]	Equivalent V_s [m/s]	ν	ρ [kg/m³]	Equivalent E [KPa]	Equivalent D [%]
0.383g	130	57	0.3	1800	15436	4
0.2g	130	70	0.3	1800	23177	3

For the lining tunnel, a Young Modulus, E, equal to 36283000 kPa and a Poisson coefficient, ν, equal to 0.2 were used. For the aboveground building, a Young Modulus, E, equal to 30000000 kPa and a Poisson coefficient, ν, equal to 0.2 were used. Unit weight of 25 kN/m³ was used for both the structure.

As regards the visco-elastoplastic analysis, the constitutive model developed by Gajo and Muir Wood (1999a and 1999b) was adopted. It is formulated within the framework of isotropic and kinematic hardening and bounding surface plasticity and it is capable of describing the general multiaxial stress-strain behaviour of granular material over a wide range of densities and mean pressures. This model was implemented in the ADINA code by the geotechnical research group of Catania university (Abate et al., 2007; 2008). The constitutive model was explained in Chapter 2.

Abate et al. 2008 performed many laboratory tests on "Plaja beach" soil in order to detect the parameters required by the Severn-Trent model. The values utilised in the present thesis are summarised in Table 4.14.
Summing up, thirty FEM analyses were performed as showed in Table 4.15.

Table 4.14: *Parameters of the Severn-Trent model used for the parametric analysis (Abate et al, 2008)*

E (kPa)	80000
ν	0.3
λ	0.03
v_{λ}	1.969
ϕ (°)	40
ψ (°)	10
R	0.1
A	0.9
k_d	1
B	0.0016
k	2
D	3%(PGA=0.2g) 4%(PGA=0.383g)

Table 4.15: FEM models analysed to perform the parametric analysis on the effect of soil constitutive model choice

Model 1	visco-elastic linear analysis with PGA=0.2g	Δz=17m
Model 2		Δz=12m
Model 3		Δz=7m
Model 4		Only aboveground structure
Model 5		Only tunnel: Δz=7m
Model 6	visco-elastic linear analysis with PGA=0.383g	Δz=17m
Model 7		Δz=12m
Model 8		Δz=7m
Model 9		Only aboveground structure
Model 10		Only tunnel: Δz=7m
Model 11	equivalent visco-elastic linear analysis with PGA=0.2g	Δz=17m
Model 12		Δz=12m
Model 13		Δz=7m
Model 14		Only aboveground structure
Model 15		Only tunnel: Δz=7m
Model 16	equivalent visco-elastic linear analysis with PGA=0.383g	Δz=17m
Model 17		Δz=12m
Model 18		Δz=7m
Model 19		Only aboveground structure
Model 20		Only tunnel: Δz=7m
Model 21	Severn-Trent model with PGA=0.2g	Δz=17m
Model 22		Δz=12m
Model 23		Δz=7m
Model 24		Only aboveground structure
Model 25		Only tunnel: Δz=7m
Model 26	Severn-Trent model with PGA=0.383g	Δz=17m
Model 27		Δz=12m
Model 28		Δz=7m
Model 29		Only aboveground structure
Model 30		Only tunnel: Δz=7m

4.7.6.1 Results in terms of dynamic bending moments and axial forces

Figure 4.69 shows the comparison between the numerical results and the analytical results (Wang, 1993) in terms of dynamic bending moment. The analytical results were achieved for the soil-tunnel No-Slip condition, since the values of dynamic bending moments varied little with the interface condition, while the dynamic axial force values were overestimated with No-Slip condition; thus this condition is more conservative. In particular, the dark blue lines show the results for the depth of the tunnel equal to 17 m; the red lines show the results for the depth of the tunnel equal to 12 me; the yellow lines show the results for the depth of the tunnel equal to 7 m. The dynamic bending moment values increased with the tunnel depth for all the models analysed and it does not depend on the peak ground acceleration nor the constitutive model analysed. These results occurred because the values of shear strain for a homogeneous soil increase with the depth, producing higher values of the dynamic bending moments for greater depth.

As regards the comparison between the numerical and analytical results, the analytical results overestimated the dynamic bending moment values for the visco-elastic linear model (Model 1, 2, 3, 6, 7,8) and for the “Severn Trent” model (Model 21, 22, 23, 26, 27, 28).

Different results were obtained for the equivalent visco-elastic linear analysis. In this case, the analytical results underestimated the values of the dynamic bending moments. Probably, the degradation of shear modulus G played a more important role than the increase in the damping ratio D, producing higher shear strain values and consequently higher values of dynamic bending moments in comparison with the analyses performed using the visco-elastic linear model and the Severn Trent model. Then, the lower dynamic bending moment was obtained with the Severn-Trent model due to soil plasticity, considered only in this model, while the higher values were obtained with the equivalent visco-elastic linear model, which considered a higher degradation of G.

Finally, as aspected, the values of dynamic bending moments achieved with a PGA=0.2g were lower than the values obtained with PGA=0.383g.

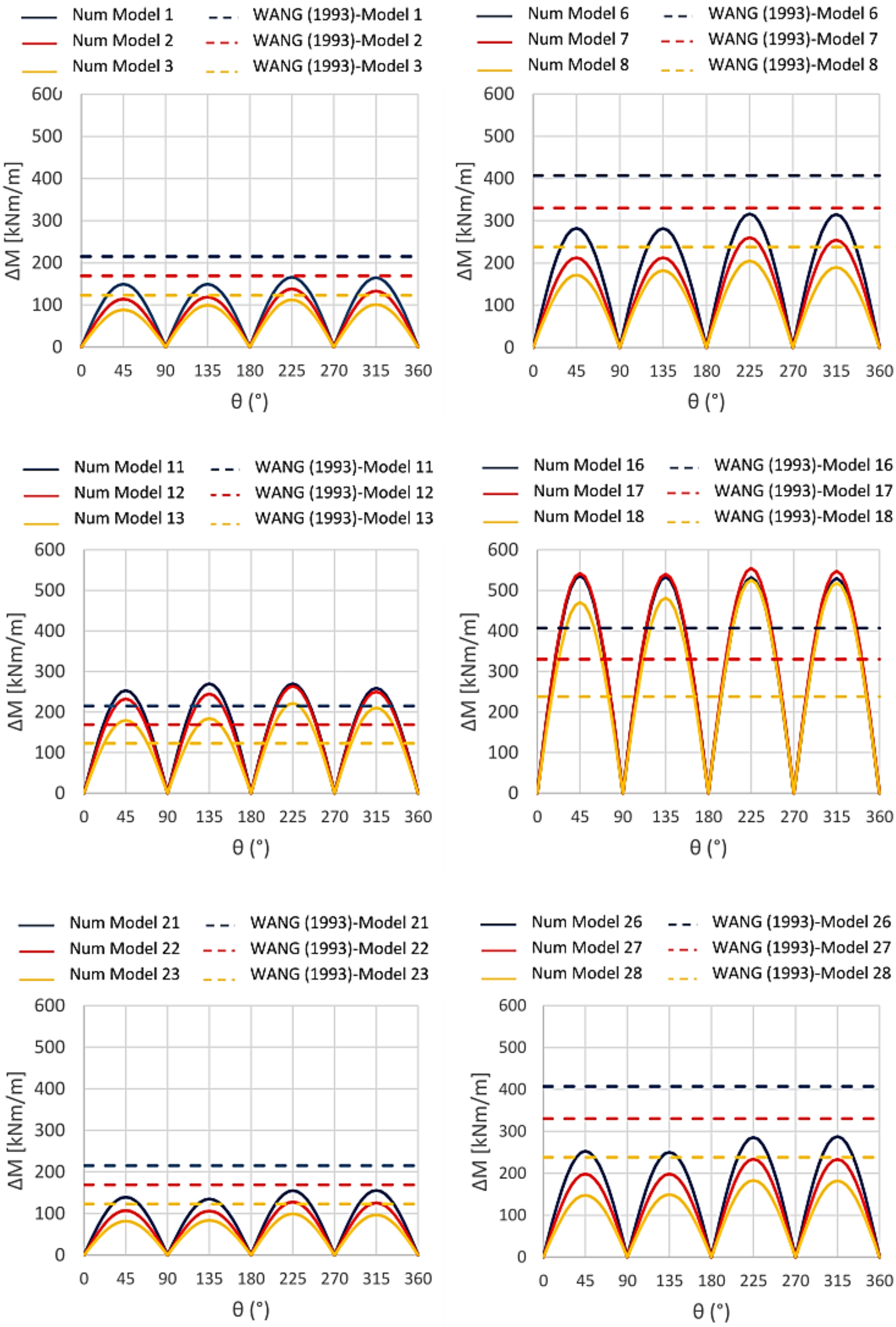

Figure 4.69: Comparison between the numerical and analytical results in terms of dynamic bending moments

Figure 4.70 shows the comparison between the numerical results and the analytical results (Wang, 1993) in terms of dynamic axial forces. As well as for the dynamic bending moment, even for the dynamic axial forces, a decrease of the values was achieved for smaller depths. Also in this case, this result was obtained because the values of shear strain for a homogeneous soil increases with the depth, producing higher values of dynamic bending moment for greater depth.

As regards the comparison between the numerical and analytical results, the analytical results underestimated the dynamic axial forces for each model analysed. Moreover, if the same geometric configuration is analysed, comparing the results of the Models 1, 6, 11, 16, 21 and 26 (dark blue lines) with the depth of the tunnel equal to 17m, similar results were achieved. The same results were obtained for the Models 2, 7, 12, 17, 22 and 27 (red lines) and for 3, 8, 13, 18, 23 and 28 (yellow lines). Consequently, the dynamic axial force results achieved for these models were very similar, showing a little variability with the chosen constitutive model.

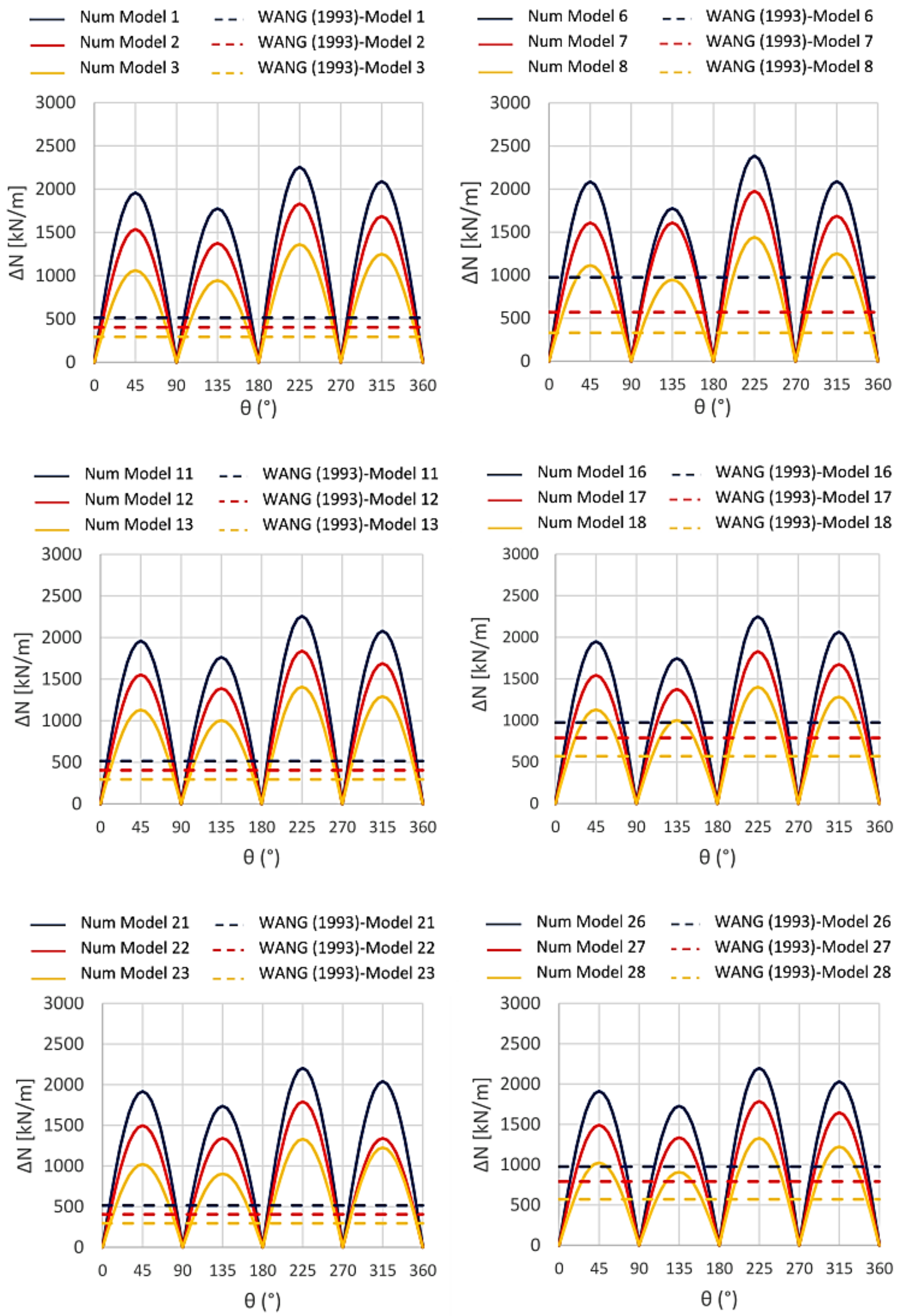

Figure 4.70: Comparison between the numerical and analytical results in terms of dynamic axial forces

Figure 4.71 shows the comparison between the dynamic bending moment for the same geometric condition, same PGA of the input motion (e.g. model 1, 11 and 21) but using a different constitutive model for the soil, to analyse the influence of the constitutive model used to describe the dynamic behaviour of the soil.

The dark blue line shows the results achieved for the visco-elastic linear analysis; the red line shows the results achieved for the equivalent visco-elastic linear analysis; finally, the yellow line shows the results obtained using the Severn Trent constitutive model for the soil. The dashed line shows the analytical results. From this Figure, it is possible to observe that the equivalent visco-elastic linear analysis overestimated the response of the tunnel line in terms of dynamic bending moment. The degradation of the elastic parameter, according to the G-γ-D for the soil analysed, involved a strong deterioration of the material, producing higher value in terms of dynamic bending moment.

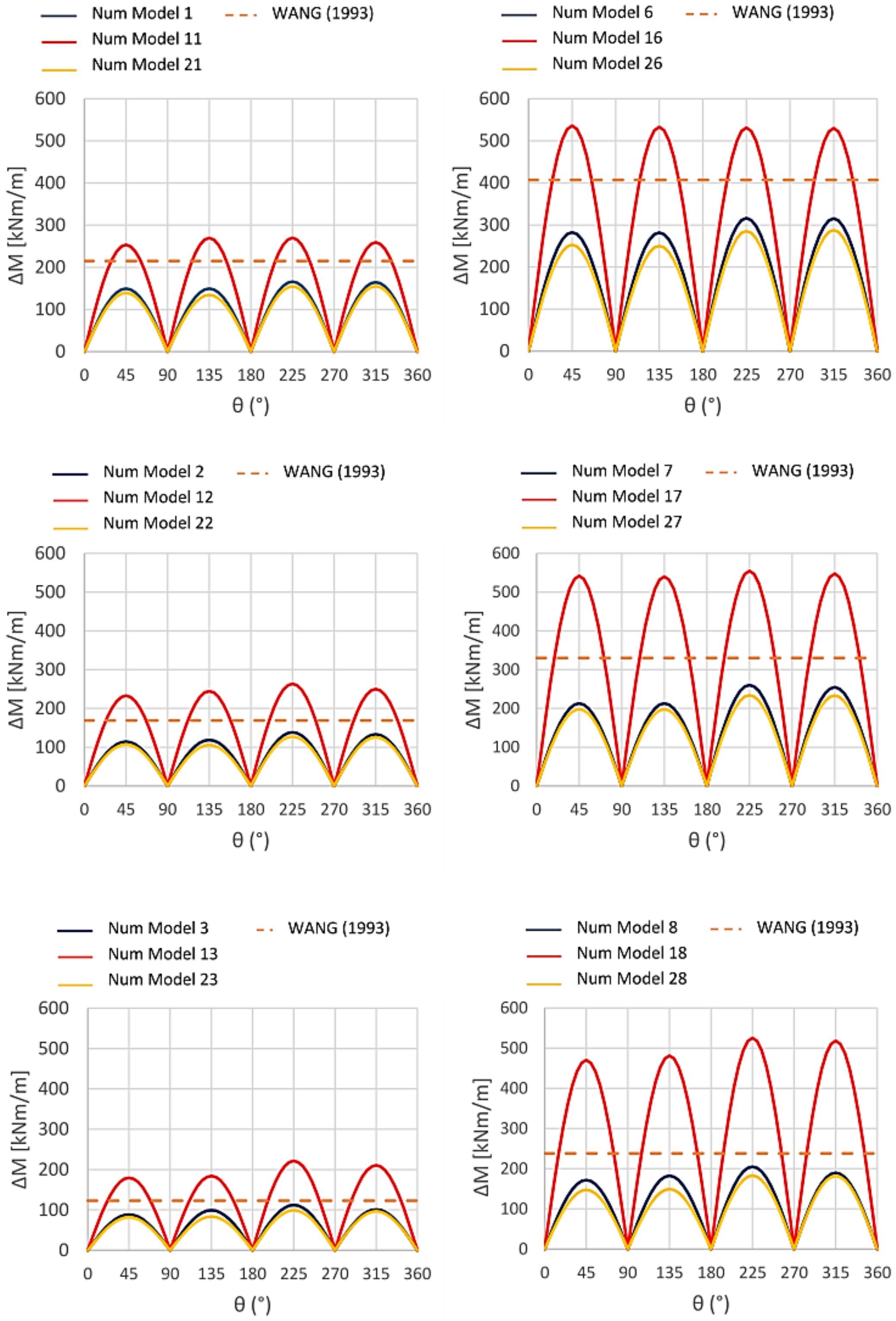

Figure 4.71: Comparison between the different constitutive models used in terms of dynamic bending moments

4.7.6.2 Results in terms of peak ground acceleration

Figure 4.72 shows the comparison between the numerical results of the analysed models in terms of peak ground acceleration along the tunnel alignment. In particular, the dark blue histogram shows the results for the model with the depth of the tunnel equal to 17 m; the red histogram shows the results for the model with the depth of the tunnel equal to 12 m; the green histogram shows the results for the model with the depth of the tunnel equal to 7 m; the yellow histogram shows the results for the model in which there is not the tunnel; the light blue histogram shows the results for the model in which there is not the aboveground structure.

From Figure 4.72, it was clear that the presence of the tunnel produced, generally, a decrease of the peak ground acceleration on the surface, for all the constitutive models used for the soil. The results of Figure 4.72 was also reported in Figure 4.73 for a clearer representation.

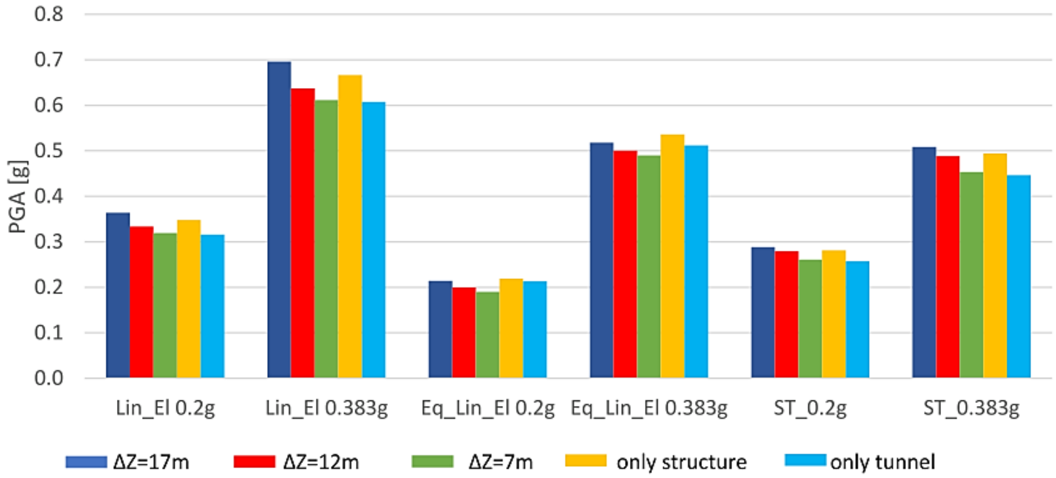

Figure 4.72: Comparison between the different analysed systems in terms of peak ground acceleration

In particular, Figure 4.73 shows the comparison between the free field alignment (F.F. Alignment) and the structure alignment (S. Alignment) for the analysed model. The three different analyses were highlighted: the region inside the dark blue line includes the visco-elastic linear analyses (from model 1 to model 5 for PGA=0.2g and from model 6 to model 10 for PGA=0.383g); the region inside the light blue line includes the equivalent visco-elastic linear analyses (from model 11 to model 15 for PGA=0.2g and from model 16 to model 20 for PGA=0.383g); the region inside the yellow line includes the "Severn Trent" analyses (from model 21 to model 25 for PGA=0.2g and from model 26 to model 30 for PGA=0.383g);

The peak ground acceleration achieved on the surface for the free field alignment was higher than the peak ground acceleration obtained along the structure alignment. This result was clear for all the analysed model. The tunnel, which is a void in the soil through which seismic waves cannot propagate, produce a decreasing of the signal that hits the aboveground structure. The gap changes with the different constitutive model used to describe the behaviour of the model. In particular, for the visco-elastic linear analysis (from model 1 to model 10 highlighted by the region delimited by the dark blue line), the gap between the two alignments is the greatest.

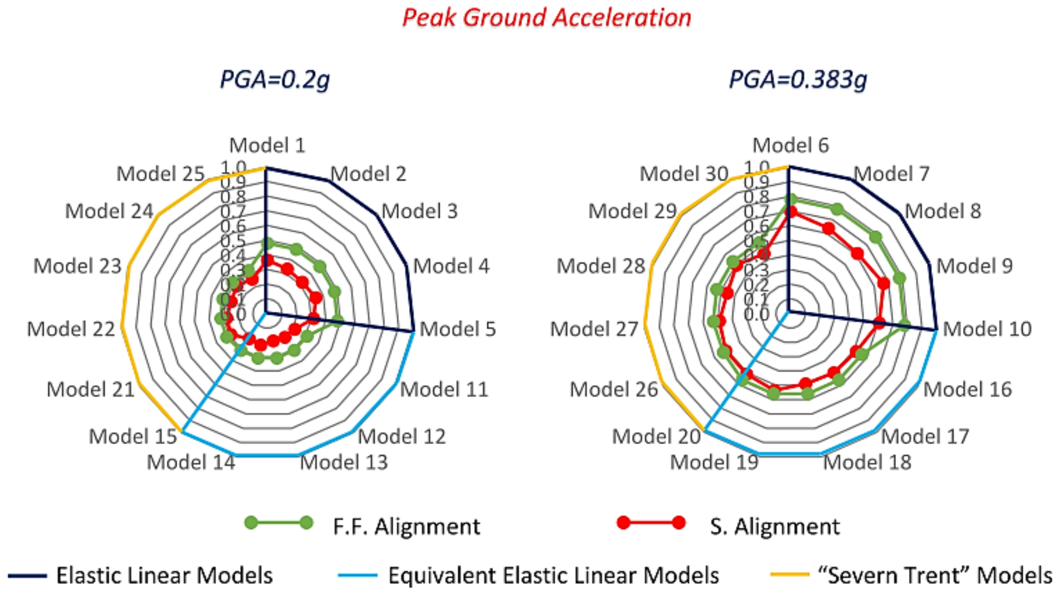

Figure 4.73: Comparison between the two alignments analysed in terms of peak ground acceleration at the soil surface

4.7.6.3 Results in terms of acceleration response spectra

Finally, Figures 4.74 and 4.75 show the results of the coupled tunnel-soil-aboveground structure system in terms of acceleration response spectra. The numerical results were compared with the response spectrum suggested by the Technical Regulation (NTC18) with a damping ratio for the structure equal to 5%. The soil analysed was characterized by a value of the shear waves velocity, V_S equal to 130 m/s, consequently, according to NTC18, the soil category is D. Figure 4.74 shows the comparison between the numerical acceleration response spectra achieved at the soil surface and the response spectra suggested by NTC18. In particular, the models in which the input motion is characterised by PGA=0.383g were showed.

A substantial gap between the numerical results and the spectrum suggested by the NTC18 for periods greater 1s was achieved. This could produce a strong error in the estimate of the spectral acceleration and consequently in the estimate of the forces impacting the aboveground structure. This result is clear for each model analysed and for each constitutive model used. Summing up, the numerical analysis of the fully coupled tunnel-soil-aboveground structure system revealed a gap with the NTC18, highlighting the importance to perform numerical analyses of the coupled soil-structure systems to take into account several aspects of dynamic interaction phenomena.

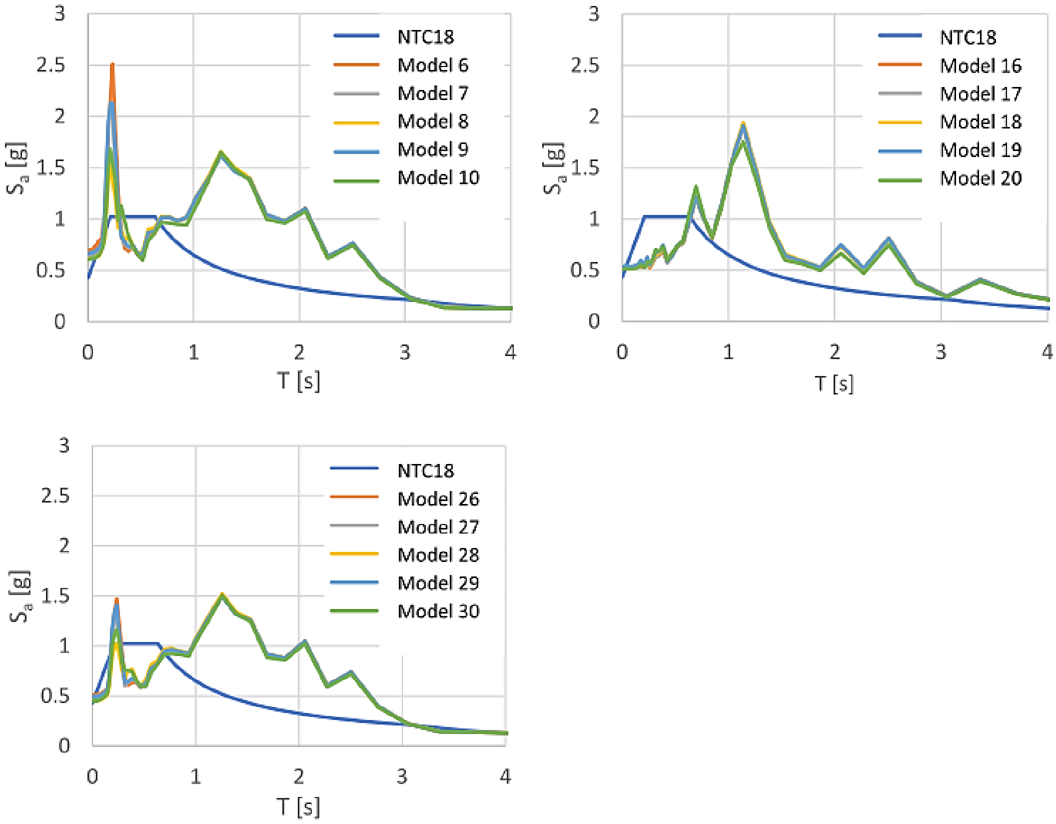

Figure 4.74: Comparison between the numerical acceleration response spectra and the response spectrum suggested by the NTC18

Figure 4.75 shows the numerical acceleration response spectra achieved for PGA=0.383g. Each figure refers to the same geometric model analysed for the three different constitutive models for the soil. In particular, the orange line shows the results obtained using the visco-elastic linear model (from Model 6 to Model 10); the grey line shows the results obtained using the equivalent visco-elastic linear model (from Model 16 to Model 20); the yellow line shows the results obtained using the Severn Trent model (from Model 26 to Model 30).

The first significant period is reached at T = 0.3s for the visco-elastic linear model and for the Severn-Trent model; while it is reached for a definitely greater value of T (1.1 s) for the equivalent visco-elastic linear model. This is due to the greater degradation of G and D obtained with the equivalent visco-elastic linear model.

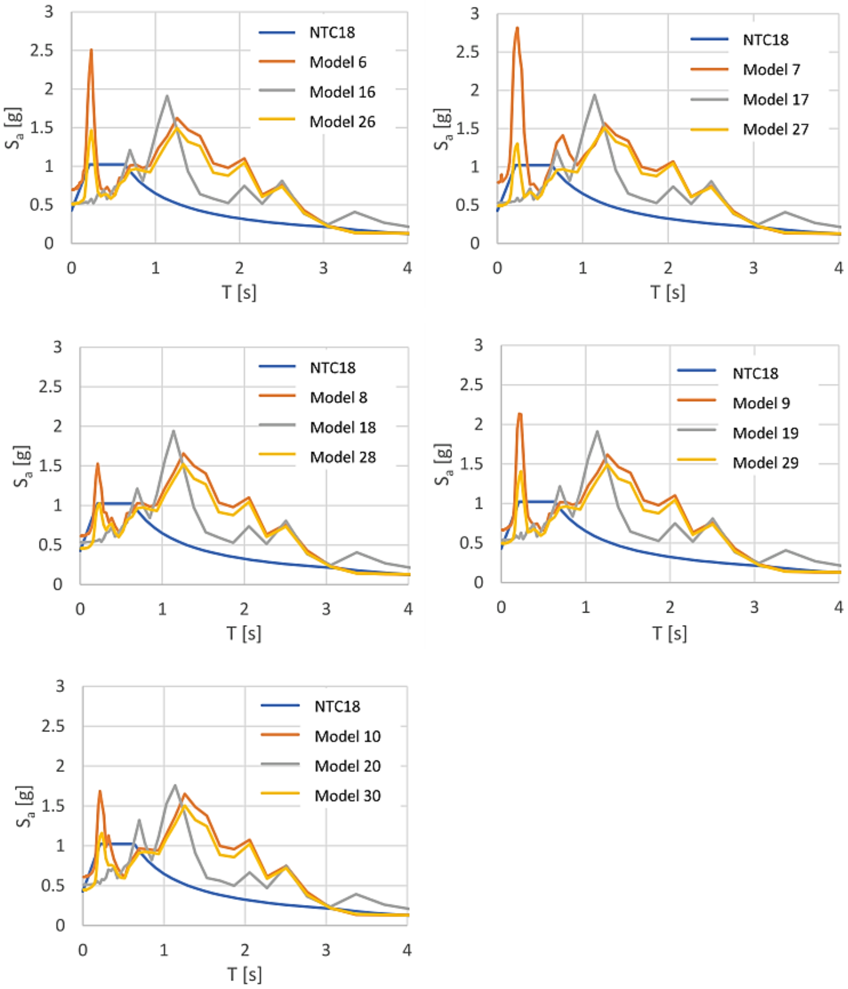

Figure 4.75: Comparison between the numerical acceleration response spectra and the response spectrum suggests by the NTC18 for the different constitutive models used for the soil

Summing up, the choice of the soil constitutive model can influence significantly the response of a soil-structure system producing in some cases more conservative results and in other cases less conservative ones.

CONCLUSIONS

In the last years, the need to build underground structures has increased in order to resolve the problems faced by transportation and utility networks. In particular, the underground structures contribute to the decrease of traffic on the roads and consequently to the reduction of air pollution. The role of underground structures has now become important within our society. Therefore, the need arose for greater attention to the dynamic design of underground structures. This work aimed to analyse some problems related to the design of an underground structure through 2D FEM analyses of fully coupled tunnel-soil-aboveground structure systems.

In order to develop the best FEM modelling for studying the behaviour of fully coupled tunnel-soil-aboveground structure systems different analyses were preliminarily performed with reference to simpler systems investigated by other researchers. In this phase, great attention was particularly devoted to the boundary conditions.

Then, a cross-section relating to the Nesima-Misterbianco segment belonging to Catania (Italy) underground was analysed through a FEM code. The tunnel is being dug using a Dual Mode TBM (Tunnel Boring Machine). The investigated area is characterised by a strong heterogeneity of the geological profile, due to the different lava flows caused by volcanic eruptions on Mount Etna in Catania; thus digging has proceeded in both the OF (Open Face) and EPB (Earth Pressure Balance) modes, switching frequently from one to the other. Geological and geotechnical information about the rocks and soils at the digging front is fundamental, firstly to define the appropriate digging mode and, consequently, to choose the correct front pressure to guarantee stability at the digging front. An error in the estimation of the front pressure can cause subsidence or uplift problems with disastrous effects in urban areas. For this reason, a simple and useful procedure was initially proposed to validate or not the soil profile established in the tunnels' design phase through the comparison between data obtained from the geotechnical survey at the design phase and data coming from HVSR method (Nakamura 1989), introduced by Nogoshi and Igarashi (1970; 1971). The HVSR method was applied on the microtremors induced on the soil surface layers by TBM during tunnelling. The new proposed procedure was successfully applied in a long segment of the Catania under-construction underground.

In a second phase, a transversal section of the underground structure in Catania with the tunnel at 17 m from the soil surface and a building on the surface located about 25 m from the axis of the tunnel was analysed. A 2D fully coupled tunnel-soil-aboveground structure finite element model was developed. Two synthetic accelerograms were adopted at the bedrock, assuming the source to be along the Hyblean-Maltese fault to refer to the scenario earthquake that occurred in eastern Sicily. Moreover, one accelerogram recorded during the earthquake that occurred in 1990 at the South-est of Sicily was used.

Finally, parametric analyses were performed. The first parametric analysis was devoted to study the effect of the interface between the tunnel and the soil comparing the numerical results with analytical results. The main analytical methods offer solutions for the two-limit conditions: i) No-Slip condition, for which there is not sliding at the soil-tunnel interface; ii) and Full-Slip condition, for which there is a complete sliding at the soil-tunnel interface. But the real condition is between the Full-Slip and No-Slip condition. So, numerical analyses with three different interface conditions were analysed: 1) No-Slip condition; 2) Full-Slip condition, 3) intermediate slip condition. The results were obtained in terms of dynamic bending moment and axial force on the tunnel. The results show that the dynamic bending moment did not substantially vary with the contact conditions. On the other hand, the dynamic axial force revealed a strong variability with the interface condition, achieving the highest values for No-Slip condition. Consequently, all the subsequent FEM analyses were performed using the No-Slip condition at the soil-tunnel interface.

At the soil-aboveground structure interface, partial soil-foundation sliding and/or foundation uplifting were considered.

The second parametric analysis was performed to analyse the effect of strong soil discontinuities at the depth of the tunnel. Numerical results were compared with analytical results obtaining a remarkable difference. The analytical solutions were efficient for homogeneous soil at the depth of the tunnel; nevertheless, an important disagreement between analytical and numerical results existed for heterogeneous soil at the depth of the tunnel. In particular, the disagreement increased with the impedance ratio, i.e. the ratio between the stiffness of the first layer and the stiffness of the second layer crossed by the tunnel. A strong soil stiffness discontinuity at the tunnel depth produces strong concentration of strains and stresses in the soil and in turn on the tunnel. Thus, the design of tunnel crossing two or more layers characterised by very different stiffnesses has to be avoided.

The third parametric analysis was carried out to analyse the influence of the depth of the tunnel and the position of the building on the surface relating to the tunnel axis. An equivalent viscoelastic linear analysis was performed. The results were obtained in terms of lining force along the tunnel, peak ground acceleration on the soil surface, acceleration response spectra, Fourier spectra and seismic forces on the building.

In general, the presence of the tunnel in the soil deposit caused a small de-amplification across the tunnel with a beneficial effect on the urban area, obtaining a larger de-amplification the less deep is the tunnel. Moreover, in terms of seismic forces on the structure, numerical results were compared with the seismic forces suggested by the Italian Technical Code (NTC18), obtaining strong differences. In particular, smaller values were obtained through numerical analyses. This result occurred because numerical analyses allowed lifting and sliding phenomena at the foundation level. These phenomena led in turn to a decrease in seismic forces on the aboveground structure and an increase in the period of the aboveground building.

The fourth and final parametric analysis was performed for investigating the effects of the choice of the soil constitutive model on the numerical modelling of the seismic response of fully coupled tunnel-soil-aboveground structure systems. In particular, three different constitutive models were used: 1) visco-elastic linear; 2) equivalent visco-elastic linear; 3) visco-elasto-plastic with kinematic and isotropic hardening.

The different constitutive model used to describe dynamic behaviour of the soil was particularly important to evaluate the dynamic bending moment and axial force along the tunnel lining, since the line forces depend on the shear strain of the soil. Consequently, the use of a constitutive model for the soil that manages to describe satisfactorily the dynamic behaviour of the soil, is fundamental to evaluate correctly the shear strain of the soil and consequently the line force along the tunnel.

References

Abate G., Bosco M., Massimino M.R., Maugeri M. (2006). “Limit state analysis for the Catania fire-station (Italy)”. In: 8th US National conference on earthquake engineering 2006, vol 11, 2006, pp 6532–6541.

Abate G., Caruso C., Massimino M.R., Maugeri M. (2007). “Validation of a new soil constitutive model for cyclic loading by FEM analysis. Solid Mechanics and its Applications”. Vol. 146, 2007, pp. 759-768. ISSN: 09250042. Codice Rivista: E156877.

Abate G., Caruso C., Massimino M.R., Maugeri M. (2008). “Evaluation of shallow foundation settlements by an elasto-plastic kinematic-isotropic hardening numerical model for granular soil”. Geomechanics and Geoengineering Journal. Vol. 3(1), pp. 27-40 ISSN: 1748-6025. DOI: 10.1080/17486020701862174.

Abate G., Massimino M.R., Maugeri M. (2015). “Numerical Modelling of centrifuge tests on tunnel-soil systems”. Bulletin of Earthquake Engineering. Volume 13, Issue 7, pp. 1927-1951, 2015. https://doi.org/10.1007/s10518-014-9703-0.

Abate G., Corsico S., Massimino M.R. (2016). “FEM Modelling of the Seismic Behaviour of a Tunnel-soil-Aboveground Building System: A Case History in Catania (Italy)”. Procedia Engineering. 158(2016), pp. 380-385. ISSN: 1877-7058. https://doi.org/10.1016/j.proeng.2016.08.459.

Abate G., Corsico S., Massimino M.R., Romano S. (2016). "FEM modelling of the Seismic behavior of a tunnel-soil-aboveground building system: the case history of Catania (Italy)".VI Italian Conference of Researchers in Geotechnical Engineering – Geotechnical Engineering in Multidisciplinary Research: from Microscale to Regional Scale, CNRIG2016. Procedia Engineering 158: 374-379. ISSN: 1877-7058.

Abate G., Massimino M.R. (2017). "Parametric analysis of the seismic response of coupled tunnel – soil – aboveground building systems by numerical modelling". Bull. Earthq. Eng. 15 (1), 443 – 467 (2017). https://doi.org/10.1007/s10518-016-9975-7.

Abate G., Massimino M.R. (2017). "Numerical modelling of the seismic response of a tunnel–soil–aboveground building system in Catania (Italy)". Bulletin of Earthquake Engineering, 15(1), 469–491. https://doi.org/10.1007/s10518-016-9973-9

Abate G., Grasso S., Massimino M.R. (2019). "The role of shear wave velocity and non-linearity of soil in the seismic response of a coupled tunnel-soil-above ground building system". Geosciences, Vol. 9, Issue 11, November 2019, Article number 473. https://doi.org/10.3390/geosciences9110473.

ABAQUS (2012). Theory and analysis user's manual, version 6.12. Providence: Dassault Systèmes SIMULIA.

Adamidis O., Gazetas G., Anastasopoulos I., Argyrou C. (2014). "Equivalent-linear stiffness and damping in rocking of circular and strip foundations". Bull Earthq Eng 12(3):1177–1200 (2014). https://doi.org/10.1007/s10518-013-9554-0

ADINA (2008), "Automatic Dynamic Incremental Nonlinear Analysis. Theory and Modelling Guide", ADINA R&D, Inc. Watertown, USA.

Agrawal P. K. et al. (1983). "Seismic Response of Buried Pipes and Structural Components", ASCE Committee on Seismic Analysis on Nuclear Structures and Materials, 1983.

AFPS/AFTES (2001). “Guidelines on earthquake design and protection of underground structures”, Working group of the French association for seismic engineering (AFPS) and French Tunnelling Association (AFTES) Version 1.

Anagnostou G., Kovari K. (1994). “The face stability of slurry- shield driven tunnels”. Tunneling and Underground Space Technology. 9(2), pp. 165-174. https://doi.org/10.1016/0886-7798(94)90028-0.

Anagnostou G., Kovari K. (1996). “Face stability in slurry and EPB shield tunneling”. Geotechnical Aspects of Underground Construction in Soft Ground. Rotterdam, Balkema, pp. 453-458. ISBN 90 5410 856 8.

Anastasopoulos I., Gazetas G., Bransby M.F., Davies M.C.R., El Nahas A. (2007b). “Fault rupture propagation through sand: Finite-element analysis and validation through centrifuge experiments”. Journal of Geotechnical and Geoenvironmental Engineering, 133(8):943-958. DOI: 10.1061/ASCE1090-0241(2007)133:8(943).

Anastasopoulos I., Gerolymos N., Drosos V., Kourkoulis R., Georgarakos T., Gazetas G. (2007). “Nonlinear Response of Deep Immersed Tunnel to Strong Seismic Shaking”, J. Geotech. Geoenviron. Eng., 2007, 133(9): 1067-1090. DOI: 10.1061/(ASCE)1090-0241(2007)133:9(1067).

Anastasopoulos I., Gerolymos N., Drosos V., Georgarakos T., Kourkoulis R., Gazetas G. (2008). “Behaviour of deep immersed tunnel under combined normal fault rupture deformation and subsequent seismic shaking”. Bull Earthquake Eng, 6:213–239. https://doi.org/10.1007/s10518-007-9055-0.

Anastasopoulos I., Gazetas G. (2010). “Analysis of cut-and-cover tunnels against large tectonic deformation”, Bull Earthquake Eng. 8:283–307. DOI: 10.1007/s10518-009-9135-4.

Argyris J. H. et al. (1973). “Recent development in finite element analysis of PCRV”. Proc. 2nd Int. Conf., SMIRT, Berlin.

Argyroudis, A., Pitilakis, K. (2012). “Seismic fragility curves of shallow tunnels in alluvional deposits”. Soil Dynamics and Earthquake Engineering, 35, 1–12. https://doi.org/10.1016/j.soildyn.2011.11.004.

Argyroudis S., Tsinidis G., Gatti F., Pitilakis K. (2017). “Effects of SSI and lining corrosion on the seismic vulnerability of shallow circular tunnels”. Soil Dynamics and Earthquake Engineering Volume 98, July 2017, Pages 244-256. https://doi.org/10.1016/j.soildyn.2017.04.016.

ASCE, (1974). Earthquake damage evaluation and design considerations for underground structures, February. American Society of Civil Engineers, Los Angeles Section.

Atkinson J.H., Potts D.M. (1977). “Subsidence above shallow tunnels in soft ground”. Journ. of Geotech. Eng. Division. ASCE GT4, Vol. 103, pp.307-325. DOI:10.1016/0148-9062(77)91056-7.

Attewell P.B. (1978). “Ground movements caused by tunnelling in soil”. Proc. Conf. on Large Ground Movements and Structures. Cardiff, July, pp. 812-948.

Attewell P.B., Taylor R.K. (1984). Ground movements and their effects on structures, pp. 132-212.

Azzaro R., Barbano M.S., Moroni A., Mucciarelli M., Stucchi M. (1999): "The Seismic History of Catania"; Journal of Seismology, 3, 3, pp. 235 - 252.

Azzaro R., Barbano M. S. (2000): "Seismogenetic Features of SE Sicily and Scenario Earthquakes for Catania. The Catania Project: Earthquake Damage Scenarios for a High Risk Area in the Mediterranean, part I: Seismotectonic Framework and Earthquake Scenarios"; CNR-Gruppo Nazionale per la Difesa dai Terremoti, Roma, pp. 9 - 13.

Banna G., Capilleri P., Massimino M.R., Motta E., (2015). “Geotechnical characterization of Mount Etna ash for its reuse preserving human health”. Volcanic Rocks and Soils – Proc. of the International Workshop on Volcanic Rocks and Soils, 2015, pp. 197-204.

Barbano M.S., Pirrotta C., Gerardi F. (2010). "Large Boulders Along the South-Eastern Ionian Coast of Sicily: Storm or Tsunami Deposits?"; Marine Geology, 2010, (275): 140 - 154.

Bardet JB, Ichii K, Lin CH. (2000) EERA: a computer program for equivalent-linear earthquake site response analyses of layered soil deposits. Los Angeles: University of Southern California, Department of Civil Engineering.

Been K., Jefferies M.G. (1985). “A state parameter for sands”. Géotechnique, 35(1), 99-112.

Bilotta E., Lanzano G., Russo G., Santucci de Magistris, Silvestri F. (2007). “Methods for the seismic analysis of transverse section of circular tunnels in soft ground”. In ISSMGE-ERTC12 workshop at XIV ECSMGE “Geotechnical Aspects of EC8 ”. Patron Editore. Chapter 22.

Bilotta E., Madabhushi S.P.G., Silvestri F. (2014a). Editorial: Round Robin Tunnel Test (RRTT). Acta Geotechnica, 9(4):561-562.

Bilotta E., Lanzano G., Madabhushi S.P.G., Silvestri F. (2014b). A numerical Round Robin on tunnels under seismic actions. Acta Geotechnica, 9(4):563-579.

Biondi G., Massimino M.R., Maugeri M. (2015). “Experimental study in the shaking table of the input motion characteristics in the dynamic SSI of a SDOF model”, Bulletin of Earthquake Engineering. Volume 13, Issue 6, pp. 1835-1869, 2015.

Boschi E., Ferrari G., Gasperini P., Guidoboni E., Smriglio G., Valensise G. (1995): "Catalogo dei Forti Terremoti in Italia dal 461 a.C. al 1980"; ING SGA, Ozzano Emilia, 973 pp. (in Italian)

Broere W. (2002). “Influence of excess pore pressures on the stability of the tunnel face”. Geotechnical Aspects of Underground Construction in Soft Ground. Toulouse, France, pp. 179-184.

Burland J. B., Roscoe P.W. (1968). “On the generalized stress-strain behaviour of ‘wet’ clay”. In: J. Heyman and F. A. Leckie (Editors), Engineering Plasticity. Cambridge University Press, Cambridge, England, 535-609.

Burland J.P. (1995). “Assessment of risk of damage to buildings due to tunnelling and excavation”. First International Conference on Earthquake Geotechnical Engineering of Tokyo. November 1-12, 1995.

Burns J.Q., Richard R.M. (1964). “Attenuation of stresses for buried cylinders”. In: Symposium on soil–structure interaction. University of Arizona, Tempe, AZ

Capilleri P.P., Massimino M.R., (2019). “Geotechnical characterization of ash collected during a recent eruptive event of Mount Etna”. Geomech. Geophys. Geo-energ. Geo-resour. Volume: 5. Issue: 4, pp. 383-403. ISSN 2363-8419.

Carranza-Torres C., Reich T., Saftner D. (2013). “Stability of shallow circular tunnels in soils using analytical and numerical models”. Proceedings of the 61st Minnesota Annual Geotechnical Engineering Conference. University of Minnesota, St. Paul Campus. February 22, 2013.

Caruso S., Ferraro A., Grasso S., Massimino M.R. (2016). “Site Response Analysis in eastern Sicily based on direct and indirect Vs measurements”. 1st IMEKO TC4 International Workshop on Metrology for Geotechnics, MetroGeotechnics 2016, pp. 115-120.

Castelli, F., Lentini, V., Maugeri, M. (2008a): "One-dimensional Seismic Analysis of a Solid-Waste Land-fill"; Proceedings MERCEA 2008, 2008 Seismic Engineering International Conference Commemorating the 1908 Messina and Reggio Calabria Earthquake, Reggio Calabria and Messina, July 8 -11,Vol.1, pp. 509 - 516.

Castelli F., Maugeri M., Mylonakis G. (2008b): "Numerical Analysis of Kinematic Soil-Pile Interaction"; Proceedings MERCEA 2008, Seismic Engineering International Conference Commemorating the 1908 Messina and Reggio Calabria Earthquake, Reggio Calabria and Messina, July 8- 11, Vol.1, pp. 618 - 625.

Castelli F., Maugeri M. (2008): “Experimental Analysis of Waste Compressibility”. In Proc. of GeoCongress 2008 March 9-12, 2008|New Orleans, Louisiana, doi.org/10.1061/40970(309)26.

Castelli, F., Lentini, V. (2013): "Landsliding Events Triggered by Rainfalls in the Enna Area (South Italy)", Proceedings of the Second World Landslide Forum, Roma, 3 - 7 October 2011, Springer eds., Volume 2, pp. 39 - 47.

Castelli, F., Lentini, V. (2016). "Monitoring of Full Scale Diaphragm Wall for a Deep Excavation"; Proceedings 1st IMEKO TC4 International Workshop on Metrology for Geotechnics, Benevento, Italy, March 17 - 18, 2016, pp. 103 - 108.

Castelli F., Castellano E., Contino F., Lentini V. (2016): "A Web-Based GIS System for Landslide Risk Zonation: the Case of Enna Area (Italy)"; Proceedings 12th International Symposium on Land-slides (ISL 2016) - Napoli, Italy, June 12 - 19, 2016, Volume 2, pp. 595 - 603, ISBN: 978-1-138-02990-3 (set of 3 volumes 978-1-138-02988-0).

Castelli F., Grasso S., Lentini V., Massimino M.R. (2016). “In situ measurements for evaluating liquefaction potential under cyclic loading”. 1st IMEKO TC4 International Workshop on Metrology for Geotechnics, MetroGeotechnics 2016, pp. 79-84.

Castelli, F., Freni, G., Lentini, V. and Fichera, A. (2017). "Modelling of a Debris Flow Event in the Enna Area for Hazard Assessment"; Proceedings I International Conference on the Material Point Method, MPM 2017, Delft, Olanda, 10 - 12 Gennaio 2017.

Castelli F., Cavallaro A., Ferraro A., Grasso S., Lentini V., Massimino M.R., (2018). “Static and dynamic properties of soils in Catania (Italy)”. Annals of Geophysics, 61,2, SE221, 2018; DOI: 10.4401/ag-7706.

Cavallaro A., Maugeri M. (2005). “Non linear behaviour of sandy soil for the city of Catania”, In book: Seismic Prevention of Damage: A Case Study in a Mediterranean CityPublisher: Wit Press PublishersEditors: Maugeri M. DOI: 10.2495/1-84564-004-7/07

Cavallaro A., Grasso S., Maugeri M., (2006). "Volcanic Soil Characterisation and Site Response Analysis in the City of Catania"; Proceedings of the 8th National Conference on Earthquake Engineering, San Francisco, 18 - 22 April 2006, paper n°. 1290, pp. 835 - 844.

Cavallaro, A., Grasso, S., Maugeri, M., (2008a): "Site Response Analysis for Tito Scalo Area (PZ) in the Basilicata Region, Italy"; Proceedings of the 4th Geotechnical Earthquake Engineering and Soil Dynamics Conference, Sacramento, 18 - 22 May 2008, ASCE - Geotechnical Special Publication (GSP) N°. 181.

Cavallaro A., Ferraro A., Grasso S., Maugeri M., (2008b). "Site Response Analysis of the Monte Po Hill in the City of Catania"; Proceedings of the 2008 Seismic Engineering International Conference Commemorating the 1908 Messina and Reggio Calabria Earthquake MERCEA'08, Reggio Calabria and Messina, 8 - 11 July 2008, pp. 240 - 251. AIP Conference Proceedings, Volume 1020, Issue PART 1, 2008, pp. 583 - 594.

Cavallaro A., Ferraro A., Grasso S., Maugeri M. (2012). "Topographic effects of the Monte Po hill in Catania (Italy)", Soil Dynamics and Earthquake Engineering. ISSN: 0267-7261. Volume 43, pp. 97-113. doi: 10.1016/j.soildyn.2012.07.022, 2012.

Chen W. F., Baladi G. Y. (1985). "Soil plasticity: theory and implementation", Elsevier, New York.

Chen W. F., Saleeb A. F. (1986). "Constitutive Equations for Engineering Materials. Vol.2 – Plasticity and Modelling". Wiley-Interscience, New-York.

Cheng, C.Y., Dasari, G.R., Leung, C.F., Chow, Y.K., Rosser, H.B. (2004). "3D numerical study of tunnel-soil-pile interaction". Tunn. Undergr. Sp. Technol. 19 (4 – 5), 381 – 382 (2004)

Chopra A.K. (2007). "Dynamics of structures, Theory and applications to earthquake engineering", third edition, Pearson, ISBN 0-13156174.

Dafalias Y. F., Popov E. P. (1975). “A model of nonlinearly hardening materials for complex loading”. Acta Mech., 21, 173-192.

Dafalias Y. F., Papadimitriou A. G. (2005). “Constitutive Modelling in Soil Plasticity. A Short Course”. Dep. Of Civil Eng., Uni. of Bari, Italy, September 27-30, 2005.

Darendeli M. (2001). “Development of a new family of normalized modulus reduction and material damping curves”. [PhD. thesis]. Austin: University of Texas; 2001.

De Barros F.C.P., Luco J.E. (1993). “Diffraction of obliquely incident waves by a cylindrical cavity embedded in a layered viscoelastic halfspace”. Soil Dyn Earthq Eng 12:159–171

De Rubeis V., Gasparini C., Maramai A., Anzidei M. (1991), "Il Terremoto Siciliano del 13 Dicembre 1990"; Proc. Contributi allo studio del Terremoto della Sicilia Orientale del 13 Dicembre 1990. National Institute of Geophisics, Roma.

di Prisco C. (1993). “Studio sperimentale e modellazione matematica del comportamento anisotropo delle sabbie”. Ph. D. thesis, Politecnico di Milano.

di Prisco C., Nova R., Lanier J. (1993). “A mixed isotropic kinematic hardening constitutive law for sand”. Modern approach to plasticity, D. Kolymbas ed., Balkema, 83-124.

Do, N. A., Dias, D., Oreste, P., Maigre, I. D. (2015). “2D numerical investigation of segmental tunnel lining under seismic loading”. Soil Dynamics and Earthquake Engineering, 72(2015), 66–76.

Dobry R., Oweis I., Urzua A. (1976). “Simplified procedures for estimating the fundamental period of a soil profile”, Bull. Seismol. Soc. Am. 66, 4. pp. 1293-1321.

Dowding C. H., Rozen A. (1978). “Damage to Rock Tunnels from Earthquake Shaking”, Journal of the Geotechnical Engineering Division, ASCE, Vol. 104, No. GT2, 175-191 February 1978.

Drucker D. C, Greenberg J. H., Prager W. (1952). “Extended limit design theorems for continuous media”, Q. Appl. Math., 9: 381-389.

Drucker D. C, Prager W. (1952). “Soil mechanics and plastic analysis or limit design”, Q. Appl. Math., 10 (2): 157-164.

Drucker D. C., Gibson R. E., Henkel D. J. (1957). “Soil Mechanics and Work-Hardening Theories of Plasticity”, Trans., ASCE, 122, 338-346.

Drucker D. C. (1959). “A definition of stable inelastic material”.J. App. Mech., 26, 101-106.

Duke, C.M., Leeds, D.J. (1959). “Effects of Earthquakes on Tunnels”, Paper Presented at the RAND Second Protective Construction Symposium, March 24 - 26.

El Nahas A., Bransby M.F., Davies M.C.R. (2006). “Centrifuge modelling of the interaction between normal fault rupture and rigid, strong raft foundations”. In: Ng C.W.W., Wang Y.H. and Zhang L.M. (eds.) Proceedings of the Sixth International Conference on Physical Modelling in Geotechnics, 6th ICPMG’ 06, 337-342, Taylor & Francis Group, London, UK.

Faccioli E., Pessina V., (2000). “The Catania Project: Earthquake damage scenarios for a risk area in the Mediterranean”. E. Faccioli & V. Pessina Editors. CNR - Gruppo nazionale per la difesa dei terremoti. ISBN: 88-900449-0-X.

FHWA (2009). “Technical manual for design and construction of road tunnels – Civil elements”, U.S. Department of transportation, Federal Highway Administration, Publication No. FHWA-NHI-09-010, March 2009.

Gajo A., Muir Wood D. (1998). “Numerical analysis of shear stack under dynamic loading”, Proc. 11th Eur. Conf. On Earthquake Engineering, Balkema, Rotterdam.

Gajo A., Muir Wood D. (1999.a). “Severn-Trent sand: a kinematic-hardening constitutive model: the q-p formulation”. Géotechnique, 49(5), 595-614.

Gajo A., Muir Wood D. (1999.b). “A kinematic hardening constitutive model for sands: the multiaxial formulation”. Int. Journal Numer. Anal. Meth. Geomech., 23, 925-965.

Ghaboussi J., Momen H. (1982). “Modelling and analysis of cyclic behaviour of sands”. G. N. Pande & O. C. Zienkiewicz (Eds.), Soil Mechanics: Transient and cyclic loads, 313-342, Wiley, New York.

Gazetas G. (2014). “Case histories of tunnel failures during earthquakes and during construction”, Proc. of the Half-Day Conference, A Tunnel/Underground Station Failure Conference, by the Israeli Geotechnical Society, 19th of January, 2014.

Gazetas G. (2015). 4th Ishihara lecture: “soil–foundation–structure systems beyond conventional seismic failure thresholds”. Soil Dyn Earthq Eng 68:23–39.

Gizzi F. T., (2006), "To What Degree Can Historical Seismicity Records Assist in Seismic Microzonation?", Engineering Geology, 87: pp. 1 - 12.

Guo J., Chen J.Y., Bobet A. (2013). “Influence of a subway station on the inter-story drift ratio of adjacent surface structures”. Tunnelling and Underground Space Technology, 2013 35: 8 – 19

Haibin H., Hao C., Jubo Z. (2014). “ The Influence of foundation excavation on the existing metro tunnel in complicated environment”, Electron. J. Geotech. Eng., vol. 19 N, pp. 3377 – 3385, 2014

Hashash Y.M.A., Hook J.J., Schmidt B. and Yao J.I-C. (2001). “Seismic design and analysis of underground structures”, Tunneling and Underground Space Technology, 16(2): 247-293.

Hashash Y.M.A., Park D., Yao J.I.C. (2002). “Viscous damping formulation and high frequency motion propagation in non-linear site response analysis”, Soil Dynamics and Earthquake Engineering Volume 22, Issue 7, September 2002, Pages 611-624, https://doi.org/10.1016/S0267-7261(02)00042-8

Hashash Y.M.A., Park D., Yao J.I.C. (2005). “Ovaling deformations of circular tunnels under seismic loading, an update on seismic design and analysis of underground structures”, Tunnelling and Underground Space Technology 20 (2005): 435–441.

Hashash Y., Musgrove M., Park D., Chi-Chin Tsai, Philips C. and Groholski D. (2018). 1D wave propagation program for geotechnical site response, v.7.0.

Hashiguchi K. (1979). “Constitutive equations of granular media with anisotropic hardening”. III Int. Conf. Num. Meth. in Geomechanics, Aechen, Germany, 435-439, Balkema, Rotterdam.

Hoeg K. (1968). “Stresses against underground structural cylinders”, J. Soil Mech. Found. Div., ASCE 94 SM4 833 - 858.

Huang Z., Pitilakis K., Tsinidis G., Argyroudis S., Zhang D. (2020). “Seismic vulnerability of circular tunnels in soft soil deposits: The case of Shanghai metropolitan system”. Tunnelling and Underground Space Technology Volume 98, April 2020, 103341. https://doi.org/10.1016/j.tust.2020.103341

Huo H., Bobet A., Fernández G., Ramírez J. (2005). “Load transfer mechanisms between underground structure and surrounding ground: Evaluation of the failure of the Daikai station”, Journal of Geotechnical and Geoenvironmental Engineering, 131(12):1522-1533.

Idriss I.M., Seed H.B. (1968). “Seismic response of horizontal soil layers”, J. Soil Mech. Found. Div., ASCE 94 SM4, 1003 - 1031.

Idriss I.M., Sun J.I. SHAKE91 (1992): a computer program for conducting equivalent linear seismic response analyses of horizontally layered soil deposits. Center for Geotechnical Modelling, Department of Civil and Environmental Engineering, University of California, Davis, 1992

Imposa S., Motta S., Capilleri P., Imposa G. (2016). "HVSR and MASW seismic survey for characterizing the local seismic response: a case -study in Catania area (Italy)" 1st International Workshop on Metrology for Geotechnics, Benevento, Italy, March 17-18, 2016.

Iwan W. D. (1967). "On a class of models for the yielding behaviour of continuous and composite systems". J. Appl. Mech, 34, 612-617.

Jacobsz S.W., Standing J.R., Mair R.J., Hagiwara T., Sugiyama T. (2004). "Centrifuge modelling of tunnelling near driven piles". Soils Found. 44 (1), 49 – 56 (2004).

JSCE, (1988). "Earthquake Resistant Design for Civil Engineering Structures in Japan". Japanese Society of Civil Engineers, Tokyo.

Kaneshiro, J.Y., Power, M., Rosidi, D., (2000). "Empirical correlations of tunnel performance during earthquakes and aseismic aspects of tunnel design". Proceedings of the Conference on Lessons Learned From Recent Earthquakes - On Earthquakes in Turkey 1999, November 8 - 11.

Kawashima K. (2000). "Seismic design of underground structures in soft ground: a review", In Fujita, Miyazaki (Eds.), Geotechnical aspects of underground construction in soft ground, Balkema, Rotterdam.

Kelly P. (2013) - Part II, Lecture notes, The University of Auckland, 2013(Kelly, P., 2013, Solid Mechanics Lecture Notes Part II, The University of Auckland. pp. 66-76.

Kyriazis P., Grigorios T., Andrea L., Maugeri M. (2014). "Seismic behaviour of circular tunnels accounting for above ground structures interaction effects". Soil Dynamics and Earthquake Engineering, 2014, 67: 1 – 15.

Kirtas E., Rovithis E., Pitilakis K. (2009). "Subsoil interventions effect on structural seismic response", Part I: validation of numerical simulations. Journal of Earthquake Engineering, 13:155-169.

Kontoe S., Zdravkovic L., Potts D., Mentiki C. (2008). "Case study on seismic tunnel response". Canadian Geotechnical Journal 45: 1743–1764.

Kontoe S, Avgerinos V, Potts DM. (2014). "Numerical validation of analytical solutions and their use for equivalent-linear seismic analysis of circular tunnels". Soil Dyn Earthq Eng 2014;66:206–19.

Kottke A.R., Rathje E.M. (2008) Technical Manual for STRATA. PEER Report 2008/10. University of California, Berkeley, California.

Kouretzis G., Bouckovalas G., Sofianos A., Yiouta Mitra P. (2007). "Detrimental effects of urban tunnels on design seismic ground motions". Proceedings of the 2nd Japan-Greece Workshop on Seismic Design, Observation, and Retrofit of Foundations, April 3-4, 2007, Tokyo, Japan.

Kouretzis G., Sloan S., Carter J. (2013). " Effect of interface friction on tunnel liner internal forces due to seismic S- and P-wave propagation", Soil Dynamics and Earthquake Engineering, 46:41-51.

Kramer S.T., (1996). Geotechnical earthquake engineering. Prentice-Hall Inc. ISBN: 0-13-374943-6.

Kuesel T. R. (1969). "Earthquake Design Criteria for Subways", Journal of the Structural Divisions, ASCE, Vol. 95, No. ST6, June 1969.

Kuhlemeyer R.L., Lysmer J. (1973). "Finite element method accuracy for wave propagation problems". Journal of the Soil Mechanics and Foundations Division, ASCE, 99(5):421-427.

Lade P. V. (1977). "Elastoplastic stress-strain theory for cohesionless soil with crve yield surfaces". Int. J. Solid Struct., 13, 1019-1035.

Lancellotta R. (1993). Geotecnica. Zanichelli.

Lanzano G., Bilotta E., Russo G., Silvestri F., Madabhushi S.P.G. (2010). Dynamic centrifuge tests on shallow tunnel models in dry sand. In: Proceedings of the VII International Conference on Physical Modelling in Geotechnics (ICPMG 2010), 561-567, Taylor & Francis, Zurich.

Lanzano G., Bilotta E., Russo G., Silvestri F., Madabhushi S.P.G. (2012). "Centrifuge Modelling of seismic loading on tunnels in sand", Geotechnical Test Journal 35(6):854-869. DOI 10.1520/GTJ104348.

Lanzo G., Silvestri F. (1999). "Risposta sismica locale, teoria ed esperienze", Hevellius edizioni, ISBN 88-86977-13- 1

Lee V.W., Karl J. (1992). "Diffraction of SV-waves by underground, circular, cylindrical cavities". Soil Dyn Earthq Eng 11:445–456

Lee S.W., Cheang W., Swolfs W., Brinkgreve R. (2009). " Plaxis-GiD Modelling of Tunnel-Pile Interaction", EURO:TUN 2009, 2nd International Conference on Computational Methods in Tunnelling, At Ruhr University Bochum, (2009)

Lo Presti D.C.F., Pallara O.. Lancellotta R., Armandi, M., Maniscalco, R. (1993). "Monotonic and Cyclic Loading Behaviour of Two Sands at Small Strains". Geotech. Testing Journal, Vol. 16, No. 4, pp. 409-424.

Loke M.H. (2013). Tutorial: 2-D and 3-D electrical imaging surveys.

Luco J.E., De Barros F.C.P. (1994). "Dynamic Displacements and stresses in the vicinity of a cylindrical cavity embedded in a half-space". Earthquake Engineering and Structural Dynamics 23: 321–340.

Lysmer J., Kuhlemeyer R.L. (1969). "Finite dynamic model for infinite media". Journal of the Engineering Mechanics Division, ASCE, 95(4):859-878.

Madabhushi G. (2014). "Centrifuge modelling for Civil Engineers". CRC Press, Boca Raton, Florida, USA, 324 p. ISBN 9780415668248.

Marshall, A.M., Haji, T. (2015). “An analytical study of tunnel-pile interaction”. Tunn. Undergr. Sp. Technol. 45, 43 –51 (2015).

Massimino M.R., Abate G., Corsico S., Louarn R. (2019). “Comparison between two approaches for non-linear fem modelling of the seismic behaviour of a coupled soil-structure system”. Geotech Geol Eng. Volume: 37. Issue: 3, pp. 1957-1975.

Masoud R.M., Mohammad H.B. (2016). “Seismic ground motion amplification pattern induced by a subway tunnel: shaking table testing and numerical simulation”. Soil Dynamics and Earthquake Engineering, 2016, 83: 81 – 97

Matsubara K., Hirasawa K., Urano K. (1995). “On the wavelength for seismic design of underground pipeline structures”, Proceedings of the First International Conference on Earthquake Geotechnical Engineering. pp. 587 - 590.

Matsuoka H., Nakai T. (1974). “Stress deformation and strength characteristics of soil under three different principal stresses”. Proc. JSCE, 232, 59-70.

Maugeri M., Cavallaro A., Grasso S. (2006). “Volcanic soil characterisation and site response analysis in the city of Catania”, Conference (San Francisco): Proceedings of the 8th National Conference on Earthquake Engineering - ISBN: 1-932884-25-4

Mentrey Ph., Willam K. J. (1995). “Triaxial Failure Criterion for Concrete and its Generalization”. ACI Structural Journal, vol. 92, pp. 311–318, May/June 1995.

Merritt J.L., Monsees J.E., Hendron A.J., Jr. (1985). “Seismic design of underground structures”, Proceedings of the 1985 Rapid Excavation Tunneling Conference, vol. 1, pp. 104 -131.

Miliziano S., de Lillis A. (2019). “Predicted and observed settlements induced by the mechanized tunnel excavation of metro line C near S. Giovanni station in

Rome". In Tunnelling and underground space technology - ISSN 0886-7798. - 86(2019), pp. 236-246.

Mitra Y.P., Kouretzis G., Bouckovalas G. (2007). "Effect of underground structures in earthquake resistant design of surface structures". In: Proceedings of Sessions of Geo-Denver 2007 Congress: Dynamic Response and Soil Properties (GSP 160). Geotechnical Special Publication, 2007.

Mohammadi J. (2010). Tunnel Face Stability Analysis in Soft Ground by EPB Method (Case Study: Tehran Metro Line 7). M'Sc Thesis. Tehran, Iran.

Monaco P., Totani G., Totani F., Grasso S., Maugeri M. (2011). "Site Effects And Site Amplification due to the 2009 Abruzzo Earthquake", WIT Transactions on the Built Environment. Volume 120, pp. 29-40, 2011.

Mroz Z. (1967). "On the description of anisotropic hardening". J. Mech. Phys. Solids, 15, 163-175.

Muir Wood D., Belkheir K., Liu D. F. (1994). "Strain-softening and state parameter for sand modeling". Geotechnique, 44, (2), 335-339.

Muir Wood D. (2004). "Geotechnical modelling". Spon Press, Taylor & Francs Group, Oxfordshire, UK. EAN: 9780419237303

Nakamura Y. (1989). "A Method for Dynamic Characteristics Estimation of Subsurface Using Microtremor on the Ground Surface". Quarterly Report of RTRI, 30(1), pp. 25-33.

Naqvi, M.W., Akhtar, M.F., Zaid, M. et al. (2020). " Effect of Superstructure on the Stability of Underground Tunnels". Transp. Infrastruct. Geotech. (2020). https://doi.org/10.1007/s40515-020-00119-6.

Navarro C. (1992). "Effect of adjoining structures on seismic response of tunnels". International Journal for Numerical and Analytical Methods in Geomechanics, 1992, 16(11): 797 – 814.

Newark N. M. (1968). “Problems in Wave Propagation in Soil and Rock”, International Symposium on Wave Propagation and Dynamic Properties of Earth Materials, 1968.

Nogoshi M., Igarashi, T. (1970). “On the propagation characteristics of microtremors”, J. Seism. Soc. Japan 23, pp. 264-280 (in Japanese with English abstract).

Nogoshi M., Igarashi T. (1971). “On the amplitude characteristics of microtremors”. J. Seism. Soc. Japan. 24, pp. 24-40 (in Japanese with English abstract).

Nova R. (2002). Fondamenti di meccanica delle terre. McGraw-Hill. EAN: 9788838608940.

NTC (2018). “Norme Tecniche per le Costruzioni”, 17/01/2018

Owen G. N., Scholl R. E. (1981). “Earthquake Engineering of Large Underground Structures”, prepared for the Federal Highway Administration, FHWA/RD-80/195, 1981.

Panzera F., Lombardo G., Rigano R. (2011). "Use of Different Approaches to Estimate Seismic Hazard: the Study Cases of Catania and Siracusa, Italy"; Bollettino di Geofisica Teorica e Applicata, vol. 52, 4, pp. 687 - 706.

Pastore V., Turello R. (2000). Geotechnical zoning of the urban area of Catania for earthquake engineering purposes. In Faccioli and Pessina.(eds), The Catania Project: Earthquake Damage Scenarios for a high risk area in the Mediterranean, 23-30, Roma: CNR-Gruppo Nazionale per la difesa dai terremoti.

Peck R.B., Hendron A.J., Mohraz B. (1972). “State of art in soft ground tunneling”. In: Proceedings of the rapid excavation and tunneling conference. American Institute of Mining, Metallurgical and Petroleum Engineers, New York, NY, pp 259–286

Pecker A., Chatzigogos C.T. (2010). “Nonlinear soil structure interaction: impact on the seismic response of structures”. Geotech Geol Earthq Eng 17:79–103

Penzien J. (2000). “Seismically-induced racking of tunnel linings”, Int.Earthquake Eng. Struct. Dyn. 29, 683- 691.

Pitilakis K., Tsinidis G., Chalatis A., Kirtas E. (2010). “ Estimation of seismic shear stresses in the perimeter of underground structures”. In: Proceedings of Sixth Hellenic Geotechnical and Geoenvironmental Engineering Conference. Volos, Greece [in Greek].

Pitilakis K., Tsinidis G., Leanza A., Maugeri M. (2014). “Seismic behaviour of circular tunnels accounting for above ground structures interaction effects”. Soil Dyn Earthq Eng 67:1–15

Pitilakis K., Tsinidis G. (2014).“ Performance and seismic design of underground structures”, In: Maugeri M and Soccodato C (eds.) Earthquake geotechnical engineering design, Geotechnical Geological and Earthquake Engineering, 28: 279-340, Springer international publishing, Switzerland.

Power M.S. Rosidi D., Kaneshiro J. (1996). “Strawman: screening, evaluation, and retrofit design of tunnels”, Vol. III, Report Draft. National Center for Earthquake Engineering Research, Buffalo, New York.

Power M., Rosidi D., Kaneshiro J., Gilstrap S., Chiou S.J. (1998). “Summary and evaluation of procedures for the seismic design of tunnels”. Final Report for Task 112-d-5.3(c). National Center for Earthquake Engineering Research, Buffalo, New York.

Power, M., Rosidi, D., Kaneshiro, J., (1998). “Seismic vulnerability of tunnels-revisited”. In: Ozedimir, L., Ed. . Proceedings of the North American Tunneling Conference. Elsevier, Long Beach, CA, USA.

Prager W. (1949) “Recent Developments in the Mathematical Theory of Plasticity”, Journal of Applied Physics 20, 235 (1949).
https://doi.org/10.1063/1.1698348

Prevost J. H. (1977). “Mathematical modeling of monotonic and cyclic undrained clay behaviour”. Int. J. Numer. Analyt. Mech. Geomech., 1, 195-216.

Prevost J. H. (1978-a). "Anisotropic undrained stress-strain behaviour of clays". J. Geotech. Eng. Div., ASCE, 104 (GT8), 1174-1194.

Prevost J. H. (1978-b). "Plasticity theory for soil stress behaviour". J. Eng. Mech. Div., ASCE, 104 (EM5), 1075-1090.

Rampello S., Callisto L., Viggiani G., Soccodato F.M. (2012). "Evaluating the effects of tunnelling on historical buildings: the example of a new subway in Rome". Geomechanics and tunnelling, 5 (3): 275-299. ISSN 1865-7362, DOI 10.1002/geot.201200017.

Rampello S., Fantera L., Masini L. (2019). "Efficiency of embedded barriers to mitigate tunnelling effects". Tunnelling and Underground Space Technology, 89: 109-124, DOI 10.1016/j.tust.2016.03.02.

Roscoe P.W., Schofield A.N., Thurairjah A. (1963). "Yielding of clays in state wetter than critical". Géotechnique, 13 (3), 211-240.

Rouainia M., Muir Wood D. (2001). "Implicit numerical integration for a kinematic hardening soil plasticity model". Int. J. for Num. and Analyt. Meth. in Geomech., 25, (13), 1305-1325.

Rowe R. (1992). "Tunnelling in Seismic Zones", Tunnels & Tunnelling, December 1992.

Sakurai A., Takahashi T. (1969). "Dynamic Stresses of Underground Pipeline during Earthquakes", Proceedings of the 4th World Conference on Earthquake Engineering, 1969.

Salim N.M., Jafaar Lafta S (2017). "The impact of driving and loading piles on existing tunnel". Imp. J. Interdiscip. Res. 3 (7), 2454 – 1362 (2017).

Schnabel P.B., Lysmer J., Seed H.B. (1972) Shake: A computer program for earthquake response analysis of horizontally-layered sites. Technical Report EERC-72/12, Earthquake Engineering Research Center, University of California, Berkeley, CA, 1972.

Schofield A.N., Wroth C.P. (1968). “Critical state soil mechanics”. McGray-Hill, New York.

Schofield A.N. (1981). “Dynamic and earthquake centrifuge modelling”. In: Proceedings of the International Conference on Recent Advances in Geotechnical Earthquake Engineering and Soil Dynamics, 1081-1100, University of Missouri-Rolla, USA.

Schwartz C.W., Einstein H.H. (1980). “Improved design of tunnel supports: vol. 1 - simplified analysis for ground structure interaction in tunneling”, Report no. UMTA-MA-06-0100-80-4. US DOT, Urban Mass Transportation Administration.

Sedarat H., Kozak A., Hashash Y.M.A., Shamsabadi A. and Krimotat A. (2009). “Contact interface in seismic analysis of circular tunnels”, Tunnelling and Underground Space Technology, 24(4):482-490.

Sharma, S., Judd, W.R., (1991). Underground opening damage from earthquakes. Eng. Geol. 30, 263 - 276.

Smerzini C., Aviles J., Paolucci R., Sanchez-Sesma F.J. (2009). “Effect of underground cavities on surface earthquake ground motion under SH wave propagation”. Earthquake Engineering and Structural Dynamics 38: 1441–1460.

St. John C.M., Zahrah T.F. (1987). “A seismic design of underground structures”. Tunneling Underground Space Technol. 2 2 , 165 - 197.

Stevens, P.R., (1977). “A review of the effects of earthquakes on underground mines”. United States Geological Survey Open File Report 77 - 313. US Energy Research and Development Administration, Reston, VA.

Tamagnini C. (2002). “Il comportamento anisotropo dei geomateriali. Parte II: Applicazione della teoria della plasticità”.

Tsinidis, G., Pitilakis, K., Anagnostopoulo, C. (2016). “ Circular tunnels in sand: dynamic response and efficiency of seismic analysis methods at extreme lining flexibilities”. Bulletin of the Earthquake Engineering, 14, 2903–2929. http://dx.doi.org/10.1007/s10518-016-9928-1.

Tsinidis G., Leanza A., Pitilakis K., Maugeri M. (2014). “Seismic Behavior of Shallow Tunnels Accounting for the Surface Structures Interaction Effects”. Conference: 2nd Eastern European Tunnelling ConferenceAt: Athens, Greece DOI: 10.13140/2.1.5150.1122.

UNI9916-DIN4150-3, (1999). Structural vibration – Part 3: Effects of vibration on structures.

Yao J., Taylor R.N., Mcnamara A.M. (2008). “ The effects of loaded bored piles on existing tunnels”, Geotech.Asp. Undergr. Constr. Soft Gr. - 6th Int. Symp., no. 1988, pp. 735 – 741, 2008.

Yeh G. C. K. (1974). “Seismic Analysis of Slender Buried Beams”, Bulletin of the Seismological Society of America, Vol.64, No. 5, 1974.

Yokota K., Imai T., Konno M. (1981). “Dynamic Deformation Charact. of Soils Determined by Lab. Tests”. OYO Tec. Rep. 3, pp. 13-37.

Wang J.-N.(1993). “Seismic Design of Tunnels: A State-of-the-Art Approach”, Monograph, monograph 7. Parsons, Brinckerhoff, Quade and Douglas Inc, New York.

Wang W.L., Wang T.T., Su J.J., Lin C.H., Sengineering C.R., Huang T.H. (2001). “Assessment of damage in mountain tunnels due to the Taiwan Chi-Chi earthquake”. Tunnelling and Underground Space Technology 16: 133–150.

Wang Z.Z., Gao B., Jiang Y.J., Yuan S. (2009). “Investigation and assessment on mountain tunnels and geotechnical damage after the Wenchuan earthquake”. Science in China Series E: Technological Sciences 52(2): 549–558.

Wang H.F., Lou M.L., Chen X., Zhai Y.M. (2013). “Structure – soil – structure interaction between underground structure and ground structure”. Soil Dynamics and Earthquake Engineering, 2013, 54: 31 – 38.

Wang G., Yuan M., Ma X. et al. (2017). “Numerical study on the seismic response of the underground subway station- surrounding soil mass-ground adjacent building system”. Front. Struct. Civ. Eng. 11, 424–435 (2017). https://doi.org/10.1007/s11709-016-0381-7.

Wang H. F. (2018). “Structure-Soil-Structure Interaction between Underground Structure and Surface Structure”. In book: Earthquakes - Forecast, Prognosis and Earthquake Resistant Construction. DOI: 10.5772/intechopen.76243.

Wang G., Yuan M., Miao Y., Wu J., Wang Y. (2018). “Experimental study on seismic response of underground tunnel-soil-surface structure interaction system”. Tunnelling and Underground Space Technology Volume 76, June 2018, Pages 145-159. https://doi.org/10.1016/j.tust.2018.03.015.

Zidan A.F., Ramadan O.M.O. (2015). “Three-dimensional numerical analysis of the effects of tunnelling near piled structures”. KSCE J. Civ. Eng. 19 (4), 917 – 928 (2015).

La borsa di dottorato è stata cofinanziata con risorse del
Programma Operativo Nazionale Ricerca e Innovazione 2014-2020 (CCI 2014IT16M2OP005),
Fondo Sociale Europeo, Azione I.1 “Dottorati Innovativi con caratterizzazione Industriale”

UNIONE EUROPEA
Fondo Sociale Europeo

Ministero dell'Università
e della Ricerca

PON
RICERCA
E INNOVAZIONE
2014 - 2020